A COMBUSTION MODEL FOR WALL-WETTING DIRECT-INJECTION DIESEL ENGINES

by

Hector Sindano B.Eng(Zambia),M.Sc(Reading)

A Doctoral Thesis
submitted in partial fulfilment of the
requirements for the award of
Doctor of Philosophy
of Loughborough University of Technology

November 1988

Supervisor: Professor J C Dent, PhD, CEng
Department of Mechanical Engineering

SYNOPSIS

The work presented constitutes an original approach to the phenomenological modelling of combustion in wall-wetting direct injection diesel engines. Starting with the modelling of fuel film development on the piston wall, the model covers essential aspects involved in mixture preparation in the engine and its subsequent combustion. Experiments using optical methods were undertaken to measure various characteristic dimensions of the fuel film along the piston wall. Predicted results are compared with empirical data obtained in engine experiments and used to improve the formulation of wall-jet equations used to describe fuel film flow. Velocity and scalar quantity profiles in the region close to the film surface are described, based on the theory of turbulent boundary layer flow over a porous flat plate with mass injection from the surface. This is done for conditions with and without combustion, thus defining the distribution of mixture strength in the gaseous stream adjacent to the wall. These principles were incorporated in an existing thermodynamic model to illustrate their influence on important engine parameters such as pressure, temperature, and heat release rate. Predictions for the formation of smoke and NOx emissions are carried out to address the problem of poor exhaust emissions associated with wall-wetting diesel engines. A description of the alterations made to improve the computational efficiency of the existing thermodynamic model is also provided. These make the implementation of the program possible on all machines equipped with standard FORTRAN 77 Compilers.

ACKNOWLEDGEMENTS

The author wishes to express his gratitude to the following:

Professor J.C. Dent for supervising this project and also for arranging and providing financial assistance in the later stages of this project.

Collegues and members of the technician staff of the Mechanical Engineering Department for their assistance in sundry ways too numerous to outline here.

The Association of Commonwealth Universities for the Scholarship that financed the early part of the programme.

The University of Zambia for a study leave to allow me to undertake this research.

My long-suffering wife for bearing the brunt of my 'Research Blues' with fortitude and grace.

And finally I am forever thankful to the Lord my God for granting me an opportunity to 'taste and see that He is Good'.

PUBLICATIONS

The following paper has been published based on part of the work reported in Chapter 5:

Sindano, H. and Dent, J.C: Modelling of Injected Fuel Film Development and Evaporation in a Wall-Wetting Direct Injection Diesel Engine. Proc. IMechE, International Conference on Combustion in Engines, 10-12 May 1988, London.

NOTATION

B	Mass Transfer Number
C_f	Friction Coefficient
C_p	Specific Heat Capacity (kJ/kg.K)
d'	Equivalent Injector Nozzle Diameter (m)
D	Binary Diffusion Coefficient (m^2/s)
Fr	Froude Number
g	Mass Transfer Conductance for high transfer rate ($kg/m^2/s$)
g^*	Mass Transfer Conductance under Reynolds Anology Conditions
h	Heat Transfer Coefficient ($kW/m^2/K$)
h_{fg}	Enthalpy of Vaporisation (kJ/kg)
H_o	Lower Calorific Value of the Fuel (kJ/kg)
I	Charge mass moment of inertia ($kg.m^2$)
k	Turbulence kinetic energy (kJ)
ℓ	Integral length scale of turbulence (m)
m	Non-Dimensionalised mass flux
m''	Mass Flux ($kg/m^2/s$)
n	Radical nuclei number density ($particles/m^3$)
N	Soot particle number density ($particles/m^3$)
P	Pressure (Pa or Bar)
Pr	Prandtl Number
Q	Charge heat content (kJ)
q''	Heat Flux (kW/m^2)
r	Stoichiometric Air/Fuel Ratio
r_j	Radius of the fuel spray (m)
R	Gas Constant (kJ/kg.K)
Re	Reynolds Number
s	Film Thickness (m)
SMD	Sauter Mean Diameter of the fuel spray (m)
t	Time (s)
T	Temperature (K)
u	Local velocity in the fuel spray (m/s)
U_{fe}	Injected fuel film equilibrium velocity (m/s)
v	Velocity normal to the direction of flow (m/s)
V	Volume (m^3)

We	Weber Number
x,y	Cartesian Coordinates
z	Non-Dimensional velocity
α	Swirl Angular Momentum ($kg.m^2/s$)
β	Mass Transfer Coefficient (m/s)
γ	Isentropic Exponent
δ	Boundary Layer Thickness (m)
ϵ	Turbulence eddy dissipation rate (m^2/s)
θ	Film Spray Angle (Degrees)
λ	Dynamic similitude length scale factor
μ	Dynamic viscosity (Pa.s)
ν	Kinematic viscosity (m^2/s)
ξ	Non-Dimensional height above the film surface
σ	Surface tension of the fuel (N/m)
τ	Shear stress (N/m^2) or Turbulence mixing time (s) (in context)
φ ϕ	Angles
ω	Swirl Angular velocity (rad/s)

SUBSCRIPTS

BP	Boiling Point condition
ch	Charge mean condition
COMB	Combustion
COND	Conduction
CONV	Convection
CR	Critical condition
EVAP	Evaporation
f	Relating to the fuel
G	Relating to the bulk gas stream
H	Relating to thermal properties
j	Fuel spray jet
m	Conditions at the axis of the fuel spray
o	Conditions at injector nozzle exit
O_2	Oxygen
RAD	Radiation

s	Pertaining to the fuel film surface
wall	On the piston wall

CONTENTS

CHAPTER 1 : LITERATURE SURVEY

1.1 INTRODUCTION

The need for an enhanced understanding of diesel engine combustion has grown significantly in the past several years due to the demand for improved fuel economy and exhaust emissions in passenger cars. Combustion models have been used by researchers to gain useful insight into the nature of diesel engine combustion. Heywood (1), and Mehta (2) have both given reviews of the various models available for this purpose. The models are generally classified into the following major categories:

i. Zero-dimensional
ii. Quasi-dimensional
iii. Multi-dimensional

A detailed discussion of these classifications has been provided by Heywood and also by Mehta. As a general rule, multi-dimensional models tend to involve long and laborious computational algorithms which, though they provide detailed information about the flow field, take up large amounts of computing time. As a result, one of the major drawbacks of multi-dimensional modelling, besides the effort required to code the algorithm, is the uncompetitive cost effectiveness. Parametric studies in diesel engines require rapidly resolving algorithms in order to highlight the significant trends on which detailed experimental investigation may be based. So it is essential when developing combustion models to apply the correct dimensional detail, bearing in mind that too simple a model will give incorrect results, while a very complex model may unnecessarily increase costs.

Phenomenological models combine attributes from zero and quasi-dimensional models to produce rapidly resolving algorithms that have found wide application in engine diagnostic and parametric studies such as that of Shahed et al (3). They are structured around thermodynamic analysis of cylinder contents, and empirical or semi-

analytical equations to describe the transfer of mass, momentum, and energy during engine operation. Unlike models that are based on the prediction of cylinder pressure from a heat release rate empirically correlated with fuel injection (Lyn (4)), several phenomenological models incorporate turbulent mixing processes using semi-analytical entrainment functions (Shahed et al (5), Dent and Mehta (6), Dent et al (7)). This enables the modelling of exhaust emissions to be related to the level of turbulence in the engine cylinder.

The present work describes the development of a mathematical model designed to evaluate the performance of a wall-wetting direct injection diesel engine. The work forms part of a more extensive project to develop a phenomenological model for predicting the performance of quiescent and swirl assisted direct injection diesel engines. Various aspects of this project have been reported in several publications (6,7) which provide a fairly accurate guide to the different stages in the development process, and more recently Kyriakides et al (8) have given the updated version.

1.2 THE CASE FOR DI DIESEL ENGINES

It is a widely held view (Monaghan (9), Cichoki and Cartellieri (10)) that the fuel economy advantage of the diesel engine is unsurpassed by any other internal combustion engine. So the rise in the cost of petroleum, coupled with supply interruptions witnessed in the last few years have inevitably led to increased research activity in the application of diesel engines to light and medium load conditions. The direct injection (DI) diesel engine offers a better fuel economy (around 10% gain) than the indirect injection (IDI) engine (9), yet almost all of today's commercially available passenger car diesel engines utilise the IDI engine (10). To understand the reason for this, it is necessary to look at the differences in design between the two types of engine.

To achieve optimum performance in diesel engines, combustion processes

need to be controlled so as to avoid excessive peak pressures in the cylinder, and rate of pressure rise. At the same time it is essential to ensure that a large proportion of the injected fuel is burnt early in the expansion stroke. Appropriate design of the combustion chamber is thus necessary to attain the desired goal.

In the DI (also referred to as the open chamber) engine, fuel is injected directly into a combustion space, usually located on the piston crown. Figures 1.1 to 1.4 show several such designs, starting with the quiescent DI engine (Fig. 1.1) in which the fuel spray is used to create the turbulence necessary for fuel/air mixing, through to the high swirl engine (Fig. 1.4).

The design of the IDI engine differs from that of the DI in that it makes use of a combustion space divided into two compartments, separated by a restricted passage (Taylor (11)). The passage is designed to induce large pressure differences during combustion, between the compartments. The chambers illustrated in Figure 1.5 come under this classification. In some versions of the IDI, the pre-combustion chamber, into which the fuel is injected, is designed to generate intense swirling air motion (swirl chamber) to enhance the mixing of fuel and air (Fig. 1.5(a)). The large pressure rise during combustion in the pre-chamber forces the hot gases containing unburnt fuel vapour into the cylinder, through the restricted passage, at a high velocity. This produces intense turbulence and fuel-air mixing, resulting in excellent conditions for combustion and reduced levels of exhaust smoke (9). As the formation of NO_x in engines is largely dependent on temperature, and linearly on the availability of oxygen (Whitehouse and Baluswamy (12), Lavoie et al (13)), the rich mixture in the pre-combustion chamber results in relatively low NO_x formation which "freezes" as the temperature drops below 2100K due to the throttling effect of the throat. Consequently, IDI engines are known to produce lower NO_x emissions (9, 10). The smoke-limited power output of a high speed DI engine can be up to 15% worse than an equivalent IDI engine (9). Fig. 1.6 shows a comparison of the smoke limited power

output, between an IDI and some DI engines. Engine speed in IDI engines is not limited by the combustion process because fuel-air mixing is controlled largely by the rate at which the charge emerges from the pre-chamber (11). In high speed engines, mean piston speeds may reach 12.2 m/s before friction horsepower limits any further speed increase (Fraas (14)), whereas combustion gases and rich fuel-air mixtures from the pre-chamber have velocities from ten to thirty times the mean piston speed (Judge (15)). The major disadvantages of the IDI engine relate to the very high compression ratios (typically 22:1) required for operation, which result in unfavourably high thermal stresses. Also the high heat loss due to intense air motion when combined with a high surface to volume ratio results in poor cold starting characteristics, which necessitate the use of glow-plugs, and significant loss in thermal efficiency. Due to high pressure in the pre-chamber, design of the IDI cylinder head needs to be more robust, which is more expensive. In view of the disadvantages associated with the IDI engine, research activity directed at the DI engine, has therefore been aimed at improving emission and noise levels, while maintaining the superior fuel economy.

1.2.1 Quiescent Chamber DI Engines

The quiescent DI engine finds much use in industrial and marine applications where, because of the low engine speed, sufficient time is available for mixture formation, based only on the turbulence generated by the spray. A very efficient fuel injection system is required in order to distribute the fuel adequately and so promote mixing. Robustness of the engine permits use of high injection pressure. As a result, quiescent chamber engines tend to use multi-hole nozzles with up to twelve holes (Lilly (16)), depending on engine bore. The use of more than 10 orifices generally results in interference between adjacent sprays, and so 4 to 10 orifices are more common (Burman and De Luca (17)). High injection pressures of the order of 1000 bar (8) are not uncommon with this design. These have a

two-fold requirement: to atomise the fuel sufficiently, and also to give the spray a high initial velocity needed for good air entrainment (Chiu et al (18)). For high speed engine applications, however, the rate of mixture formation in quiescent engines is not adequate, hence the application of the swirl chamber design is adopted in all passenger car engines.

1.2.2 Swirl Chamber DI Engines

In order to improve mixing processes, a well controlled air movement consisting mostly of swirl and squish (16) is introduced in the DI engine cylinder. This creates an environment favourable for the generation of turbulence, which has been identified (Dent (19)) as a significant mechanism for enhancing fuel/air mixing. The swirl element is generated by a suitably designed inlet port, shaped in one of the following most commonly utilised designs:

i. Masked valve: a typical example is shown in Figure 1.7. These are seldom used in production engines due to poor volumetric efficiency. They find much use, however, in research applications (for example Urlaub (20)) due to the versatility they offer for varying swirl ratio (i.e. Ratio of Swirl Revolutions to Engine Revolutions).

ii. Helical port: this generates swirl by imparting a spiral flow to the inlet air (Fig. 1.8).

iii. Directed port: here, the inlet port is introduced into the cylinder tangential to the wall in order to deflect the flow into a forced vortex (Fig. 1.9).

Although the helical port is aerodynamically better suited to the generation of swirl (16), limited cylinder-head space favours the directed port, hence its wider application.The squish component,

which is also essential in the formation of turbulence, depends on the ratio of the bore to the combustion chamber diameter (Fig. 1.10).

The optimisation of combustion chamber design to produce optimum swirl over a wide range of engine operating conditions is usually done experimentally. In spite of the advantage of working with in-cylinder measurements of swirl, the practical difficulties encountered lead to methods for evaluating swirl, based on steady state flow laboratory rigs as in the work of Urlaub (20), Watts and Scott (21), and Davis and Kent (22). The principle involved in relating steady flow rig data to in-cylinder swirl has been well illustrated by Morris and Dent (23) who demonstrated that similarity between the two systems is characterised by a ratio of the jet momentum flux to that of the cross swirl. A review by Morris (24) of various studies on the effects of swirl on engine performance shows evidence of an optimum swirl intensity for mixture formation at any given engine speed. The results of Watts and Scott (21), illustrated in Figure 1.11, show fuel consumption passing through a minimum, and the mean effective pressure through a maximum, as swirl level is varied, corresponding to the optimum swirl value. Similar trends were also reported by Alcock (25), and are corroborated by the results of Urlaub (20) shown in Figure 1.12 to illustrate the effect of injection timing on optimum swirl, represented by maximum mean effective pressure, and in Figure 1.13 to show swirl effect on smoke emission. At each engine speed, four values of smoke emission are possible corresponding to different mask heights (hence swirl intensity), and for engine speed higher than about 1350 rpm, the 10 mm mask gives minimum exhaust smoke. Any further increase in the mask height (e.g. to 14 mm) leads to higher smoke values. Care should be taken when attributing the results in Figures 1.12 and 1.13 solely to the effect of swirl since masked valves can also produce a tumbling air motion (Gosman et al (26)) and large scale turbulent mixing which will have an influence on the course of combustion. However, this appears to be dependent on the configuration used for positioning the shroud (Pinchon and Baritaud (27)). The configuration used by Urlaub (Figure 1.7) is designed to

direct the intake flow to provide maximum swirl. An identical configuration (Fig. 1.14) used by Pinchon and Baritaud (27) was found to generate mostly swirling motion. In any case, the photographic results of Lee (28) demonstrate that only swirl motion persists in the vicinity of TDC and in the expansion stroke at a level that would significantly influence the mixing of fuel and air. Urlaub's results may thus be taken to demonstrate the effect of air swirl.

1.3 THE DI ENGINE MODEL

The phenomenological DI diesel engine model being developed in a project of which the present contribution is a part, was first reported in a paper by Dent and Mehta (6). The phenomenological approach was chosen due to its competitiveness, in terms of processing time, to produce fairly accurate parametric and diagnostic results of performance over the full load range of an engine. This method of analysis addresses the problem from observed physical and empirical characteristics, such as the dominant role of air entrainment and turbulent mixing in diesel engine mixture formation, and avoids unnecessary computational rigour in favour of empirically derived expressions. As a result, the method can sometimes suffer from over-simplification of very complex phenomena, leading to inaccurate results. But once care and prudence have been exercised in the choice of governing equations, it has been consistently demonstrated that useful predictions such as those reported by Shahed et al (3), and also Kyriakides et al (8) can be made concerning engine performance.

As the early version of the model only addressed the quiescent chamber engine design, it was inapplicable to high speed diesel engines which rely, for satisfactory fuel/air mixing, on a high level of air movement. This reason, combined with the absence of exhaust emissions predictions, established the need for extending the model. The extended model, which included aspects of swirl and exhaust emissions (smoke) was reported in a subsequent paper by Dent et al (7). The model showed good agreement with published experimental data, and

also attempted to address the problem highlighted by the results of Nagao et al (29), and Watts and Scott (21), on the effects of over-swirling on smoke emissions. However, the model still lacked the accuracy to correctly predict magnitudes of smoke emission, although the trends were favourably predicted. Further development of the smoke model was thus necessary in order to improve the magnitudes of the smoke, and to include NO_x predictions. Kyriakides et al (8) describe the incorporation of NO_x emissions predictions in detail, including the effects of Exhaust Gas Recirculation (EGR). Once again the model predicted trends favourably, although absolute magnitudes could only be approximated. A point highlighted by the authors was that the program did not perform well when details relating to engines with very high injection pressure were to be modelled. This was attributed to the impingement of a significant quantity of the injected fuel on the piston walls, forming a thin liquid film . This suggests that the parts of the model used to describe mixture formation when jet impingement occured, were unsatisfactory and needed to be addressed once again. Although this problem was only observed in the quiescent version of the model, and was not considered a significant drawback in modelling swirl assisted DI engines, its importance is now felt when the model is used to study high-speed diesel engines designed to deposit a large proportion of the injected fuel on the walls of the combustion chamber (Neitz and D'Alfonso (30), Martin and Ahmad (31)). This has brought about the need for a further development of the model to take into account the wall-wetting direct injection diesel engine.

1.4 LITERATURE RELATING TO WALL-WETTING ENGINES

Pioneering work in developing the wall-wetting engine is attributed to Meurer (32) who developed the M.A.N. M-Combustion System. The engine was designed for heavy duty vehicles, and differs from conventional DI diesel engines in the method of mixture formation. In the M-system, fuel injected through a single-hole nozzle is deposited as a thin film on the walls of a spherical combustion bowl located in the piston

crown (Fig. 1.3). This creates extreme charge stratification in which the reactants are separated physically as well as spatially. This significantly reduces the fuel surface area to about 1/16th that afforded by droplet surface area (Meurer (33)), with the benefit of a reduced initial evaporation rate. Air swirl generated by a suitably designed inlet port, is intensified by forcing the charge into the combustion bowl during compression, so as to enhance evaporation of the fuel. The fuel, thus, only leaves the wall in the form of vapour, and is then steadily supplied for combustion through turbulent and thermal mixing processes (20) set up due to air motion, and density gradients. As a result of the reduction in premixed charge at the start of combustion, the maximum cylinder pressure is reduced as is the rate of pressure rise. As a consequence a significant reduction in engine noise is obtained (Urlaub (34), Neitz and Müller (35)). In addition, the engine has distinct advantages that make it readily adaptable to multifuel operation through the incorporation of a spark plug (Chmela (36)). Compared to other DI engines, the wall-wetting engine has relatively low NO_x emission levels, due to the lower combustion temperature that is associated with the engine. Figure 1.15 illustrates some typical results, showing NO_x emission over a wide load range for DI (stratified and conventional), and also IDI engines, together with those for a wall-wetting engine.

The smoke and unburnt hydrocarbon emission levels associated with wall-wetting engines have been found to be poor under certain load conditions (Martin and Ahmad (31), Zinner (37)). During low load conditions (idling and start-up) the poor exhaust emission characteristics have been attributed (35) to the fact that more fuel reaches the walls, and the low temperature leads to a slower rate of evaporation of the fuel. The incomplete combustion which results has been held responsible for the unpleasant exhaust odour. This is especially the case in wall-wetting engines where high levels of aldehyde concentration have been observed (35) in the exhaust. Urlaub (38) identifies the level of aldehyde concentration as the significant yardstick for measuring the intensity of exhaust gas odour. Figure

1.16 shows the effect of the injector nozzle diameter on exhaust gas aldehyde concentration. The results were obtained in a 125 mm bore and 142 mm stroke engine. It would appear from the figure that reducing the injector nozzle diameter improves the quality of the exhaust during low load operation. This may be attributed to the higher injection velocity which leads to improved turbulent mixing between fuel and air. This has been identified in quiescent chamber engines (19), where nozzle diameter variation plays a significant role in the generation of jet-induced turbulence. However there is a limit to which the reduction in nozzle diameter offers a solution for reducing exhaust emissions due to the fact that satisfactory full load operation cannot be achieved with very small nozzle diameters (35). A way round this problem is to modulate the fuel spray throughout the load range. At low load conditions the fuel spray is directed towards the centre of the combustion chamber while at high load most of the fuel is deposited on the piston wall. This principle has been used to design the "Controlled Direct Injection" (CDI) diesel engine (which has been described by Neitz and D'Alfonso (30). The change in spray direction is achieved by means of a specially designed pintle nozzle illustrated in Figure 1.17. The advantages of the 'CDI' over the conventional wall-wetting system apply only when operating under low load conditions and are given by Monaghan (39) as follows:

1. High relative velocity between fuel and air ensures good mixing so that smoke is minimised.

2. Only about 10% of the injected fuel reaches the wall (compared to around 90% in the conventional wall-wetting engine), so that unburnt hydrocarbons are reduced.

3. The long injection period ensures that combustion noise is kept low even at higher loads.

A noticeable shortcoming with the 'CDI' design is the increase in fuel consumption and smoke emission in the high-load range (35).As a result of the difficulties associated with trying to control

exhaust gas emissions in wall-wetting engines, the engine has enjoyed little commercial success, and is mostly limited to heavy duty vehicles such as in military applications where the need for multi-fuel applicability, and reduced engine noise, is overriding. This poor performance, especially when viewed in terms of the amount of past research activity in the field, has been attributed (31) to a general lack of understanding of the combustion processes involved. It is therefore necessary to address the problem from a fundamental standpoint, keeping in mind that an improved understanding of the processes would result in marked improvements in the performance of the wall-wetting engine.

The difficulties encountered when attempting to formulate a mathematical model for mixture formation in a wall-wetting diesel engine are well documented (Urlaub (34), Meurer and Urlaub (40)). As a result most attempts at modelling have only dealt with sub-processes and have mostly been of a qualitative nature used to supplement analysis of experimental data (Martin and Ahmad (31), Müller (41), Klanner (42)). Qualitatively, mixture formation in a wall-wetting engine is considered made up of the following sequence of mutually interacting subprocesses (34):

(a) Propagation of the film on the wall,
(b) Evaporation from the film into a gaseous boundary layer formed above the film,
(c) Turbulent mixing of the air distributed vapour and combustion.

A detailed look at each of these processes in turn follows, showing the present state of knowledge and understanding of the various processes.

1.4.1 Film Propagation

Although the pattern of film propagation is central to the characterisation of mixture formation, it is dealt with only slightly

in the literature (Urlaub (34), Meurer (43)), mostly by assigning approximate or mean values for surface area covered by the film. For example, Meurer (32) gives the area covered by the film as 40% of the combustion chamber surface area which value is later improved to 50% (34,40). These values are based on a physical inspection of the combustion bowl after running the engine. Müller (41) gives detailed experimental results showing the development of the film during motoring (Fig. 1.18) as well as during firing (Fig. 1.19). No attempt was made by him to correlate the development of the film with engine operating conditions. However the experimental data obtained constitute the most detailed experimental analysis of fuel film development available in the literature and are therefore very useful for providing an empirical insight into the mechanisms involved, and for validating mathematical models. His results show that the wetted surface area is not represented by a constant percentage of the combustion bowl surface area, but rather depends on the following parameters:

i. Nozzle geometry and direction of spray
ii. Swirl velocity
iii. Injection timing
iv. Load
v. Engine speed
vi. Physical properties of the fuel (especially density and viscosity).

In any case, almost all of Müller's results were well below 40%. It is possible that the higher injection pressure in Meurer's result accounted for the increased wetted area.

In order to completely characterise the flow of the film in the combustion chamber, the following parameters need to be determined;

i. Surface area of the film patch,
ii. Velocity of the film,
iii. Penetration,

iv. Film thickness.

Apart from the experimental work of Müller discussed above, the fluctuation of these variables in the engine with crank position is not documented in any literature. Meurer and Urlaub (40, 43) have dealt, to a limited extent with the propagation of the film (Fig. 1.20) along the piston wall. They concluded that although their experimental work on a test rig show a cushion of vapour forming between the film and the combustion chamber walls (ladenfrost phenomenon), this can scarcely be expected to occur at the operating pressures in automotive operation. As a result, simpler fluid mechanics formulations can be used to derive equations for penetration and velocity decay. Urlaub's theoretical studies of film propagation are described (34) as based on a simplified friction-heat-mass transfer analogy which is more commonly referred to as the Reynolds Analogy. The actual equations employed are not provided, so that it is not possible to evaluate the effectiveness of the model. The results are given in terms of mass of fuel evaporated (Fig. 1.21) and not penetration or surface area. The film velocity is assigned a constant value once jet impingement has occured, representing the mean relative velocity between the film and the swirl velocity (Fig. 1.22). But, as Klanner (20) has demonstrated, once the film has impinged on the wall, it experiences an exponential decay in velocity from a maximum value to a terminal velocity consistent with a balance of the interfacial and wall shear forces. It is possible to carry out a force balance on a control element of fluid shown in (Fig. 1.23) to derive the equation obtained by Klanner for velocity of the film, U_f, as:

$$U_f = \frac{C_f \rho_G U_G^2 s}{4 \mu_f} + \left[U_{fo} - \frac{C_f \rho_G U_G^2 s}{4 \mu_f}\right] . \exp\left(- \frac{2\mu_f}{\rho_f . s^2} t\right) \qquad (1.1)$$

where U_{fo} is the nozzle exit velocity (i.e. velocity of time t = 0) of the film and s the film thickness. By making t approach infinity, it becomes apparent that the equation is composed of a decaying component resulting from loss of momentum due to friction, and a uniform

component representing the effect of swirl. By non-dimensionalising eqn. (1.1) in the form shown in eqn.(1.2), Klanner was able to show theoretically, the response of film thickness with time as shown in Fig. 1.24.

$$\frac{U_f - U_{fe}}{U_{fo} - U_{fe}} = \exp\left[- \frac{2\mu_f}{\rho_f} \cdot \frac{t}{s^2} \right] \qquad (1.2)$$

U_{fe} is the constant terminal velocity which is given by equation (1.3), and illustrated in Figure 1.25, showing agreement with the model results of Meurer and Urlaub in Figure 1.20.

$$U_{fe} = U_G + \frac{2\mu_f}{C_f \cdot \rho_G s} - \left[\frac{4\mu_f}{C_f \cdot \rho_G \cdot s} U_G + \left(\frac{2\mu_f}{C_f \cdot \rho_G s} \right)^{2\ 1/2} \right] \qquad (1.3)$$

The uniform component represented by equation (1.3) has also been investigated by Squire (44) in considering flow visualisation in wind tunnels. By assuming unit width (Fig. 1.26) on an element of film, Squire shows that the change in thickness, ds, in time dt is represented by the amount of fluid flowing into the element, less the amount flowing out. Mathematically, this can be expressed as follows:

$$\frac{\partial s}{\partial t} = - \frac{\partial}{\partial x} \int_0^s U \, dy - \frac{\partial}{\partial z} \int_0^s V \, dy \qquad (1.4)$$

The partial differential equation in (1.4) is non-linear and not amenable to an analytical solution. However, by neglecting variables that have comparatively very low orders of magnitude, Squire (44) simplified the equation to give a solution of the following form:

$$\frac{\partial s}{\partial t} = - [As^2 + Bs^3] \qquad (1.5)$$

Both equations (1.3) and (1.5) assume that flow in the liquid film can be considered laminar, despite the air stream boundary layer experiencing turbulent flow. In both equations the injected velocity

component is much lower than that in wall-wetting engines where film flow is turbulent and unsteady (34). In the case of equation (1.5), the initial velocity is in fact zero (i.e. the film is initially at rest before the air stream acts on it).

It is clear from the foregoing, that some simplifying assumptions are necessary in order to formulate a working model for film propagation. Urlaub (34) suggests the following simplifications:

(i) Uniform film thickness

(ii) Uniform surface temperature

(iii) Diminution of the film surface area occurs to an equal extent with the overall thinning of the film. In other words, the surface area of the film halves, due to evaporation, when the film thickness has halved.

The first of these assumptions, though it greatly simplifies the analysis, does not accurately represent observed physical phenomena. It has been empirically demonstrated (41,42), and indeed a simple continuity consideration would show, that if the breadth of a liquid film increases as it flows, and mass conservation is assumed, then the film tapers at its leading edge. The second assumption is not far removed from observed phenomena, as work on liquid film cooling (45) has demonstrated that after the initial adjustment in the film temperature as it comes in contact with the hot gas stream, and the combustion chamber wall, the temperature settles for all practical purposes, at a uniform value. In the evaporation film case, this will be the saturation temperature. By making the suggested correction to the first assumption, the third assumption suggests a film patch drying up on the edges first and moving inwards. It is, therefore, a reasonable assumption to make.

1.4.2 Evaporation of the Film

Events on the gas-side of the film are much more complex and far less understood or touched upon in the literature. Apart from the vaporisation of the film, there is also turbulent mixing between the air and vapour streams (by boundary layer entrainment). There is a considerable body of published literature covering recent developments in the vaporisation of thin films (Shembharkar and Pai (45), Kanury (46), Warner and Emmons (47), Zucrow and Graham (48), Zucrow and Sellers (49)). The techniques that are being developed provide a fairly reliable tool for analysing fuel film evaporation in the engine. Qualitative analyses (34) show remarkable evidence (Fig. 1.21) that the rate of evaporation plays a major role in controlling the heat release rate in wall-wetting engines. Klanner (42) relates the rate of evaporation of the fuel to the rate at which film thickness reduces:

$$\dot{m}'' = - \rho_f \frac{ds}{dt} \qquad (1.6)$$

where s is the film thickness. This means that the diminution of the film has to be determined prior to the evaluation of evaporation. To calculate change in film thickness with time, Klanner used an exponential decay equation with fuel temperature as the controlling parameter:

$$\frac{ds}{dt} = - \frac{A\beta'}{\rho_f R_f T_f} \cdot \exp \left[- \frac{B}{T_f} \right] \qquad (1.7)$$

β' is the mass transfer coefficient between the film surface and the gaseous stream, corrected to take into account a phenomenon known as the "blocking effect" (Marxman (50)) whereby the presence of mass transfer at the surface leads to a reduction in the transfer of heat. The corrected coefficient is given in terms of the heat transfer coefficient as:

$$\beta' = \frac{h'}{\frac{h}{\beta}\left[1 - \frac{P_s}{P}\right]} \qquad (1.8)$$

where h' is the heat transfer coefficient, similarly corrected between the film and the gaseous stream, P_s the saturation vapour pressure on the surface which is assumed to be at the fuel temperature, and P the total cylinder pressure. The fuel film temperature, T_f, in equation (1.7) is derived by carrying out an energy balance on the liquid film, giving the following differential equation:

$$\frac{dT_f}{dt} = \frac{1}{\rho_f C_{pf} S}\left[h'T_G - h_f T_w - (h' + h_f) T_f - \frac{\beta' AL}{R_f . T_f}\left(\frac{1-T_f/T_{cr}}{1-T_{BP}/T_{cr}}\right)\right]^{0.38} \times \exp\left(-B/T_f\right) \qquad (1.9)$$

h_f is the heat transfer coefficient between the fuel film and the walls of the combustion chamber. The shortcoming in the foregoing analysis appears to be that Klanner only considered laminar effects not just within the liquid film (which would be acceptable according to Squire's analysis (44)) but his method of calculating mass transfer between the film and the boundary layer suggests that similar treatment is assumed for the gaseous phase. It is therefore expected that equation (1.6) would yield lower rates of evaporation than those expected in the engine.

Effects of High B on $\dot{m}''$

Although the corrections made above to β and h refer to laminar diffusion whereby high vapour pressure results in an interference between heat and mass transfer, an identical phenomenon in turbulent heat and mass transfer has been identified by Marxman (50), and also by Spalding (51). Instead of expressing mass flux from the film surface in terms of the familiar expression given below;

$$\dot{m}'' = g\,B \tag{1.16}$$

in the presence of a high mass tranfer rate from the surface, modification to equation (1.16) to account for the effect of reduced skin friction is necessary. This takes the following form:

$$\dot{m}'' = g\left(\frac{C_f}{C_{fo}}\right) B \tag{1.17}$$

where C_f is the resultant skin friction when mass transfer is high, and C_{fo} is the friction coefficient in the absence of mass transfer. This use of friction reduction to represent a reduction in mass transfer is based on Reynolds analogy between heat-mass and friction. The factor C_f/C_{fo} can be shown (Kays and Crawford (52), Lees (53)) to be given by the following expression:

$$\frac{C_f}{C_{fo}} = \frac{\ln(1+B)}{B} \tag{1.18}$$

where B is the mass transfer number defined as the ratio of enthalpy difference between the bulk air stream, and the liquid surface assumed to be at its boiling point, to the enthalpy of vaporisation of the film. The derivation of equation (1.18) can be better explained, analytically, by considering turbulent flow over a flat plate (this is illustrated in Chapter 4) together with the analogy between the transfer of heat and friction (Kays (54)). Substituting equation (1.18) into equation (1.17) gives an equation similar to that developed by Spalding (55):

$$\dot{m}'' = g^* \ln(1 + B) \tag{1.19}$$

where g* represents the mass transfer conductance which, from Reynold's Analogy, can be given as:

$$g^* = \frac{h}{C_p} \tag{1.20}$$

The mean heat transfer coefficient, h, between the film and the air stream is estimated from the standard correlation for turbulent flow over a flat plate (Schlichting (56)), so that equation (1.20) can be given as:

$$g^* = \frac{\rho_G \alpha_a}{\ell} \cdot \bar{N}u_l \tag{1.21}$$

and the Nusselt number, $\bar{N}u_l$, as:

$$\bar{N}u_l = 0.037\ Re_l^{0.8}\ Pr^{1/3} \tag{1.22}$$

A constant velocity based on half the maximum swirl magnitude has been used in the literature to evaluate Re_l (31). It is, however, the instantaneous difference between air velocity and the velocity on the film surface that must be used if accurate estimation of evaporation is to be made.

The mass transfer number, B, defined earlier in this section, can be formulated so as to include the effects of combustion as well as conduction from the piston and flame radiation to the vapourising film. Equation (1.23) gives the resulting expression:

$$B = \frac{C_{pf}\,(T_G - T_{BP}) + \frac{m_{O_2,G}}{r} \cdot H_o + \left(\frac{q''_{COND} + q''_{RAD}}{g^*}\right)}{h_{fg} + C_{pf}\,(T_{BP} - T_{ref})} \tag{1.23}$$

The relative significance of conduction and radiation is minor compared to convective effects. Radiation contributes an equivalent of 20% of the contribution due to convective heat transfer, and conductive effects from the wall are negligible (34). The following simplified expression has therefore been used in the analysis of

evaporation in wall-wetting engines (31).

$$B = \frac{C_p\,(T_G - T_{BP}) + \dfrac{mO_{2,G}}{r}\,.\,H_o}{h_{fg} + C_{pf}\,(T_{BP} - T_{wall})} \qquad (1.24)$$

1.4.3 Combustion

Combustion in the wall-wetting diesel engine is a combination of reaction in the boundary layer, and vapour phase combustion (20,31). Initial mixture formation occurs in air layers directly above the film, then a thermal mixing motion sets in (20) carrying the less dense burning masses on spiral paths towards the centre of the combustion chamber. Fresh air is simultaneously displaced towards the periphery, providing more oxygen for combustion near the wall. This thermal separation process is governed by a ratio of the density of the surrounding charge, and that of the burning mass. The centrifugal force on packets of burning mass, given by equation (1.25) below, determines the rate at which these regions are moved towards the axis of the combustion chamber:

$$\gamma_b = r\,\omega^2 \qquad (1.25)$$

where ω is the swirl angular velocity, and r the position radius of the burning mass under consideration, defined by Urlaub (20) as:

$$r = r_b \cos\left[(\phi - 1)^{1/2}\,.\,\psi\right] \qquad (1.26)$$

where r_b is the radius of the combustion chamber, ψ the angular displacement of the burning mass, and ϕ the ratio of the surrounding charge density to that of the burning mass, ρ_G/ρ_b. Equation (1.26) describes the path followed by burning mass towards the centre of the combustion chamber, thus by implication, it represents the mixing length for fuel and air on a large (integral) scale. It is, however,

the intricate inter-mixing on a molecular scale that is responsible for the reactions between fuel and oxidant (Magnussen (57)). In free jets, and also in multi-hole nozzle diesel engines, successful attempts at describing this mixing process exist (7,19), and some of the generalised approaches can be adapted to the wall-wetting engine (Plee (58)). However, no specific attempt has been made in the literature to formulate a model for mixing processes in a wall-wetting engine. Figures 1.27 to 1.31 show the results of a CONCHAS model calculation of the turbulence field in a spherical combustion chamber of a wall-wetting engine. The regions of high turbulence in Fig. 1.27 (marked 'H') represent areas in which fuel and air would mix and react favourably, and these correspond to areas of high swirl velocities (55). The basis of the mixing mechanism in an engine operating the MAN M-System was briefly explored by Dent (19), who considered a reaction zone above the film surface to separate the fuel and oxidant (Fig. 1.32). The rate of combustion was then considered to be controlled by the rate at which oxygen is supplied to the reaction zone. Figure 1.21 shows the result of a calculation for the rate of evaporation carried out by Urlaub (34), compared with the heat release diagram obtained on a wall-wetting engine. It may be concluded from the comparison in Figure 1.21 that sufficient oxidant is available in the layers above the fuel film to react with all the evaporated fuel. Combustion thus proceeds at a rate proportional to the rate of evaporation, as suggested by Urlaub.

From the observations made in the last paragraph it is apparent that combustion in the wall-wetting engine proceeds at a rate controlled by the lower flux-between air entrainment and fuel evaporation and diffusion - to the reaction zone. Mathematically, this may be expressed as follows:

$$\dot{m}''_{COMB} \propto MIN\left[\dot{m}''_{f}, \frac{\dot{m}''_{O2}}{r}\right] \qquad (1.27)$$

where r is the stoichiometric oxidant/fuel ratio. The experimental

data depicted in Figure 1.21 suggest that evaporation rate is slower than air flux to the reaction zone.

Marxman and Gilbert (50,59) have investigated air flux to the reaction zone, in a burning boundary layer with mass diffusion from the wall, a phenomenon very similar to that considered here, and conclude that although the mass fraction of oxidant approaches zero in the vicinity of the flame (Fig. 1.33) the gradient of oxygen concentration, however, becomes very high in the same vicinity. So they suggest calculating the transport rate of oxygen into the burning zone using the standard transport equation:

$$\dot{m}_{02} = \rho_u \, (\epsilon + D) \frac{\partial m_{02}}{\partial y} \qquad (1.28)$$

A detailed examination of air entrainment in the wall region is explored in a subsequent section of the present work dealing with the mathematical basis for the proposed combustion model.

1.5 DISCUSSION OF THE LITERATURE STUDY

It is clear from the literature surveyed in this chapter that much work remains to be accomplished in order to arrive at a consistent and coherent fundamental method of analysis for wall-wetting diesel engines. Most of the literature quoted above set out to investigate particular sub-processes within the very complex field of heterogenous combustion in diesel engines, and so do not offer a complete picture on which engine development can be based for solving some of the problems. For example, Urlaub devotes a significant portion of one of his papers (20) to the evaluation of the effects of swirl and the possibility of prescribing an optimal swirl intensity at any engine speed. Müller's work (41), on the other hand deals entirely with the behaviour and propagation of the fuel film on the combustion chamber wall using an entirely empirical approach and offering minimum analytical solutions. Other papers have dealt with exhaust emissions (35,38), potential of the engine for high speed applications (30), and

various other aspects of the engine. The one point that comes through from the literature is the high potential that the wall-wetting engine appears to have for replacing the IDI diesel as a prime mover in high speed passenger car engines (58). The reasons for this superiority can be attributed to various reasons amongst which the following are the most significant (31, 34, 35, 39):

i. Potential for lower fuel consumption than that obtainable from IDI diesels.
ii. Much lower engine noise and rates of pressure rise than in typical DI diesels.
iii. Easily adaptable for multifuel application.
iv. Low fuel injection pressures.
v. Low compression ratios.
vi. Reduced combustion temperatures.
v. Low NO_x emission.

The high hydrocarbon emissions and exhaust gas odour, however, have prevented a wider application of this engine, in spite of the associated advantages outlined above. The need for an improved understanding of the formation of pollutant emissions in this type of engine has thus, been clearly identified.

1.6 OUTLINE OF PRESENT OBJECTIVES

The present work aims at providing a feasible and coherent technique of formulating the processes of mixture formation in a wall-wetting DI diesel engine mathematically, based on empirical and semi-analytical equations. Starting from the impingement of the fuel jet on the combustion chamber wall, a mathematical model will be developed to study the interaction between swirl air and the film surface, and the nature of combustion, through to the formation of exhaust soot and NO_x emissions. Processes outlined above have been made analysable by certain simplifying assumptions consistent with observed physical

behaviour. These are outlined and given wherever they have been first introduced. The developed model will then be incorporated into a thermodynamic model developed and reported in an earlier publication (8), to show the resulting engine performance. Comparison of the data with experimental results will be made and experiments to characterise film developments will be undertaken to verify model predictions.

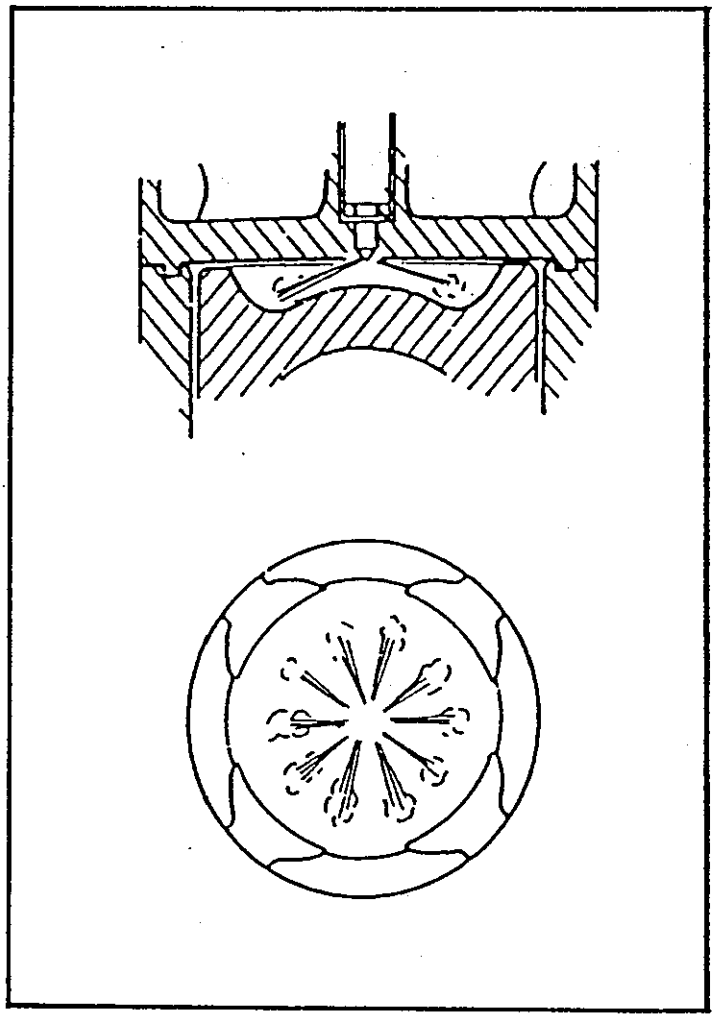

FIGURE 1.1: DIRECT INJECTION QUIESCENT CHAMBER GENERALLY USED IN LARGE ENGINES (16)

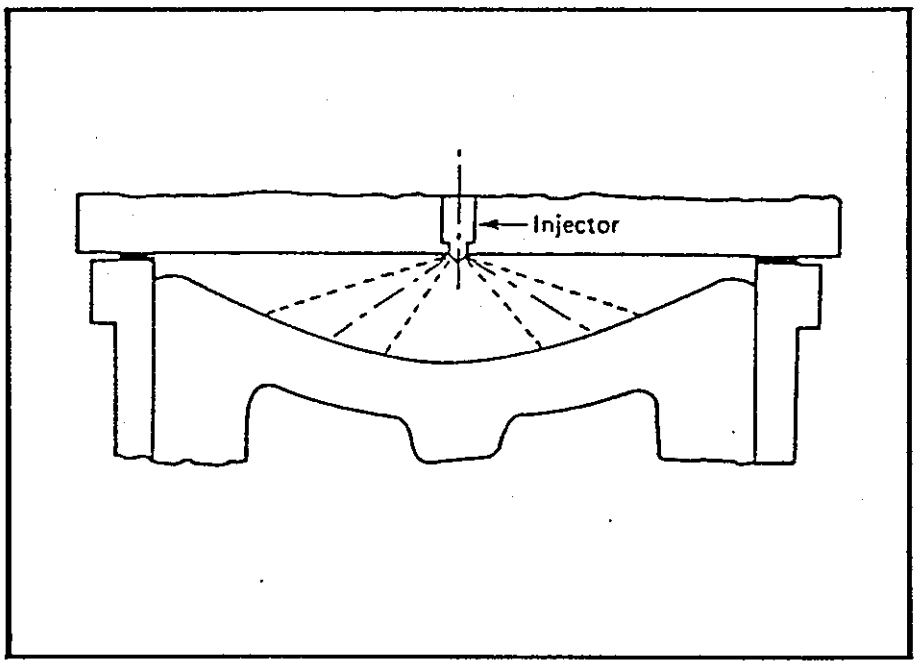

FIGURE 1.2: QUIESCENT COMBUSTION SYSTEM APPLIED MOSTLY TO ENGINES ABOVE 150 mm BORE (16)

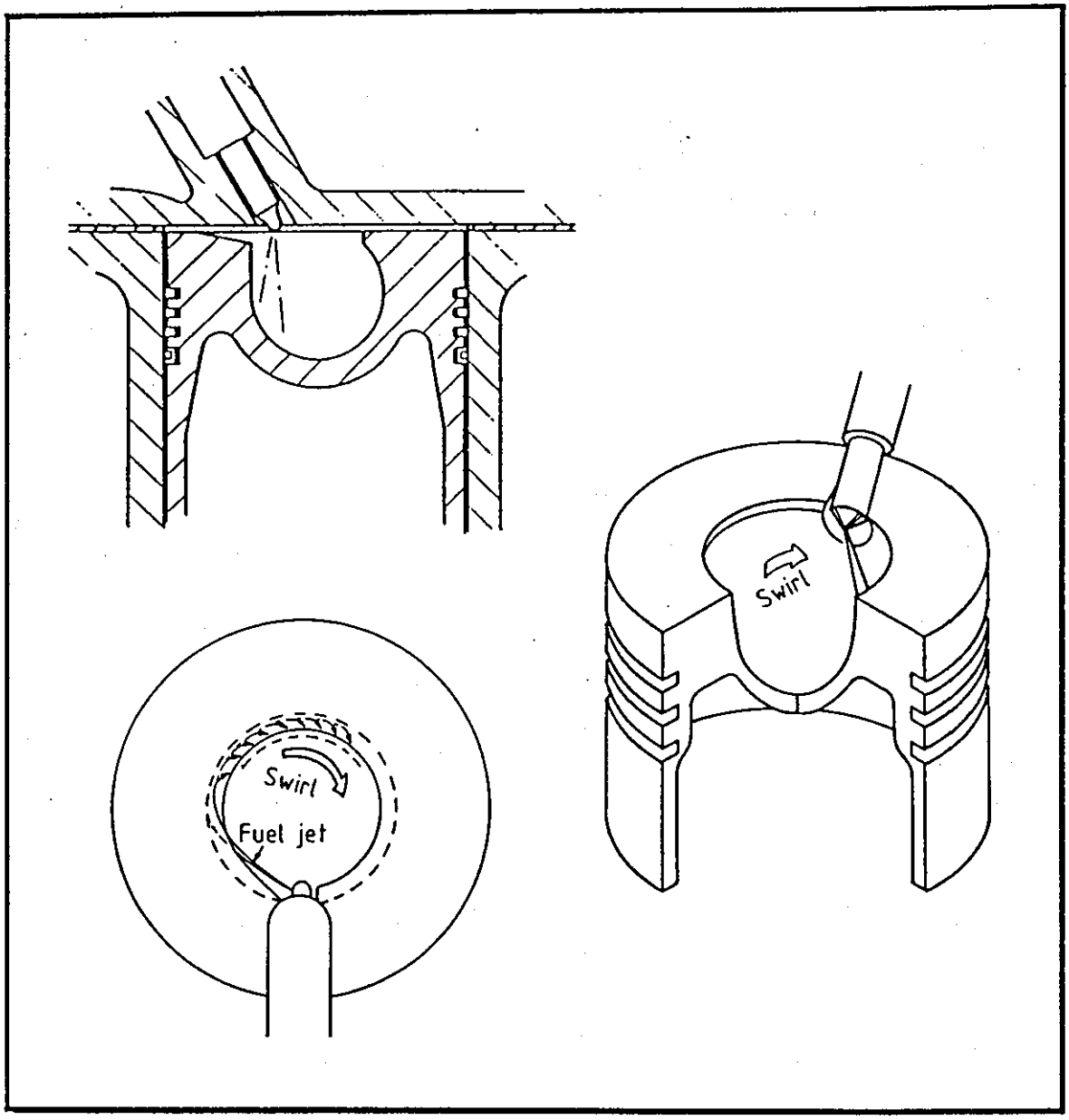

FIGURE 1.3: M-SYSTEM SPHERICAL CAVITY PISTON
(Wall-Wetting)

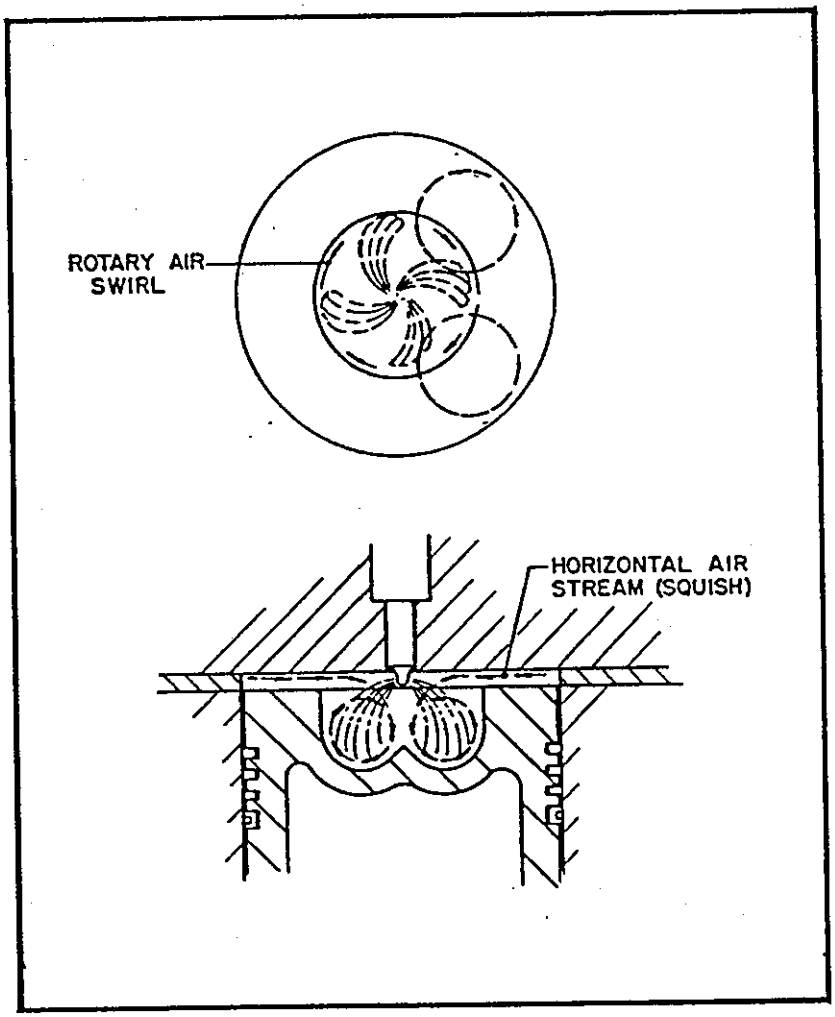

FIGURE 1.4: DIRECT INJECTION DEEP BOWL CHAMBER WITH SWIRL (15)

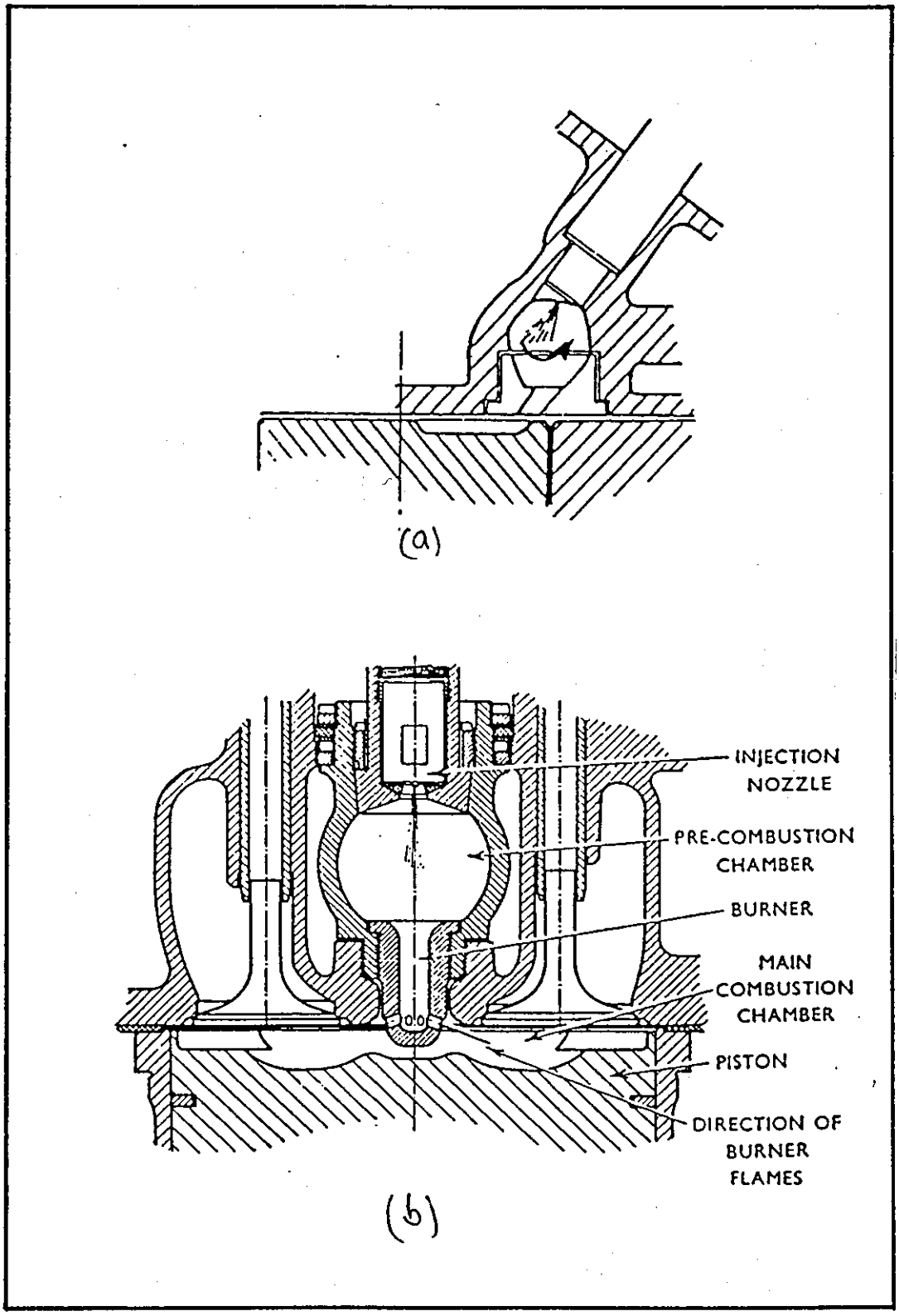

FIGURE 1.5: INDIRECT INJECTION COMBUSTION CHAMBER (15,16)

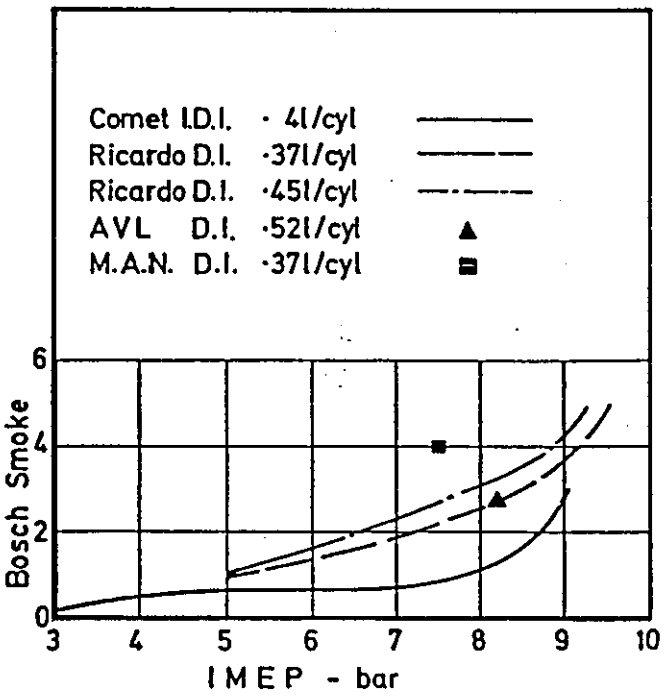

D.I. and I.D.I. smoke levels at 25 rev/s

FIGURE 1.6: COMPARISON OF SMOKE LEVELS IN VARIOUS ENGINES AT 25 rps (58)

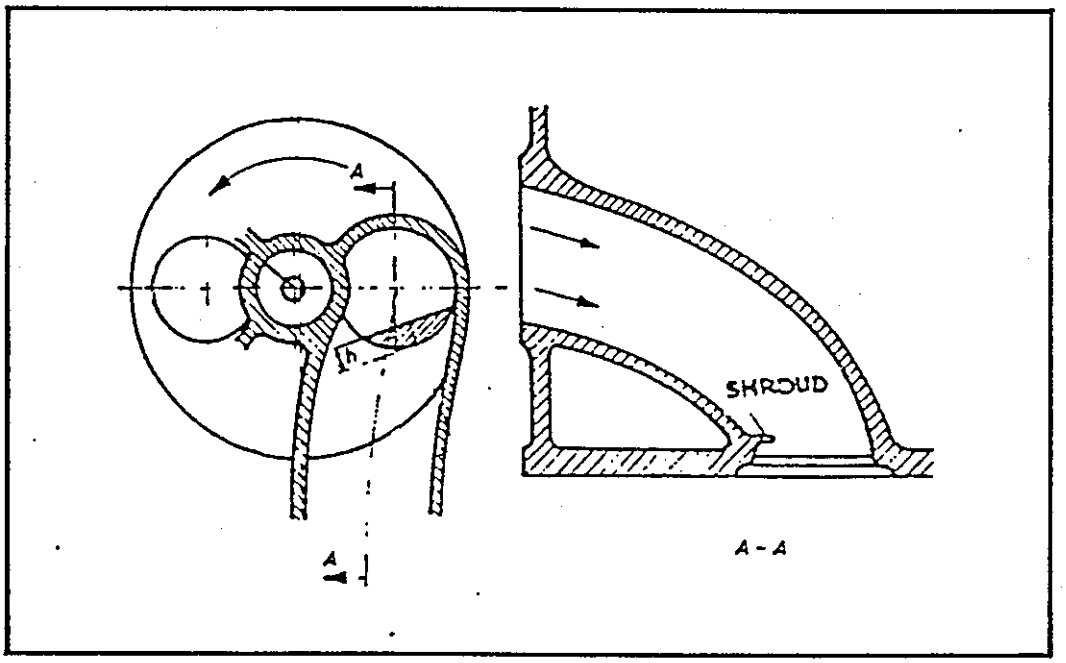

FIGURE 1.7: SWIRL GENERATING MASKED VALVE (20)

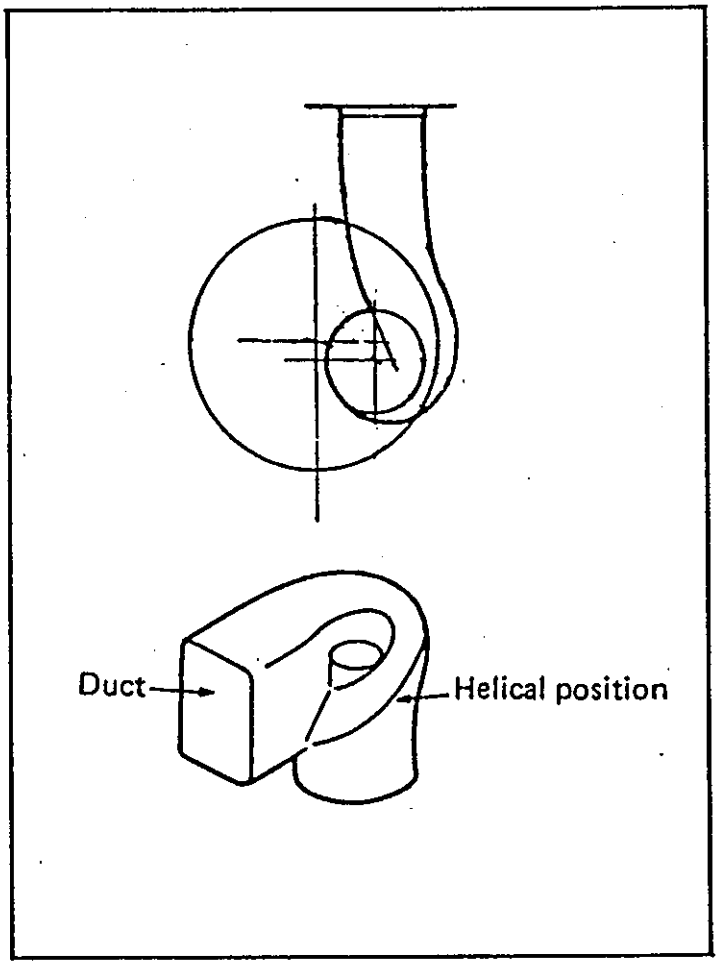

FIGURE 1.8: SCHEMATIC OF A HELICAL PORT (16)

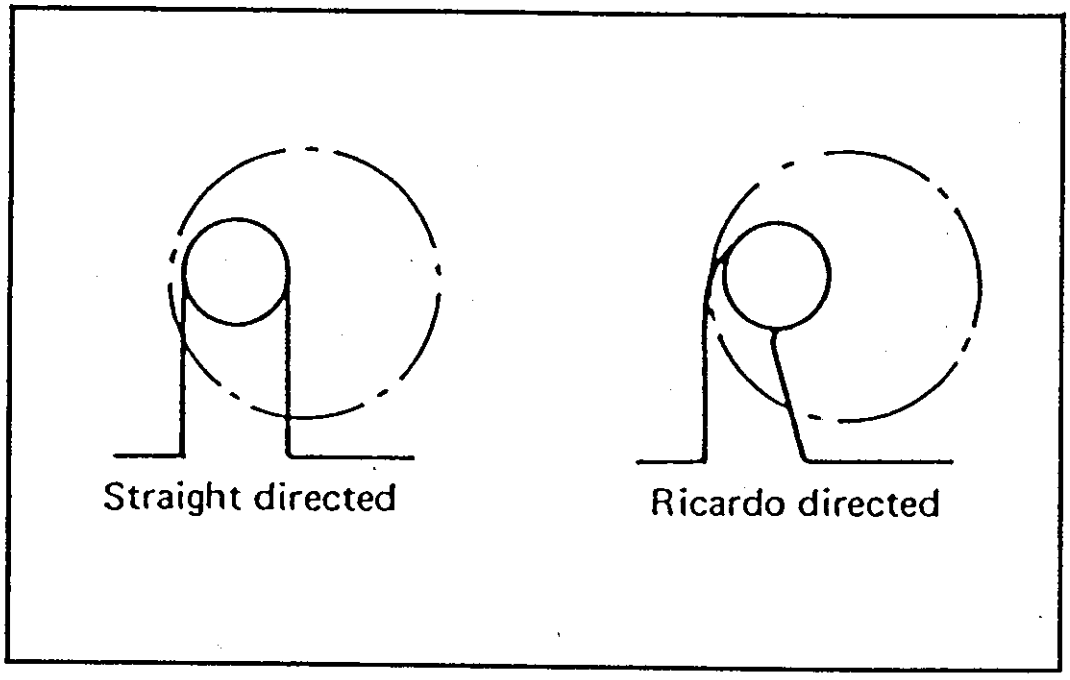

FIGURE 1.9: DIRECTED PORT DESIGNS (16)

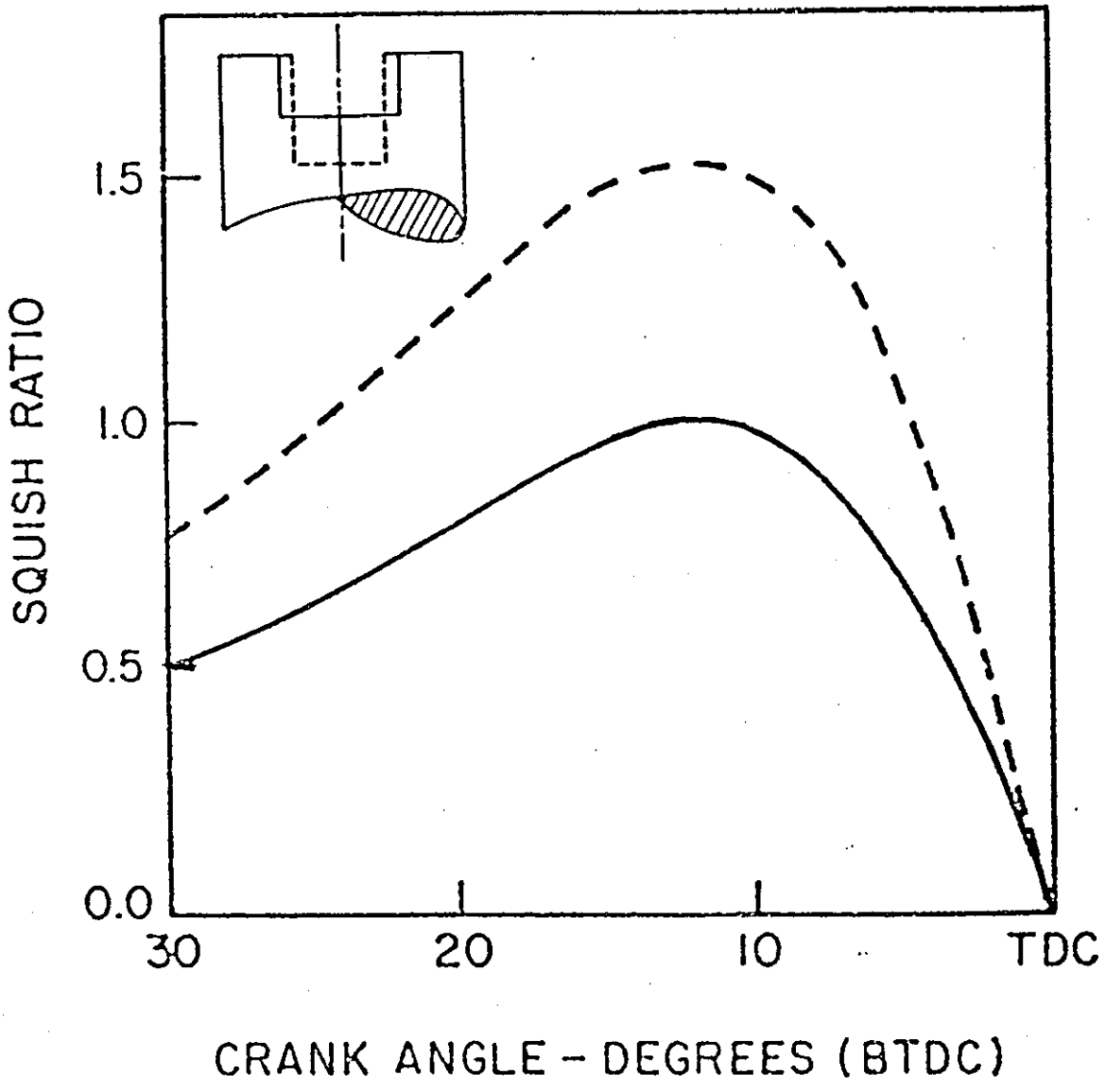

FIGURE 1.10: EFFECT OF BOWL DIAMETER ON SQUISH (22)

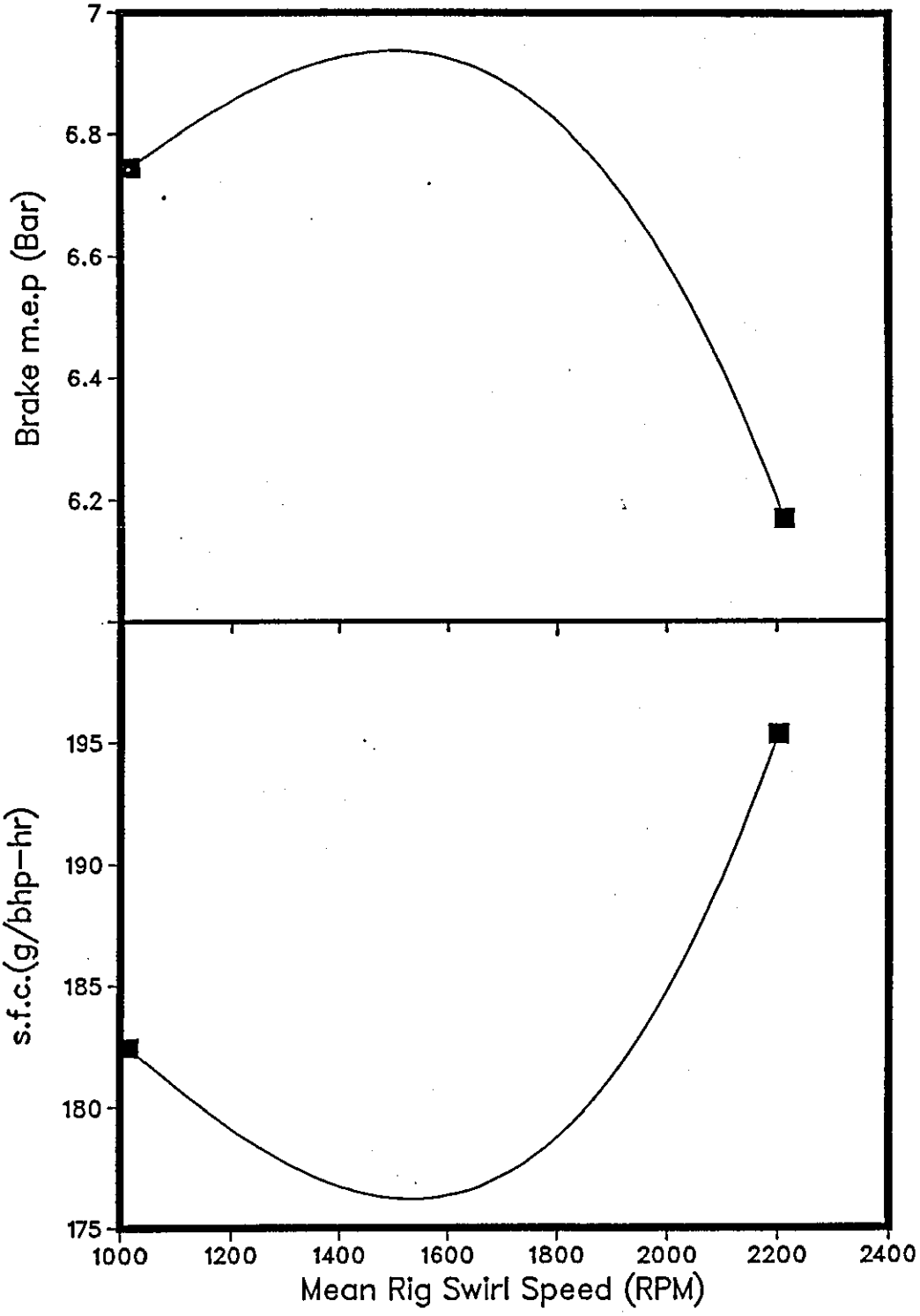

FIGURE 1.11: EFFECT OF SWIRL ON ENGINE PERFORMANCE (21)

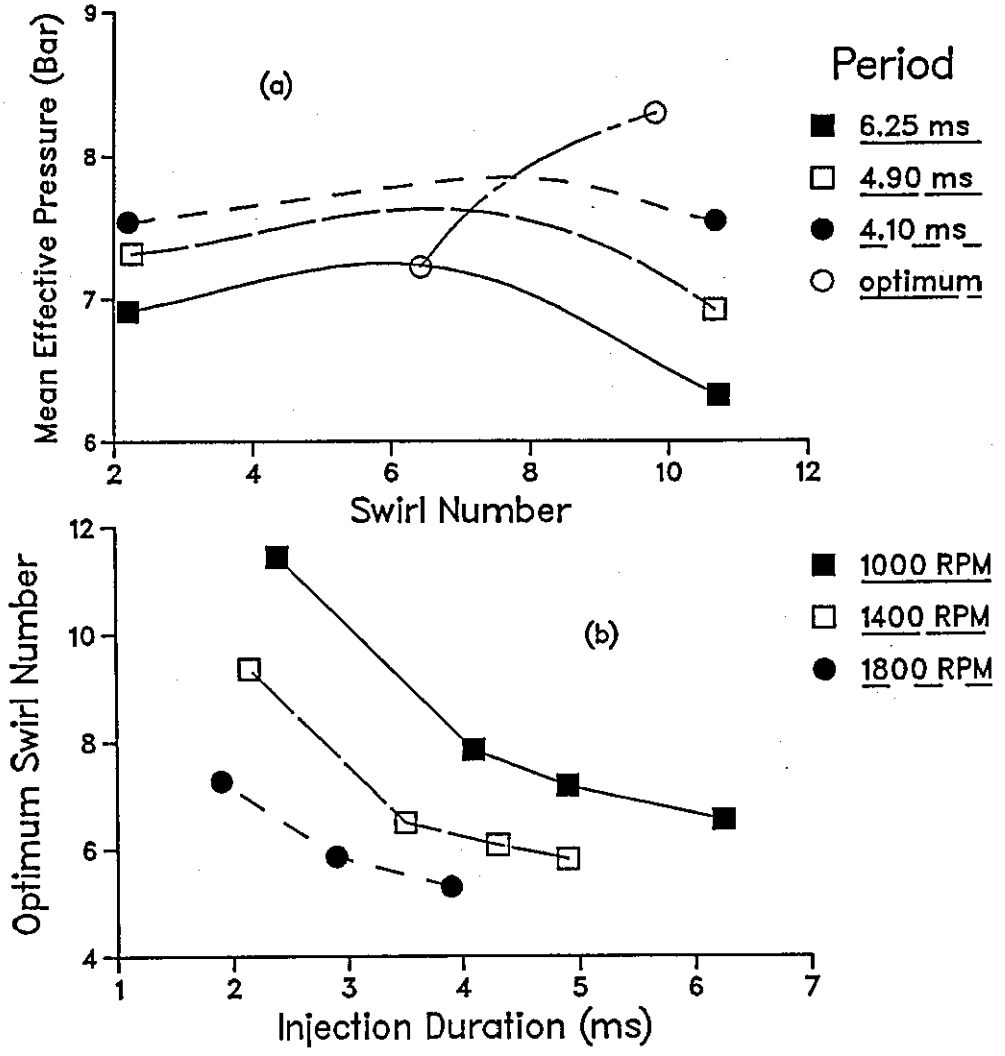

FIGURE 1.12: EFFECT OF INJECTION DURATION ON OPTIMUM SWIRL RATE IN A DI DIESEL ENGINE (20)

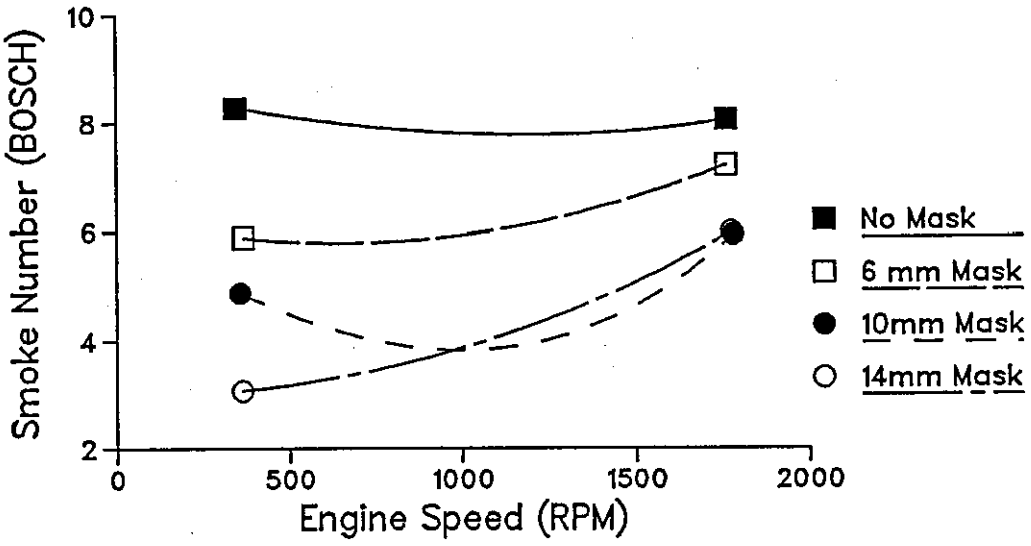

FIGURE 1.13: EFFECT OF ENGINE SWIRL ON SMOKE EMISSION (24)

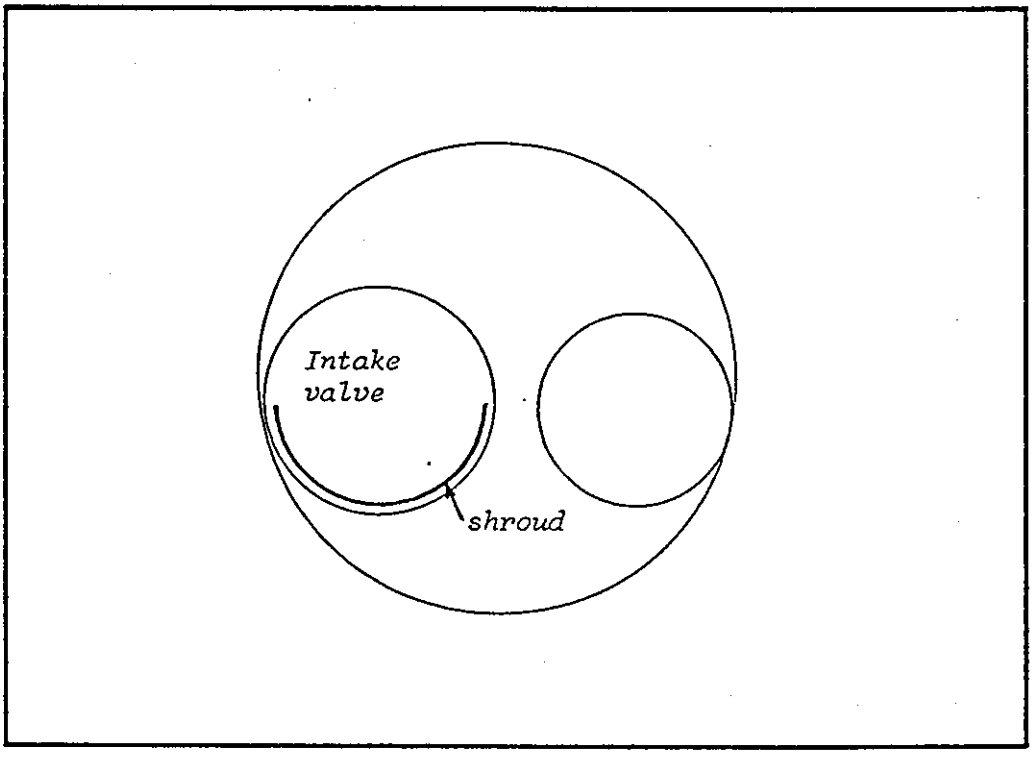

FIGURE 1.14: SHROUD CONFIGURATION FOR MAXIMUM SWIRL GENERATION (24)

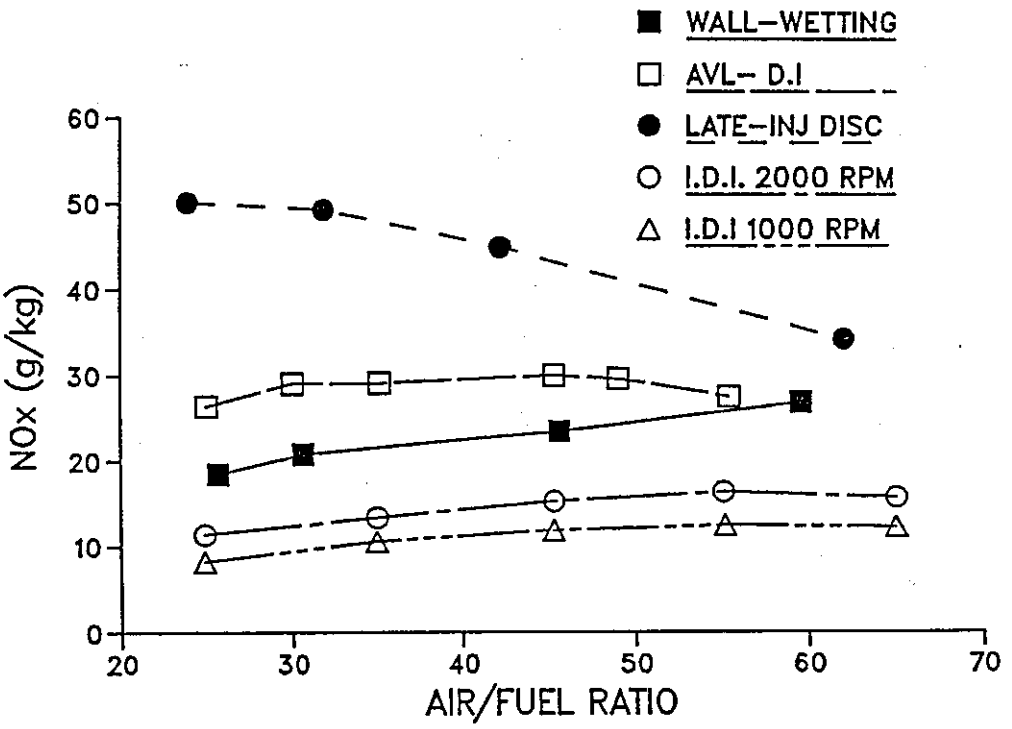

FIGURE 1.15: COMPARISON OF NOx EMISSIONS FROM DIFFERENT ENGINES AS A FUNCTION OF AIR/FUEL RATIO (58)

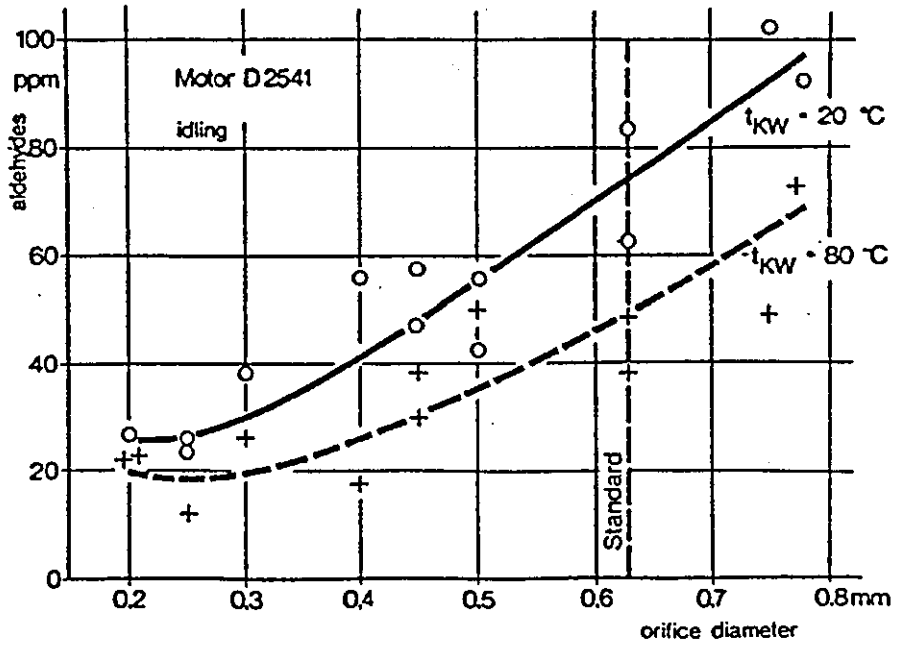

FIGURE 1.16: EFFECT OF INJECTOR NOZZLE DIAMETER ON UNBURNT HYDROCARBON EMISSIONS (35)

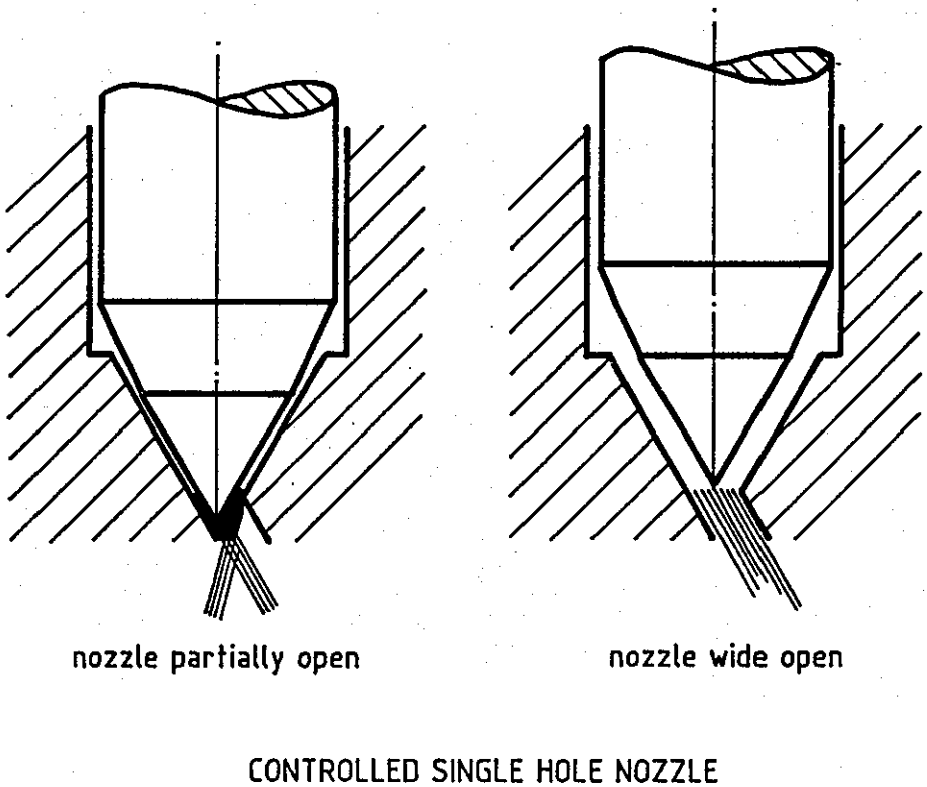

FIGURE 1.17: MODULATION OF THE CONTROLLED SINGLE HOLE NOZZLE (35)

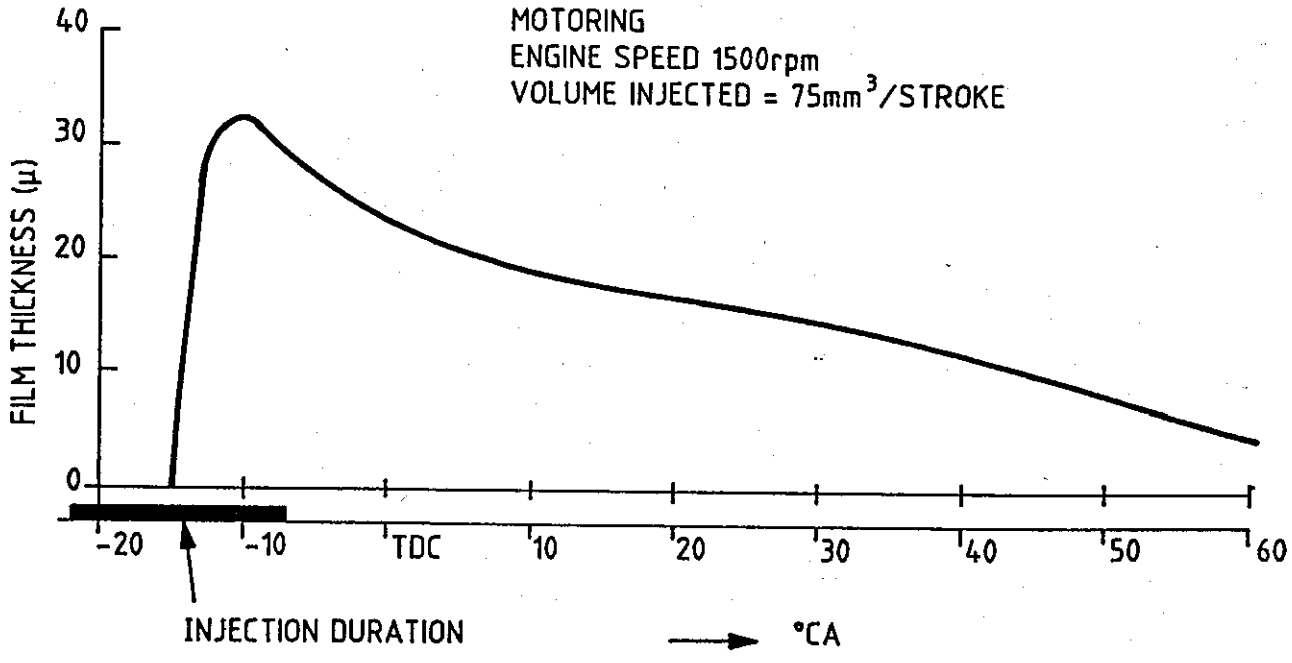

FIGURE 1.18: FILM DEVELOPMENT IN A MOTORED ENGINE (41)

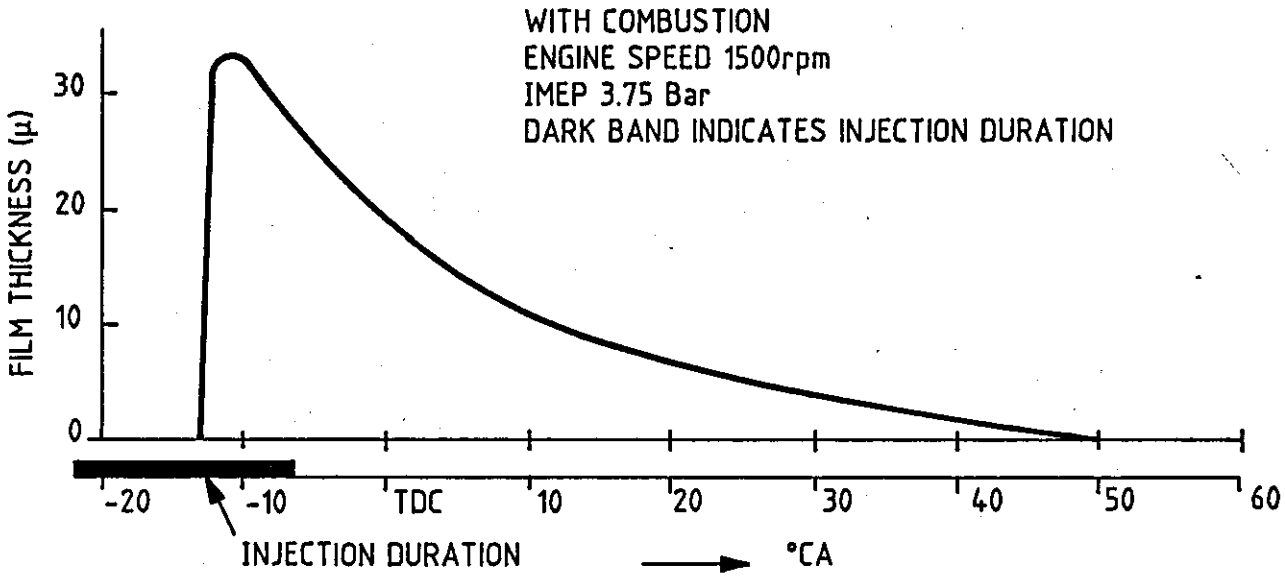

FIGURE 1.19: FILM DEVELOPMENT INA FIRED ENGINE (41)

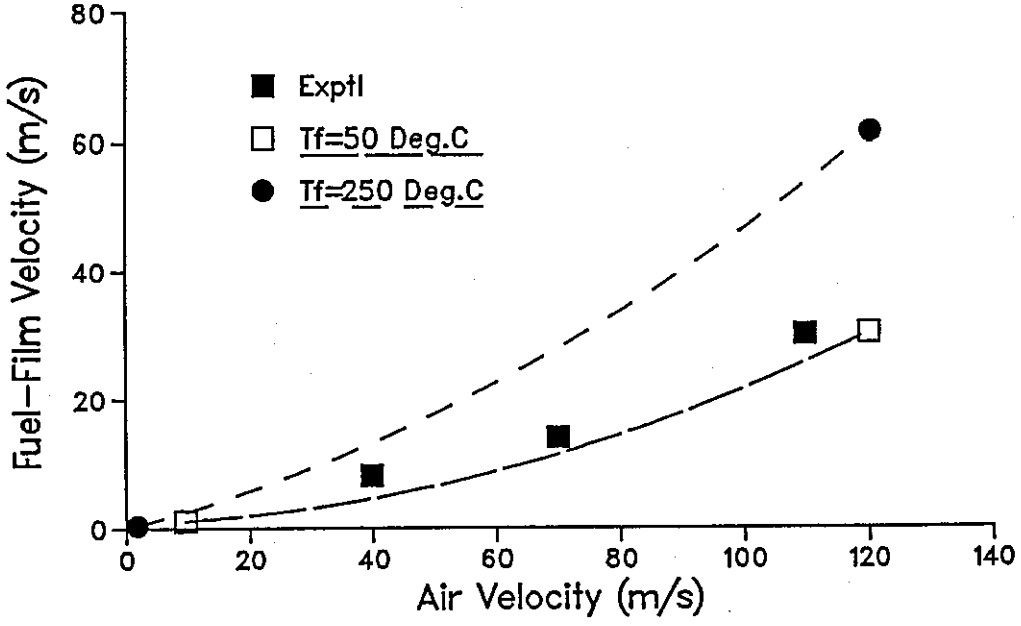

FIGURE 1.20: CALCULATED FUEL-FILM VELOCITY FROM THE MODEL OF URLAUB (34)

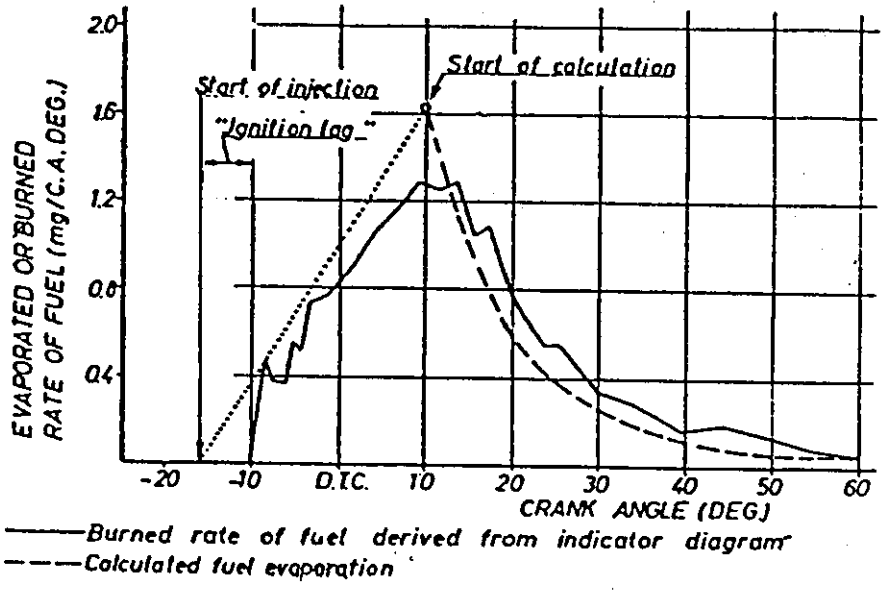

FIGURE 1.21: HEAT RELEASE DIAGRAM OF AN M-SYSTEM ENGINE (DIESEL FUEL, 1000 rpm) (34)

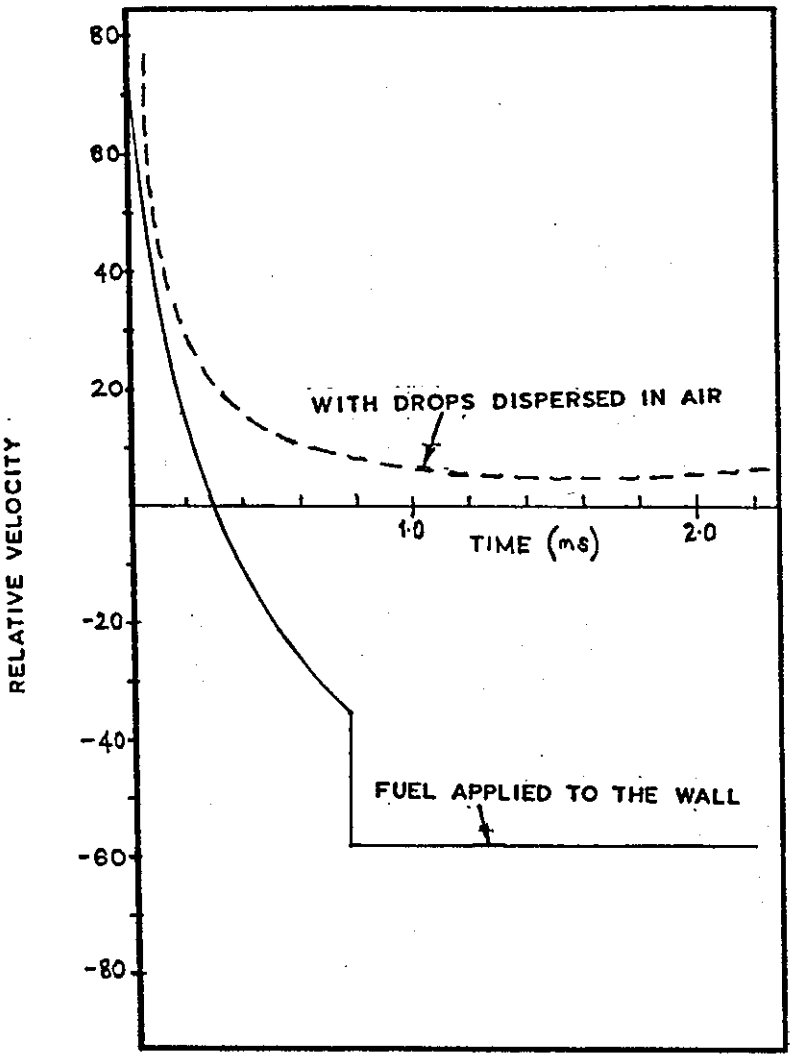

FIGURE 1.22: MEAN RELATIVE VELOCITY BETWEEN FUEL AND AIR (40)

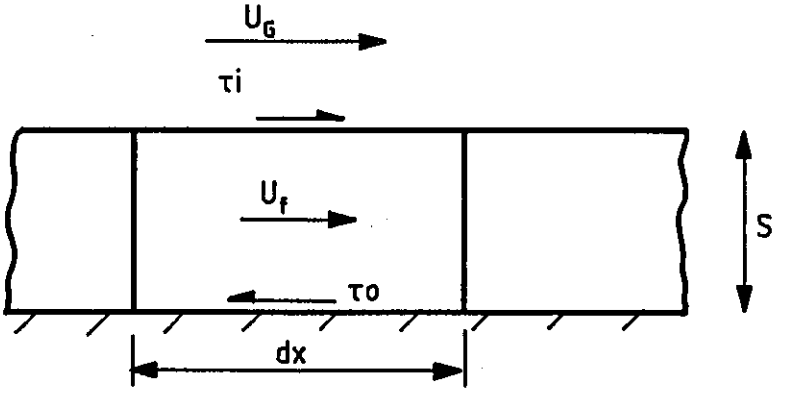

FIGURE 1.23: SHEAR STRESS BALANCE ON AN ELEMENTAL FILM SECTION

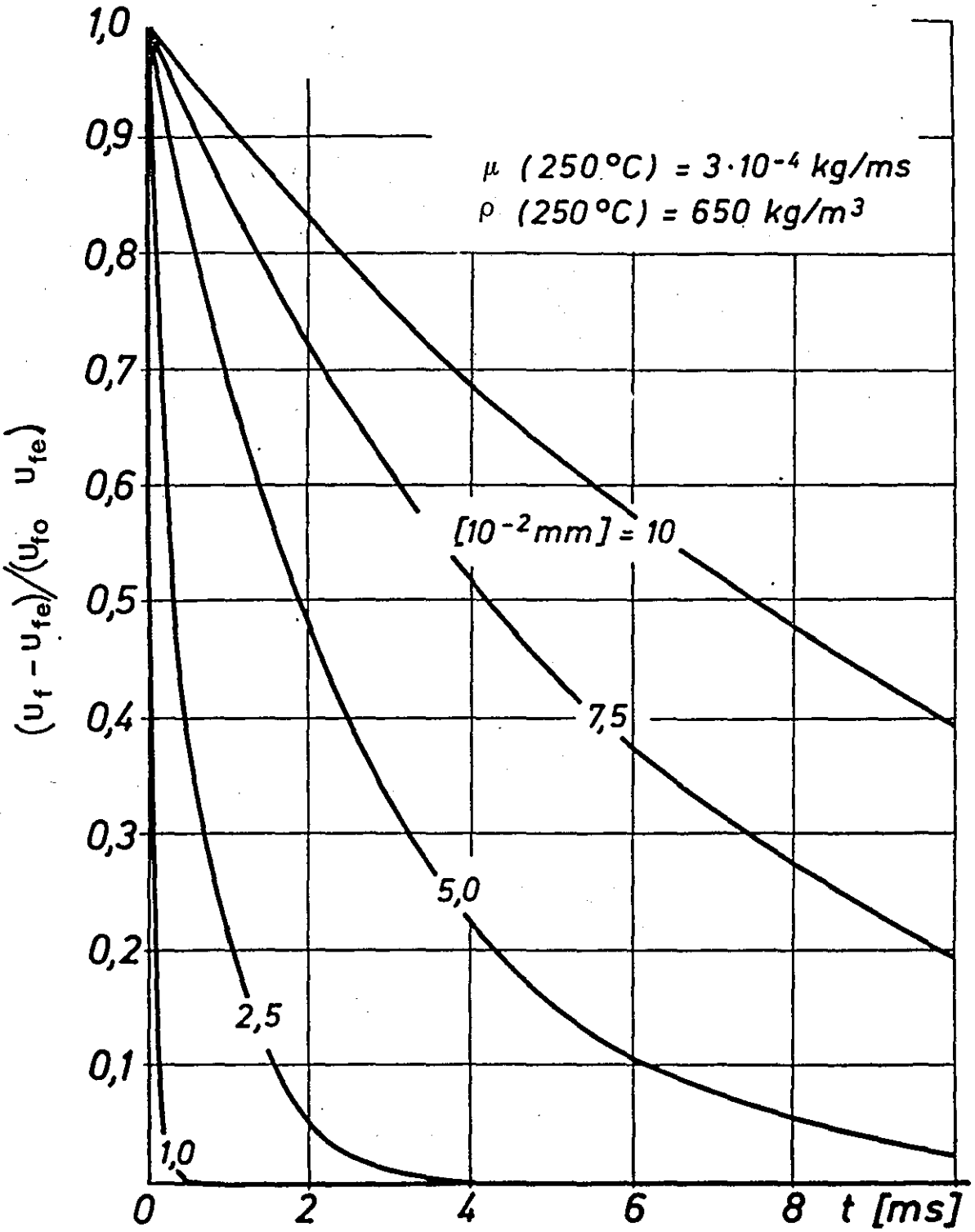

FIGURE 1.24: NORMALISED FUEL-FILM VELOCITY (42)

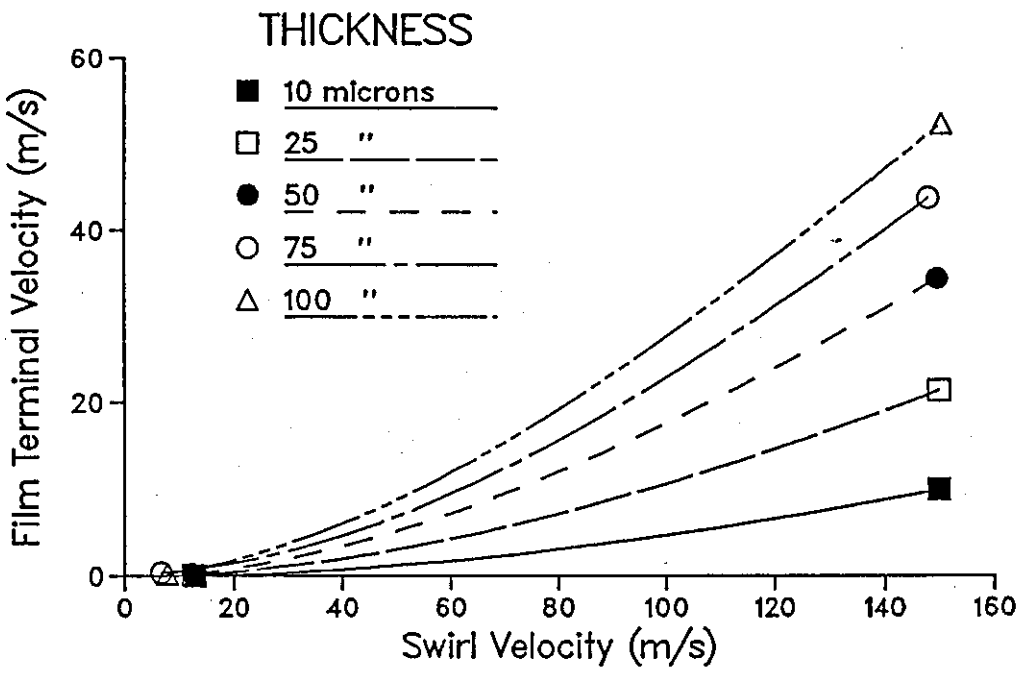

FIGURE 1.25: EFFEFT OF SWIRL ON THE CONSTANT COMPONENT OF FILM VELOCITY (42)

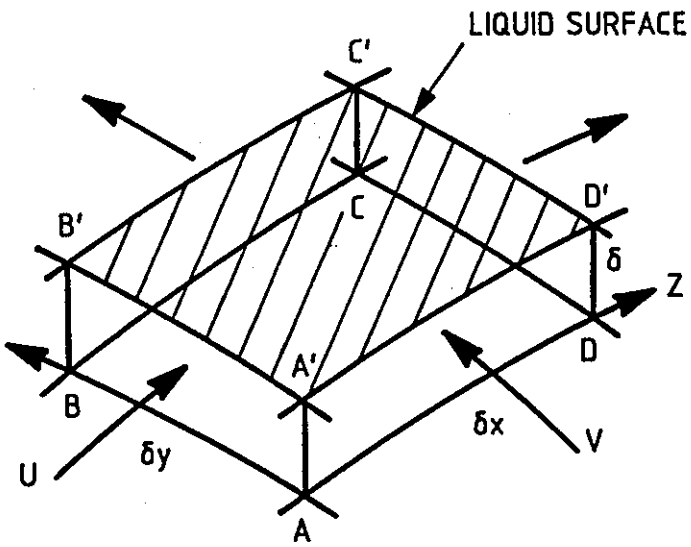

FIGURE 1.26: MASS BALANCE ON AN ELEMENTAL FUEL FILM VOLUME (44)

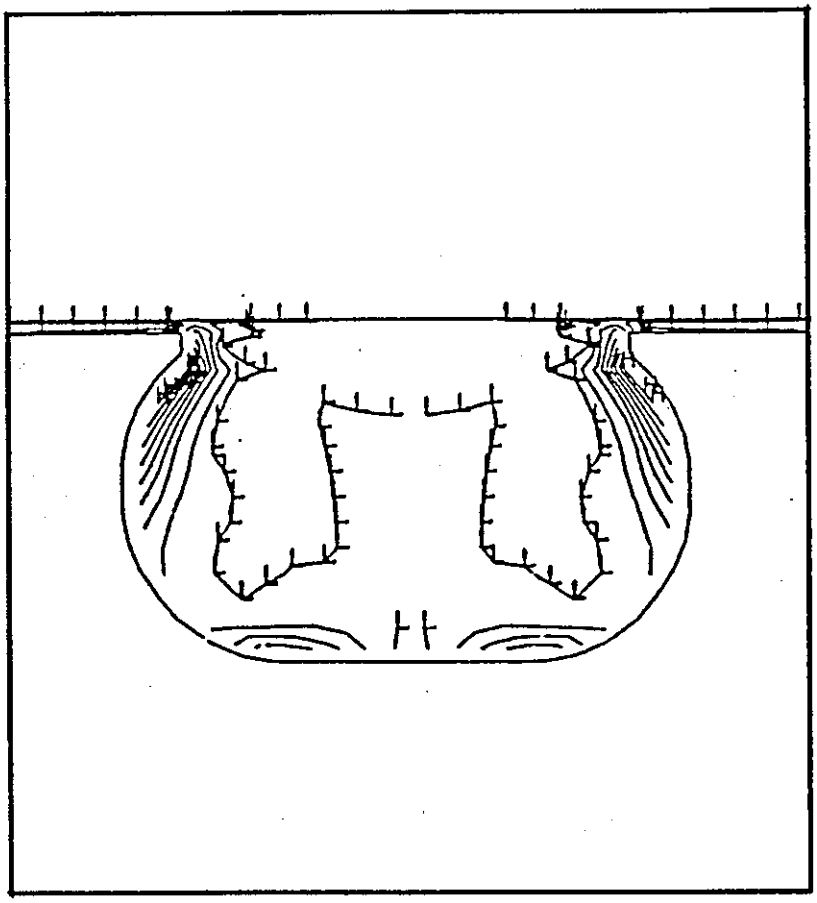

FIGURE 1.27: COMPUTED TURBULENCE KINETIC ENERGY IN THE COMBUSTION BOWL - 'L' SHOWS THE LOCATION OF LOW ENERGY (58)

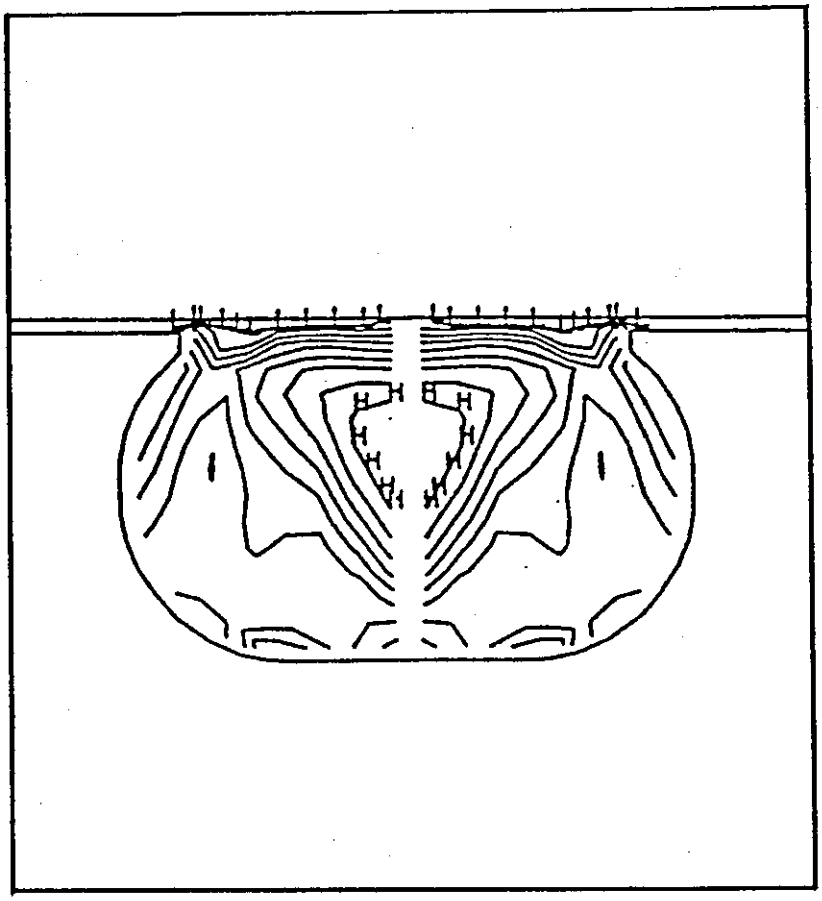

FIGURE 1.28: COMPUTED TURBULENCE DIFFUSIVITY. HIGH VALUE CONTOURS ARE DENOTED BY 'H' (58)

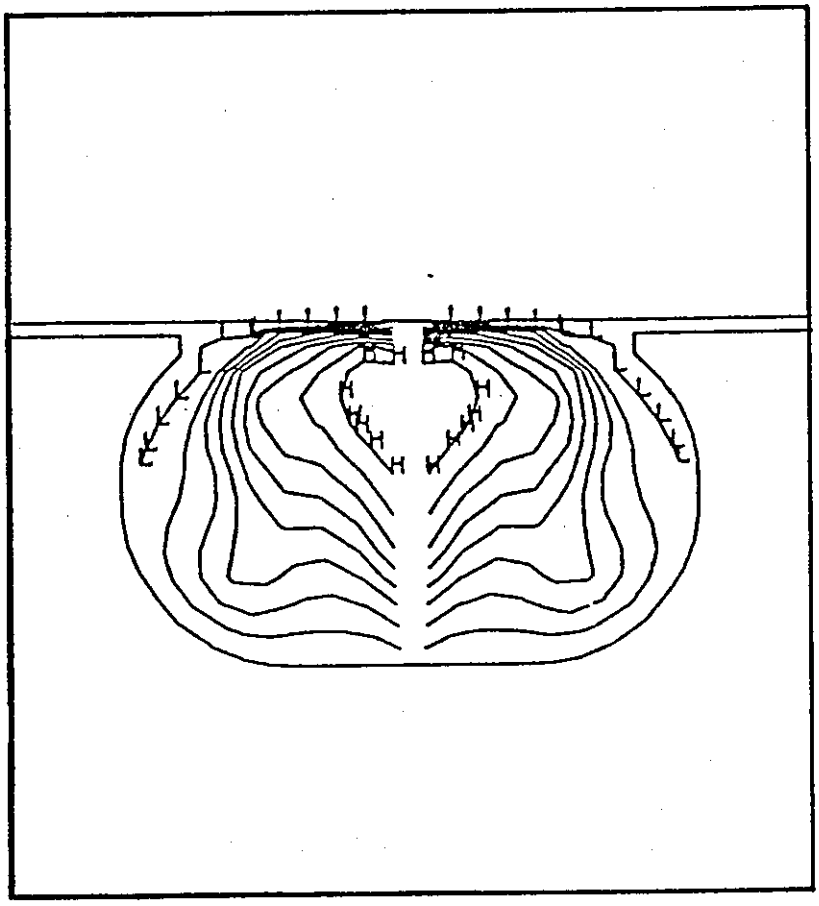

FIGURE 1.29: COMPUTED TURBULENCE MIXING RATE (58)

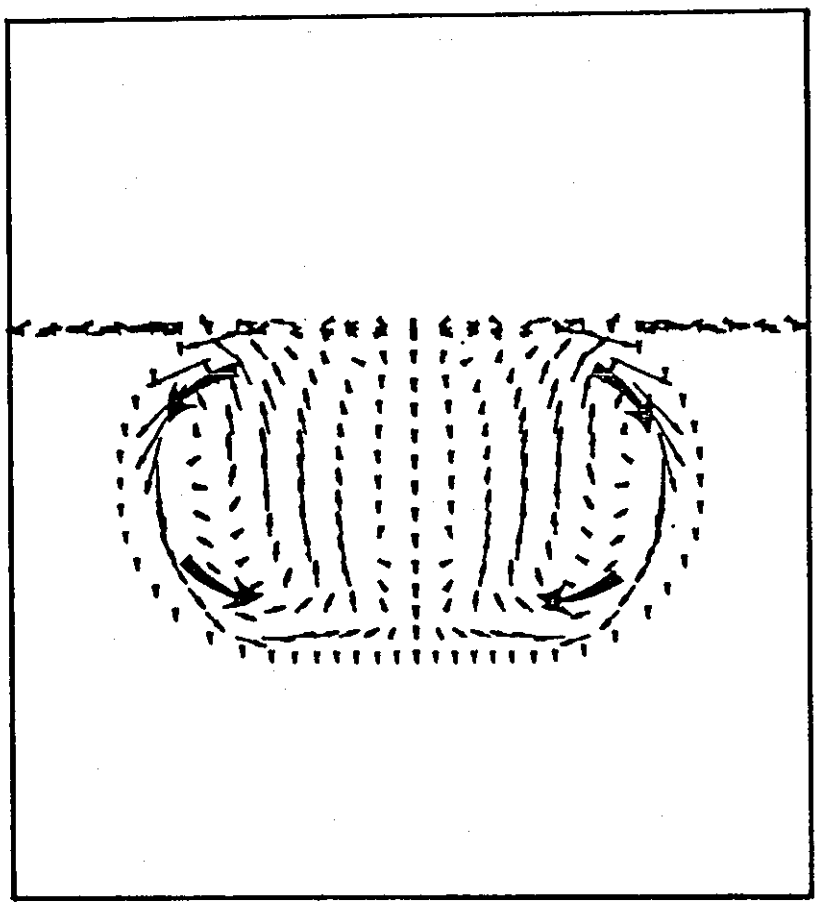

FIGURE 1.30: COMPUTED VELOCITY FLOW-FIELD SHOWING RADIAL AND AXIAL VELOCITIES (58)

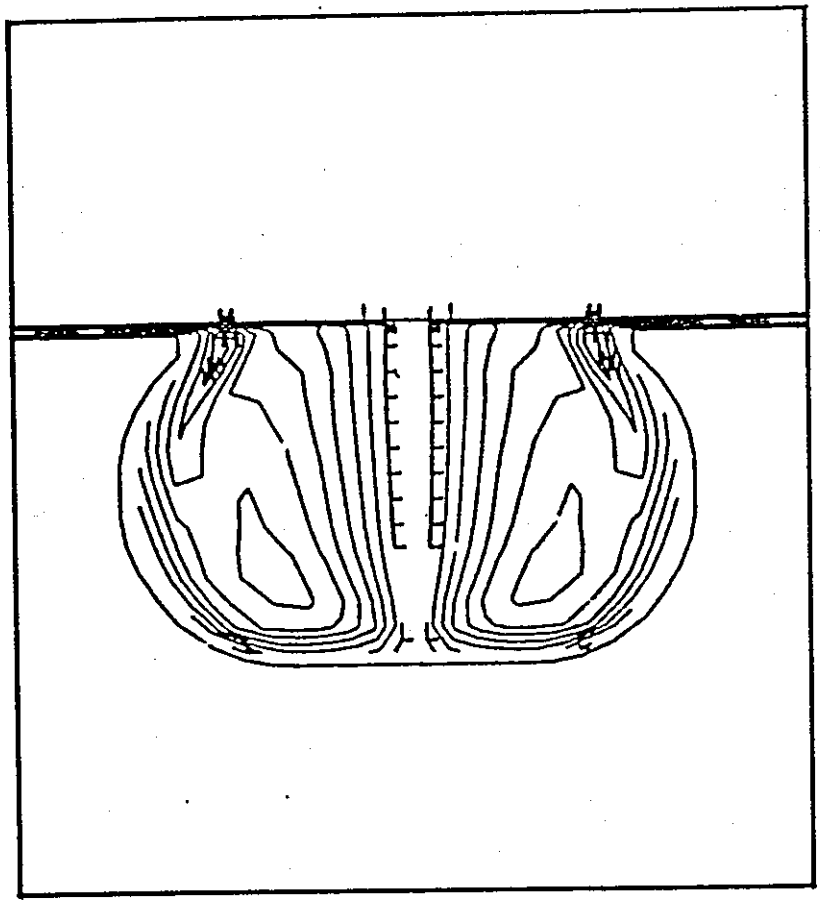

FIGURE 1.31: COMPUTED VELOCITY FLOW-FIELD SHOWING SWIRL STRUCTURE; LOW VALUE CONTOURS ARE NEAR THE BOWL AXIS (58)

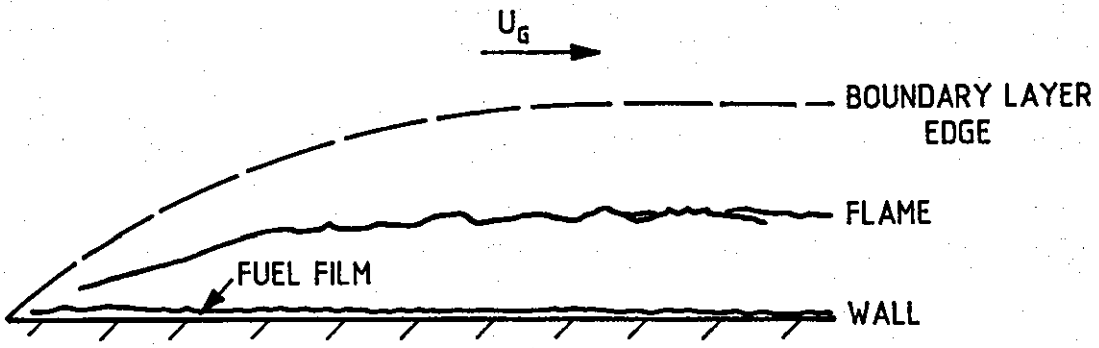

FIGURE 1.32: STRUCTURE OF THE BOUNDARY LAYER OVER A BURNING VOLATILE FUEL

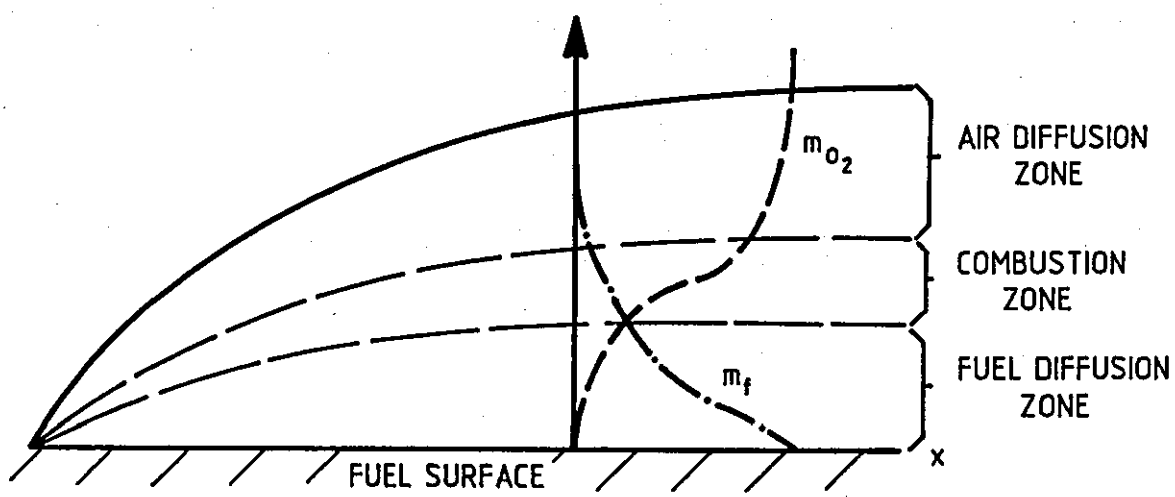

FIGURE 1.33: CONCENTRATION PROFILES IN A BURNING BOUNDARY LAYER

CHAPTER 2

ASPECTS OF EXISTING MODEL

2.1 INTRODUCTION

Originally it was intended to develop a single program to cater for both swirl assisted and quiescent type engines, however, two programs have developed dealing with the two engine types separately. The two programs have developed from a common source, and so exhibit a number of similarities between them.

In this chapter a general description of the two programs as updated and reported by Kyriakides et al (8) is given. Points of weakness in the design of some of the routines are raised and in the last section of the chapter, modifications made by the present author to remedy these weaknesses are discussed. It must be pointed out here that most of these weaknesses do not refer so much to the accuracy in the representation of the physical phenomena involved as to the general convenience of applying the model to a diverse set of conditions. A typical example, which will be discussed in detail at a latter stage, has been to replace all references in the program to a commercial package available on the university mainframe, for solving systems of linear equations, with a Gaussian elimination routine. This was considered desirable as it removed the restriction imposed on the user; of having access to an identical commercial package, in order to successfully implement the program on a microcomputer. This and many other modifications will be discussed in some detail and, wherever possible results of comparisons between the various modifications and their corresponding original algorithms will be presented in graphical form.

Similarity between the two programs has meant that only a detailed description of the quiescent model is sufficient. Hence under the heading for the swirl model, only differences between the two models

are highlighted, and a detailed description of the extra features is provided.

2.2 THE QUIESCENT ENGINE MODEL

The objective in developing the quiescent model was described by Dent and Mehta (6) as being the "accurate performance prediction over the full load range of an engine ... with economic use of computer time". To achieve this goal, the governing conservation equations were simplified by making use of similarity profiles for velocity and scalar quantities, and an empirical function employed to describe the distribution of fuel droplets in the spray. A simple chemically reacting system was also assumed in which the reactants were only allowed to combine in stoichiometric proportions. The theoretical and conceptual basis of the model is outlined in reference (6) in a fairly detailed but concise form.

A comprehensive listing of the computer code for the early version of the simulation program, is given in reference (60). The model has the capability to predict the effect of engine speed, load, injection timing, and boost pressure when the load conditions, including the level of exhaust gas recirculation, are specified and the following input parameters supplied;

(1) Engine specifications:
- stroke
- bore
- compression ratio
- connecting rod length
- geometrical description of the cylinder bowl
- injector nozzle dimensions
- valve timing.

(2) Discretised fuel injection pressure diagram (alternatively a trapezoidal shape could be assumed).

The model only simulates events during the closed period of the engine cycle (i.e. from inlet valve closure to exhaust valve opening) and yields instantaneous values for the following variables at each crank angle, for presentation in graphical form:

(1) Cylinder pressure (P_a)
(2) Temperature in the burning zone (T_j)
(3) Mean charge temperature (T_{ch})
(4) Cumulative quantity of fuel injected
(5) The following fuel mass fractions:
    - evaporated
    - burned
(6) Heat flux from the charge to the cylinder walls
(7) Rate of air entrainment into the jet or burning zone
(8) Heat release rate
(9) Net soot formed (i.e. formed less oxidised) and the oxidation rate
(10) Equilibrium concentration of combustion product species
(11) Concentration of NO_x, based on chemical rate kinetics.

The quantity of fuel injected, and fuel mass fractions are integrated over the whole closed period in order to compare the results with the experimentally obtained total quantity of fuel injected. Similar integrations are also carried out for the exhaust emissions (soot and NO_x), so that at exhaust valve opening the values are corrected to NTP and displayed as the level of engine emissions in the exhaust.

A brief outline flow-chart of the model is given in Figure 2.1 to illustrate the sequence of operations and their inter-relations. Details of the swirl model are also included on the same figure, shown in dashed enclosing boxes.

In the following sections, the computational methodology employed in the model to calculate pressure, temperature and volumes of the burning region will be addressed in some detail. The contents of the

cylinder are divided into two conceptual regions referred to as the surrounding air, and the burning zone (Fig. 2.2). During injection, the burning zone is considered to be spatially distributed around the fuel spray while the remainder of the air in the cylinder constitues the surrounding zone. After the end of injection, the spatial distribution of either zone is not explicitly defined, although it is recognised that thermodynamic conservation laws may be applied to both regions to determine their respective temperatures, volumes, and the total pressure in the cylinder. Energy balancing has been applied to the two regions by simultaneously solving the non-flow energy equation, (two equations - one for each of the zones), and the semi-perfect equation of state (another two equations). The equations involved are described in the following paragraphs.

2.2.1 Non-flow Energy Equation

Equation (2.1) represents the non-flow energy equation as applied to the two hypothetical zones, taking into account the various constituents contained within each volume.

$$\sum m_i \bar{C}_{vi}\, dT + \sum \bar{C}_{vi}\, T\, dm_i + dQ_L - pdV - dm_f \cdot H_o = 0 \qquad (2.1)$$

The first two terms on the left represent the change in internal energy of the cylinder charge. The incremental loss of heat from the region is represented by dQ_L, and pdV represents the work done by the charge on its surroundings. The extra term, $dm_f.H_o$ only applies to the burning zone and represents the chemical heat released due to the combustion of a fixed mass of fuel, dm_f, having a calorific value H_o.

2.2.2 Equation of State

The semi-perfect equation of state in differential form can be expressed as follows:

$$PdV + VdP = \sum R_i\, T\, dm_i + \sum R_i\, m_i\, dT \qquad (2.2)$$

where m_i represents the mass of component i in the zone under consideration. The assumption of a simple chemically reacting system implies that only three components are identified in either zone: Fuel vapour, air and combustion products. R_i is the specific gas constant for the respective component.

2.2.3 Energy Balance

The four equations derived from equations (2.1) and (2.2) constitute a linear system which must be solved simultaneously. The equations, which have been outlined in detail by Mehta (2), can be shown to have the following general form:

$$
\begin{aligned}
A_{11}\, dT_j + P dV_j + 0 \quad + 0 \quad &= B_1 \\
A_{21}\, dT_j - P dV_j - V_j dP + 0 \quad &= B_2 \\
0 \quad - P dV_j - 0 \quad + M_a C_v\, dT \quad &= B_3 \\
0 \quad + \frac{dV_j}{V} - \frac{dP}{P} + \frac{dT}{T} \quad &= B_4
\end{aligned}
$$

To render the equations amenable to solution by numerical techniques, they are presented in matrix form as follows:

$$
\begin{bmatrix}
A_{11} & P & 0 & 0 \\
A_{21} & -P & -V_j & 0 \\
0 & -P & 0 & M_a C_v \\
0 & \frac{1}{V} & \frac{-1}{P} & \frac{1}{T}
\end{bmatrix}
\cdot
\begin{bmatrix} dT_j \\ dV_j \\ dP \\ dT \end{bmatrix}
=
\begin{bmatrix} B_1 \\ B_2 \\ B_3 \\ B_4 \end{bmatrix}
\qquad (2.3)
$$

The Crout reduction method (61) was originally employed to solve the equations to yield the following values: increment in the temperature

of the burning zone (dT_j); increment in the volume of the burning mass (dV_j); and increments in total cylinder pressure (dP) and the temperature of the 'surrounding zone' (dT). The modified Euler's method is used to integrate these quantities over the closed period of the engine, from inlet valve closure to exhaust valve opening.

2.2.4 Spray Characteristics

The injected fuel spray is dealt with in two sections representing the free jet portion, and the impinged region close to the piston walls (Fig. 2.3). In each of these regions similarity profiles for the distribution of velocity and mass concentration must be defined in order to describe the process of fuel-air mixing.

i. Free Jet Region

The profiles of velocity and mass concentration in a circular two-phase jet emerging from a nozzle with a uniform velocity, into a stagnant fluid, are given by Abramovich (62) by the following equations:

$$\text{Velocity profile :} \quad \frac{U}{U_m} = (1 - Y_p^{1.5})^2 \qquad (2.4)$$

$$\text{Concentration profile :} \quad \frac{C}{C_m} = 1 - Y_p^{1.5} \qquad (2.5)$$

where U is the local velocity at the normalised radius Y_p ($= Y/r_j$) and U_m is the jet centreline velocity. C is the local fuel mass fraction and C_m the mass fraction at the jet centre-line. The radial growth of the jet with penetration is given by equation (2.6) which is also based on the results of Abramovich:

$$\frac{dr_j}{dx} = 0.11 \left(\frac{\rho_j + \rho_a}{\rho_j}\right) \qquad (2.6)$$

To determine the distribution of fuel droplet sizes in the spray, the representation of the fuel spray into conceptual sectors needs to be considered. In order to simplify the complexity of the two-phase jet so that the phenomenological approach may be realistically applied, the structure of the fuel spray was divided into eleven radial sectors as illustrated in Figure 2.4. The radial positions of each of the sectors was chosen so as to correspond with Simmon's (63) correlation for droplet size distribution. The cumulative volume fraction of injected fuel, having a normalised droplet diameter of D_i (defined below) or higher, is given by Simmons as:

$$V_{cf} = \exp (0.05328\ D_i - 0.54174\ D_i^2) \qquad (2.7)$$

where V_{cf} = cumulative volume fraction of injected fuel constituted by droplets greater and equal to D_i.

$$D_i = \frac{d_i}{SMD}$$

d_i = droplet diameter in class i (as defined below)

SMD = Sauter mean diameter

Equation (2.7) is valid in the range $0.082 < D_i < 3$. Mehta (2) assumed eleven classes of droplet diameters to exist in this range, with the largest droplets on the jet axis and the smallest at its edge. The computed radial positions of these classes correspond to the radial positions of the sectors in the spray model. Entrained air is then distributed throughout the sectors according to the similarity profile given by equation (2.5). Hence, each sector contains a mono-disperse fuel spray with droplets of a uniform diameter.

The SMD is calculated from the following relationship based on the experimental results of Knight (64):

$$SMD = 8\,\Delta P^{-0.458}\,Q^{0.209}\,\nu_f^{0.215} \qquad (2.8)$$

where ν_f is the kinematic viscosity of the fuel, ΔP the pressure drop across the injector nozzle orifice, and Q the volumetric fuel flow rate.

It is widely known, from experimental evidence, that mass flow-rate in the jet increases as one traverses in the downstream direction. This is because the jet entrains large amounts of the surrounding fluid as it spreads (see Figure 2.4). This constitutes the most significant integral scale mixing mechanism in quiescent chamber diesel engines. The entrainment rate in the model is calculated from the expression of Ricou and Spalding (65) given as:

$$\frac{\dot{m}_{aE} + \dot{m}_f}{\dot{m}_f} = 0.32\,\frac{x}{d_o'} \qquad (2.9)$$

where $\dot{m}_{aE}$ and $\dot{m}_f$ are mass flow rates of air entrained and fuel injected in the time it takes the jet to penetrate to a distance x. d_o' is the equivalent jet diameter defined by:

$$d_o' = d_o\,(\frac{\rho_f}{\rho_a})^{1/2} \qquad (2.10)$$

where d_o is the nozzle orifice diameter.

The methods used in the original model to account for the effect of combustion on velocity and scalar quantitity similarity profiles and to redistribute droplet sizes on evaporation are discussed in detail in references (2) and (6). The modified approach is discussed in detail in Section 2.4.9.

ii. Wall Jet Structure

The quasi-steady analysis for wall-jet flow, neglecting the effects of wall friction, is described by Rajaratnam (66) and schematically

illustrated in Figure 2.3. The onset of impingement in the engine is determined from simple geometric considerations of the piston bowl and the jet penetration, based on the equations provided by Giralt et al (67). Description of scalar quantity profiles in the wall-jet are based on the assumption that equations (2.4) and (2.5) hold over the cross-section of the wall-jet by letting the wall correspond to the axis of an equivalent free-jet. Variation of maximum velocity in the wall-jet is given (66) by the following equation:

$$U_m = 1.03 \frac{U_o \cdot d_o'}{X_w} \qquad (2.11)$$

where X_w is the wall-jet penetration, obtained by integrating equation (2.11) with respect to time yielding:

$$X_w = (2.06\ U_o\ d_o' t)^{1/2} + C \qquad (2.12)$$

Entrainment of air into the wall-jet is calculated from the following equation of Hertel (68):

$$\frac{\dot{m}_{aw} + \dot{m}_f}{\dot{m}_f} = 0.865 \frac{X_w}{d_o'} \qquad (2.13)$$

The possibility of interference between adjacent wall-jets when long injection durations are involved, is accounted for by assuming entrainment into the wall-jet to be negligible when interference occurs.

2.2.5 Turbulent Mixing

At the end of injection, the structure of the jet starts to disintegrate, and air entrainment as computed from equations (2.9) and (2.13) is no longer valid. By assuming the idea of an idealised turbulent mixer after Corrsin (69), Dent (19) postulates that the transport processes by which available air continues to be drawn into the jet plume are described by turbulent mixing which is controlled by the kinetic energy input into the flow. This idea is developed to

provide the dissipation rate of turbulence kinetic energy from which the governing equations for mixing rate are determined. As the mixing process in reacting media takes place on a molecular level (57), Kolmogorov microscales of turbulence are employed. The length, time, and velocity scales are defined in terms of the dissipation rate of turbulence (ϵ), and the kinematic viscosity of the fluid (ν), by the following relationships (70):

i. Length scale, $\eta = (\nu^3/\epsilon)^{1/4}$

ii. Time scale, $\tau = (\nu/\epsilon)^{1/2}$

iii. Velocity scale, $U = \eta/t = (\nu\epsilon)^{1/4}$

The dissipation rate of turbulence (ϵ) is defined, after Corrsin, as follows:

$\epsilon = \gamma$. [Specific rate of energy input to the flow]

where γ is a constant representing the fraction of the input energy that is directly involved in the dissipations of turbulence. Dent (19) has derived an expression for ε in quiescent diesel engines in terms of injection variables and engine speed by the expression:

$$\epsilon = C \left(\frac{N}{\theta_{ip}}\right)^3 \left(\frac{V_f}{nd_o^2}\right)^2 \qquad (2.14)$$

where N is the engine speed, θ_{ip} is the injection period in degrees crank angle, V_f the fuel volumetric delivery rate per stroke of the injection pump. n is the number of holes in the injector nozzle, each with a diameter d_o, and C is a known constant.

For large scale eddy structure, the mixing time, τ, is characterised by:

$$\tau = \left(\frac{L^2}{\epsilon}\right)^{1/3} \qquad (2.15)$$

where the length scale L, is taken to be the nozzle orifice equivalent diameter, d_o'. By mass conservation considerations, Dent and Mehta (6) show that the rate of mass transfer of air into the jet plume is given by:

$$\frac{dm_a}{dt} = - C_1 \, m_a / \tau \qquad (2.16)$$

where m_a is the mass of air available in the surroundings, for entrainment. The constant C_1 was evaluated by equating the mean entrainment rate during injection with the right hand side of equation (2.16).

2.2.6 Exhaust Smoke Modelling

The modelling of exhaust emissions in the model is discussed in detail by Kyriakides et al (8) and only a brief overview is outlined here. The model adopts the soot formation mechanism postulated by Tesner et al (71), with the eddy dissipation concept developed by Magnussen (57) to describe soot formation and oxidation in turbulent flames. Tesner et al postulated that soot formation occurs in three separate stages, viz; spontaneous formation of radical nuclei - which are the pre-cursors of soot formation, the formation of soot particles around the nuclei, and the destruction of the nuclei. Formation of radical nuclei was given by the following expression:

$$\frac{dn}{dt} = n_o + (f - g)n - g_o n N \quad (\text{particles}/m^3/s) \qquad (2.17)$$

where n_o represents spontaneous rate for the formation of radical nuclei, defined by the following equation:

$$n_o = A_o \, \bar{C}_{fu} \exp\left(-\frac{E}{RT}\right) \quad (\text{particles}/m^3/s) \qquad (2.18)$$

$\bar{C}_{fu}$ is the time mean concentration of fuel in the burning zone, in kg/m^3. The term $-g_o nN$ in equation (2.17) represents the rate of destruction of active particles on the surface of soot particles whose concentration, N, is derived from the following formation equation:

$$\frac{dN}{dt} = (a - bN)n \quad (particles/m^3/s) \tag{2.19}$$

A similar term for the destruction of active particles also appears here, although the coefficient b is of the order of a hundred times (10^{-13}) larger than g_o (10^{-15}). The mean rate of radical nuclei combustion is adapted from Magnussen (57) and modified by Mehta (2) to account for the effects of instantaneous variation of $\bar{C}_{min}$, and $\bar{C}_{fu}$ to give

$$\frac{dn}{dt} = - \dot{m} r^* \psi n \frac{\bar{C}_{min}}{\bar{C}_{fu}} \tag{2.20}$$

which can be compared with the original expression:

$$\frac{dn}{dt} = - \dot{m} \frac{\psi}{1-r^*\psi} . n \frac{\bar{C}_{min}}{\bar{C}_{fu}} \tag{2.21}$$

Where $\dot{m}$ represents the transfer rate of mass between the fine structure of turbulence, and the bulk fluid. It is defined, for nearly isotropic turbulence, as:

$$\dot{m} = 23.6 \left(\frac{\nu \epsilon}{k^2}\right)^{3/4} \tag{2.22}$$

where ν is the kinematic viscosity, ϵ the rate of dissipation of turbulence kinetic energy, and k the turbulence kinetic energy. Methods of calculating k and ϵ utilised in the model are outlined in detail by Kyriakides et al.

The possible cause for the departure between equations (2.20) and (2.21) is that the model uses instantaneous quantities for concentrations $\bar{C}_{fu}$ and $\bar{C}_{min}$. This implies that towards the end of combustion the term $r^*\psi$ approaches unity, and also $\bar{C}_{fu}$ approaches zero, making equation (2.21) indeterminate. The conditions under which these turbulence parameters were formulated, however, implied the use of the time mean value of concentration (72), expressed mathematically as:

$$\bar{C} = \frac{1}{T} \int_o^T C \, dt \qquad (2.23)$$

This is because, in the analysis of turbulence, time averaging is used to treat statistically steady flows (e.g. bunsen flames), while periodic flows (e.g. internal combustion engines) are treated using ensemble averaging. Instantaneous values computed in the model at each crank angle can be compared to the ensemble averaged value at the same crank position, hence equation (2.20) is used in the existing model.

The rate of oxidation of soot particles during combustion was developed around the kinetically controlled mechanisms proposed by Lee et al (73) for laminar diffusion flames and modified (6) to include effects of turbulence to give the following expression:

$$\frac{dN}{dt} = - \frac{6.51}{s \, d_s} \frac{Po_2}{T^{1/2}} Nr^*\psi \exp \left[- \frac{E}{RT} \right] \quad (\text{particles}/m^3/s) \qquad (2.24)$$

where P_{02} is the partial pressure of oxygen, and T the absolute temperature of the burning zone. r^* is the mass fraction occupied by five structures, and ψ the fraction of fine structures reacting.

2.2.7 Modelling for NO_x Emissions

The formation of NO in engines has long been identified to be a non-

equilibrium process. Fairly accurate results have been obtained by many researchers by assuming that it is controlled by the Zel'dovich mechanism. This is represented by the following two equations:

$$\begin{aligned} &(a)\quad N_2 + O \rightleftharpoons NO + N \\ &(b)\quad O_2 + N \rightleftharpoons NO + O \end{aligned} \qquad (2.25)$$

with equation (a) as the rate determining step. The mechanism is highly dependent on temperature and only linearly dependent on the concentration of oxygen atoms. Consequently, NO_x emissions are largely produced early in combustion when both oxygen concentration and temperaature are high. As a result, EGR is a very effective method of reducing NO_x emissions due to a reduction in temperature and the available oxygen. The conceptual sectorisation of the spray illustrated in Figure 2.4 allows the formation of emissions (NO_x and Smoke) to be related to the concentration similarity profile, and also to the rate of air entrainment which determines the availability of air in each sector. Both emissions subroutines are designed so that they can either be called in each sector (only during injection), using local variables as input, or called only once at each crank position using global values as input.

Two assumptions are made in order to arrive at an approximate rate equation for the rate of the kinetic mechanism:

i. The C-O-H system is in equilibrium and is not affected by dissociations of N_2.

ii. N atoms are assumed to change concentration by a quasi-steady process.

With these two assumptions, it can be shown (8) that the formation rate for NO is given by:

$$\frac{1}{V}\frac{d}{dT}\left([NO] \cdot V\right) = 2(1-\alpha^2)\frac{R_1}{1+\alpha K} \qquad (2.26)$$

where $K = R_1/R_2$

$$R_1 = k_1 [N]_{eq} \cdot [NO]_{eq}$$

$$R_2 = k_2 [N]_{eq} \cdot [O_2]_{eq}$$

k_1 and k_2 represent the forward rate constants for reactions (a) and (b) respetively, in expression (2.25), and α is the ratio of NO concentration to its equilibrium concentration at the same temperature and pressure. Square brackets indicate the molar concentration of the species enclosed, and when subscripted by eq, refer to the equilibrium concentration of the same species.

The method described by Kyriakides et al for evaluating equilibrium concentrations in the cylinder at every crank angle, is based on a partial equilibrium technique, in which only atom-mass balances of Nitrogen and Oxygen are considered (i.e. for the following species: N_2, O, NO, N and O_2). The iterative algorithm adopted to solve for these components was computationally inefficient with the result that to achieve convergence, CPU time much in excess of that utilised for all the other computations in the program, was required. A different procedure based on a total equilibrium consideration has been incorporated instead. Details of the technique are given in a subsequent section of this chapter.

2.3 THE SWIRL ENGINE MODEL

The structure of the swirl model is similar to that described for the quiescent engine. The presence of significant air movement, however, means that the following features require modification in order for the effects of swirl to be incorporated:

a. Free jet trajectory
b. Wall-jet flow
c. Air entrainment function
d. Turbulent mixing rate

The predictions for soot and NO_x are effected with the same equations utilised for the quiescent model, with changes made to the turbulence characterising parameters in equations (2.21) and (2.24). In order for these modifications to be implemented, it is necessary to incorporate a routine for computing swirl.

2.3.1 Generation of Swirl

The model does not compute the formation of swirl during the induction stroke since, as earlier mentioned, only events during the closed period are considered. However, from a given value of swirl ratio at inlet valve closure, the model computes the intensity of swirl at every crank angle until exhaust valve opening.

The intensification of swirl motion in the model is based on the work of Dent and Derham (74). By applying the principle of conservation of angular momentum to the cylinder contents from inlet valve closure, swirl intensity at any crank angle during compression is obtained. Neglecting frictional effects on the walls, and assuming solid body swirl results in the following expression for conservation of angular momentum:

$$\frac{d}{dt}(I_c \cdot \omega_c) = 0 \qquad (2.27)$$

where I_c and ω_c are the moment of inertia and the angular velocity, respectively, during compression. For a deep bowl cylindrical chamber of diameter d_B in an engine with a bore B, Dent and Derham have demonstrated that the moment of inertia of cylinder contents is given by:

$$I = \frac{m_t}{2} \cdot \frac{\left[\frac{\pi B^4}{16} \cdot \frac{\ell(\theta)}{V_B} + \frac{d_B^2}{4}\right]}{\left[\frac{\pi B^2}{4} \cdot \frac{\ell(\theta)}{V_B} + 1\right]} \qquad (2.28)$$

where m_t is the trapped air mass in the cylinder, and $\ell(\theta)$ the instantaneous stroke. The volume V_B refers to the bowl. The moment of inertia during the induction period can be approximated (74) by:

$$I = \frac{m_t}{2} \left(\frac{B^2}{2}\right) \qquad (2.29)$$

Hence the angular velocity of the cylinder charge is given by:

$$\omega = \frac{\omega_o(\pi \frac{B^2}{4} \ell(\theta) + V)}{\pi \frac{B^2}{4} \cdot \ell(\theta) + V.(d_B/B)^2} \qquad (2.30)$$

By specifying the swirl intensity at the closure of the inlet valve, ω_o, the instantaneous swirl at any angle during compression, can thus be computed. The assumption of solid body rotation results in the following expression for the tangential velocity at the walls of the combustion chamber:

$$U_t = \omega . r_B \qquad (2.31)$$

where r_B is the radius of the combustion bowl. This method of calculating angular velocity assumes that swirl increases uniformly throughout the cylinder, during compression. However, the angular velocity in the cylinder will be higher in the central zone (Fig. 2.5) directly above the combustion bowl, than in the annular space (20). This effect results from the fact that the radial air motion (squish) illustrated in the work of Dent and Derham (74) causes air packets to be transported to the central zone, increasing the angular momentum there. A different approach, based on the work of Urlaub (20), has been adapted in the proposed wall-wetting engine model to account for this effect. The simplifying assumptions of solid body swirl and conservation of angular momentum have been maintained.

2.3.2 Free Jet Trajectory

The trajectory of a jet issuing into a cross-flow has been investigated experimentally and analytically by Sinnamon et al (75). Their analytical approach is based on conservation equations applied to the jet as well as the air, to yield equations for the following variables.

i. Decay of axial velocity with penetration (U_m in Figure 2.6)

ii. Jet radial growth (b in Figure 2.6)

iii. Deflection of the jet due to entrainment of fluid with a component of momentum normal to the initial jet spray direction (θ)

iv. Fuel mass concentration at the jet axis, and its variation with penetration.

The algebraic form of these equations are outlined in section 2.4.8 when discussing modifications made by the author. The equations are integrated along the length of the jet, so that it is necessary to

determine the penetration prior to carrying out the integration. This is calculated from the empirical correlation of Chiu et al (18) given below:

$$\frac{X - X_w}{X} = 0.35 \left(\frac{X_w . J_a}{d_o' . J_f}\right)^{0.44} \qquad (2.32)$$

where X_w = Penetration in the presence of swirl
J_a = Cross swirl momentum
J_f = Momentum of the fuel spray
X = Penetration in the absence of swirl.

Also derived from the work of Sinnamon et al is the expression for the rate of air entrainment into the jet, given by:

$$\frac{d\dot{m}_E}{ds} = 2\pi r_j \, (\rho_m . \rho_a)^{1/2} \, (\alpha|U_m - U_t| + \lambda|U_n|) \qquad (2.33)$$

where subscript m refers to values on the axis of the jet, t to the tangential component of velocity, and n to the normal component. The empirical constants α and λ are assigned the values of 0.035 and 0.05 respectively by Sinnamon et al.

In order to derive all the dimensions of the jet from the equations of Sinnamon et al, it is necessary to solve simultaneously four differential equations representing conservation of mass (two equations), and the conservation of momentum (another two equations). To avoid solving the whole system of equations, radial growth of the jet was assumed to follow the steady state equation of Abramovich (62) given in equation (2.6), modified according to Adler and Baron (76) as:

$$\frac{dr_j}{dx} = 0.11 \left(\frac{\rho_j}{\rho_a + \rho_j}\right) \left(\frac{\Delta U_m}{U_m + U_t}\right) \qquad (2.34)$$

where ΔU_m is the excess centreline velocity $(U_m - U_t)$, and U_t the tangential component of air velocity.

Steady state similarity profiles are also assumed for the distribution of fuel mass fraction, in line with other workers (18, 75, Adler and Lyn (77).

2.3.3 Effect of Wall Impingement

A model of the wall-jet structure, based on the work of Spalding (51) and also that of Escudier and Nicoll (78) is used to characterise penetration along the piston wall, and air entrainment into the impinged portion. Details of the analytical basis are discussed in reference (8). Inherent in this treatment of the wall-jet is the assumption that the fuel jet may be treated as a gaseous jet, and air entrainment is then computed using the following equation from Escudier and Nicoll:

$$\dot{m}''_{ENT} = \rho_G U_G [0.03 Z_E - 0.02] \qquad (2.35)$$

which has units of mass flux ($kg/m^2.s$). Z_E is the velocity profile shape parameter defined (78) as the ratio of the law of the wall velocity at the outer edge of the boundary layer, to the bulk gas velocity. This may be expressed algebraically as:

$$Z_E = \left.\frac{U^+}{U_G}\right|_{y=\delta} \qquad (2.36)$$

where U^+ is the expression for the law of the wall velocity which will be discussed in detail in Chapter 4. The method used in the model to evaluate Z_E is outlined by Kyriakides et al.

The resulting entrainment level is obtained by adding the free jet to the wall jet component.

2.3.4 Turbulent Mixing

The resultant mixing time in swirl engines combines the component due to injection with that due to air swirl so as to give the mixing rate as (7):

$$R_{MIX} = \frac{R_{inj} \cdot R_{swi}}{R_{inj} + R_{swi}} \qquad (2.37)$$

where the mixing rate, R, is defined by the reciprocal of mixing time. Equation (2.14), which has been used to derive the turbulence energy dissipation rate in the quiescent model, describes the component due to the injection process. In the swirl model, it is necessary to include the effect of air motion on the level of turbulence, and hence equation (2.38), based on the work of Dent et al (7), is used to determine the swirl component for the dissipation rate.

$$\epsilon = \frac{\omega^3 d_B^2}{32} \qquad (2.38)$$

Once the mixing time has been evaluated using the relation given under section 2.2.5 and equation (2.37), the rate of fuel-air mixing is then calculated from the same expression as used in the quiescent model, i.e. equation (2.16).

2.4 MODIFICATIONS MADE TO THE COMBUSTION MODEL BY THE PRESENT AUTHOR

By taking advantage of the similarities between the two programs discussed above, once again it is only necessary to describe in detail the changes made to only one program, it being understood that similar changes have been effected in the other version wherever appropriate. The swirl engine model has been chosen for detailed descrition as it includes most of the features of the quiescent model.The following is a list of all the changes made to the swirl engine model, which will be discussed in the paragraphs that follow:

i. Incorporation of an 'Introductory Front-End' and associated routines.

ii. Incorporation of a new routine for the characterisation of piston bowl geometry.

iii. Use of Gaussian Elimination instead of a 'NAG' Library Routine.

iv. New Algorithm for evaluating the equilibrium composition of

exhaust products.

v. Re-casting of the NO kinetic rate equation.

vi. Re-writing soot formation routine.

vii. Replacing soot oxidation routine with one that accounts for oxidation due to the OH-radical in fuel-rich regions.

viii. New iterative routine, based on the assumption of Lewis number equal to unity, so that the mass transfer numbers B_m and B_H should be equal.

ix. Dispensing with the use of an experimental injection pressure diagram in favour of a sinusoidal fuel delivery rate.

x. Development of an Exhaust/Induction routine.

xi. Replacement of vectorised solution of Sinnamon's equation with an algebraic routine based on the solution of the complete set of equations.

xii. Redefinition of fuel spray dispersion.

The other significant change, which may not require separate categorisation, but nevertheless having a profound influence on the behaviour of the model, is the adoption of a constant $\hat{t}$ time step rather than one that is determined by the chosen engine speed.

2.4.1 Introductory Front-End

In order to make the program easily accessible and 'user-friendly', an introductory front-end has been incorporated. This serves the purposes of assisting the user to create the required input data files in the right format, and also to be able to change run-conditions

rapidly and conveniently. Once the files have been created, subsequent runs of the program are achieved simply by calling the relevant data files. This is a major change from the old versions of the program in which the data (engine dimensions mostly) were incorporated in the coding of the program. To model a different engine, therefore, necessistated some re-programming. A sample terminal dialogue, illustrating the working of this routine, has been incorporated in Section 6.4.1.

2.4.2 Determination of Piston Bowl Geometry

Although the nature of the model renders it less sensitive to piston bowl geometry, certain aspects of the geometry have a very significant and noticeable effect. The bowl diameter, for example, determines the swirl intensity in the vicinity of TDC, which in turn affects the mechanism of mixing, a process central to the operation of a diesel engine. Bowl depth, on the other hand has an effect on entrainment in that it determines the impingement of the jet, which is associated with reduced air entrainment - another form of mixing. The method used to specify bowl geometry (surface area and volume) required considerable input data, and was specific to a particular piston bowl shape. This, obviously, limits the effectiveness of the model in that it becomes less versatile. A generalised approach has been developed and incorporated into the model. This requires only 6 dimensions (see Figure 2.7) to characterise any combustion bowl shape. Details of the method used are given in Appendix B.

2.4.3 Changes in Numerical Techniques

It was demonstrated in section 2.2.3 that the governing equations for the energy balance of cylinder contents can be presented in a matrix form, which is then solved using the Crout Reduction method. A 'NAG' package on the university mainframe was used to achieve this. However, as the system of equations is very small (four equations), there is no loss in computing time if a direct method, such as

Gaussian elimination is employed. In fact, for systems of equations less than ten, it is recommended practice (61) to use the direct approach. A Gaussian elimination routine has thus been incorporated in the program, dispensing with the need to invoke the 'NAG' library. Due to the simplicity of the system involved, no observable gains in numerical accuracy or losses in computational time are noticed when the above modification is implemented. The advantage in using the new routine is that it makes the whole program "self-contained". As mentioned in the introduction to this chapter, this removes the need for the user to have access to an appropriate 'NAG' package to be able to successfully implement the model on a micro-computer.

A rapidly converging iteration routine useful in the solution of equations of the form $x = f(x)$, has been incorporated. Steffens algorithm (given in detail in reference (61)), which has quadratic convergence, is used to obtain values of mass transfer under the assumption of Lewis number equal to unity. A detailed discussion of the equation iterated in the model, will be outlined in Chapter 4. In Figure 2.8 the value of B as calculated from the new technique is illustrated.

2.4.4 Equilibrium Composition of Combustion Products

By assuming that the combustion reaction can be approximated by the following chemical reaction;

$$C_n H_m + \text{Air} \longrightarrow H + O + N + H_2 + OH + CO + NO + O_2 + CO_2 + N_2 \quad (2.39)$$

a new algorithm has been developed (Appendix A) which converges rapidly by making use of the Newton-Raphson iterative technique for systems of non-linear equations.

The two techniques, as can be expected, yield different results with

the new procedure converging much faster than that used by Kyriakides et al. A further improvement was the use of a fixed mass (12, 13, Shahed et al (79)) to define V_b, the required volume in the rate kinetic equation instead of V_j derived from energy balance calculations. This is because V_j contains unburnt vapour and air beside combustion products, whereas V_b represents a volume of combustion products resulting from complete combustion of a fixed mass of fuel.

The modification to the NO kinetic rate equation involves the use of NO mass fractions rather than concentration (kg/m^3) as is the case in equation (2.26). The reason for this is that the rate of change of V in equation (2.26) cannot be defined analytically, and the method used to evaluate it (from the energy balance matrix) causes instabilities when charge temperatures become too high. The rate equation can be expressed in terms of mass fractions of NO by the equation below (Ferguson (80)):

$$\frac{dX_{NO}}{dt} = \frac{60}{\rho}(1-\alpha^2)\frac{R_1}{1+\alpha K} \qquad (2.40)$$

where X_{NO} = NO mass fraction
ρ = Change density
α = X_{NO}/X_{NO} eq.

R_1 and K retain the same definitions as in equation (2.26).

2.4.5 Modifications to the Soot Model

Although there have been some changes made to the soot formation routine, these have basically been a re-casting of the equations of

Tesner et al (71) with the turbulence considerations of Magnussen (57) taken into account. So the discussion given earlier in 2.2.6 is valid under the present modifications. The major changes have dealt with the oxidation routine. It is a generally held view, according to Appleton (81), that the Nagle and Strickland-Constable model (82) provides the best method for estimating soot oxidation in combustion systems. However, according to a study by Neoh et al (83), this same model has been found to under-estimate oxidation rates in fuel-rich zones or near stoichiometric conditions. To counter this under-estimation, Ahmad, Plee and Myers (84) have included an extra term to account for oxidation due to the OH-radical, as suggested by Fenimore and Jones (85). Hence they express the rate of soot oxidation by the following equation:

$$\frac{dm_s}{dt} = -\frac{60}{\rho_s} \cdot \left(\frac{m_s}{d_s}\right) [m''_{O2} + m''_{OH}] \qquad (2.41)$$

where m'_{O2} is the reaction rate on soot surfaces due to oxygen (in $g/cm^2.s$), and m'_{OH} a similar rate due to the OH radical. The calculation of m'_{O2} is based on the Nagle and Strickland-Constable model, expressed as follows:

$$m''_{O2} = 12\left[\frac{k_a \cdot P_{O2}}{1+k_2 P_{O2}} \cdot x + k_b \cdot P_{O2} (1-X)\right] \ (g/cm^2.s) \qquad (2.42)$$

where k_2, k_a, and k_b are defined as follows:

$$k_a = 20. \ \exp(-30\,000/RT) \quad (g/cm^2.s.Atm)$$

$$k_2 = 21.3 \exp(4\,100/RT) \quad (Atm^{-1})$$

$$k_b = 4.46 \times 10^{-3} \exp(-15\,200/RT) \quad (g/cm^2.s.Atm)$$

P_{O2} is the partial pressure of oxygen and X is the fraction of the soot surface that is covered by reactive sites. This is defined by:

$$X = \frac{1}{1 + \frac{k_t}{k_b . P_{O2}}} \qquad (2.43)$$

where $k_t = 1.51 \times 10^{-5} \exp(-97\,000/RT)$ g/cm^2.s for the OH-term, the following equation, after Fenimore and Jones, is used:

$$\dot{m}''_{OH} = 1.63 \times 10^4 . \alpha . \frac{P_{O2}^{1/4} . P_{H2O}^{1/2}}{T^{1/2}} \exp(-37\,800/RT) \quad g/cm^2.s \qquad (2.44)$$

where α = Collision efficiency (A value of 0.1 is suggested)

P_{H2O} = Partial pressure of H_2O (Atm)

R = Gas constant (cal/mole.K)

T = Absolute temp.

Substituting equations (2.42) and (2.44) into (2.41) provides an expression for the net soot mass concentration in g/cm^3. Ahmad et al (84) have also used Magnussen's approach to account for the effect of turbulence on the chemical kinetics, and use the equation (2.41)) as a source term for their multi-dimensional model. For the phenomenological approach, however, the source term is a sufficient parameter for characterising soot formation and oxidation, and it has been demonstrated by Mehta (2) after Magnussen that turbulence effects may be incorporated simply by multiplying all the kinetic terms by the rate of transfer of mass between the bulk fluid and the fine structure of turbulence. This is defined (57) by:

$$r^* . \psi = \frac{C_{pr}}{C_{pr} + 4.45\, C_{fu}} \qquad (2.45)$$

where C_{pr} and C_{fu} are, respectively, the concentration of combustion products and fuel, in kg/m^3. The constant 4.45 is the value for r, defined by:

$$r = 1 + (\frac{O_2}{F})_{stoic.} \tag{2.46}$$

where $(\frac{O_2}{F})_{stoic.} = 3.45$

Equation (2.45) has been applied to equations (2.17) and (2.19) to include turbulence effects. r* and ψ have the same meanings as in equation (2.24).

2.4.6 Sinusoidal Fuelling Rate

Among the input data required to implement the model is an injection pressure diagram. Kyriakides et al make use of pressure diagrams experimentally obtained at the conditions to be modelled. This was considered an improvement over the earlier version of the model (2) in which trapezoidal injection pressure diagrams were assumed. However, as it may not always be possible, or even practical to obtain injection pressure diagrams at every condition to be modelled, the present modification makes it only necessary to specify injection duration (θ_i) and quantity of fuel injection (Q) per stroke. It is worth pointing out here that θ_i, and Q are not additional input variables as they were also necessary in the version discussed by Kyriakides et al. So the number of input variables have been reduced by the present modification. The following sinusoidal fuelling rate is assumed :

$$\frac{dq}{d\theta} = \frac{\pi Q}{2\theta_i} \cdot \sin(\frac{\pi\theta}{\theta_i}) \tag{2.47}$$

where dq is the volume of fuel injected in the crank interval $d\theta$. Equation (2.47) is formulated in such a way that the following relation is satisfied:

$$Q = \int_{\theta_{io}}^{\theta_{ie}} q \, d\theta \qquad (2.48)$$

where θ_{io} is the crank angle at the start of injection, and θ_{ie} the angle at the end of injection. Based on equation (2.47) and the equation for injection pressure derived by Dent (14), the instantaneous injection pressure, ΔP_{inj}, is then given by:

$$\Delta P_{inj} = \frac{\rho_f}{2} \left[\frac{6N \frac{dq}{d\theta}}{C_d \frac{\pi n d_o^2}{4}} \right]^2 \qquad (2.49)$$

where N is the engine speed in RPM, n the number of holes in the injector nozzle, d_o the diameter of each hole, C_d the discharge coefficient, and ρ_f is the fuel density. Figure 2.9 compares the injection pressure diagram resulting from the use of equation (2.47) with a typical injection pressure diagram.

2.4.7 Exhaust/Induction Routine

Figure 2.10 shows a schematic diagram of the physical processes of exhaust and induction. A fundamental model of these processes has been developed based on the work of Sherman and Blumberg (86). The objectives of the model are as follows:

i. To describe mass flow during intake and exhaust processes so as to estimate pumping and valve throttling effects on volumetric efficiency.

ii. To allow for the inclusion in the program, of calculations for mean effective pressure.

The thermodynamic formulation is based on applying the open system energy balance to the control volume consisting of the cylinder working volume. This can be written, in terms of the change in internal energy, as:

$$dU = dQ - dW + h_i dm_i + h_e\, dm_e \qquad (2.50)$$

where dm_i and dm_e flow through the intake and exhaust manifolds, respectively, and h_i and h_e the respective enthalpies. dW is the work term, and dQ the heat transfer to the cylinder walls. Sherman and Blumberg have written equation (2.50) in terms of temperatures and heat capacities and show that by combining with the perfect gas law, the change in cylinder pressure, dP_c, is obtained as a first order differential equation:

$$dP_c = \frac{1}{V}\left[-\gamma P_c\, dV + (\gamma - 1)\, dQ + R\gamma(T_i dm_i + T_e dm_e)\right] \qquad (2.51)$$

From mass conservation considerations in the cylinder, Horlock and Woods (87) have derived the following expression for the change in charge temperature:

$$\frac{dT_c}{T_c} = \frac{dP_c}{P_c} + \frac{dV_c}{V_c} - \frac{R_c\, T_c}{P_c V_c}(\dot{m}_i + \dot{m}_e) \qquad (2.52)$$

Equations (2.51) and (2.52) are solved simultaneously using a forth order Runge-Kutta integration. Before the solution to the two equations can be sought, it is necessary to specify dV, dQ, dm_i, and dm_e. dV is easily evaluated from the equation for piston motion which is used in other parts of the main model. Mass flow rate through the inlet and exhaust valves (dm_i and dm_e) are approximated by

isentropic compressible flow equations as applicable to flow through nozzles, and modified by means of a discharge coefficient. Steady flow conditions are assumed during each time step, and the mass flow rate through either valve is given by:

$$\frac{dm}{dt} = C_d \cdot A_v \cdot P_u \cdot F \left(\frac{2}{RT_u}\right)^{1/2} \qquad (2.53)$$

where:

$$F = \sqrt{\frac{\gamma}{\gamma-1} \left(\frac{P}{P_u}\right)^{2/\gamma} \left[1 - \left(\frac{P}{P_u}\right)^{(\gamma-1)/\gamma}\right]} \quad \text{for subsonic flow}$$

$$= \sqrt{\frac{\gamma}{\gamma+1} \left(\frac{2}{\gamma+1}\right)^{2/(\gamma-1)}} \quad \text{for sonic flow (choked)}$$

P_u = Upstream pressure
P = Downstream pressure
C_D = Discharge coefficient
A_v = Minimum flow area at the valve
T_u = Upstream temperature.

The variation of discharge coefficient with valve lift is given by Sherman and Blumberg, after the work of Kastner et al (88) by:

$$C_D = 1 - 1.5 \left(\frac{L}{D}\right) \qquad (2.54)$$

The high discharge coefficient (approaching 1) at low lift (approaching zero) was attributed to the absence of a tendancy, by the flow, to separate, and so is approximated to isentropic flow. This, however, neglects the effects of friction which increase drastically as lift approaches zero. Thus, the results of Tabaczynski (89) which show discharge coefficient approaching zero as valve lift becomes very small, are considered more realistic. This is also the trend shown by

Fukutani and Watanabe (90) which is illustrated, together with a 6th-order Chebyschev polynomial fit used in the present model, in Figure 2.12. Equation (2.54) thus, only represents the discharge coefficient for relatively large value lifts (typically L/D > 0.05). To characterise the nature of the flow, it is assumed that the valve seat has a conical shape, and that flow through it is divided into the following regimes:

i. Early stages of valve lift when minimum area corresponds to the frustrum of a cone.

ii. When the minimum area corresponds to the annular area i.e:
Port Area less area of valve stem.

These two regimes are illustrated in Figure 2.11. In the first regime, it can be shown that the area is given as:

$$A_f = \pi D^2 \, Cos\alpha . \, [1 + \frac{1}{2} (\frac{L}{D}) \, Sin \, 2\alpha] . (\frac{L}{D}) \qquad (2.55)$$

where L = Valve lift
D = Inlet port nominal diameter
α = Valve seat angle (typically 45^o)

Sherman and Blumberg suggest that this regime occurs in the range:

$$0 \leqslant (\frac{L}{D}) \leqslant 0.125$$

In the second regime the flow is through a section with an annular cross-sectional area given by:

$$A_f = \frac{\pi D^2}{4} (1 - \beta^2) \qquad (2.56)$$

where β is the ratio of the valve stem diameter to the valve nominal diameter. By equating equations (2.55) and (2.56) and solving for $\frac{L}{D}$, the limiting value for the transition from the first to the second regime is then given by:

$$\frac{L}{D} \leqslant \frac{[1 + (1-\beta^2)\sin\alpha]^{1/2}}{\sin 2\alpha} - 1 \qquad (2.57)$$

The variation of valve lift as a function of crank angle is derived from the diagrams in Figure 2.13, as suggested by Sherman and Blumberg. By defining the acceleration ratio (see Fig. 2.13(a)) as;

$$r = \frac{a_{max}}{a_{min}} \qquad \text{(this is -ve)} \qquad (2.58)$$

then it is possible to derive the following equations for the normalised valve lift:

$$\text{For } \theta_0 \leqslant \theta \leqslant \theta_1 : \frac{L}{L_{max}} = a_{max} \cdot \frac{\theta^2}{2} \qquad (2.59)$$

$$\text{For } \theta_1 \leqslant \theta < \theta_2 : \frac{L}{L_{max}} = a_{min} \cdot \left(\frac{\theta^2}{2} - \hat{\theta}.\theta + \frac{\hat{\theta}^2}{2}\right) + 1 \qquad (2.60)$$

$$\text{For } \theta_2 \leqslant \theta \leqslant \theta_f : \frac{L}{L_{max}} = a_{max} \cdot \left(\frac{\theta^2}{2} - \theta_f.\theta + \frac{\theta^2}{2}\right) \qquad (2.61)$$

where all angles are defined with respect to Figure 2.13. Once the acceleration ratio, r, has been specified, then the maximum acceleration is defined by $a_{max} = r.\ a_{min}$ where a_{min} is calculated as follows:

$$a_{min} = \frac{1}{\frac{\hat{\theta}^2}{2} + \theta_1(r-1)(\hat{\theta} - \frac{\theta_1}{2})} \qquad (2.62)$$

By assigning a value of zero at valve opening (i.e. when $\theta = \theta_o$), then:

θ_f =[Valve closure]-[valve opening]

$\theta_m = \theta_f/2$

$\theta_1 = \frac{\theta_m}{1-r}$

$\theta_2 = \theta_f - \theta_1$

Hence it is only necessary to specify three variables to characterise valve lift:

1. Valve timings
2. Valve acceleration ratio, r
3. Crank angle at which lift is to be determined.

Figure 2.14 shows the effect on valve lift, of the acceleration ratio, r, and in Figures 2.15 to 2.18, typical solutions from the Exhaust-Induction subroutine are illustrated. Where dimensions of the valves are not specified, values in the following range are recommended by Lilly (16):

$$0.43\ B \leqslant D_i \leqslant 0.46\ B$$
$$0.35\ B \leqslant D_e \leqslant 0.37\ B$$

where B is the cylinder bore.

2.4.8 Modified Fuel Spray Characterisation

An analytical model consisting of integral continuity and momentum equations for a steady-state gas jet has been developed, based on the work of Sinnamon et al (75), discussed earlier. The difference between the present approach and that described in section 2.3.2 above

is the comprehensive treatment in the present work, of the four equations expressing the conservation of fuel mass, total jet mass and the conservation of horizontal and vertical components of momentum, given below:

i. Conservation of Fuel Mass

The flow-rate of fuel mass at any cross-section of the jet is constant. This is expressed by the following equation:

$$\frac{d}{dS}\left[\int_C u\rho dA\right] = 0 \qquad (2.63)$$

ii. Conservation of Total Jet Mass

At any cross-section of the jet, the rate of increase in the jet mass is equal to the entrainment rate:

$$\frac{d}{dS}\left[\int \rho u \, dA\right] = \frac{dm_E}{dS} \qquad (2.64)$$

The entrainment function of Ricou and Spalding (65) is used to express express the rate of air entrainment along the jet, leading to equation (2.33) shown earlier.

iii. Conservation of Momentum

The horizontal component of the jet momentum is given by the following equation (see Figure 2.19 for the nomenclature):

$$\frac{d}{ds}[\cos\theta \int \rho U^2 dA] = U_s \cdot \cos\phi \frac{dm_E}{ds} - F_d.\sin\theta \qquad (2.65)$$

The corresponding vertical component is:

$$\frac{d}{ds}[\sin\theta \int \rho U^2 dA] = U_s \cdot \sin\phi \frac{dm_E}{ds} + F_d.\cos\theta \qquad (2.65)$$

Where F_d = Aerodynamic drag force on the jet.

Although the effects of drag in changing jet momentum are included in equations (2.65) and (2.66), Sinnamon et al argue, on the basis of their experimental results, that if air entrainment rate is sufficiently large, spray deflection can be adequately accounted for by the component of momentum in the entrained air, having a direction identical to that in which the jet deflects. And the drag coefficient can then be made equal to zero. This argument has also been adapted in the present model, although provisions have been included for making drag coefficient greater than zero to allow for conditions where computed air entrainment does not adequately account for observed jet deflection.

Since the position of the jet has been moved to the centre of the bowl, and the x and y axes are defined such that the y-axis is in the direction of injection and the x-axis perpendicular to it (see Figure 2.19), the normal and vertical components of swirl air are re-cast as follows:

$$U_t = U_s \cdot \text{Cos}\ (\theta + \phi) \qquad (2.67)$$

$$U_n = U_s \cdot \text{Sin}\ (\theta + \phi) \qquad (2.68)$$

where U_s is the local swirl velocity defined by ωr, and the angles θ and ϕ have the definitions illustrated in Figure 2.19. Equations (2.63) to (2.66) can be represented in matrix form as follows:

$$[A_{ij}] \cdot \begin{bmatrix} \frac{dC_m}{ds} \\ \frac{dU_m}{ds} \\ \frac{dr_j}{ds} \\ \frac{d\theta}{ds} \end{bmatrix} = \begin{bmatrix} 0 \\ E_f \\ U_s E_f \cdot \frac{\cos \phi}{\cos \theta} - C_d \tan \theta \frac{U_n|U_n|}{2\pi} \\ U_s E_f \cdot \frac{\sin \phi}{\sin \theta} + C_d \cos \theta \frac{U_n|U_n|}{2\pi} \end{bmatrix}$$

where $E_f = (\frac{\rho_m}{\rho_a})^{1/2} [\alpha|U_m - U_t| + \lambda|U_n|]$

$i,j = 1 \ldots 4$

The elements A_{ij} are defined by Sinnamon et al. Gaussian elimination is used to solve for the derivatives dC_m/ds, dU_m/ds, dr_j/ds, and $d\theta/ds$, which are then integrated using the modified Euler's numerical technique. The solution gives values of fuel mass fraction and velocity at the jet axis (C_m and U_m respectively), the radius of the jet, r_j, and the deflection of the jet centre-line, θ, at any position in the local direction of the spray. Additionally, the entrainment function is solved, thus completely defining the jet. Sinnamon et al recommend the use of a more general form of the steady-state similarity profile expression in equation (2.5) in order to match experimental with analytical results. Their equation, thus, takes the following form:

$$f(Y_p) = K_1 - K_2 Y_p^{1.5} \qquad (2.69)$$

Constants K_1 and K_2 afford greater flexibility in adjusting the model to respond to a wide range of injection nozzle designs. So equation (2.69) has been used in the program although K_1 and K_2 have both been assigned a value of one.

2.4.9 Structure of the New Zones

The method proposed by Mehta (2) for the redistribution of fuel drops in the spray, was based on a calculation of the volume of fuel in each sector from Simmon's correlation, given earlier in equatin (2.7). This approach has several inherent weaknesses some of which are briefly described below:

(i) Simmons' equation bears no relationship with the fuel concentration profile as given by equation (2.5). As a result, the fuel mass fraction in each sector becomes independent of jet trajectory calculations.

(ii) Droplet diameters in a given sector are uniform along the entire length of the jet, varying only in the radial direction.

(iii) Fuel evaporation results in a reduction of droplet numbers, but not diameters which are reduced, instead, by a complicated redistribution process.

Given that the representation of the fuel spray is the single most important component of the model, it is essential to give as accurate a method as can be achieved within the constraints of phenomenological modelling. A new strategy has thus been incorporated to try and improve on the weaknesses outlined above. This new method, which has the added advantage of simplifying the handling of the simultaneous occurance of evaporation and the issuing of new fuel droplets into a given sector, is illustrated in Figure 2.20. It is based on the tracking of individual fuel/air 'packages' in time, spatial position, as well as mass and energy content. The eleven radial sectors described earlier are retained, but, in addition, the spray is also progressively 'sectored' along its length, into discrete packages' such as that 'shaded' in Figure 2.20. When the computation has been advanced by the time step, dt, the change in jet penetration, dx, defines the instantaneous length of the leading 'package' (i.e. fuel injected in the first instant plus present increment in air

entrainment rate). The rest of the trailing 'packages' are each assumed to follow the history of their respective leading 'package' (only with respect to penetration and entrained air mass). Each 'package' is further sub-divided into eleven radial sectors as proposed by Mehta. Droplet diameters in each sector are determined from Simmons' correlation, based on the fuel volume fraction in the sector as calculated from the equations of Sinnamon et al (75) described earlier. This is done only as the 'package' issues from the nozzle. At subsequent time intervals, the number and diameter of droplets in each sector reduces due to evaporation. Since no transfer of mass is allowed between adjacent 'packages', fuel mass in all the packages reduces only due to combustion and entrained air is distributed into all the sectors by the concentration profile in equation (2.5). To ensure mass conservation in the jet, equation (2.70) is checked at every crank position during injection:

$$m_f = \int_0^{R_j} \rho C\, U\, dA \qquad (2.70)$$

The local velocity, U, is defined by equation (2.4), while density is assumed to be linearly proportional to the concentration profile:

$$\rho = \rho_G + C(\rho_f - \rho_G) \qquad (2.71)$$

In order that the rest of the program proceeds as before (i.e. with only eleven radial sectors), quantities in the various packets are integrated along the length of the jet before passing them on to the other subroutines. The scheme associated with the new zoning is illustrated in Figure 2.21.

2.5 FINAL ADJUSTMENTS TO THE MODELLING CONCEPT

A subroutine (REDIST) to deal with the redistribution of both fuel vapour and droplets at each time step has been included. This has been necessitated by the fact that when the model is operated with all the modifications described in section 2.4, the combustion rate during

injection drops adversely after the initial sharp rise resulting from ignition of the pre-mixed charge. This was initially attributed to the low entrainment rate resulting from the use of Dent and Derham's (74) equation for computing swirl in the cylinder, which results in a profile that remains low for most of the compression stroke and only rises close to TDC (as illustrated in figure 2.22). The corresponding air entrainment component due to swirl is thus lower. The swirl generating equation used in the wall-wetting model (this is described in detail in chapter 3), based on the work of Urlaub(20) was used to try and alleviate this problem. However the reduction in heat release rate after the initial pre-mixed charge was burned continued to be a problem. This led to the incorporation of the new subroutine to distribute fuel outwards from the core of the jet. This solves the problem by providing additional fuel for combustion in regions of the jet where all the fuel would, otherwise , have been burned in the pre-ignition stage thus enhancing the mixing of fuel and air.

To demonstrate the effectiveness of the model in predicting engine cylinder parametres , the following conditions ,which refer to a single cylinder experimental engine, were fed as input to the program.

Stroke	= 90.54 mm
Bore	= 93.67 mm
Conn. Rod Length	= 154.0 mm
Comp Ratio	= 19.1
Injector Nozzle Orifice Dia.	= 0.23 mm
Number of Holes	= 4

The data, which are tabulated in Table 2.1 below, cover four engine speed conditions ranging from 1000 to 4000 RPM. Figures 2.23 to 2.26 show the resulting pressure diagrams, and the corresponding temperatures, heat release rate and mass fractions are shown in figures 2.27 to 2.30. Also shown are the respective air entrainment fluctuations with crank angle.

To obtain reliable smoke emission trends, it was found necessary to

make two changes to Tesner's equations in order to account for the variable density in engine operation as opposed to the empirical conditions under which the equations were derived, and also to allow for the contribution of swirl intensity to turbulence to be be effective. The first of these tasks was achieved by incorporating a ratio of the densities in the manner shown below:

$$[\text{ Equation (2.17) and Equation (2.19)}].(\bar{\rho}/\rho)$$

This is a fairly standard procedure for taking into account density fluctuations which is sometimes refered to as the 'Howarth-Dorodnitsyn Transformation' (50). It has the effect of correcting the fluctuations in particle number density that are caused by the volumetric expansion of the region under consideration. The second task was achieved by slightly altering the application of Magnussen's eddy dissipation concept so that the assumption that all the mass contained in the fine structure of turbulence takes part in combustion was incorporated. The result is that the term $r^*.\psi$ which was included by Magnussen in the equations of Tesner in order to account for turbulence effects, now changes to just r^*. This changes the response to swirl intensity because the mixing time , which is a function of swirl intensity, no longer cancels out of the equation, as was hitherto the case (this latter case is demonstrated in equation 2.45).

Figures 2.31 to 2.34 show the resulting smoke and NOx results when operating under the same conditions outlined ealier. The NOx results are not affected by these later changes however.

2.6 CLOSURE

Generally, the results from the model compare favourably with experimental data over a range of engine speed (from 1000 to 4000 RPM) In their conclusion, Kyriakides et al (8) pointed out that more work was required in further developing the NO model. The new algorithm for calculating equilibrium composition of combustion

products thus forms a contribution towards achieving that goal. It is hoped that the new strategy for zoning the jet spray, may lead to a better understanding of the causes of inaccurate performance in the model, when handling thick sprays injected at high pressure. Although the algorithm has slowed the program down tremendously, it is still much faster than the NOx routine described by Kyriakides et al, and so is an improvement on a comparative basis.

Table 2.1: SWIRL INPUT DATA

DATA SET NO.	ENGINE SPEED (RPM)	INJECTION TIMING (Deg. CA)	INJECTION DURATION (Deg. CA)	IGNITION DELAY (Deg. CA)	FUEL DELIVERY (mm**3/STR)
1	4000	-11.3	24.5	10.2	34.1
2	3000	-7.5	20.0	8.7	35.5
3	2000	-13.9	13.9	6.8	34.1
4	1000	-8.1	8.1	6.1	28.1

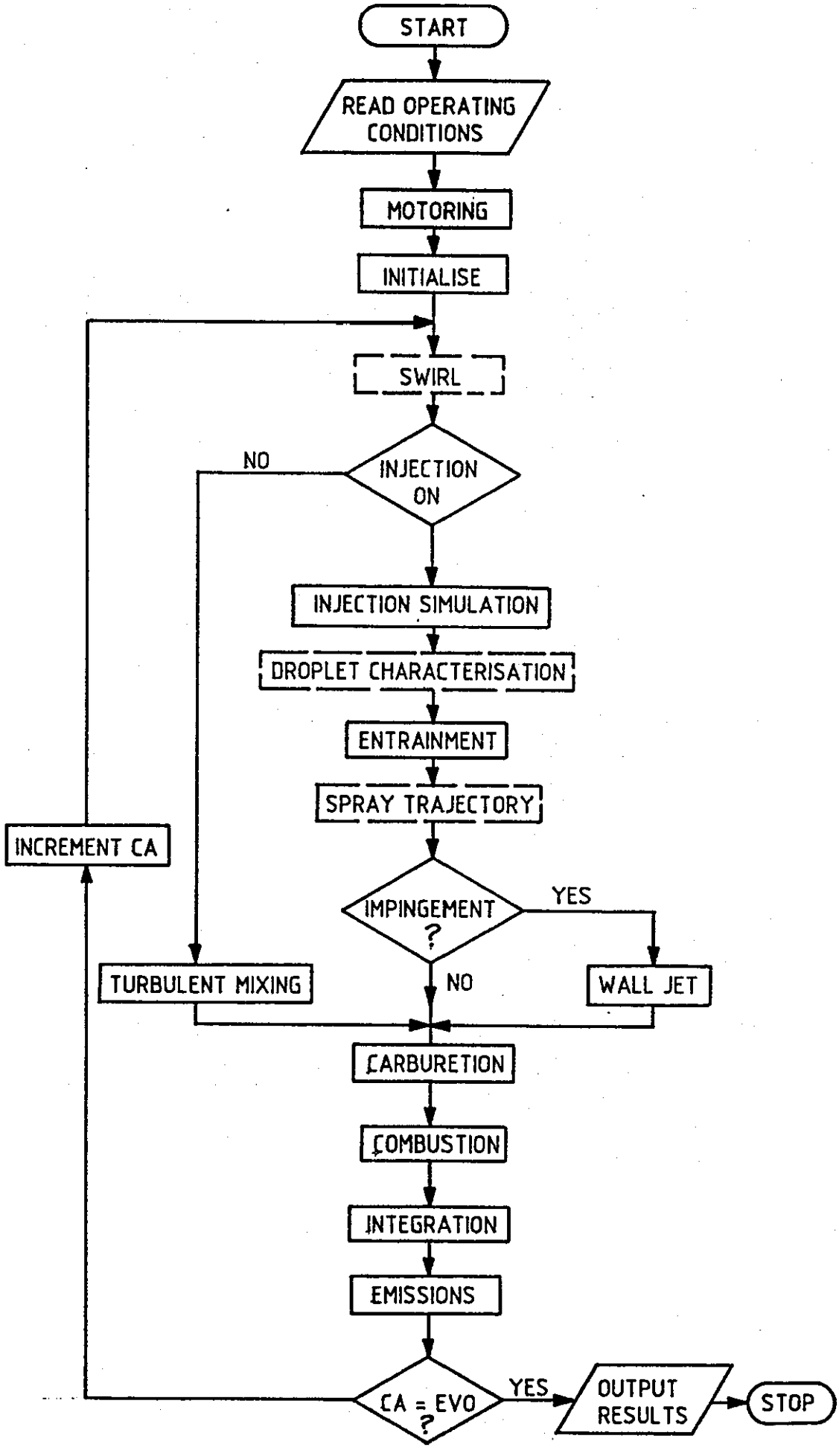

FIGURE 2.1: DIESEL ENGINE COMBUSTION MODEL GENERALISED FLOW-CHART

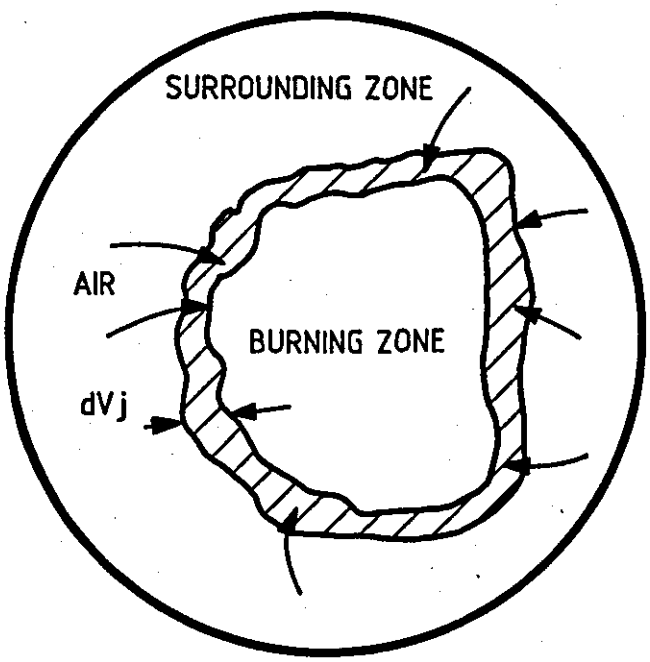

FIGURE 2.2: CONCEPTUAL STRUCTURE OF THE CYLINDER CHARGE DURING COMBUSTION

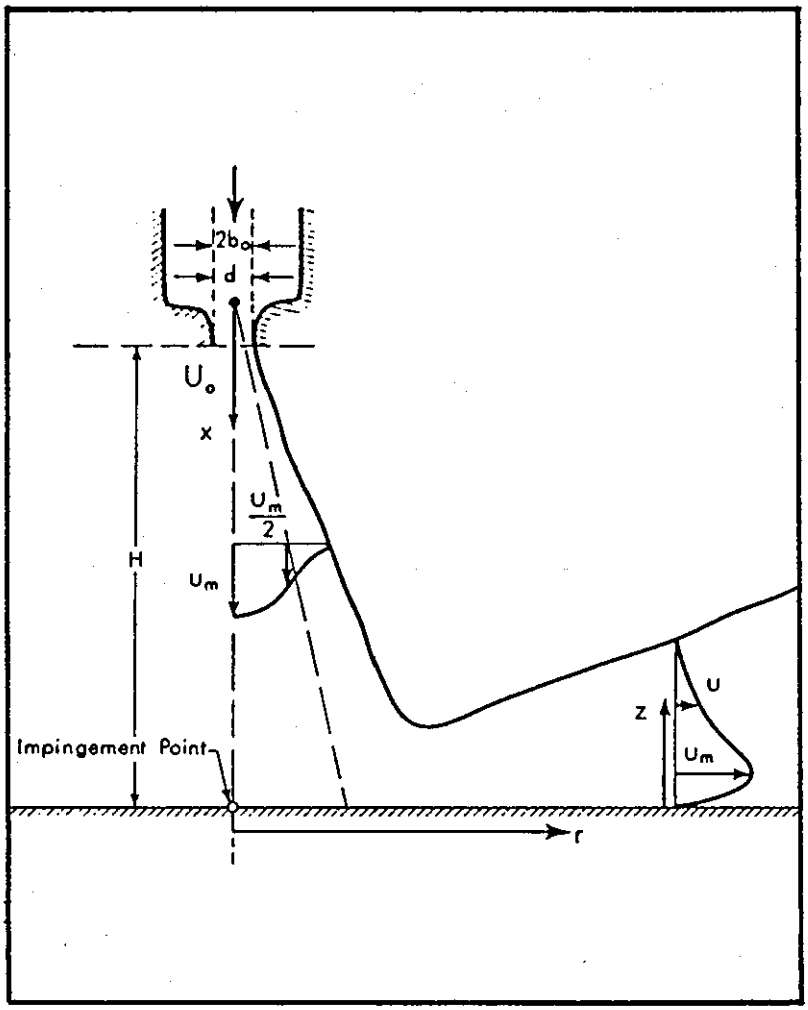

FIGURE 2.3: RADIAL WALL JET PRODUCED BY AN IMPINGING CIRCULAR JET (66)

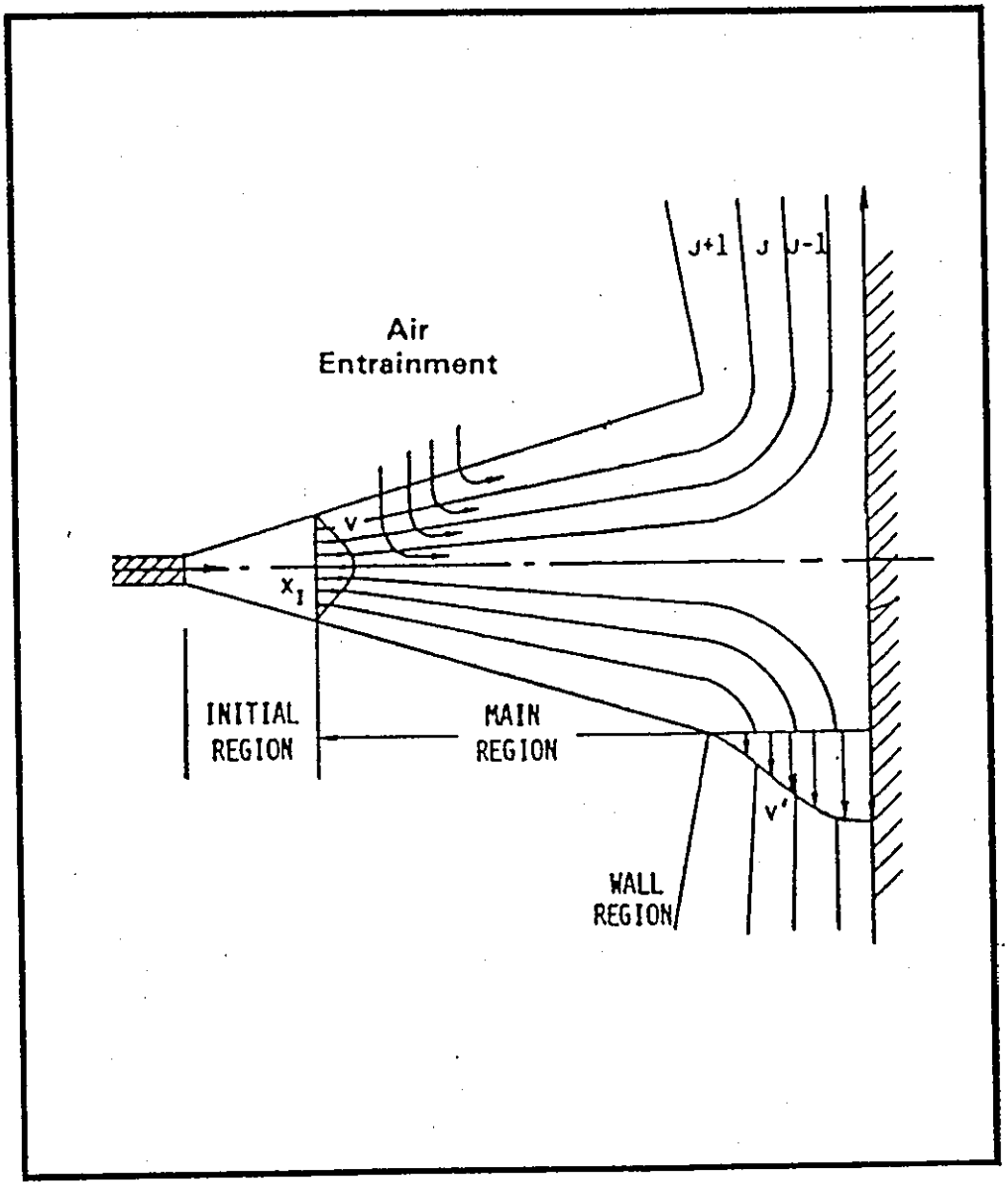

FIGURE 2.4: GEOMETRY OF THE SPRAY MODEL

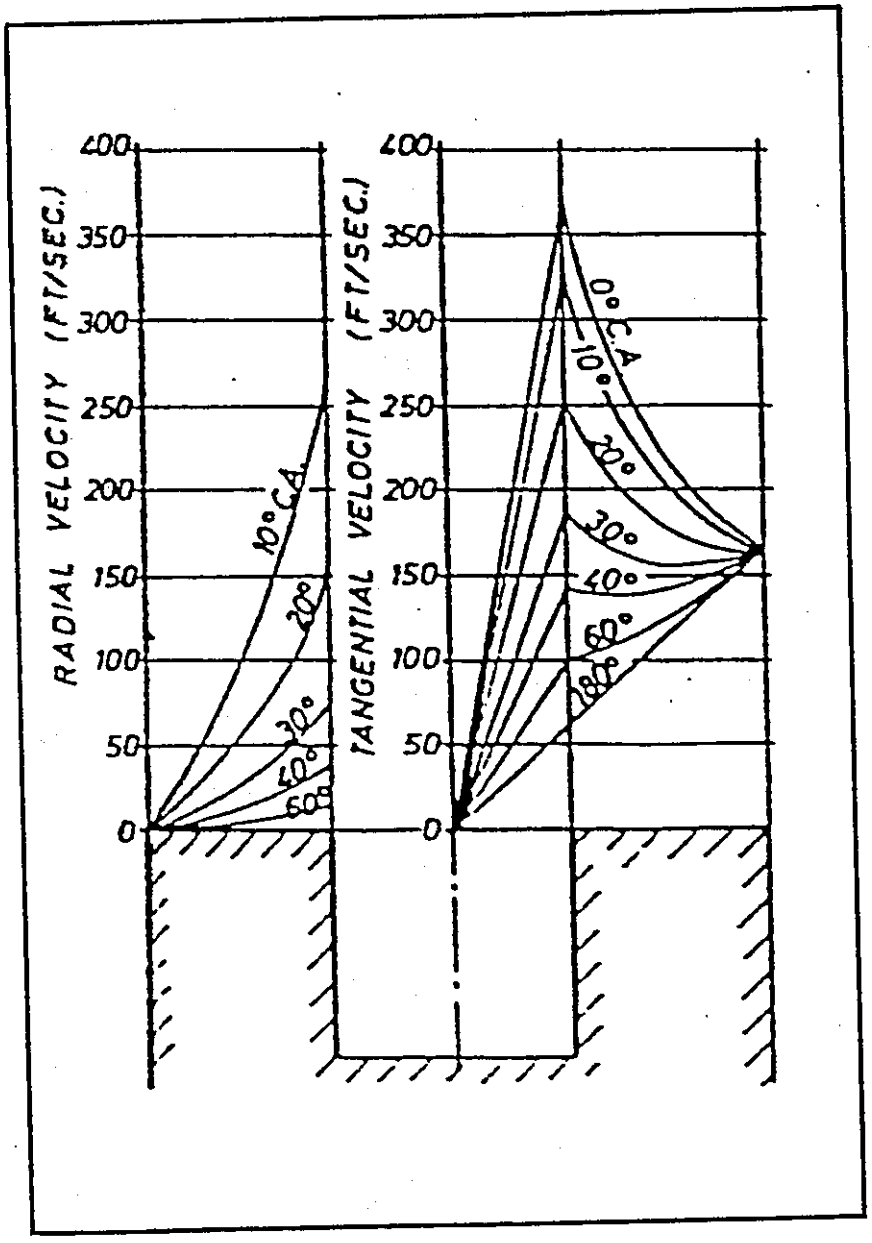

FIGURE 2.5: COMPUTED VELOCITY FLOW FIELDS (40)

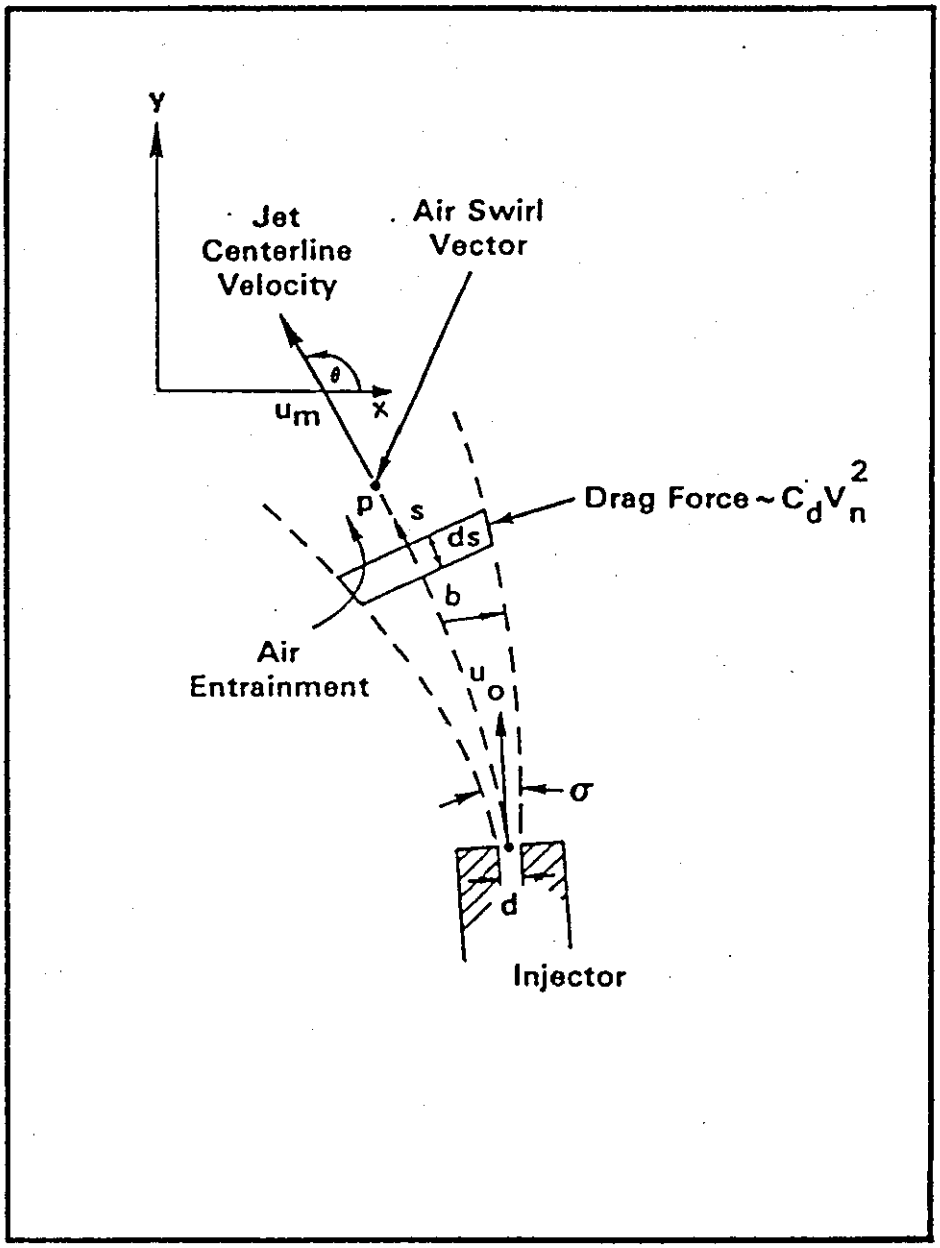

FIGURE 2.6: FUEL SPRAY TRAJECTORY (75)

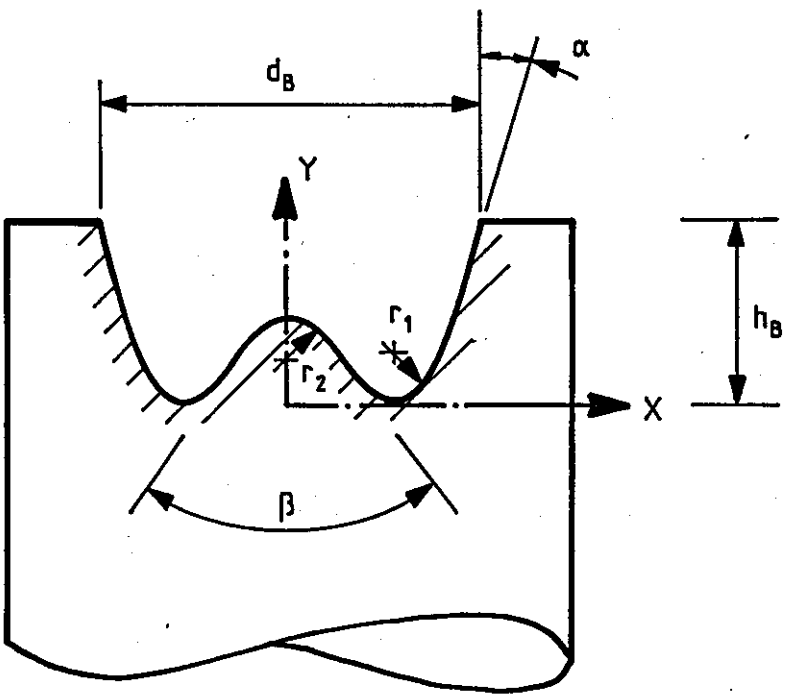

FIGURE 2.7: COMBUSTION BOWL NOMENCLATURE

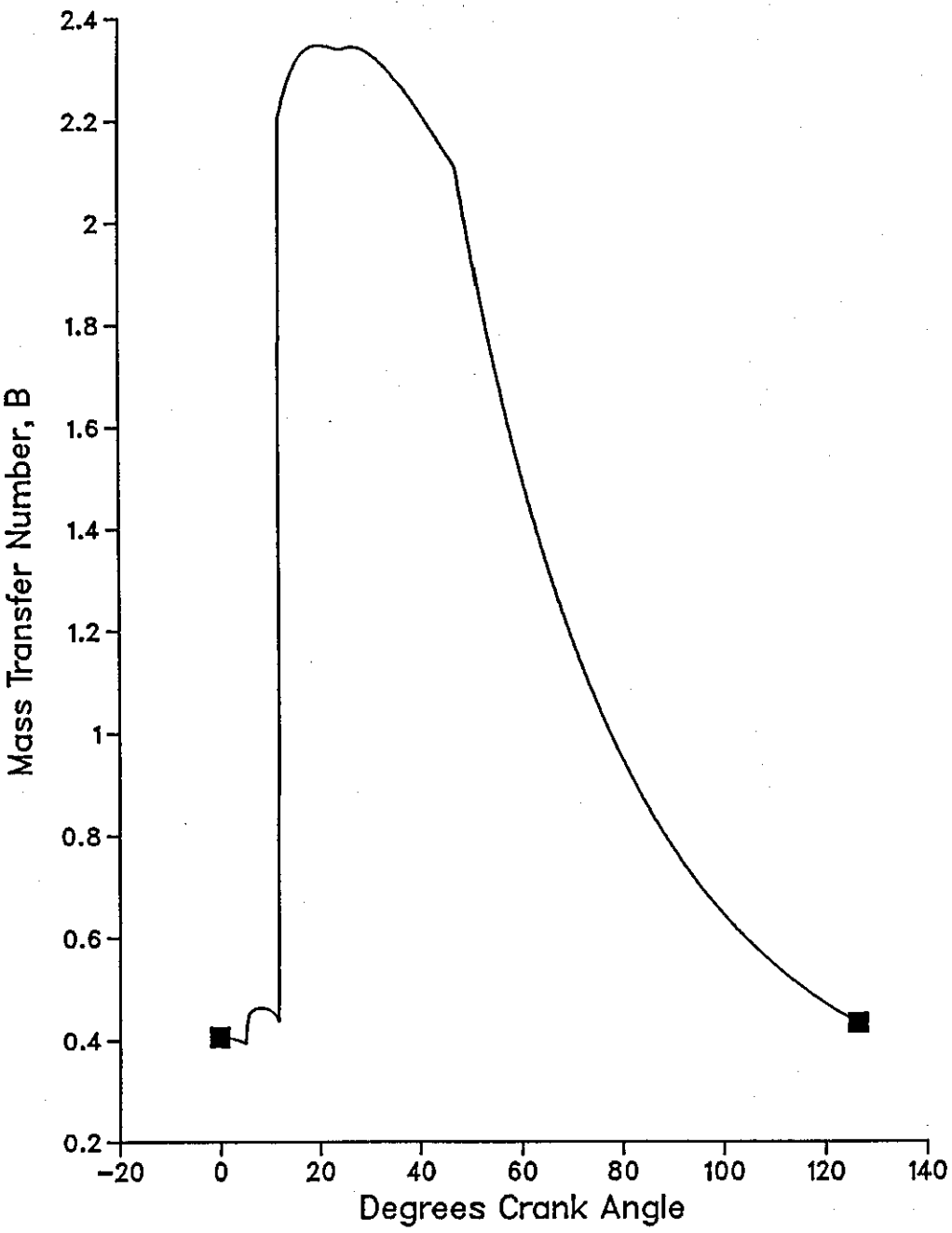

FIGURE 2.8: ITERATION SCHEME FOR MASS TRANSFER NUMBER (B)

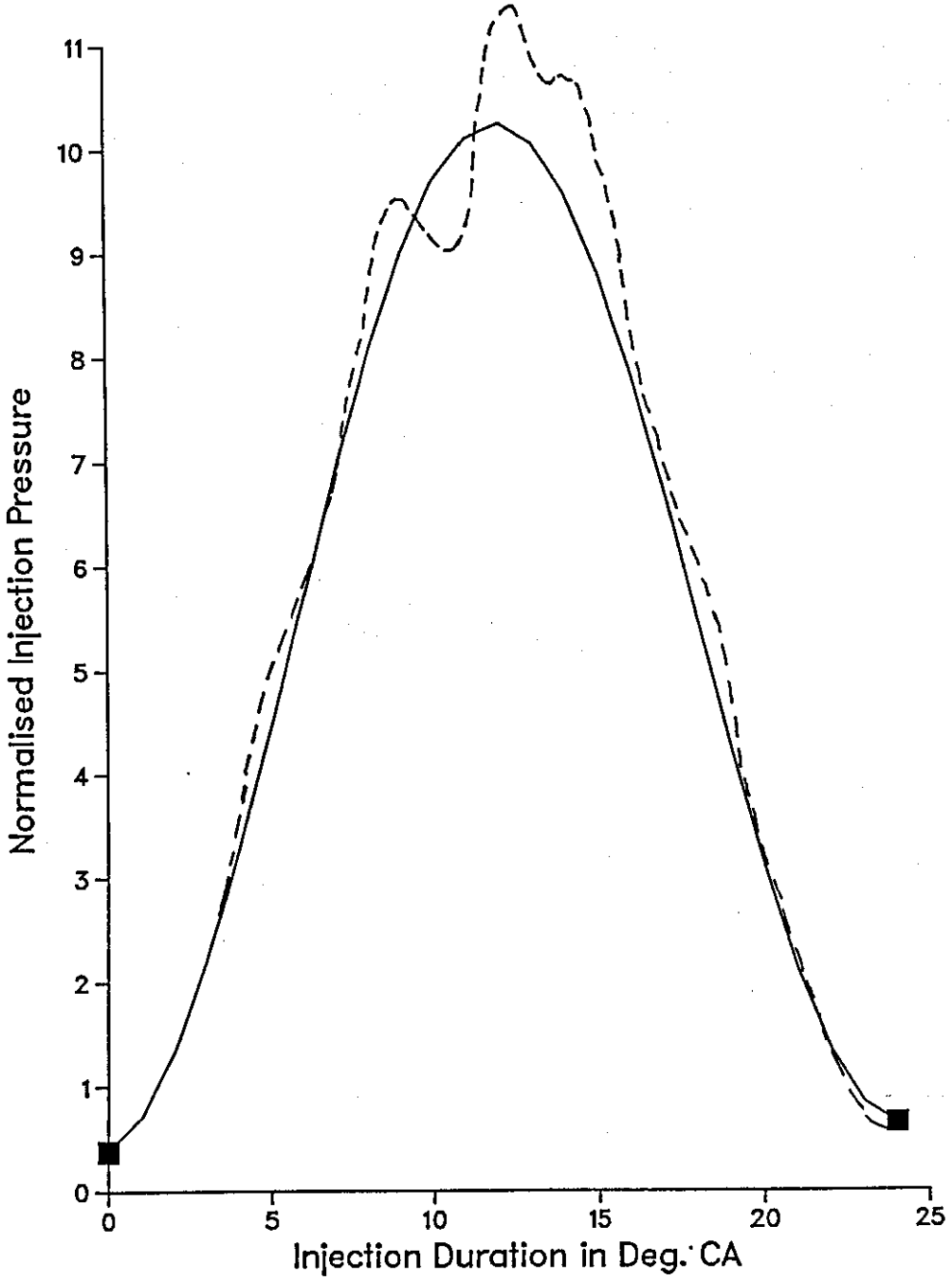

Figure 2.9: Comparison Between Experimental Injection Pressure Diagram and that resulting from Sinusoidal Fuelling

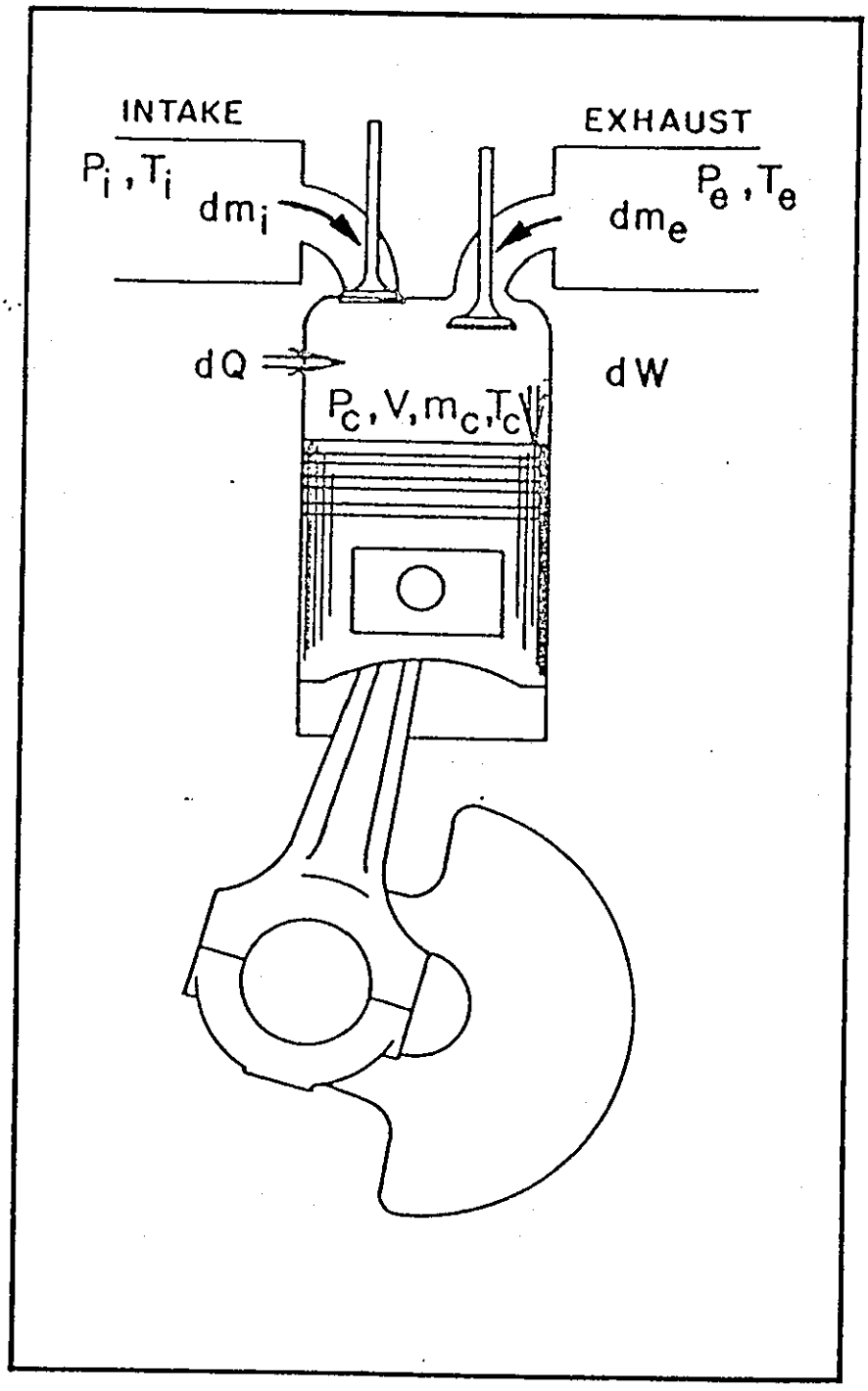

FIGURE 2.10: SCHEMATIC OF HEAT AND MASS FLOW PROCESSES IN INDUCTION/EXHAUST MODEL (86)

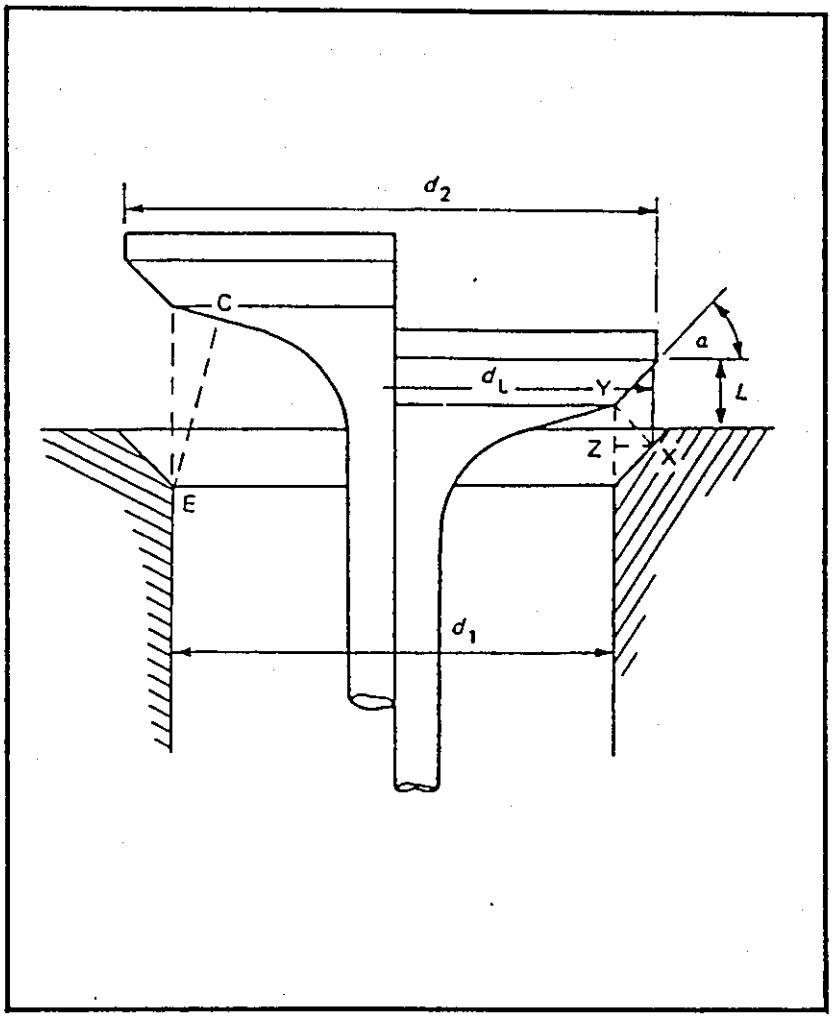

FIGURE 2.11: SCHEMATIC OF VALVE FLOW REGIMES (16)

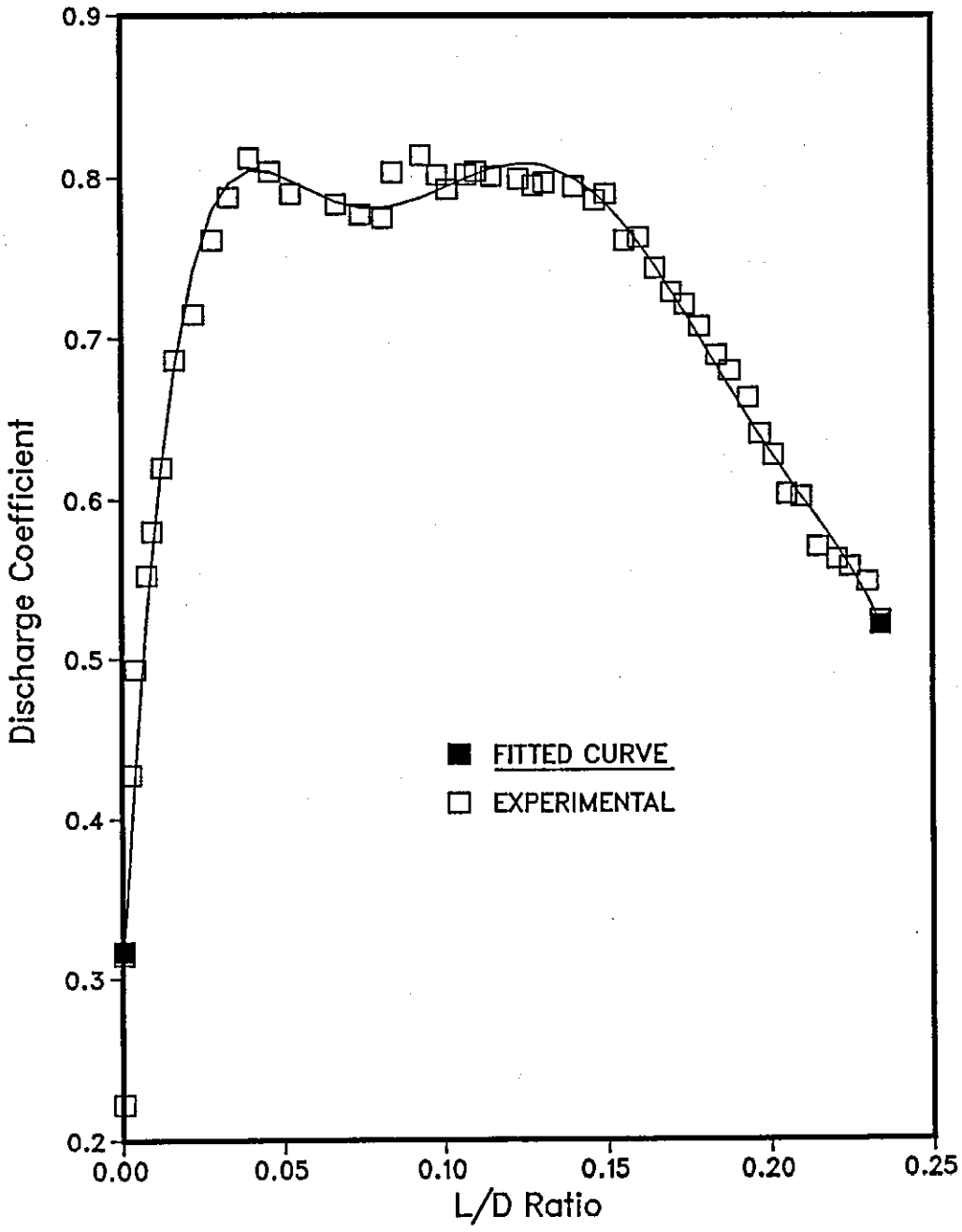

FIGURE 2.12: CHEBYSCHEV FIT FOR DISCHARGE COEFFICIENT FROM THE RESULTS OF REFERENCE (90)

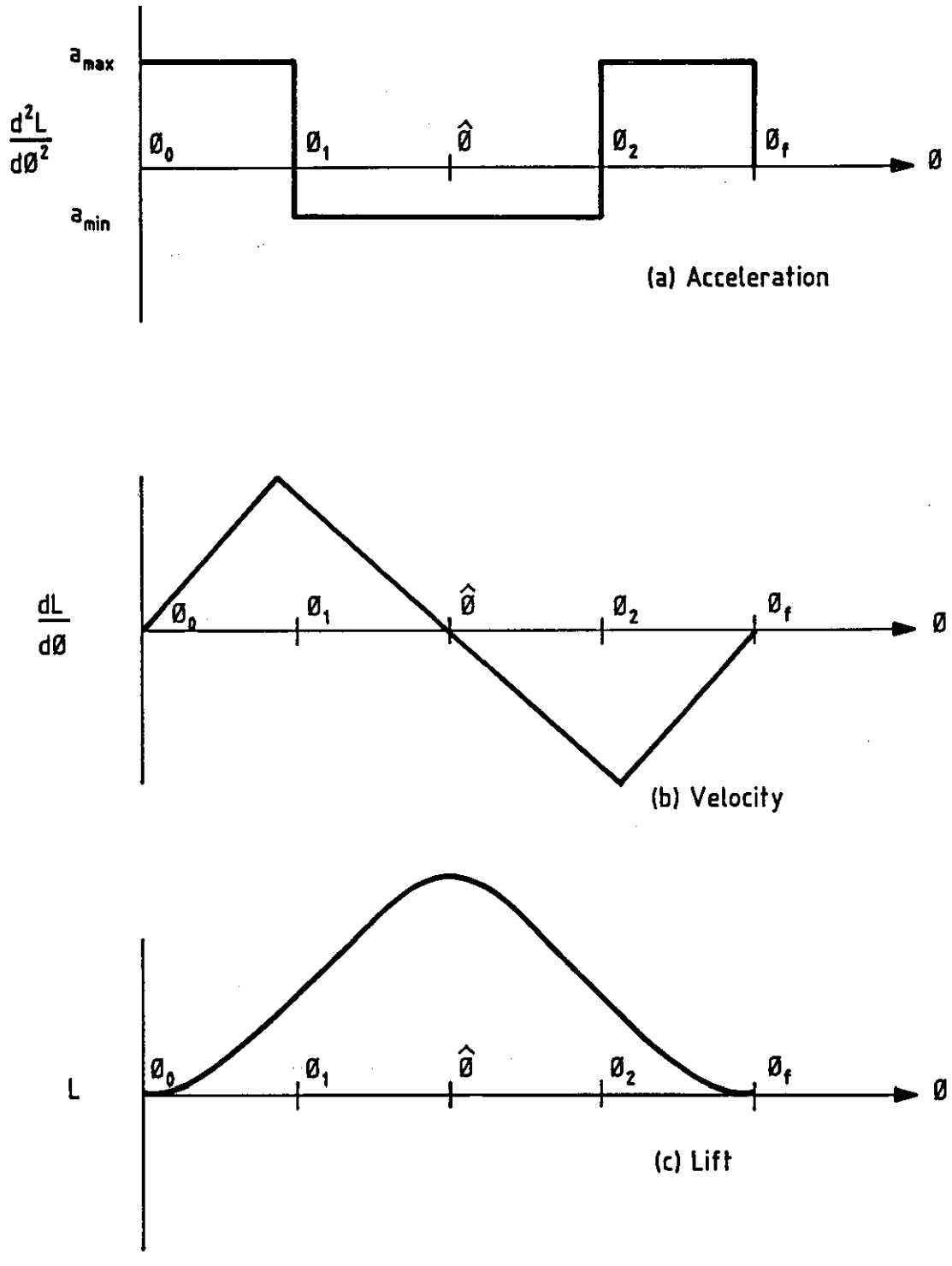

FIGURE 2.13: VALVE KINEMATICS CHARACTERISTICS

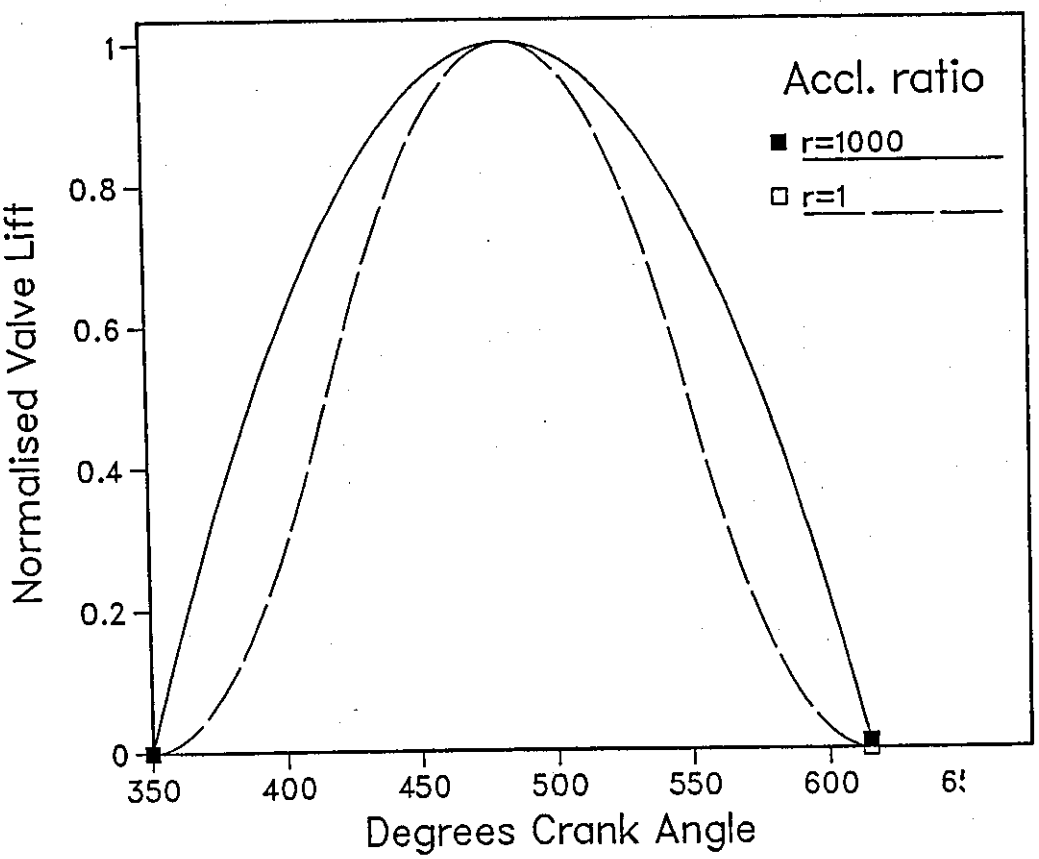

FIGURE 2.14: EFFECT OF ACCELERATION RATIO ON NORMALISED VALVE LIFT

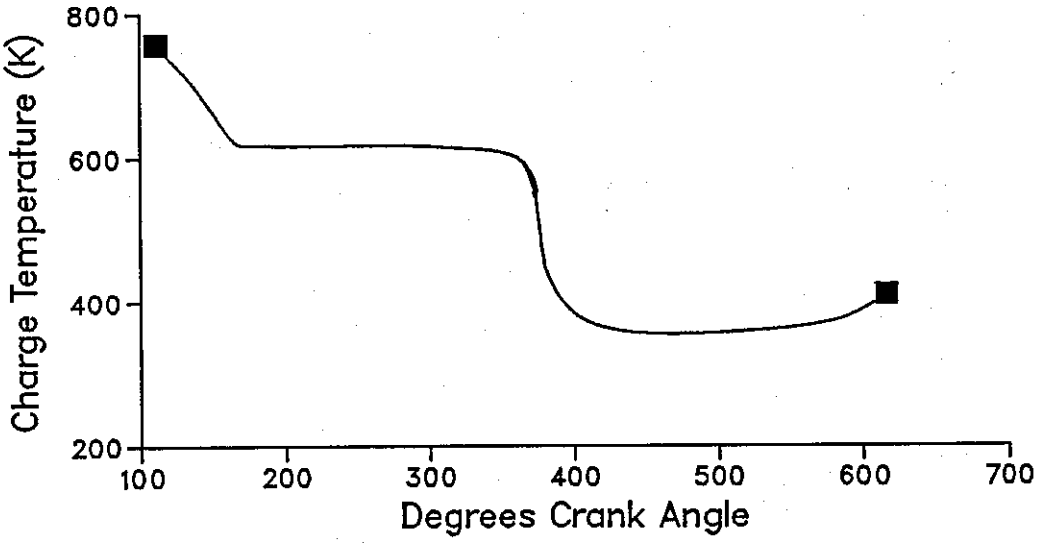

FIGURE 2.15: CYLINDER CHARGE TEMPERATURE

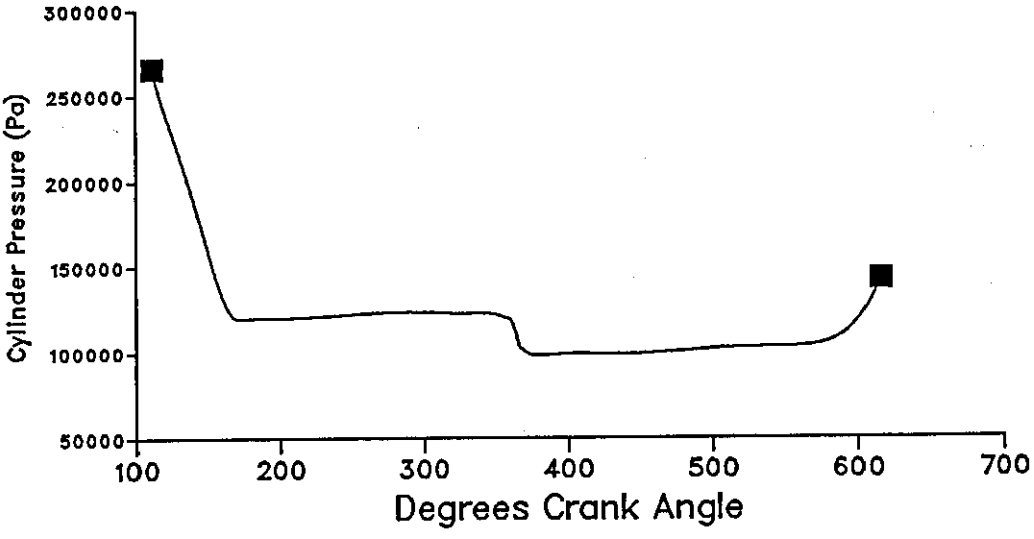

FIFURE 2.16: CYLINDER CHARGE PRESSURE

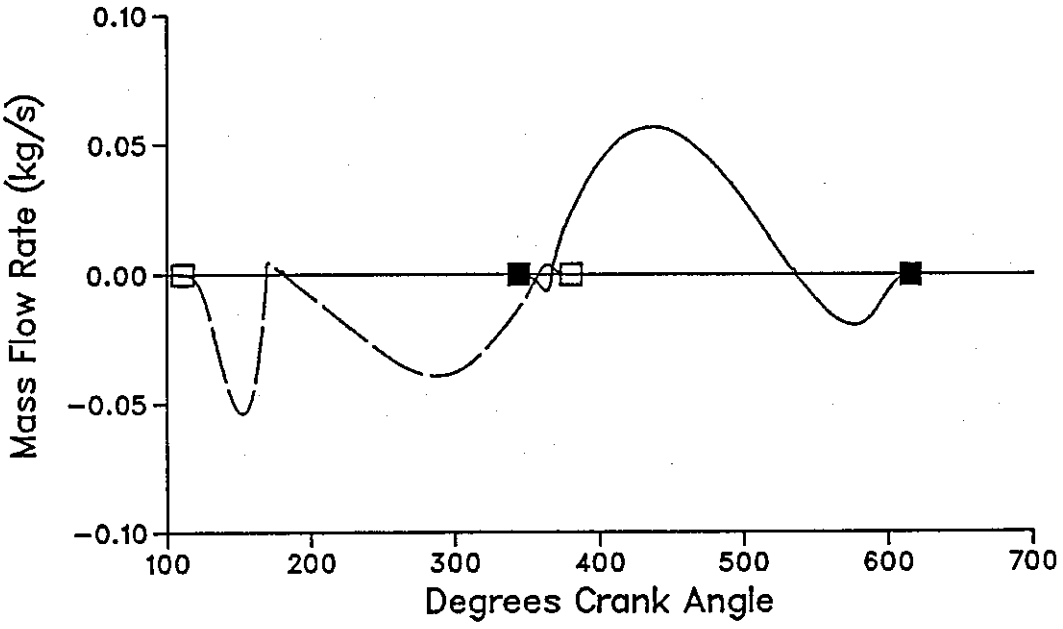

FIGURE 2.17: MASS FLOW RATE THROUGH THE VALVES DURING EXHAUST (DOTTED) AND INDUCTION (SOLID)

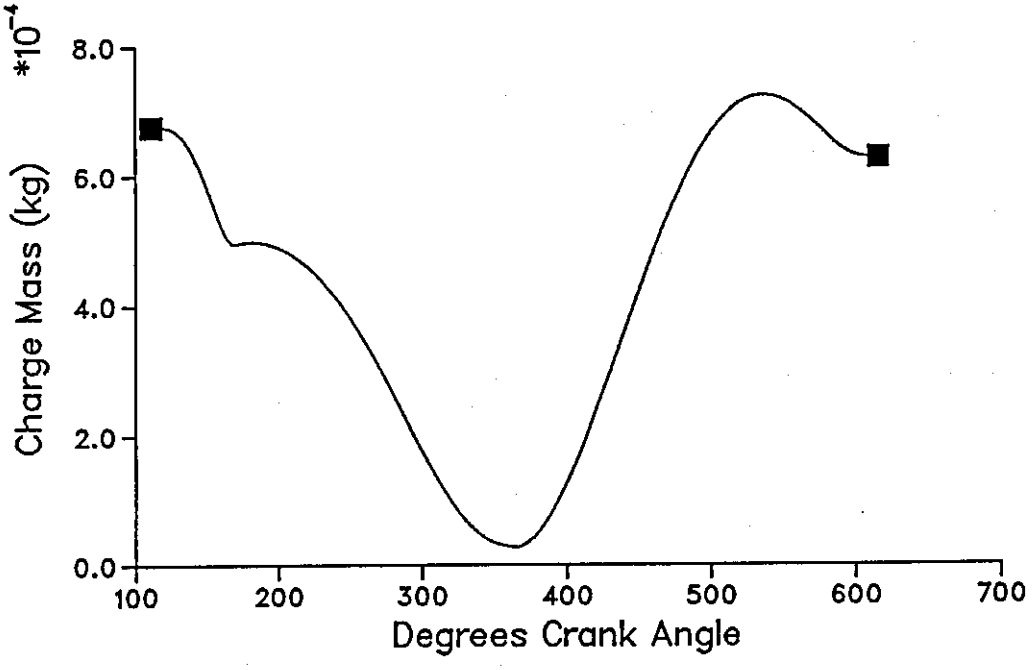

FIGURE 2.18: FLUCTUATION OF CYLINDER CHARGE MASS DURING EXHAUST AND INDUCTION

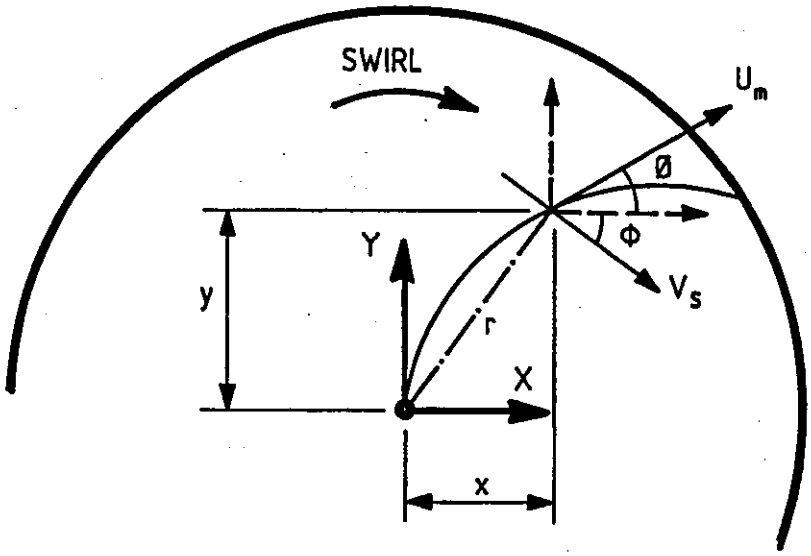

FIGURE 2.19: SPRAY JET TRAJECTORY

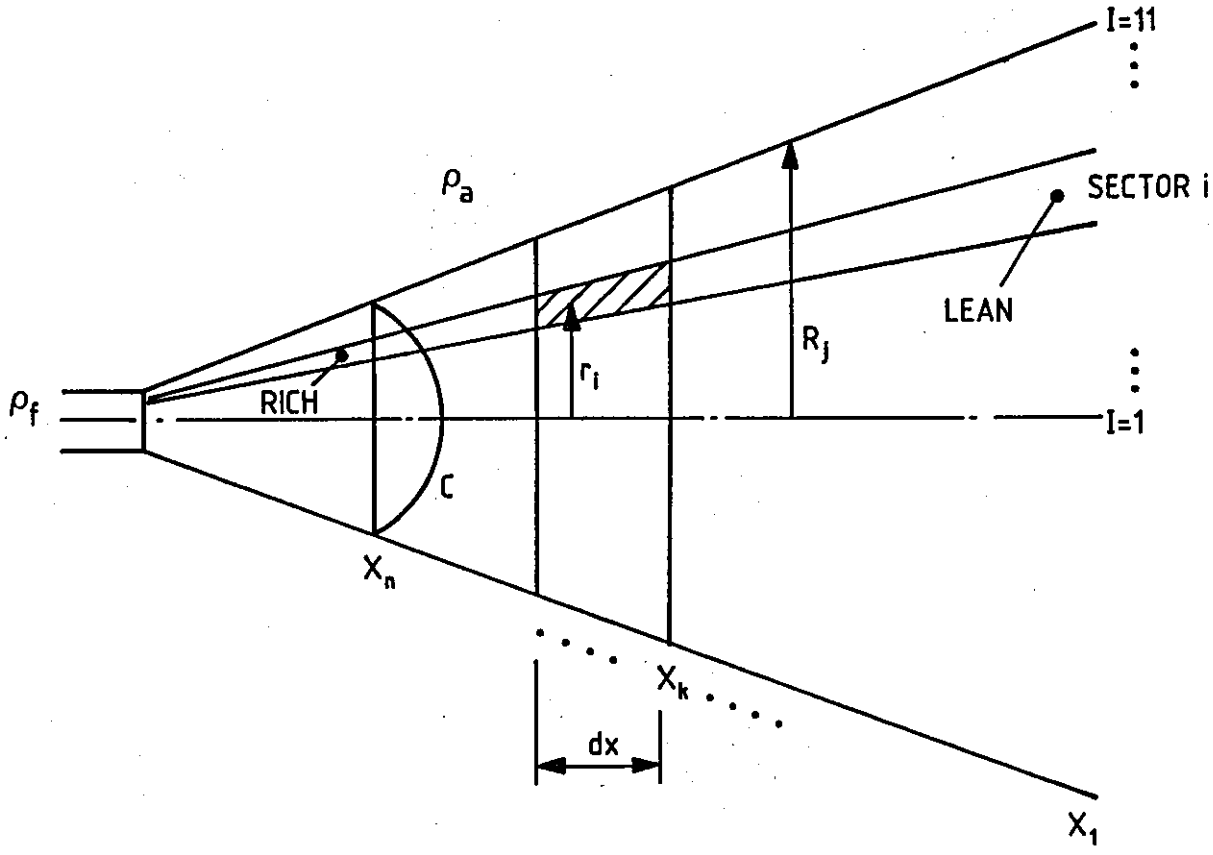

FIGURE 2.20: ZONING OF THE FUEL SPRAY

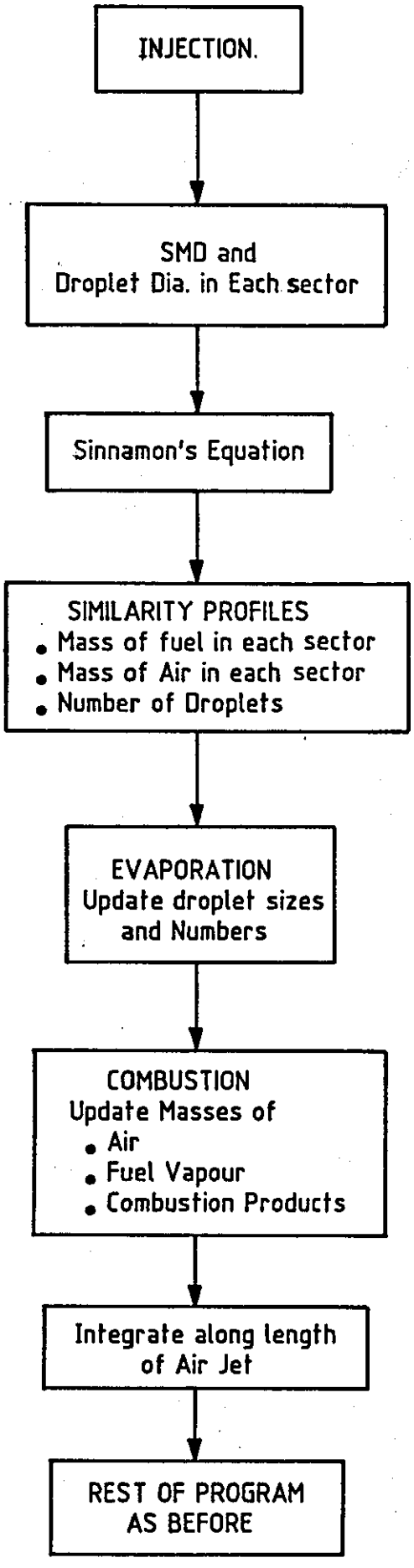

FIGURE 2.21: RESTRUCTRUCTURED APPROACH FOR DROPLET DISTRIBUTION AND COMBUSTION

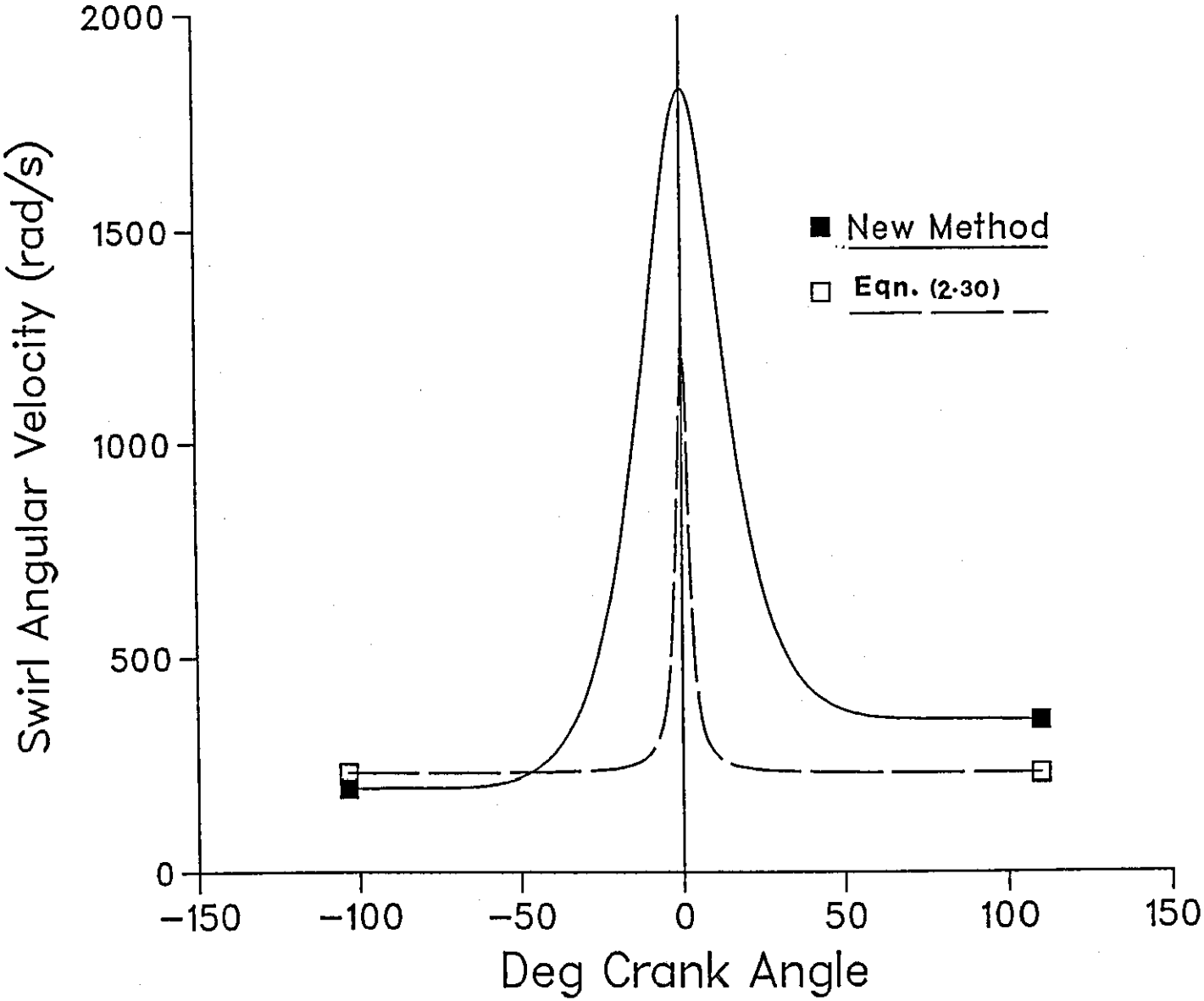

Figure 2.22: Comparison Between Swirl Velocity Computed using Equation (2.30) and the new method.

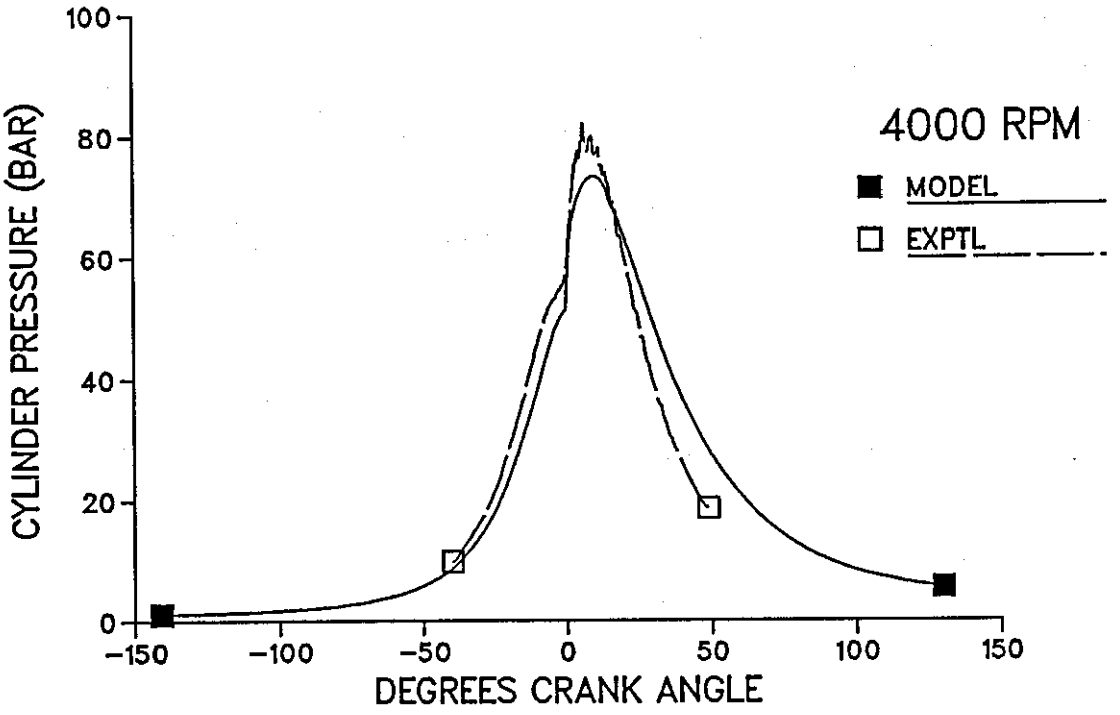

Figure 2.23: Predicted and Experimental Cylinder Pressure at 4000 RPM

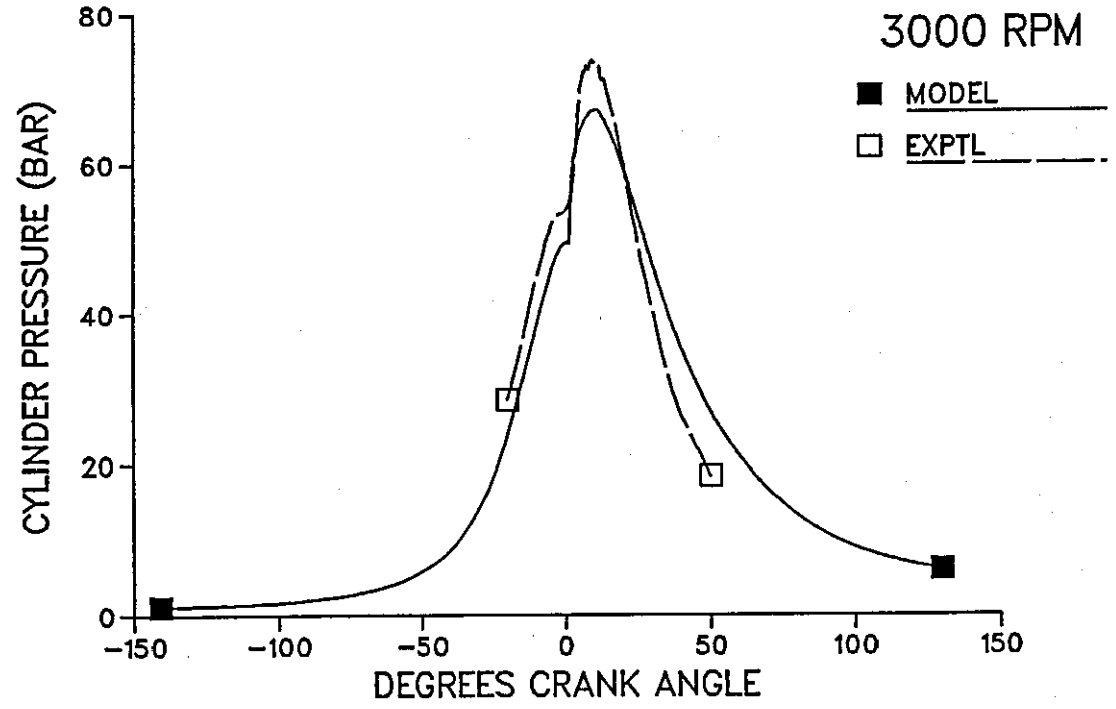

Figure 2.24: Predicted and Experimental Cylinder Pressure at 3000 RPM

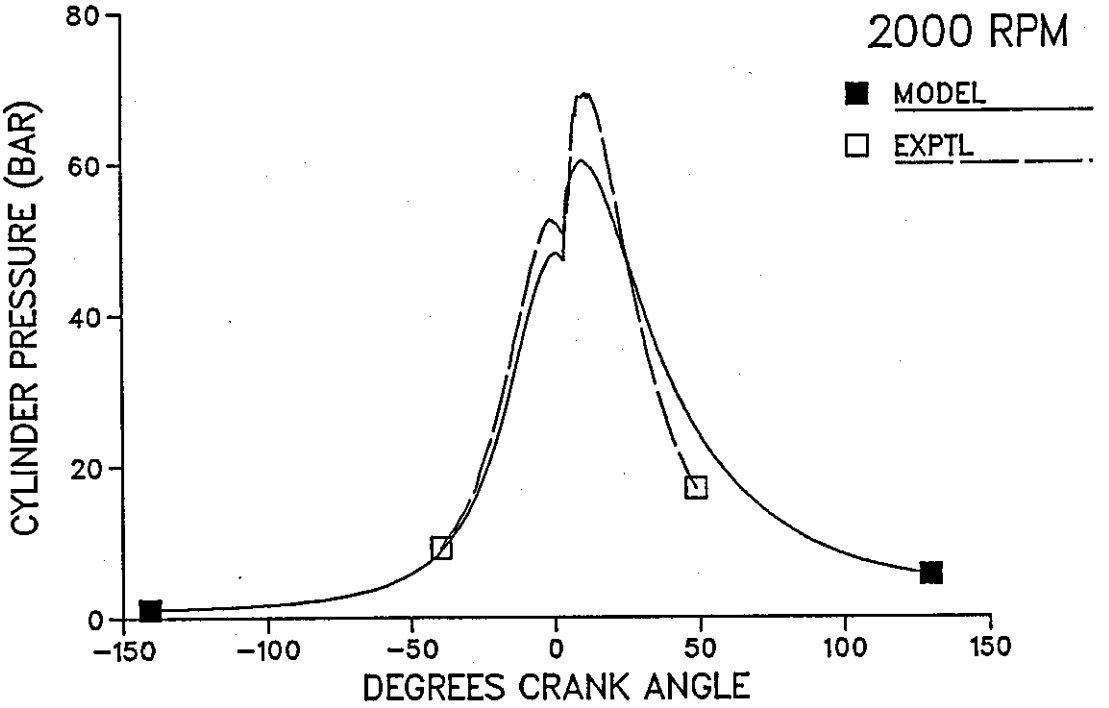

Figure 2.25: Predicted and Experimental Cylinder Pressure at 2000 RPM

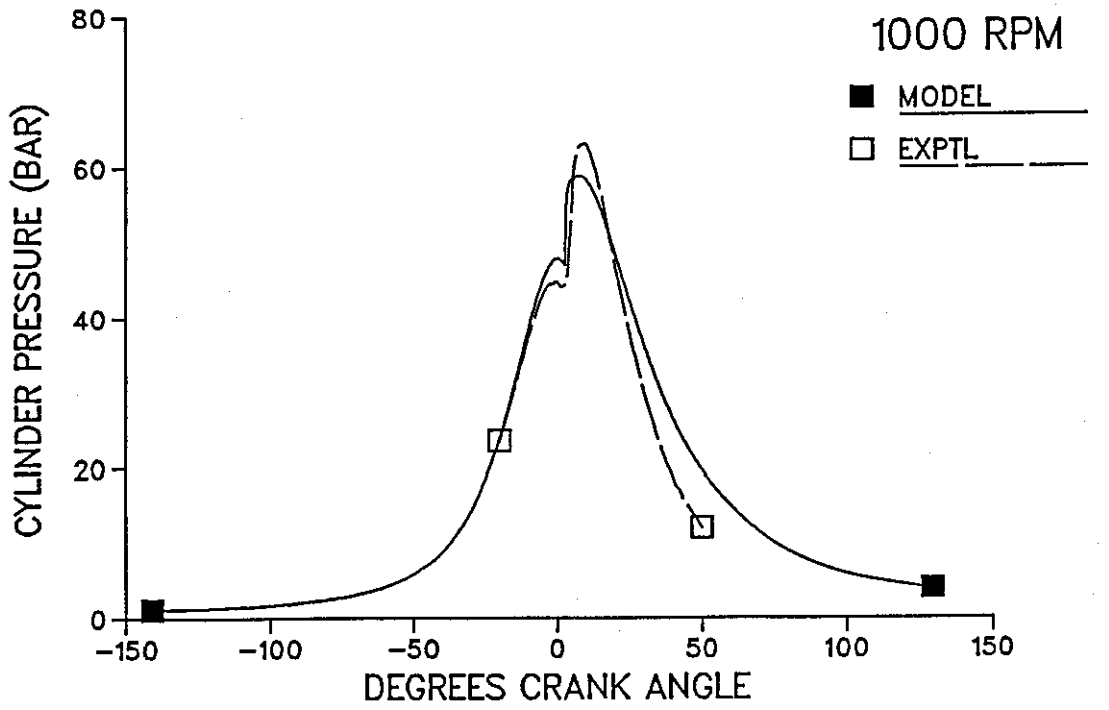

Figure 2.26: Predicted and Experimental Cylinder Pressure at 1000 RPM

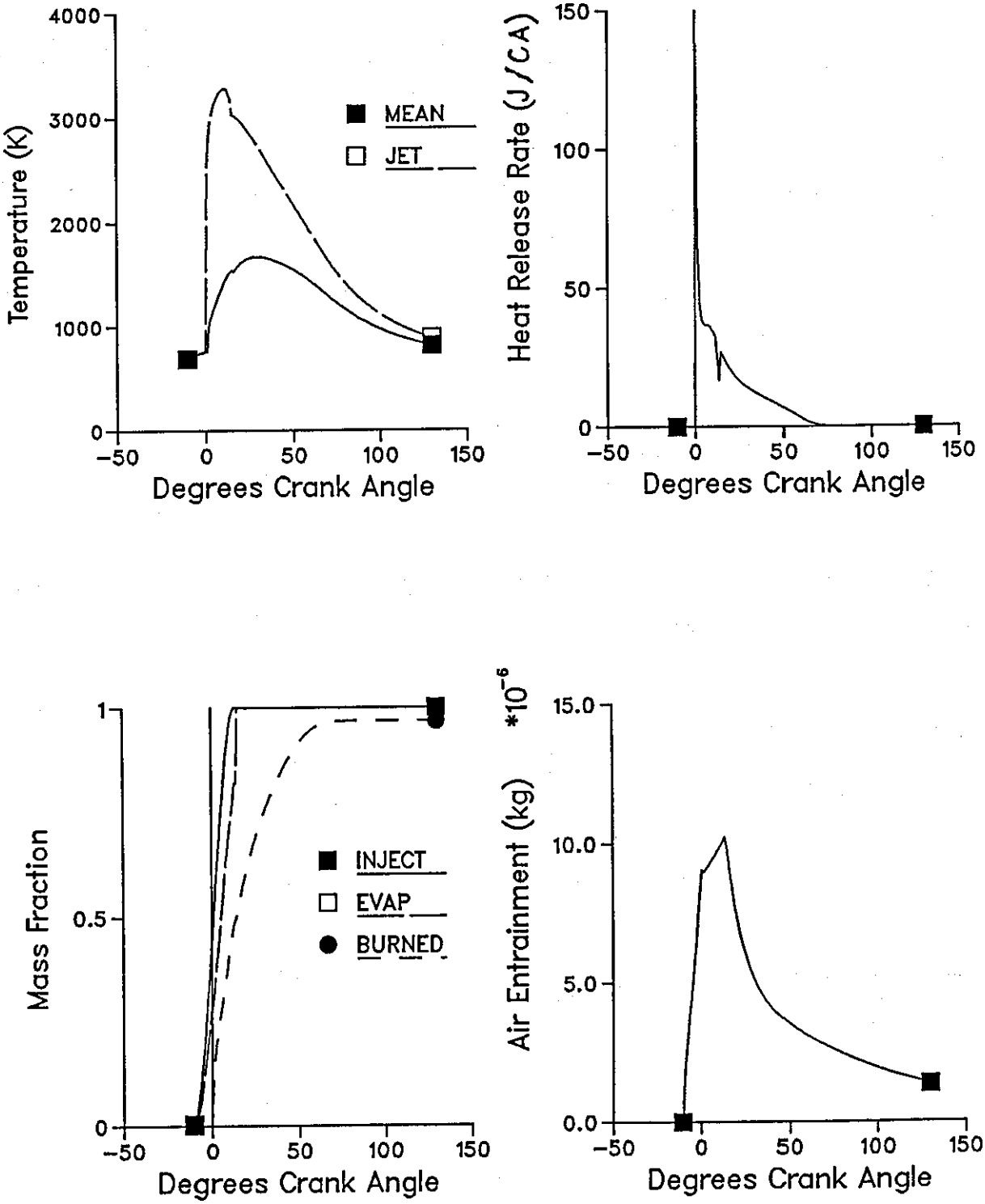

Figure 2.27: Computed Performance Indicators at 4000 RPM

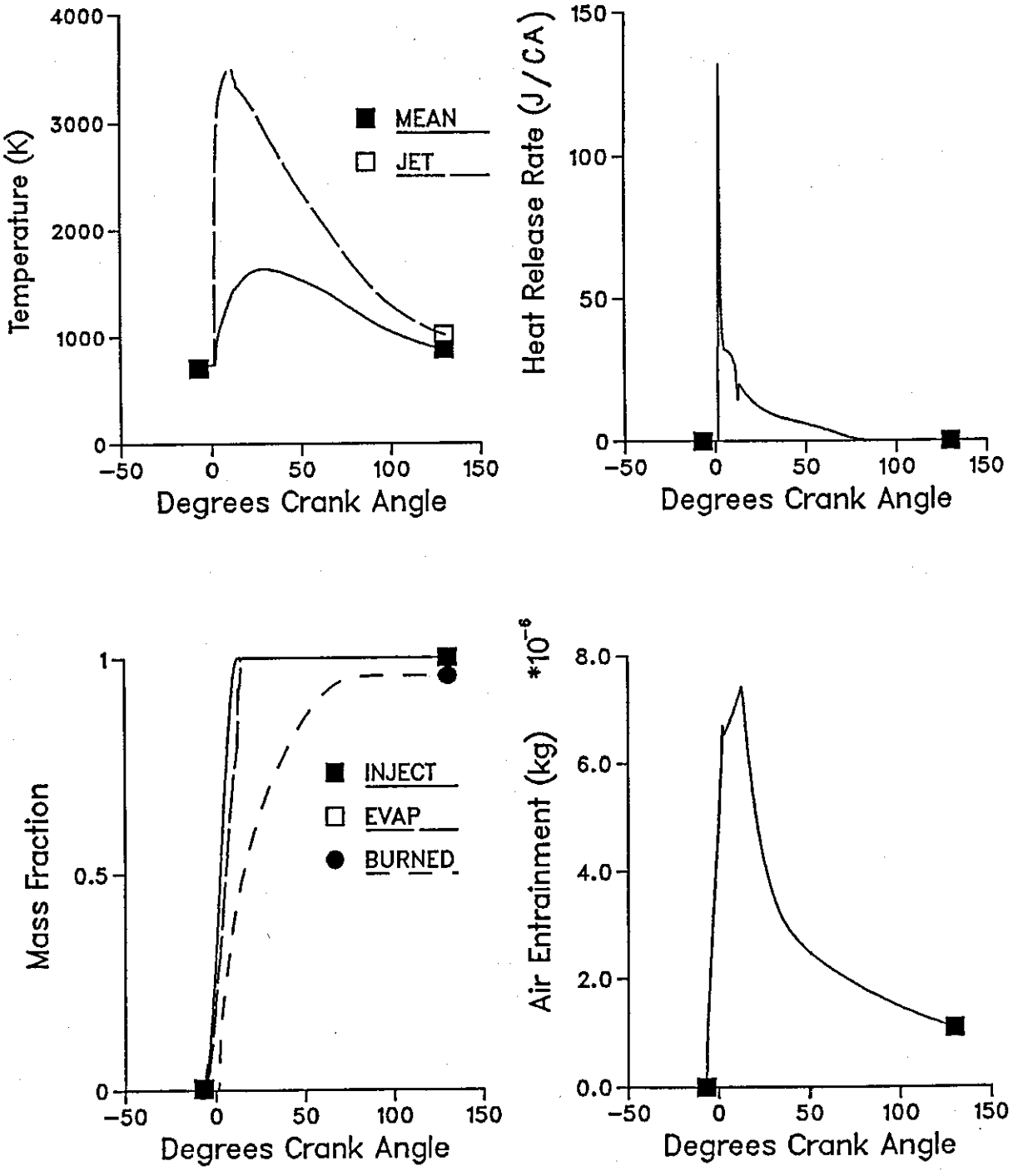

Figure 2.28: Computed Performance Indicators at 3000 RPM

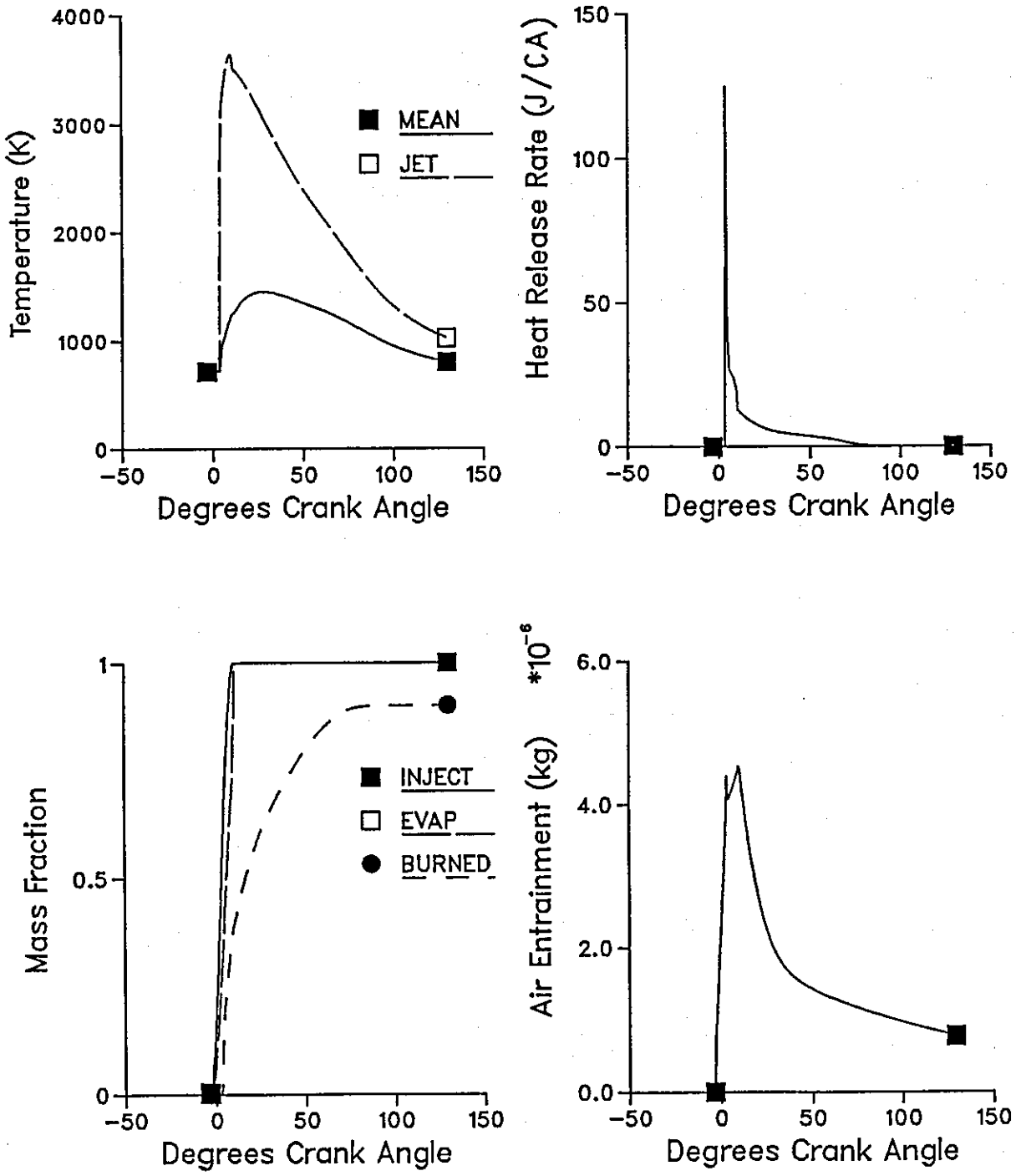

Figure 2.29: Computed Performance Indicators at 2000 RPM

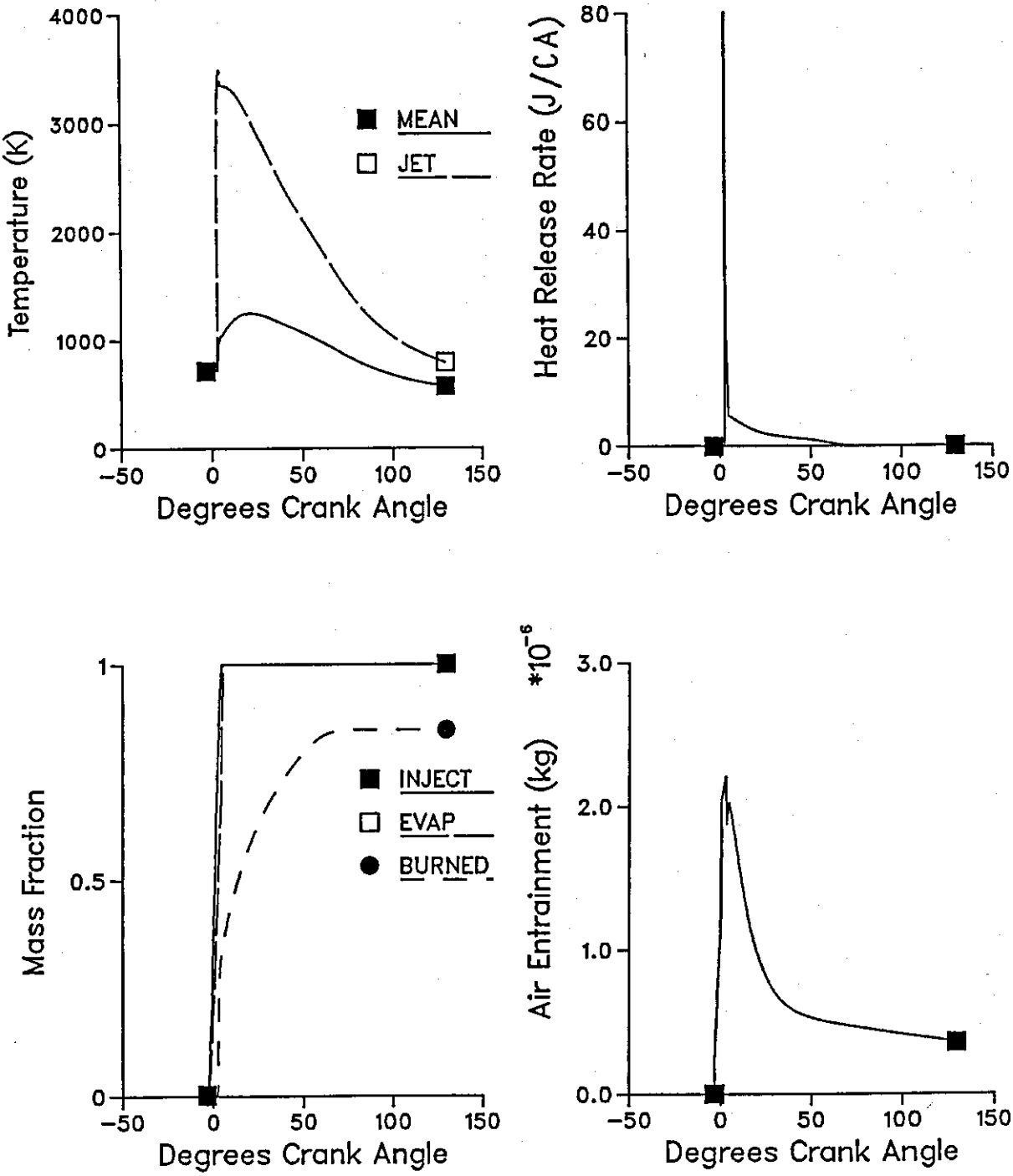

Figure 2.30: Computed Performance Indicators at 1000 RPM

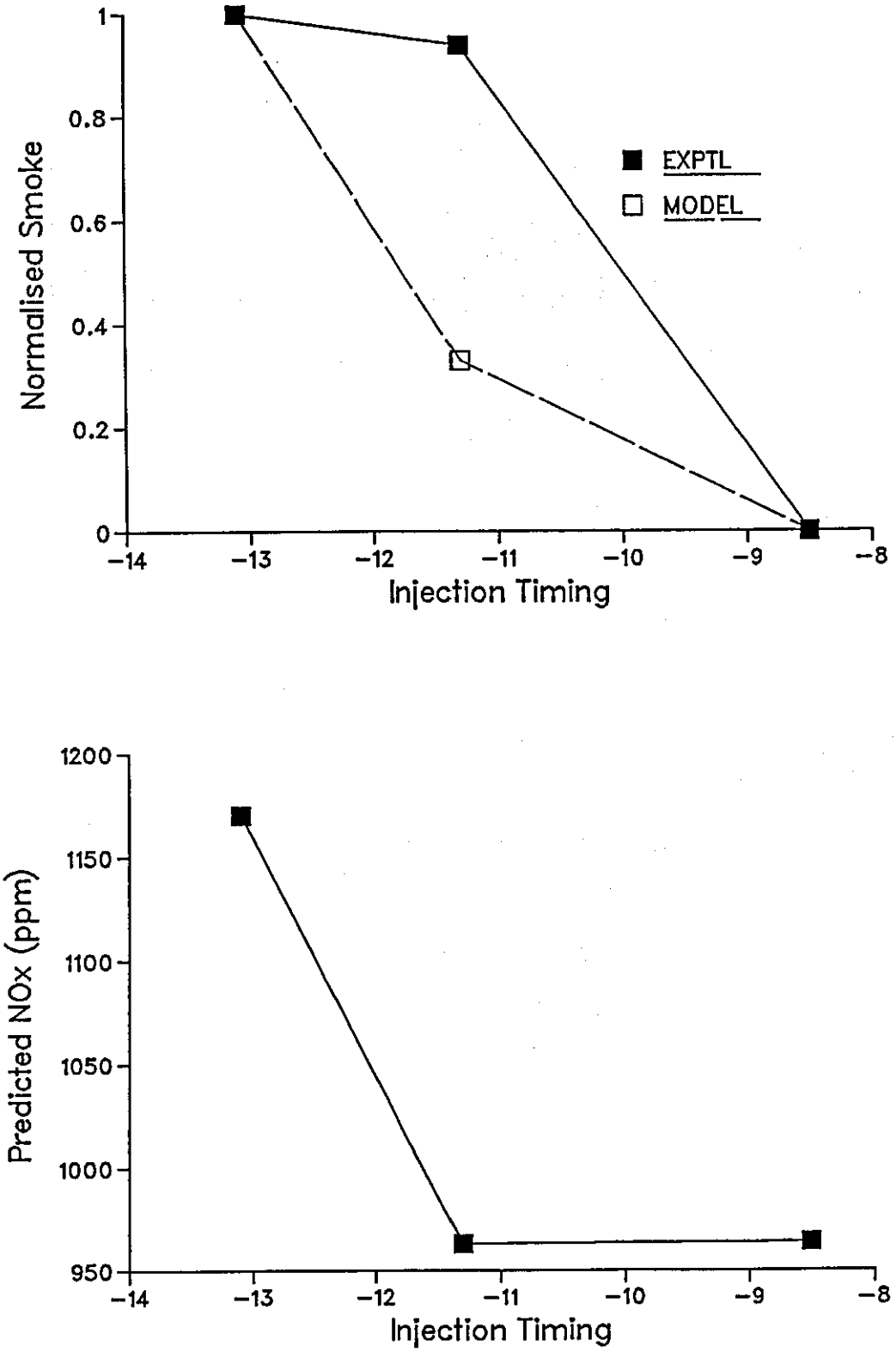

Figure 2.31: Computed vs. Experimental Exhaust Emissions at 4000 RPM

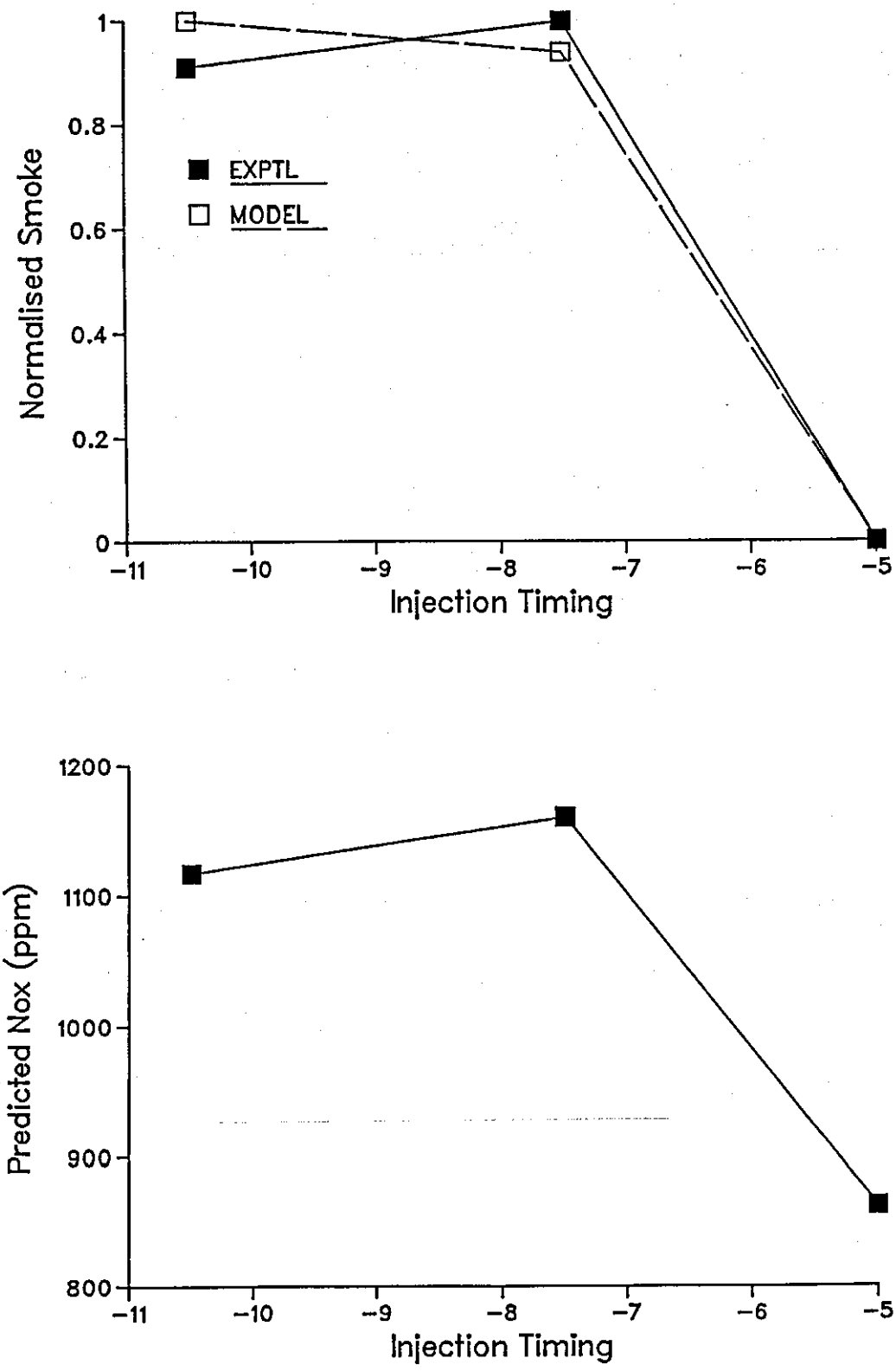

Figure 2.32: Computed vs. Experimental Exhaust Emissions at 3000 RPM

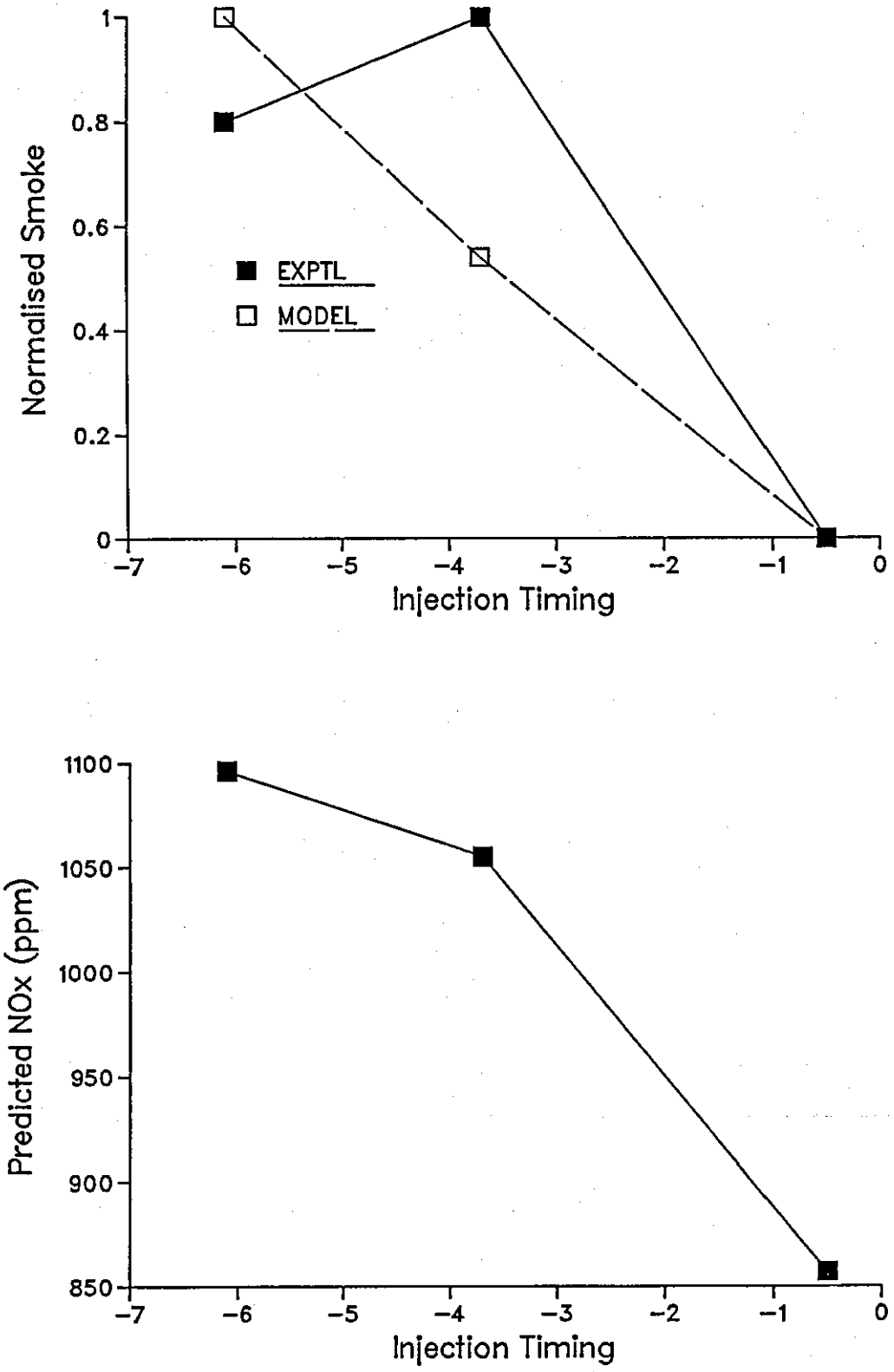

Figure 2.33: Computed vs. Experimental Exhaust Emissions at 2000 RPM

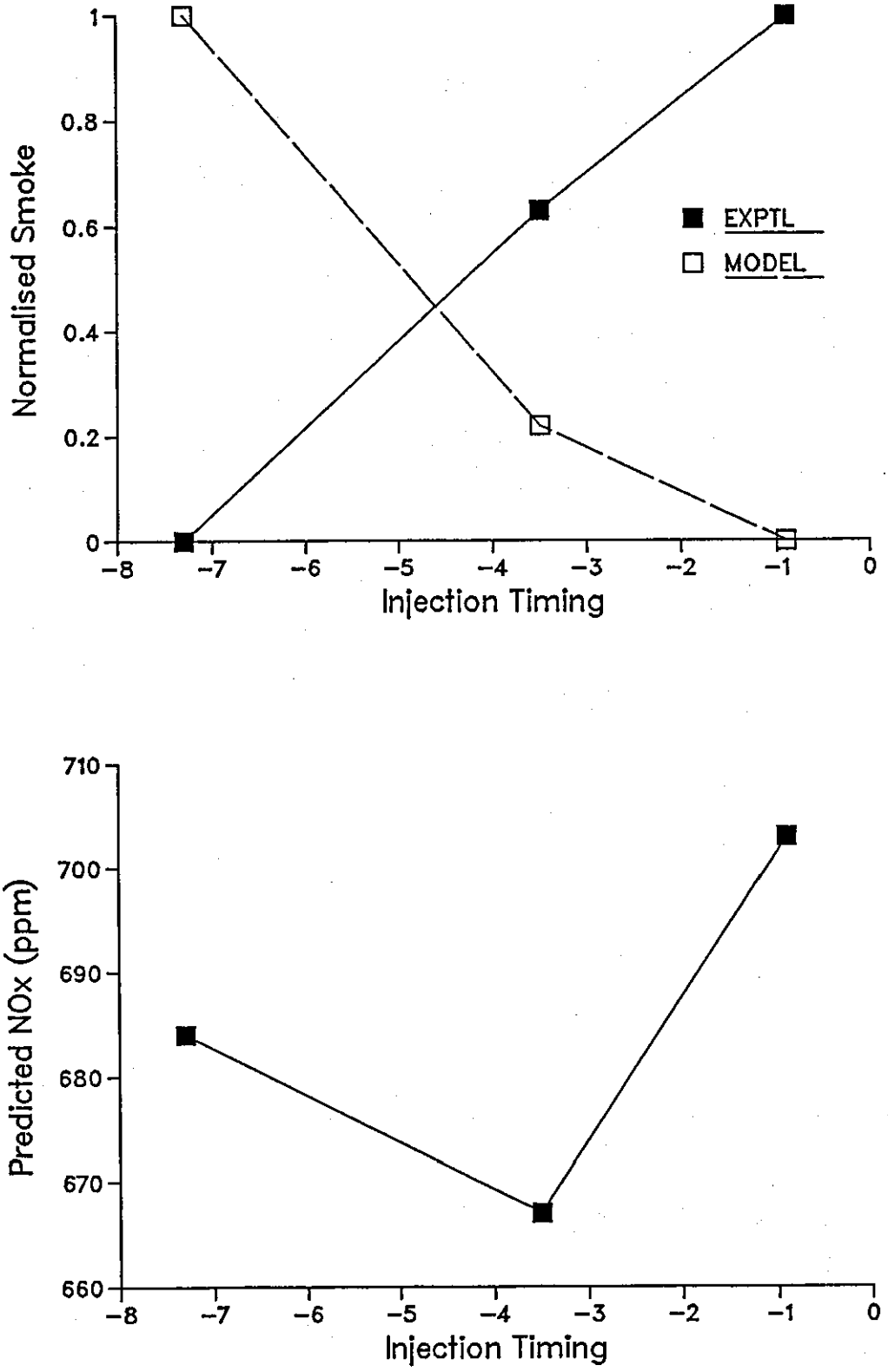

Figure 2.34: Computed vs. Experimental Exhaust Emissions at 1000 RPM

CHAPTER 3

AIR MOTION AND FILM FLOW DEVELOPMENT

3.1 INTRODUCTION

In the review of the literature, an attempt was made at explaining the complexity of the nature of events that occur within the engine cylinder. It was pointed out that, although much of this complexity cannot be avoided if a detailed analysis of the flow field is to be obtained, fairly accurate equations can be derived by neglecting details that are not essential to the general characterisation of the flow. Examples of this are the assumption of uniform temperature in the fuel film, and also linking the rate of diminution of the wetted area due to evaporation, to the rate of change in film thickness. In this and the next chapter, an outline of the mathematical equations that form the basis of the proposed model, are given. The equations are derived from fundamental fluid mechanics expressions, directed to meet the specific requirements for wall-wetting type diesel engines. This chapter deals with equations for the intensification of air swirl during compression, and the development of the fuel film on the combustion chamber wall. As the model deals only with the events during the closed period (i.e. from inlet valve closure to the opening of the exhaust valve), methods of generating swirl during the induction stroke are not discussed although a brief summary of these processes may be found in a paper by Dent and Derham (74). In the proposed model, swirl ratio at the start of compression is one of the required input parameters.

In most wall-wetting engines, the combustion bowl takes a hemispherical form such as that illustrated in Fig. 1.3. The flow field in such a configuration requires a more detailed analysis than is proposed here for accurate characterisation. In the present study, an equivalent cylindrical chamber (Fig. 3.1) is used, with dimensions

chosen to coincide with the ratios illustrated in Figure 3.2, which were also used by Urlaub (34), and also to yield the same compression ratio.

3.2 AIR MOTION IN THE COMBUSTION BOWL

The mixing of fuel with air within the cylinder, and the level of convective heat losses are both influenced by the intensity of air motion. In the case of wall-wetting engines, air motion is also an essential requirement for mixture formation as it enhances the rate of evaporation of the fuel film, and also induces turbulence. As the air transfers from the cylinder into the combustion bowl, its motion is composed of swirl and squish components. Swirl motion refers to the rotational flow of air about an axis, while squish - a characteristic of engines with a deep bowl - refers to the radial flow of air into the bowl (Fig. 3.3)

It is possible to derive simplified equations to describe both components by treating each component separately (74). However, it is essential to realise that the two components are not entirely independent as squish motion forms the mechanism by which angular momentum is transferred into the central region, increasing swirl intensity there. The method of analysis adopted in this work is based on the approach of Urlaub (20), which takes into account the reduction of angular momentum in the annular space as this gets transferred to the central zone as illustrated in Figure 3.3. Details of the derivation are given in Appendix C, and only a brief discussion of the essential considerations is outlined below.

When the piston moves upward during compression, through a distance ds as illustrated in Fig. 3.4, a portion of air in the annular space, dm_a, is transferred to the central zone. If the corresponding change in the annular volume is given by dV_a, then dm_a is given by:

$$dm_a = \rho_a \left(1 - \frac{V_a}{V}\right) dV_a \qquad (3.1)$$

where V_a is the volume of the annular space, and V the total confined volume. All variables refer to an instantaneous crank position. dV_a may be evaluated from equation (3.2).

$$dV_a = \pi r_B y \, dr \qquad (3.2)$$

The distance y is made up of the clearance height, y_o, and the instantaneous stroke, s, so that equation (3.2) may be expressed in the form shown in equation (3.3).

$$dV_a = \pi r_B (y_o + s) \, dr \qquad (3.3)$$

By assuming that air in the cylinder rotates as a solid body, with angular velocity ω, then the transfer of dm_a into the central region will increase angular momentum there by $d\alpha_c$, expressed mathematically as follows:

$$d\alpha_c = r_B \cdot U_t \cdot dm_a \qquad (3.4)$$

where U_t is the tangential velocity in the central zone at radius r_B. At inlet valve closure, U_t has a known magnitude expressed by equation (3.5).

$$U_{to} = \omega_o \cdot r_B \qquad (3.5)$$

Substituting eqns. (3.1), (3.2), and (3.3) into (3.4) and integrating from bottom dead centre to TDC, yields the total angular momentum transferred to the central zone:

$$\alpha = \omega_o \cdot \int_s^o \left[r_B + \int_s^o \frac{dV_a}{r_B (y_o + s)}\right]^2 dm_a \qquad (3.6)$$

The angular momentum in the central zone at TDC is the sum of the component transferred from the annular space with that present in the zone at the start of compression. This latter component is calculated from the following equation:

$$\alpha_o = I_o \cdot \omega_o \tag{3.7}$$

where I_o is the moment of inertia of masses in the central zone at the start of compression, which is given by:

$$I_o = \pi r_B^2 \, y \, \rho_a \tag{3.8}$$

The corresponding angular velocity in the central zone at the end of compression is given by:

$$\omega = \frac{\alpha + \alpha_o}{I} \tag{3.9}$$

where I is the moment of inertia in the central zone at TDC, calculated using an expression similar to equation (3.8).

3.2.1 Computational Algorithm

At the start of compression, the following variables are sufficiently defined so as to be determined:

i. Volume of trapped air, Va_o, which is present in the annular space:

$$Va_o = \frac{\pi}{4} (B^2 - d_B^2) (y_o + s) \tag{3.10}$$

ii. Mass of air contained within the central zone:

$$ma_o = \rho_a \frac{\pi d_B^2}{4} (s + y_o + h_B) \tag{3.11}$$

iii. Moment of inertia of air in the central zone:

$$I_o = \frac{1}{2} m a_o \cdot r_B^2 \tag{3.12}$$

iv. The angular velocity in the central zone equals that in the whole cylinder:

$$\omega_o = \frac{\pi . N . (SR)}{30} \tag{3.13}$$

where SR is the swirl ratio, and N the engine speed in RPM.

v. The angular momentum in the central zone is given by:

$$\alpha_o = I_o \cdot \omega_o \tag{3.14}$$

During the compression stroke, the following variables are calculated at every crank angle:

$$dV_a = \frac{\pi}{4} (B^2 - d_B^2)\, ds \tag{3.15}$$

$$S_{1\theta} = \frac{dV_a}{\pi r_B (Y_o + s)} \tag{3.16}$$

As the algorithm marches forward in time, $S_{1\theta}$ is summed at subsequent crank angles so that the cumulative term, SI_1, represents the inner integral in eqn. (3.6):

$$SI_1 = \sum_{\theta=IVC}^{\theta_i} S_{1\theta} \tag{3.17}$$

where IVC refers to the crank angle at inlet valve closure, which is here taken to represent start of compression.

The mass of air transferred to the central zone in every crank angle interval is calculated from equation (3.1), and the integration of equation (3.6) is thus completed as follows:

$$S_2 = \sum_{\theta=IVC}^{\theta_i} [(r_B + SI_1)^2 \cdot dm_a] \qquad (3.18)$$

Multiplying S_2 by ω_o, calculated at the start of compression, yields the cumulative angular momentum transferred to the central zone:

$$\alpha_\theta = \omega_o \cdot S_2 \qquad (3.19)$$

giving the total angular momentum in the central zone, $\alpha_{T\theta}$ as:

$$\alpha_{T\theta} = \alpha_\theta + \alpha_o \qquad (3.20)$$

The total mass of air in the central zone is obtained by summing dm_a values from equation (3.1) to give:

$$ma_\theta = ma_o + \sum_{\theta=IVC}^{\theta_i} dm_a \qquad (3.21)$$

so that the instantaneous moment of inertia in the central zone is given by equation (3.22).

$$I_\theta = \frac{1}{2} ma_\theta \cdot r_B^2 \qquad (3.22)$$

and the angular velocity, ω_θ, is obtained as in equation (3.23).

$$\omega_\theta = \frac{\alpha_{T\theta}}{I_\theta} \qquad (3.23)$$

Figures 3.5 - 3.7 show the effect of varying speed, compression ratio, and combustion bowl diameter, on the level of generated swirl, as calculated from equation (3.9) above. The calculated velocity flow

field is illustrated in Figure 2.4, based on the calculations by Meurer and Urlaub (40). A major shortcoming of the results is the symmetry in the air flow about TDC. This would not be observed in engine operation as viscous effects in the flow would lead to a decay in swirl intensity. This, however, should not affect the results if, during combustion, mixing related parameters are calculated using variables that are less dependent on swirl intensity. For example, it may be necessary to relate turbulence level to the energy input into the flow as used by Corrsin (69), which will increase with combustion. Also, the swirl intensity at TDC is considered to be the significant variable in evaluating the kinetic energy contained in the flow (7). The dotted lines in Figure 3.5(a) and 3.6(a) show, qualitatively, the effect of friction on swirl intensity.

3.3 FILM FLOW DEVELOPMENT

The theoretical treatment of flow in a thin liquid film has been dealt with by Hewitt and Hall-Taylor (91) in the study of two-phase flow, Lees (53) and Warner and Emmons (47), with regard to film cooling and in the investigation of boundary layer separation on aerofoils, by Squire (44). In all of these applications, flow in the film is assumed to be two-dimensional without significant loss of accuracy. However, unless more complicated considerations are included in the analysis , as in the work of Calvert and Williams (92), simple two-dimensional analysis such as that used by Nicklin and Koch (93) leads to inaccurate trends such as the increase in interfacial (i.e. between the liquid film and the bulk gas) shear stress resulting in a thickening of the film. Physically, this implies that as the swirl intensity in the engine increases, so does the thickness of the film. This is opposite to the observed trend both in the engine, as observed by Müller (41), and in the experiments performed by the author. It is also common practice to assume laminar flow within the film (44, 45), even when the gaseous stream may be turbulent (45). The flow regime in the fuel film in wall-wetting diesel engines is, however, turbulent and non-steady (34). It is also unsuitable for analysing with the two-dimensional approach without some means of accounting for the

spread of the jet as it develops along the piston wall (i.e. the third dimension).

A brief look at the physics of thin liquid film flow is necessary in order to identify the governing dimensionless parameters. Fulford (94) suggests that flow in a thin film can be described as either steady and uniform, steady and non-uniform, or unsteady and non-uniform; depending on the respective magnitudes of three dimensionless numbers : Reynolds, Weber, and Froude. The role of these numbers in characterising the flow regime in liquid films is outlined in some detail below.

i. Reynolds Number

Both Fulford (94) and Craik (95) point out that in thin film flow, the characteristic dimension in the Reynolds number is the film thickness. Hence the following equation is used to define the Reynolds number:

$$Re_s = \frac{Us}{\nu_f} \qquad (3.24)$$

Fulford characterises the laminar-turbulent transition by Reynolds number in the range 250-500. For a film developing in a typical wall-wetting engine, Re_s has maximum values in the region of 300, based on the results of Müller (41).

ii. Weber Number

Weber number is defined as the ratio of inertial to surface tension forces, and is important in flows which are characterised by free surface effects. In the flow of a fluid in a thin film, Weber number affects the velocity of propagation of surface waves (96). It is defined mathematically by:

$$We_s = \frac{U}{\left(\frac{\sigma}{\rho s}\right)^{1/2}} \qquad (3.25)$$

where σ is the surface tension of the liquid. Surface effects are considered essential in the analysis of flow, when We_s is small. According to Fulford (94) capillary surface effects in the film will become significant when We_s is in the region of unity. When We_s is large, it may be neglected in flow analysis calculations.

iii. Froude Number

The Froude number is the dimensionless ratio of inertial forces to gravity forces. In flows with a free surface, Froude number has a significant role in characterising the flow regime. It is defined, in thin film flow (94), as the ratio of the mean film velocity to the relative velocity of propagation of a wave carried on the film surface. Mathematically it is expressed by the following equation:

$$Fr_s = \frac{U}{(gs)^{1/2}} \qquad (3.26)$$

Froude and Weber numbers, together, determine the condition of the surface of the film, i.e. whether smooth or covered with waves. Gravity waves appear when Fr_s is between 1-2 while capillary waves become significant when We_s is about unity. Although turbulent flow is invariably wavy, the presence of waves on the film surfaces does not, of itself, signify turbulence (94). Hence the analysis of flow in thin liquid films can be quite complicated and not easily amenable to analytical solution without the introduction of simplifying assumptions. Since the film encountered in wall-wetting engines is non-uniform (decelerates very rapidly upon impingement), unsteady (being transient), and turbulent, the proposed model is only a simplified approach to a very complex flow problem. The fact that the development of the film is essentially three-dimensional means that

methods of accounting for the spread of the film have to be incorporated in the solution. In Appendix D momentum considerations are applied to a two dimensional control element to derive the following fundamental equation for the decay of velocity in the film:

$$\frac{dU_x}{dt} = \frac{(\tau_i - \tau_o)}{\rho s} - U_x \frac{q}{A} \qquad (3.27)$$

where τ_i and τ_o are the shear stress at the film/air interface and at the wall respectively. q accounts for the loss of momentum due to evaporation, so that if the mass flux from the surface, $\dot{m}''$, is used, then the following equation results:

$$\frac{dU_x}{dt} = \frac{1}{\rho s} [\tau_i - \tau_o - U_x \dot{m}''] \qquad (3.28)$$

The reduction in film thickness due to evaporation can be expressed as:

$$\frac{ds}{dt} = - \frac{\dot{m}''}{\rho} \qquad (3.29)$$

From the work of Squire (44), the variation in film thickness with time may be expressed according to the following equation:

$$\frac{ds}{dt} = - AS^2 - BS^3 \qquad (3.30)$$

where the contants A and B are defined as follows:

$$A = C_1 \frac{\lambda}{2} \left(\frac{a^3}{\nu_G}\right)^{1/2}$$

$$B = \frac{\lambda}{3} \left(\frac{a^2}{\nu_G}\right) \qquad (3.31)$$

$$\lambda = \frac{\mu_G}{\mu_f}$$

$$a = \frac{U_G}{X}$$

and C_1 is an empirically determined constant. Equation (3.30) does not include effects of evaporation while equation (3.29) neglects jet spread and attributes all thinning of the film to evaporation. The resultant film thickness may be obtained by combining the two equations:

$$\frac{ds}{dt} = -(As^2 + Bs^3 + \frac{\dot{m}''}{\rho}) \qquad (3.32)$$

The shear stresses in equation (3.28) are calculated using standard boundary layer equations for flow on a flat plate.

$$\tau = \frac{1}{2} C_f \rho U^2 \qquad (3.33)$$

For interfacial shear stress, τ_i, the friction coefficient is calculated from the standard equation for turbulent flow over a flat surface:

$$\frac{C_{fi}}{2} = 0.037\ Re_G^{-0.2} \qquad (3.34)$$

where Reynolds number is defined in terms of the relative velocity of the air stream:

$$Re_G = \frac{|U_G - U_x| \cdot \ell}{\nu_G} \qquad (3.35)$$

Equation (3.34) is also used to calculate shear stress at the piston wall, C_f, by defining Reynolds number in the fuel film as shown in equation (3.24).

Due to evaporation at the film surface, the friction coefficient at the interface, C_{fi}, experiences a reduction which can be expressed

mathematically according to the following set of empirical equations as given by Marxman (50):

$$C'_{fi} = C_{fi} \ln (1 + B)/B \qquad B \leqslant 5 \tag{3.36}$$

$$C'_{fi} = C_{fi} (1.2) B^{-0.77} \qquad 5 \leqslant B \leqslant 100 \tag{3.37}$$

where B is the mass transfer number whose definition and significance will be given in a subsequent chapter. In Fig. 3.8 the effect of mass transfer on the friction factor is illustrated by plotting the equations in (3.37).

3.3.1 Simplified Consideration of 3-Dimensionality

From the introductory discussion on film propagation, emphasis was made of the importance of a 3-dimensional approach to the investigation of the film under engine conditions. Fig. 3.9 shows a simplified diagram of a film patch developing on a flat surface. The velocity profile across the surface of the film is considered to be parabolic, and given by the following equation:

$$U_z = U_x \left(1 - \frac{z^2}{b^2}\right) \tag{3.38}$$

In section 3.4.1 of this chapter, it will be shown that the velocity profile of the gas in the vicinity of a solid wall is described by the following two parameter profile equation, suggested by Escudier and Nicoll (78)

$$Z = Z_E \left(1 + \frac{\ln \xi}{\ell}\right) + \frac{1}{2} (1 - Z_E) (1 - \cos \pi \xi) \tag{3.39}$$

where the variable ℓ may be defined as:

$$\ell = \frac{0.4\ Z_E}{\left(\frac{C_f}{2}\right)^{1/2}} \qquad (3.40)$$

Z is the normalised velocity profile defined by U_Y/U_G, and ξ is a non-dimensionalised height above the solid wall, defined as y/s. By substituting equation (3.40) into (3.39) and considering no air entrainment into the liquid film, So that Z_E takes on a value of unity, then equation (3.39) takes on the following form:

$$U_y = U_z\ [1 + 2.5\left(\frac{C_f}{2}\right)^{1/2} .\ \ln\xi] \qquad (3.41)$$

U_z replaces U_G in equation (3.41) due to the fact that the surface of the film is assumed to be at the same velocity as the air with which it is in contact. Since equation (3.38) has been assumed for the profile across the width of the film, it is clear that U_z is not uniform and so is preferred in place of the uniform U_G which will result in a straight line profile across the film width.

Fig. 3.10 shows quantitatively, the velocity profiles represented by equation (3.38) and (3.41).

By applying the principle of conservation of mass between the nozzle exit and any position along the flow direction, an expression is obtained for the breadth of the film, b:

$$\frac{\pi d_o^2}{4} U_o = 2 \int_o^b \int_o^s U_y\ dy.dz \qquad (3.42)$$

Substituting equations (3.38) into (3.41) and the resulting expression into equation (3.42) and integrating yields the following equation:

$$\frac{\pi d_o^2}{4} .\ U_o = 2.s\ [1 - 2.5\ (\frac{C_f}{2})^{1/2}](\frac{2b}{3})\ U_x \qquad (3.43)$$

which may be re-arranged to give the breadth of the film patch as illustrated in equation (3.44).

$$b = \frac{0.589\, d_o^{\,2}\, U_o}{s\left[1 - 2.5\left(\frac{C_f}{2}\right)^{1/2}\right]U_x} \qquad (3.44)$$

Equations (3.28) and (3.32) have to be solved simultaneously to provide s and U_x, which are then used to evaluate equation (3.44).

3.4 WALL-JET APPROXIMATION FOR FILM FLOW

The results of experiments performed by the author, to be discussed in detail later, demonstrate that by utilising wall-jet theory with minor modifications to the empirical relations, simpler equations may be derived that describe the motion of the fuel film on the piston wall. This simplification improves CPU run time of the computer model, and thus keeps within the target for developing a model for parametric and diagnostic engine investigations with a reasonable accuracy and a rapidly resolving algorithm.

3.4.1 A Review of Literature Relating to the Wall Jet

Historically, the first analytical treatment of the wall jet is attributed to Glauert (97) who investigated both laminar and turbulent flow cases. Basically, a wall jet is defined as the flow of a fluid discharged from a nozzle, through a surrounding fluid, so as to impinge and flow along a solid wall. The surrounding fluid may be quiescent as in Glauert's case, or flowing at a steady or unsteady velocity as in the work of Bradshaw and Gee (98).

Among its many uses, wall jet theory has been applied to the analysis of the downward directed jet of a vertical take-off aircraft (97),

protection of refractories in steel-making furnaces (Chesters et al (99)), and the working of the blown flap on aircraft wings (Kruka and Eskinazi (100)) to provide additional thrust and lift. A sketch of the tangential wall jet issuing into a moving stream is illustrated in Figure 3.11, showing the associated fully developed velocity profile.

Based on physical reasoning, Glauert was able to show that flow in the wall jet cannot conform to a single overall similarity solution. He thus divided the flow into an inner and outer region on either side of the maximum velocity, U_m, and treated each of the two regions separately. Kruka and Eskinazi (100), Gartshore and Newman (101), and Schartz and Cosart (102) have all made a similar division although the point of division does not coincide with the position of maximum velocity since the measurements of Bradshaw and Gee (98) demonstrate the existence of significant shear stress there, whereas Glauert's theory assumes it to be zero. The assumption of a division at the maximum velocity is not expected to significantly affect the accuracy of the simplified approximation adopted here as the work of Bradshaw and Gee (98), and also that of Kruka and Eskinazi (100) shows that the exact position lies just below maximum velocity (58, 60).

The presence of a point in the flow with zero shear stress implies that loss of momentum in the inner region is due to frictional stresses at the wall only, and not affected much by events in the outer layer. A velocity profile with two components is thus necessary, with one component accounting for mass and momentum transfer to the wall, and the other dealing with interactions between the jet and the mainstream. Since there is considerable agreement in the literature, concerning the suitability of the universal 'Law-of-the-wall' equation to describe flow in the inner layer (Kruka and Eskinazi (100), Rajaratnam (62), Schartz and Cosart (102)) one of the two components in the velocity profile must be a representation of this law, which has the form shown below:

$$z = f(y^+) \tag{3.45}$$

where z is the non-dimensionalised velocity defined by U/U_G, and y^+ is a form of Reynolds number based on the friction velocity and height above the wall:

$$y^+ = \frac{\left[\frac{\tau_o}{\rho}\right]^{1/2} \cdot y}{\nu} \qquad (3.46)$$

Escudier and Nicoll (78) demonstrated, after the work of Spalding (51), that the complete velocity profile function has the following form:

$$z = z_E \left(1 + \frac{\ln \xi}{\ell}\right) + \frac{1}{2}(1 - z_E)(1 - \cos \pi \xi) \qquad (3.47)$$

in which interactions with the free stream are represented by the second term on the right hand side of the equation, which is based on Coles' (103) 'Law-of-the-Wake' in a form recommended by Spalding (51). Z_E is a profile parameter, physically interpreted as the ratio of the 'Law-of-the-Wall' velocity at the outer edge of the wall jet to the main stream velocity (78), and ℓ is given by the following equation:

$$\ell = \ln (E\, y^+_\delta) \qquad (3.48)$$

where y^+_δ = value of y^+ at the outer edge of the jet

E = Empirical constant given the value of 6.542

The function for the 'Law-of-the-Wall' as given by Escudier and Nicoll (78) is as follows:

$$Z = 2.5 \ln (E\, y^+) \qquad (3.49)$$

For most practical purposes, the hydrodynamic properties of the inner region may be considered identical to those of a thin liquid film

flowing on a solid surface in the presence of a parallel, co-flowing air stream. This is because the significant cause for loss of momentum in the film is due to frictional stresses at the wall, which is also the case in the inner region of the wall-jet. The maximum velocity in the wall-jet may thus be taken to correspond with the velocity on the upper surface of the liquid film.

The variation of maximum jet velocity along the wall has been shown from considerable experimental evidence (66, 100, 104, 105) to have the following form:

$$U_m = C\, U_o \left(\frac{d_o}{x}\right)^a \qquad (3.50)$$

where a, c = Certain empirical constants

d_o = Injector nozzle diameter

x = Distance along the wall, in direction of flow

U_o = Injector nozzle exit velocity.

The exponent 'a' varies depending on the ratio between the bulk stream, U_G and the injected fluid velocity at the nozzle exit, U_o. From the experimental results of Kruka and Eskinazi (100), equation (3.51) gives the empirical correlation relating the exponent 'a' to the velocity ratio, represented by β.

$$a = \frac{1.06}{1-\beta} - \frac{1}{2} \qquad (3.51)$$

The constant C has been assigned various values by different workers, although most of these are around 3.5. Table 3.1 shows empirical values of 'a' and c used by some of the researchers. For purposes of this work a value of 3.5 was adopted.

To relate flow conditions in the wall-jet to those under a liquid-film/air-stream system, the concept of the equivalent nozzle diameter

is used. This enables the injection of a liquid fuel through an orifice of diameter d_o into gaseous surroundings, to be considered as equivalent to the injection of air through an orifice of diameter d_o' into air (23), where d_o' is defined by:

$$d_o' = d_o \left(\frac{\rho_f}{\rho_G}\right)^{1/2} \tag{3.52}$$

where subscripts G and f refer to the air and fuel respectively.

3.4.2 Penetration of Film Along the Wall

The equation for the penetration of the fuel film along the piston wall, is derived by integrating equation (3.50) to give the expression in eqn. (3.53).

$$x = [(a + 1)\, C\, U_o\, d_o'^{a}\, t]^{\frac{1}{1+a}} + x_o \tag{3.53}$$

x_o in equation (3.53) refers to the initial penetration when the potential core is present in the cross-section of the jet. The potential core refers to a 'wedge-like' region close to the injector nozzle (66), in which the velocity is undiminished, at U_o. So x_o may be determined by subsituting $U_x = U_o$ in equation (3.50), yielding the equation below:

$$x_o = C^{1/a} \cdot d_o' \tag{3.54}$$

3.4.3 Surface Area of the Film

In Fig. 3.9(a) the assumed shape of the film patch was given to illustrate the parabolic velocity profile across its width characterised by equation (3.38). The same set of equations that describe the shape in Fig. 3.9(a) are also used to derive the equation for the surface area. The hatched element in Fig. 3.9(b) represents the elemental area, dA, expressed mathematically by:

$$dA = \frac{r^2}{2} d\,\emptyset \tag{3.55}$$

where r represents the position vector for the outer edge of the film as illustrated in Fig. 3.9(a). Derivation of this parameter is outlined in detail in Appendix E yielding an expression of the film shown in equation (3.56).

$$r = x \cdot \left[\frac{1 - (\frac{\tan \emptyset}{\tan \theta})^2}{\cos^a \emptyset} \right]^{\frac{1}{1+a}} \tag{3.56}$$

x is the film penetration given by equation (3.53). The total surface area covered by the film patch is, therefore, obtained by integrating equation (3.55) across the film surface width:

$$A = \int_{-\theta}^{\theta} \frac{r^2}{2} d\,\emptyset \tag{3.57}$$

3.4.4 Development of Film Thickness

Section 3.3 it was pointed out that the film thickness could be evaluated through the simultaneous solution of equations (3.28) and (3.32) to give an analytical approach. However, by making use of the implied momentum decay function in equation (3.50), together with the principle of conservation of mass, as discussed in section 3.3.1, and combining equation (3.44) with equation (3.29) in order to account for evaporation, the following expression is derived for the film thickness:

$$S = \frac{0.589\, d_o^2\, U_o}{b(1 - 2.5\, f)\, U_x} - \int_o^t \frac{\dot{m}''}{\rho} dt \tag{3.58}$$

where f is the square root of the friction coefficient term, $C_{fi}/2$. The breadth of the film, b, is approximated, from experimental data

obtained by Rajaratnam (66), and also those obtained by the author, to have the following linear form:

$$b = x \cdot \tan \theta + b_o \qquad (3.59)$$

Here again x is the penetration given by equation (3.53), and θ is the jet spread angle (see Fig. 3.9(a)) which was empirically determined.

The second term on the right hand side of equation (3.58) accounts for the reduction in film thickness due to evaporation at the film surface. The two components are evaluated separately, and the results combined to yield the resultant film thickness, using the computational procedure illustrated in Fig. 3.12.

The following dimensions of the fuel film are thus completely satisfied at any spatial or temporal position during injection, by means of the following equations:

i. Penetration

$$x = [(a+1)C\, U_o\, d_o{}'^{a} t]^{\frac{1}{1+a}} + x_o \qquad (3.53)$$

ii. Breadth

$$b = x.\tan \theta + b_o \qquad (3.59)$$

iii. Thickness

$$S = \frac{0.589\, d_o{}^2 U_o}{b(1-2.5f)U_x} - \int_o^t \frac{\dot{m}''}{\rho}\, dt \qquad (3.58)$$

iv. Surface Area

$$A = \int_{-\theta}^{\theta} \frac{r^2}{2}\, d\phi \qquad (3.57)$$

v. Velocity of the Film

$$U_m = C\, U_o \left(\frac{d_o'}{x}\right)^a \qquad (3.50)$$

The distribution of velocity and scalar quantities in the bulk stream, especially in the boundary layer adjacent to the film surface are dealt with in the next chapter.

3.4.5 Modifications to Presented Theory

The basis of the theory discussed above for describing film flow parameters, was based on one fundamental assumption:- that the flow of a liquid film on a solid surface could be approximated to the flow of the inner layer of a wall-jet. In order to take into account any possible inaccuracies due, for example to the neglect of the effect of momentum transfer from the outer region into the inner layer, provision for incorporating experimentally obtained correlations was included. This was done by working out all the major parameters, listed in the foregoing section, in terms of the penetration. By making measurements of penetration, which will be discussed in detail in Chapter 5, a correlated equation could be used in place of equation (3.53), to work out the velocity (by differentiating), the surface area, and the breadth. These possible modifications are discussed in Chapter 5 together with the discussion of other experimental results.

Table 3.1: Empirical Values of 'a' and 'C' in the Wall-Jet Equation

WORKER	VALUE OF C	VALUE OF a
Rajaratnam (62)	3.5	0.5
Sigalla (59)	3.45	0.5
Kruka & Eskinazi (60)	3.5	variable
Bradshaw & Gee (58)	3.5	0.53

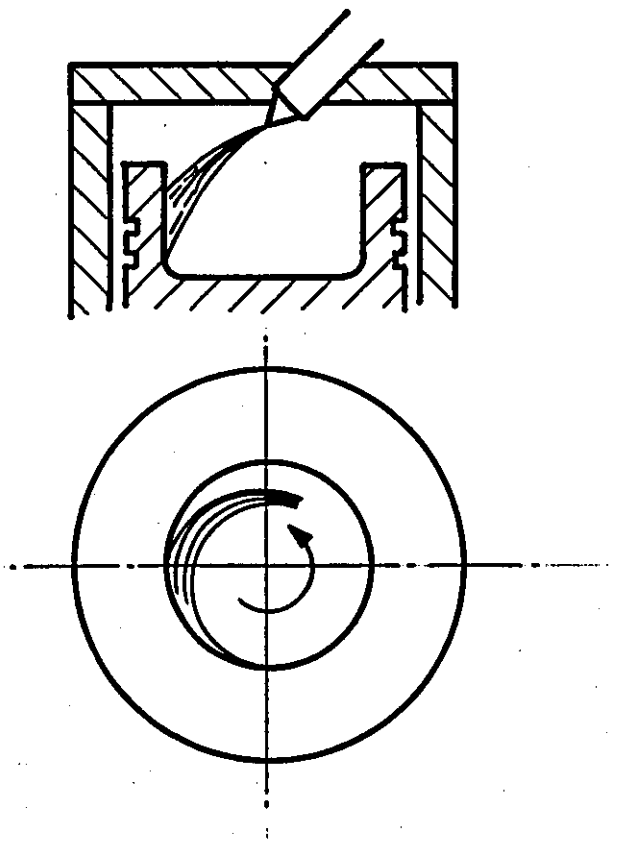

FIGURE 3.1: EQUIVALENT CYLINDRICAL BOWL

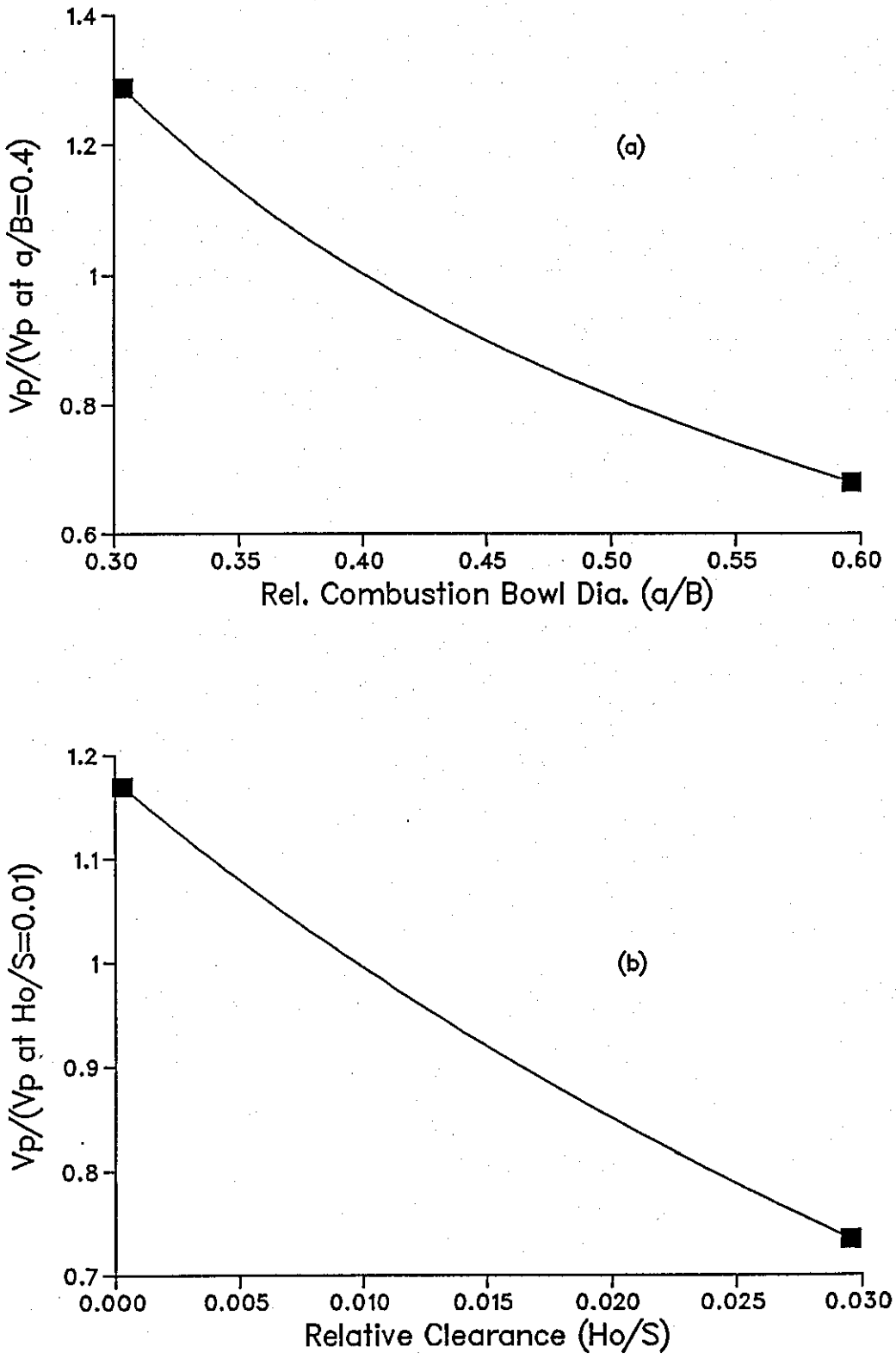

FIGURE 3.2: RELATIVE AIR PERIPHERAL VELOCITY, Vp, AT THE COMBUSTION CHAMBER WALL

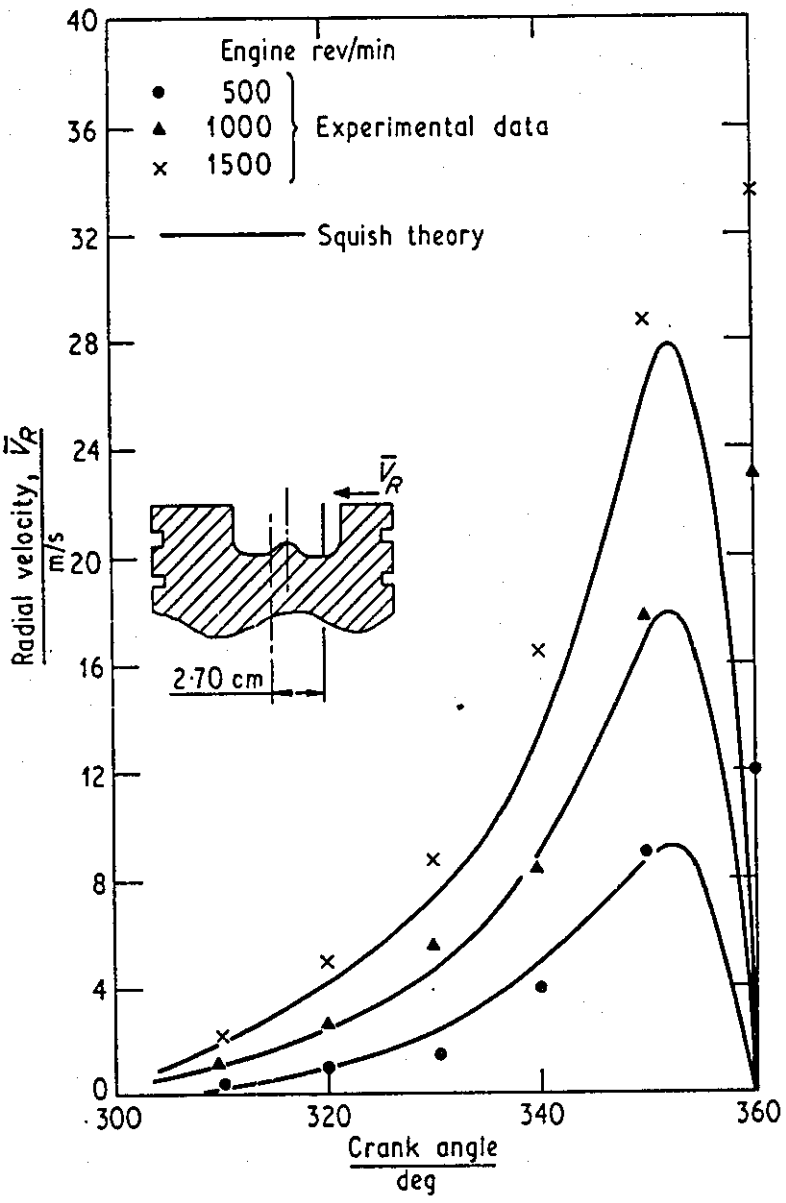

FIGURE 3.3: RADIAL VELOCITY AT THE EDGE OF THE COMBUSTION BOWL (74)

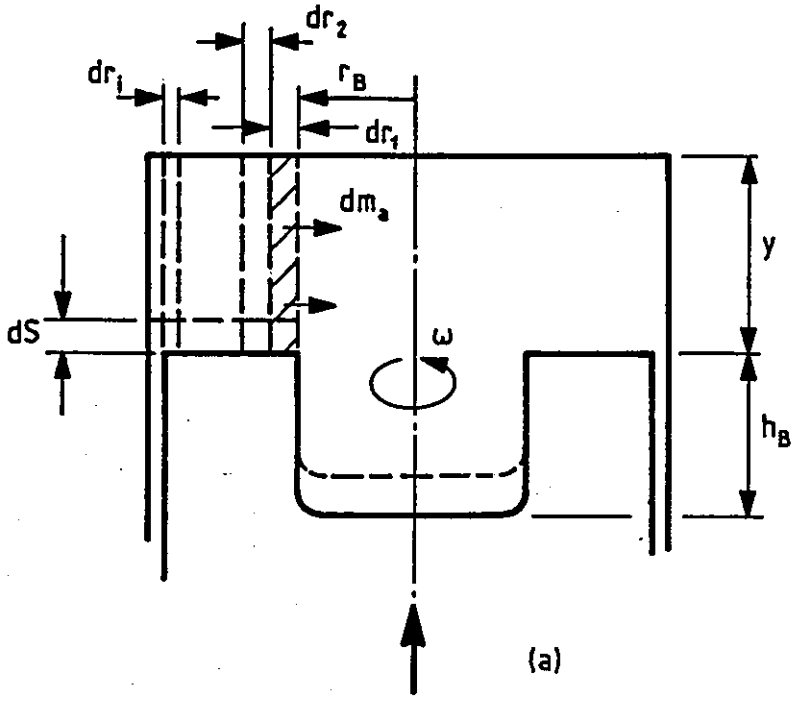

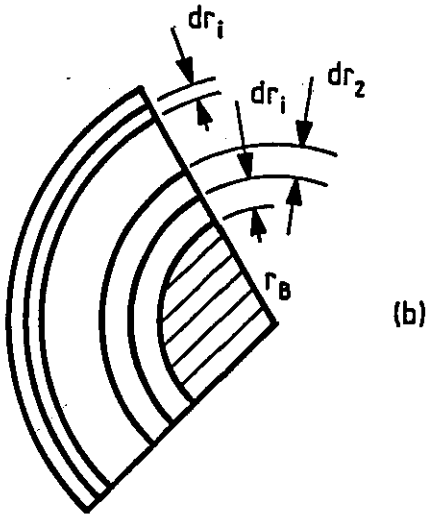

FIGURE 3.4: AIR MOTION DURING COMPRESSION

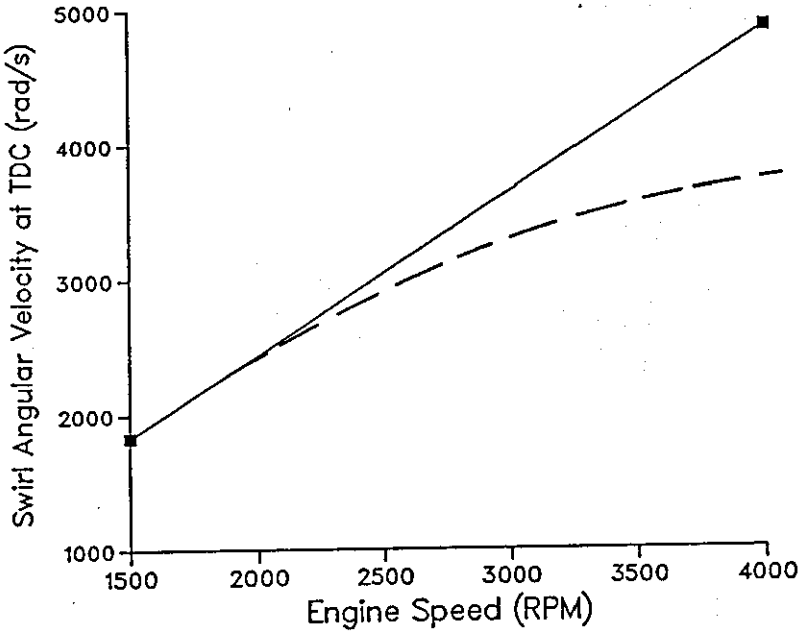

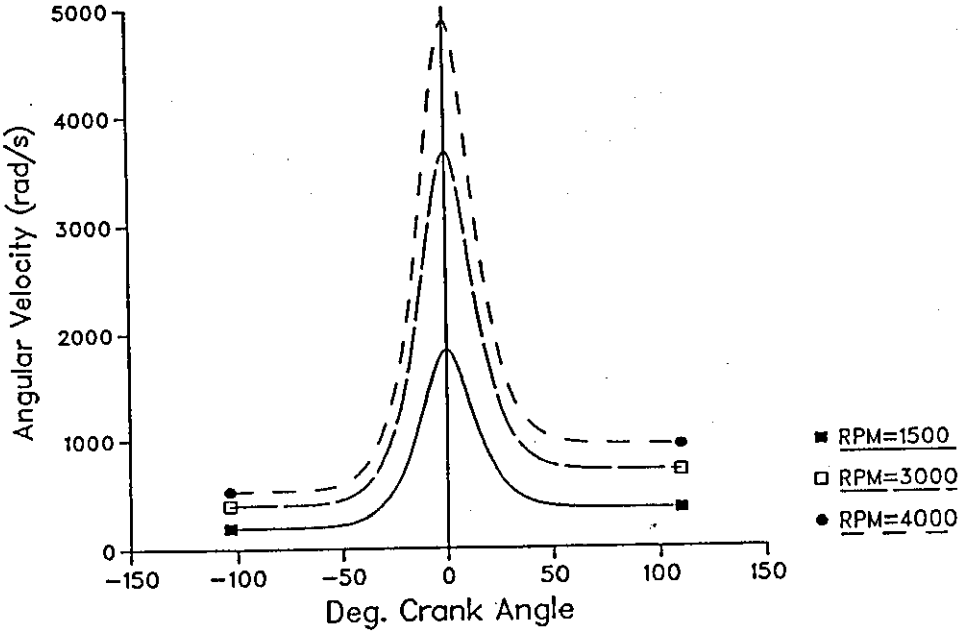

FIGURE 3.5: EFFECT OF ENGINE SPEED ON AIR SWIRL VELOCITY

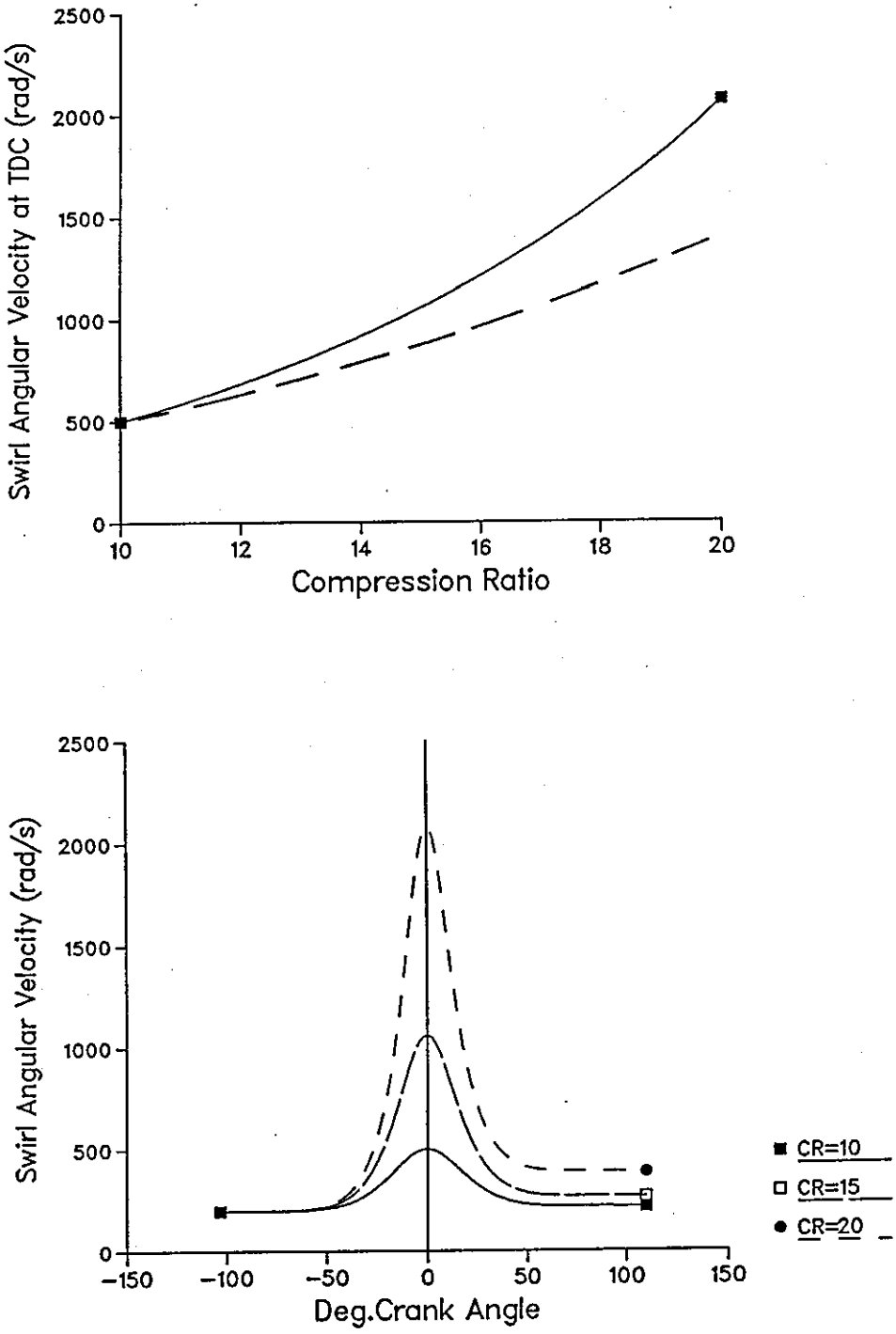

FIGURE 3.6: EFFECT OF COMPRESSION RATIO ON SWIRL VELOCITY

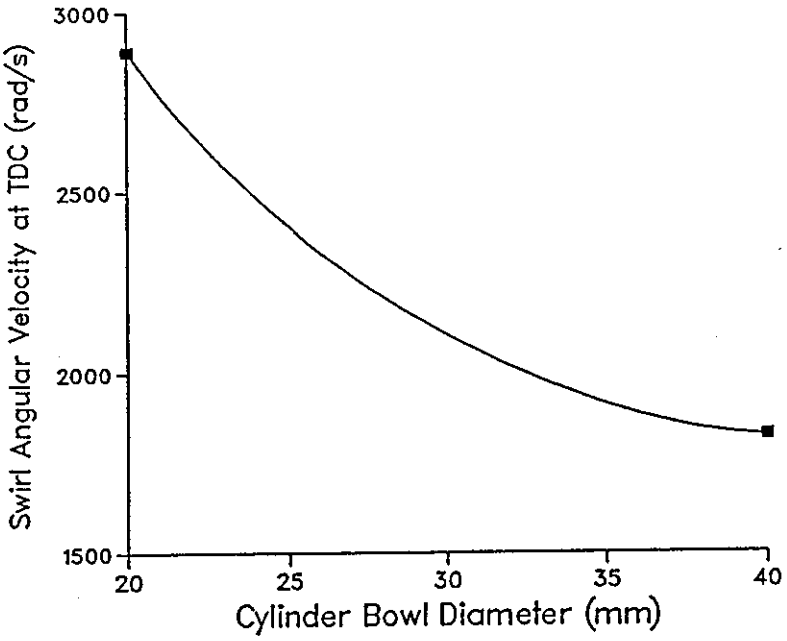

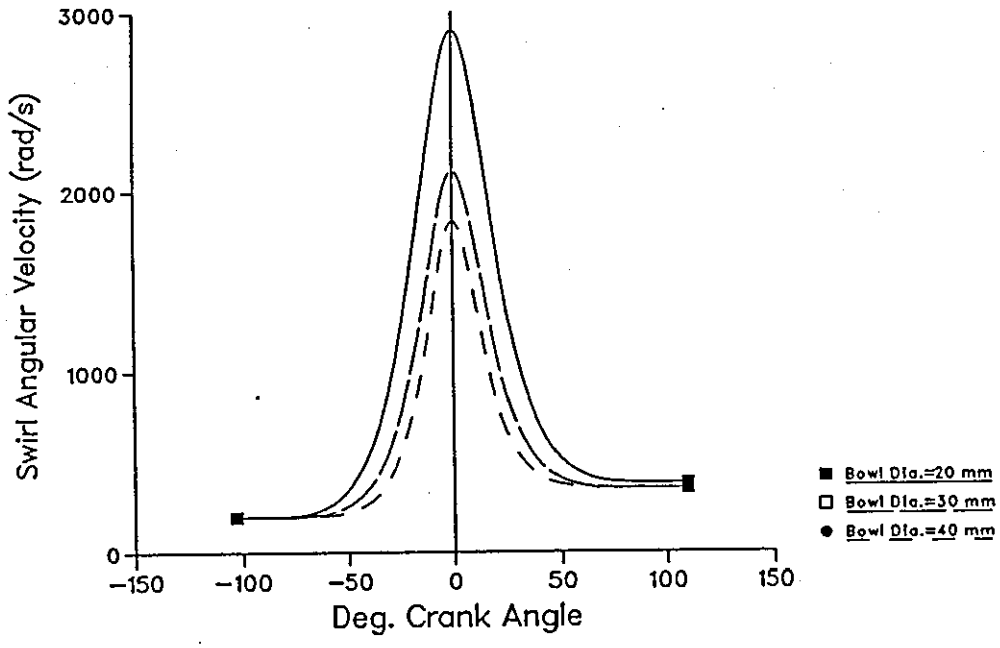

FIGURE 3.7: EFFECT OF CYLINDER BOWL DIAMETER ON SWIRL VELOCITY

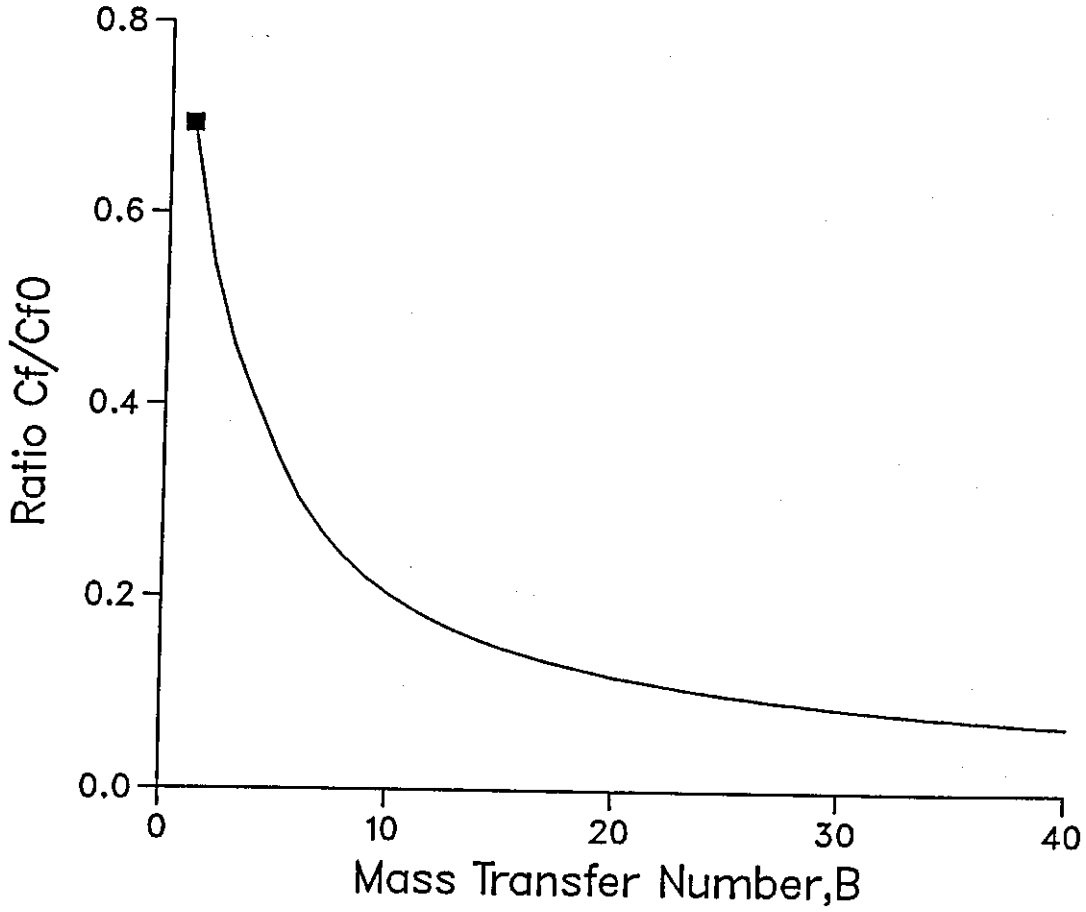

FIGURE 3.8: EFFECT OF EVAPORATION ON SKIN FRICTION

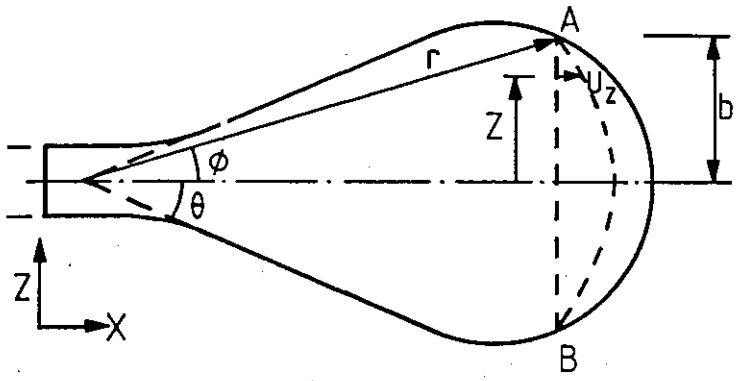

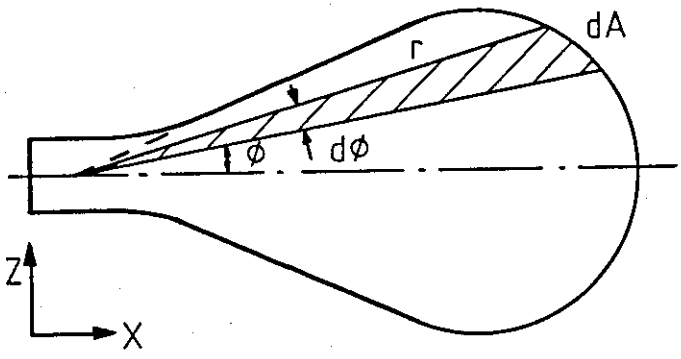

FIGURE 3.9: NOMENCLATURE FOR FILM SURFACE DEVELOPMENT

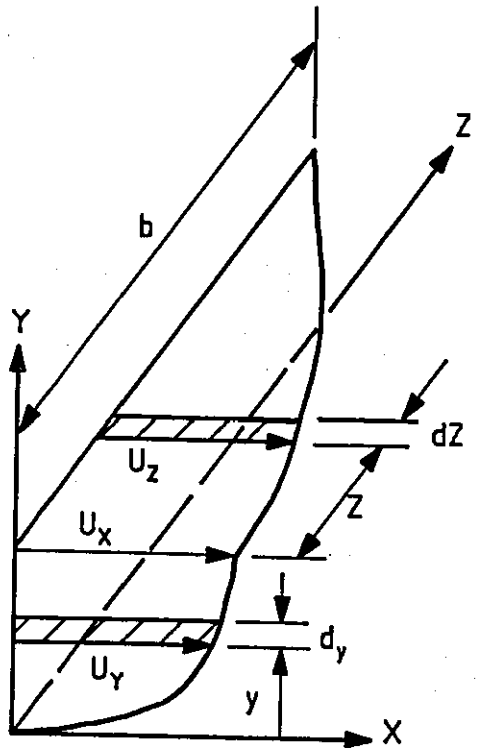

FIGURE 3.10: VELOCITY PROFILES IN THE FUEL FILM

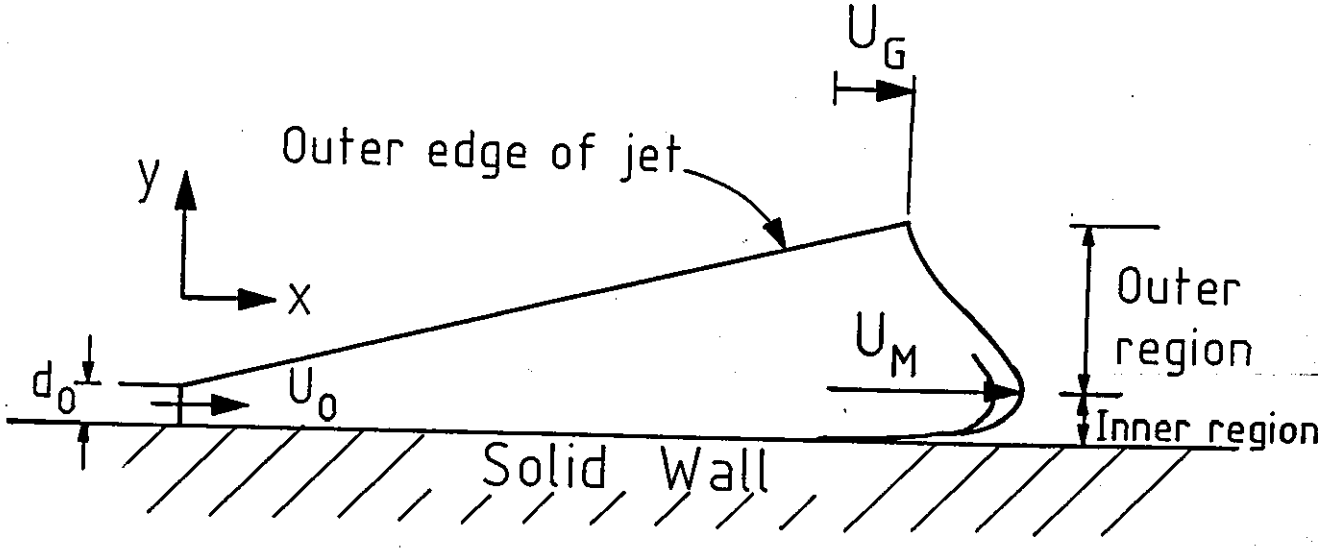

FIGURE 3.11: STRUCTURE OF THE WALL-JET

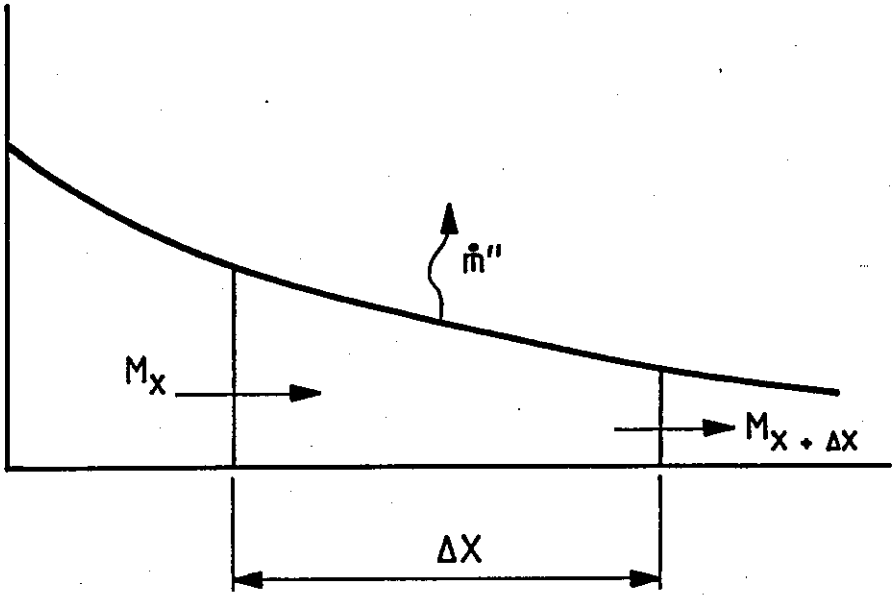

Thinning of the film by evaporation and mass conservation :

$$S = \underbrace{\frac{0.589\left(d_0^1\right)^2 U_0}{b\left(1 - 2.5\, C_f\right) U_m}}_{\text{Thinning due to Interfacial Shear}} - \underbrace{\int_0^t \frac{\dot{m}''\, dt}{\rho}}_{\text{Thinning due to Evaporation}}$$

FIGURE 3.12: COMPUTATIONAL PROCEDURE

CHAPTER 4

ANALYSIS OF CARBURETION PROCESSES

The variation in density and composition of gases flowing past the injected fuel surface, combined with the high initial velocity of the film produce turbulent, non-steady, curvilinear flow in the engine (Urlaub (34), Meurer and Urlaub (40)). This transient and heterogeneous flow is extremely difficult to model analytically with sufficient accuracy. A phenomenological approach, thus, offers a more practical means of attempting to describe the governing processes.

The major factors affecting the preparation of the combustible mixture in a diesel engine are those that influence the evaporation of the fuel, and its subsequent mixing with air. The relative magnitudes of such influences may logically be expected to vary, depending on whether the period being considered is before combustion (ignition delay period), or during combustion. The mixing processes between fuel vapour and air are further influenced by the presence of the jet structure (during injection), which induces turbulence in the cylinder. It has thus been necessary, in organising the structure of the model, to sub-divide the processes into three time zones: the period before ignition, that with both combustion and injection, and the post-injection period with or without combustion.

4.1 MIXURE FORMATION: A CONCEPTUAL FRAMEWORK

The principle of operation of the wall-wetting diesel engine has been outlined in Chapter 1, and also briefly, in Chapter 3. The most prominent feature has been identified as the deposition of a large proportion of the injected fuel in the form of a liquid film on the piston wall. In order to render the processes involved in mixture preparation amenable to analysis, it has been necessary to define a working conceptual framework.

The first major assumption, which is inherent in the derivation of the equation characterising air swirl motion in Chapter 3, is that the rotation of air throughout the process does not experience a change in direction. Secondly, it is assumed that all the injected fuel in the cylindrical chamber such as that shown in Figure 3.1, spreads on the vertical walls of the bowl, and that the bottom of the bowl and the top of the piston are not wetted. Figure 4.1 shows the resulting schematic diagram of the flow structure between the fuel and the air, based on the last two assumptions. The evaporating fuel is assumed to mix with the 'entrained' air, forming a combustible mixture within a boundary layer above the film surface.

Experimental work of Zucrow and co-workers (48, 49), on film cooling, has demonstrated that when a liquid film evaporates into a gaseous stream, it forms a layer of vapour adjacent to the wall, which persists for relatively long time durations to allow for a boundary layer type analysis to be used in determining concentration profiles. Williams (106) has shown in his text, that significant simplification can be achieved in the analysis of many combustion problems, without much loss of accuracy, by applying the Shvab-Zel'dovich formulation. Strehlow (107) points out that this approach is particularly useful in diffusion flames. The major thrust of the formulation is summarised in the following assumptions:

i. Steady flow is assumed
ii. Pressure gradient in the direction of flow is negligible
iii. Diffusion coefficients for all species are equal (Binary diffusion is assumed).
iv. Lewis number is unity
v. Chemical reaction occurs in a single step.

4.2 MASS TRANSFER INTO THE BOUNDARY LAYER

Figure 4.2 shows an enlarged diagram of the elemental section with length Δx shown in Figure 4.1. The element is treated as a flat plate, with a turbulent boundary layer flowing over a vapourising liquid surface. As illustrated, mass is transferred from the bulk stream into the boundary layer, by the process of turbulent entrainment. Simultaneously, there is also the transfer of mass from the fuel surface into the boundary layer as the fuel evaporates. In the next two sections, the governing equations for these processes are outlined in some detail.

4.2.1 Air Entrainment Function

The entrainment of bulk fluid into a turbulent boundary layer forms a very significant element in the analysis of processes of mixture preparation in wall-wetting engines. An inaccurate function here is likely to lead to unreliable results from the model, since the combustion process depends on the availability of air. When applied to engine processes, the entrainment function should be able to respond accurately to the effects of air compressibility, bulk stream temperature fluctuations, bulk stream velocity, and the intensity of mass injection from the wall into the boundary layer. It has thus, not been possible to find a suitable function in the literature, capable of representing the above requirements in the most favourable form for developing a phenomenological model.

The equations of Escudier and Nicoll (78) were chosen to define the entrainment function because they contain some of the variables relating to the parameters that will influence air entrainment in engine operation, as outlined in the paragraph above. The mathematical expression of these functions are outlined in (4.1):

$$\dot{m}''_{ENT} = 0.75\ (1 - Z_E)\,\rho_G\,U_G \qquad Z_E \leq 1 \tag{4.1}$$

$$\dot{m}''_{ENT} = (0.03\ Z_E - 0.02)\,\rho_G\,U_G \qquad Z_E > 1$$

where ρ_G and U_G are the density and velocity in the bulk air stream. Z_E is the velocity profile shape parameter defined (78) as the ratio of the "Law of the Wall" velocity at the outer edge of the boundary layer, to the bulk stream velocity, mathematically expressed in Chapter 2 by equation (2.36). A detailed expression for the "Law of the Wall" velocity will be given in due course, in the discussion of the velocity profile in the boundary layer.

When the function given in (4.1) is plotted out, it shows a discontinuity where Z_E changes from being less than unity to being greater. Since this discontinuity cannot be related to any observed phenomena in engine operation, the equation suggested earlier by Spalding (51) for $Z_E > 1$, was considered more appropriate. This has the following form:

$$\dot{m}''_{ENT} = 0.03\ (Z_E - 1)\,\rho_G\ U_G \qquad Z_E > 1 \tag{4.2}$$

Figure 4.3 shows the two functions plotted together to illustrate the improvement in the function when equation (4.2) is included.

The work of Spalding (51), and later that of Escudier & Nicoll (78), was based on boundary layers in which the injected fluid from the wall was also gaseous. In the case of boundary layers developing over an evaporating liquid, Z_E takes on a slightly different meaning. Instead of merely expressing the ratio of velocities given in equation (2.36) and characterising the shape of the velocity profile, it is here taken to represent the ratio of the momentum fluxes represented by the bulk stream and the boundary layer velocity as calculated from the "Law of the Wall" velocity at the edge of the boundary layer. This introduces a new definition for Z_E, given in (4.3), based on the principle of the equivalent diameter.

$$Z_E = Z_{Eo}\,\left(\frac{\rho_f}{\rho_G}\right)^{1/2} \tag{4.3}$$

where ρ_f is the density of the vaporising fluid, and Z_{Eo} is the value of Z_E calculated from eqn. (2.36). This correction was made only in respect of the particular applications of the model being proposed. As will be demonstrated later, this modification leads to improved results for entrainment during engine modelling.

4.2.2 Evaporation from the film surface

To define the rate of evaporation from the film surface, a conserved property, $\emptyset$, is defined to satisfy the governing equation for species concentration in a 2-dimensional boundary layer (54):

$$\rho u \frac{\partial \emptyset}{\partial x} + \rho v \frac{\partial \emptyset}{\partial y} = \frac{\partial}{\partial y} (\lambda_m \frac{\partial \emptyset}{\partial y})$$

where $\lambda_m = \rho (D + \epsilon_\emptyset)$

Neglecting derivatives in the x-direction and integrating, yields:

$$\dot{m}''\emptyset - \lambda_m \frac{d\emptyset}{dy} = \dot{m}'' \emptyset_o$$

where $\dot{m}'' = \rho v$

The equation may be re-arranged as follows:

$$\dot{m}'' \frac{dy}{\lambda_m} = \frac{d\emptyset}{\emptyset - \emptyset_o}$$

which, when integrated across the thickness of the boundary layer yields:

$$\ln \left(\frac{\emptyset_G - 1}{\emptyset_o - 1}\right) = \dot{m}'' \int_o^\delta \frac{dy}{\lambda_m} \qquad (4.4)$$

The mass transfer number, B, when expressed in terms of a conserved

scalar quantity, $\emptyset$, may be defined (54) as follows:

$$B = \frac{\emptyset_G - \emptyset_o}{\emptyset_o - \emptyset_T} \tag{4.5}$$

where $\emptyset_o$ refers to the value of the quantity $\emptyset$ on the surface of the film (in the bulk stream), and $\emptyset_T$ is its value in the transferred phase. Applying the second assumption in Section (4.1) to equation (4.5), implies that $\emptyset_G$ has a value of zero. $\emptyset_T$ will have a value of 1 when $\emptyset$ refers to fuel vapour mass fraction. Hence the following is the form in which the equation appears in some parts of the model.

$$B = \frac{- \emptyset_o}{\emptyset_o - 1} \tag{4.6}$$

Substituting equation (4.6) into (4.4) yields the following expression:

$$\ln (1 + B) = \dot{m}'' \int_o^{\delta} \frac{dy}{\lambda_m} \tag{4.7}$$

which may be re-arranged to give the fuel mass flux from the wall by:

$$\dot{m}'' = \frac{\ln (1 + B)}{\int_o^{\delta} \frac{dy}{\lambda m}} \tag{4.8}$$

The quantity $1./(\int_o^{\delta} \frac{dy}{\lambda m})$ defines the mass transfer conductance (54), more commonly referred to by g* which, from Reynolds Analogy, may be defined by the following ratio:

$$g^* = \frac{h}{C_p} \tag{4.9}$$

where h is the heat transfer coefficient between the gaseous boundary layer and the film surface, and C_p the heat capacity of the bulk fluid. In the proposed model, h has been calculated from the standard correlation for turbulent boundary layer flow over a flat plate of length L (56):

$$h = 0.037\ R_L^{0.8}\ P_r^{1/3}\ \frac{k}{L} \qquad (4.10)$$

The combustion bowl diameter is used to represent the characteristic length, L, and k is the thermal conductivity of the boundary layer.

4.3 MIXTURE FORMATION BEFORE COMBUSTION

A system such as that represented in Figure 4.2 may be treated as flow of a turbulent boundary layer over a porous flat plate, with mass injection from the wall (51). This section presents the equations that result from such a treatment, which are used to determine velocity and fuel vapour concentration profiles within the boundary layer. Equations are also provided dealing with rates of mass transfer into the boundary layer due to the evaporation of the fuel film, and the entrainment of air.

4.3.1 Velocity Profile in the Boundary Layer

The transfer of mass from the wall into the boundary layer has been shown by the experimental work of Wooldridge and Muzzy (108) to have an effect on the nature of the velocity profile. High rates of mass transfer lead to a reduction in skin friction (109), which in turn results in a variation of the velocity profile. The two-component equation derived by Spalding (51) accounts for the effect of the bulk stream on the velocity profile, by incorporating a "wake" component. The mathematical expression is thus made up of the "Law of the Wall" component - first term on the right hand side of equation (4.11) - and the "Law of the Wake" component.

$$Z = f^{1/2}\ U^+ + \frac{1}{2}\ (1 - Z_E)\ (1 - \cos \pi \xi) \qquad (4.11)$$

Z is a non-dimensionalised velocity defined by U/U_G, and Z_E is defined earlier, in Chapter 2. ξ is a non-dimensionalised height above the

film surface, defined as y/δ where the boundary layer thickness, δ, is illustrated in Figure 4.2. The friction factor, f, is more usually expressed as $C_f/2$.

By making use of the law of the wall expression as derived by Black and Sarnecki (110), the effect of evaporation on the velocity profile is accounted for. The equation is given in (4.12) below.

$$U^+ = 2.5 \left\{ \ln (Ey^+) + \frac{m_o}{1.6 f^{1/2}} [\ln (Ey^+)]^2 \right\} \qquad (4.12)$$

The quantity y^+ is a non-dimensionalised distance above the film surface defined by:

$$y^+ = \frac{y (\tau_o/\rho_f)^{1/2}}{\nu} \qquad (4.13)$$

and m_o is the normalised rate of evaporation from the surface, defined by equation (4.14).

$$m_o = \frac{m''_o}{\rho_G U_G} \qquad (4.14)$$

where ρ_G and U_G are the density velocity pertaining in the bulk stream respectively. The variable E is tentatively (51) defined as:

$$E = 6.542 \left(1 + \frac{m_o \cdot z_E}{f}\right)^{1/2} \qquad (4.15)$$

The modified friction coefficient, taking into account its reduction due to mass transfer effects, is given by:

$$f = \left(0.4 \frac{z_E}{\ell} - 0.625\, m_o \cdot \ell\right)^2 \qquad (4.16)$$

where the value of ℓ is inversely proportional to the turbulence length scale in the boundary layer, and is defined by the following equation:

$$\ell = \ln\left[2.6168\, R \left(\frac{z_E}{\ell} + 1.5625\, m_o \cdot \ell\right)\right] \qquad (4.17)$$

Substituting equations (4.12) and (4.16) into (4.11) and simplifying by neglecting the $(\ln \xi)^2$ term, yields the velocity profile in the boundary layer as:

$$Z = D \ln \xi + Z_E + \frac{1}{2}(1 - Z_E)(1 - \cos \pi \xi) \qquad (4.18)$$

D is defined by equation (4.19).

$$D = 2.5 (f^{1/2} + m_o . Z_E)^{1/2} \qquad (4.19)$$

Equation (4.18) defines the required velocity profile, taking into account the effect of evaporation. Under certain operating conditions (large m_o) the friction coefficient as expressed by equation (4.16) experiences a discontinuity which is not explained by observed physical phenomena in the engine. So the equations in (4.20), suggested by Marxman (50), were adapted instead.

$$\left.\begin{aligned} f &= f_o \left[\frac{\ln(1+B)}{B}\right] \quad \text{for} \quad B < 5 \\ f &= 1.2B^{-0.77} f_o \quad \text{for} \quad 5 \leqslant B \leqslant 100 \end{aligned}\right\} \qquad (4.20)$$

where f_o is the friction coefficient in the absence of mass transfer from the film surface. The total skin friction drag by a turbulent boundary layer flowing over a flat plate of length ℓ is given by Schlichting (50), by the following correlation:

$$f_o = 0.037 R_\ell^{-0.2} \quad \text{for} \quad 5 \times 10^5 < R_\ell < 10^7 \qquad (4.21)$$

where Reynolds number, R_ℓ, is defined as:

$$R_\ell = \frac{\ell U_G}{\nu} \qquad (4.22)$$

4.3.2 Fuel Concentration Profiles

As outlined earlier, the distribution of fuel vapour mass concentration in the air stream is assumed to be entirely within the

gaseous boundary layer above the film surface. The species mass fraction of any gaseous constituent, is a conserved scalar property of the boundary layer (54). So it must satisfy the following set of two dimensional boundary layer equations:

(i) Momentum :

$$\rho u \frac{\partial u}{\partial x} + \rho v \frac{\partial u}{\partial y} = \frac{\partial}{\partial y} (\mu_t \frac{\partial u}{\partial y}) - \frac{dP}{dx} \qquad (4.23)$$

(ii) Conserved Scalar, $\emptyset$:

$$u \frac{\partial \emptyset}{\partial x} + v \frac{\partial \emptyset}{\partial y} = \frac{\partial}{\partial y} (\lambda_\emptyset \frac{\partial \emptyset}{\partial y}) \qquad (4.24)$$

where $\lambda_\emptyset$ may be expressed as follows:

$$\lambda_\emptyset = \rho (D_\emptyset + \epsilon_\emptyset) \qquad (4.25)$$

$D_\emptyset$ is the diffusity for $\emptyset$, and $\epsilon_\emptyset$ the corresponding eddy diffusivity. Equations (4.23) and (4.24), when combined with the continuity and energy conservation equations, form a coupled set of parabolic equations which Partankar and Spalding (111) have solved by means of finite difference techniques. For purposes of the proposed model, however, it is necessary that further simplification is made by applying the principle of Couette flow analysis to the gaseous boundary layer. This implies that derivatives in the direction of flow are negligible when compared with those perpendicular to it (56). Applying this simplification to equations (4.23) and (4.24), and integrating, yields equations (4.26) and (4.27):

$$\dot{m}''_o u - \mu_t \frac{du}{dy} = - \tau_0 \qquad (4.26)$$

$$\dot{m}''_o \emptyset - \lambda_\emptyset \frac{d\emptyset}{dy} = \dot{m}''_o \emptyset_o \qquad (4.27)$$

where the mass flux, ρv, in equations (4.23) and (4.24) has been replaced by $\dot{m}'_o$ defined earlier. Eliminating $\dot{m}'_o$ and combining the two equations yields the following equation:

$$\lambda_\emptyset \frac{d\emptyset}{\phi - \phi_o} = \mu_t \frac{du}{u + \frac{\tau_o}{\dot{m}''_o}} \qquad (4.28)$$

Equation (4.28) relates the distribution of the scalar quantity, $\emptyset$, to the velocity profile. A semi-empirical solution to the equation has been derived by Spalding (51), based on the "two-parameter" principle utilised earlier to describe the velocity profile equation. The resulting equation, giving the distribution profile in terms of the conserved scalar quantity, $\emptyset$, is:

$$\emptyset - \emptyset_G = D_o \ln \xi + (\emptyset_E - \emptyset_G)[1 - \frac{n}{2}(1 - \cos \pi \xi)] \qquad (4.29)$$

For Lewis number equal to unity, which is assumed for all calculations in this model, the term D_o is defined (51) by:

$$D_o = \frac{(\emptyset_E - \emptyset_o)}{Z_E} D \qquad (4.30)$$

where D is the same as that defined earlier in equation (4.19). $\emptyset_E$ represents the value of $\emptyset$ in an equivalent couette flow, at the edge of the boundary layer, defined as follows:

$$\frac{\emptyset_E - \emptyset_o}{\emptyset_o - 1} = \frac{m_o . Z_E}{f} \qquad (4.31)$$

and the constant n is assigned a value of 0.63 (51). The implication of assuming that all the fuel is distributed within the boundary layer, is that $\emptyset_G$ in equation (4.29) may be assumed equal to zero, thus yielding the following form in which the equation appears within the computer model:

$$\emptyset = D_o \ln \xi + \emptyset_E [1 - \frac{n}{2}(1 - \cos \pi \xi)] \qquad (4.32)$$

To determine $\emptyset_o$, the fuel vapour mass fraction on the film surface, it is assumed that the fuel vapour/air system is in equilibrium. The vapour mass fraction is thus related to the saturated vapour pressure,

P_s, at the prevailing surface temperature, T_f. By assuming a perfect gas mixture, then the mole fraction of the fuel vapour is equal to the partial pressure fraction (P_s/P), so that the fuel vapour mass fraction may be expressed as:

$$\phi_o = \frac{(\frac{P_s}{P})\, W_f}{W'} \tag{4.33}$$

where W' is the equivalent molecular weight of the mixture defined by:

$$W' = (\frac{P_s}{P})\, W_f + [1 - (\frac{P_s}{P})]\, W_a \tag{4.34}$$

where W_f and W_a are the molecular weights of fuel and air respectively. P is the total pressure in the bulk stream. Equation (4.33) may, thus, be recast in the form shown in (4.35) to give the mass fraction of fuel vapour on the film surface;

$$\phi_o = \frac{P_s}{\gamma P + (1-\gamma)P_s} \tag{4.35}$$

where γ is the ratio W_a/W_f.

Antoine's Relationship is used to evaluate P_s, the saturation vapour pressure on the film surface. It has the following mathematical form:

$$\log_{10} P_s = a + \frac{b}{T_f + C} \tag{4.36}$$

which gives pressure, P_s, in mm Hg, and the fuel surface temperature T_f is usually given in degrees Celcius. The following constants, which apply to n-Dodecane (112), have been used to approximate diesel properties in the model:

a = 7.0
b = -1625.93
c = -92.9 (T_f in Absolute Degrees, K)

Only T_f, the temperature on the film surface, remains unkown in the above expressions (P is calculated from the energy balance considerations discussed in Chapter 2). Inherent in the assumption Le = 1 is the condition that the mass transfer number, B, will be the same irrespective of whether enthalpy or mass fraction is used as the conserved property in equation (4.5). This leads to the following expression:

$$\frac{-\phi_o}{\phi_o - 1} = \frac{C_{Pa}\,(T_G - T_f)}{h_{fg} + C_{Pf}\,(T_f - T_{ref})} \qquad (4.37)$$

This equation can be re-arranged and written in the form shown below:

$$T_f = f(T_f) \qquad (4.38)$$

which is the required form for the application of Steffen's rapidly converging iteration algorithm (61). Convergence in most cases is achieved in less than 10 cycles. When bulk gas temperature, T_G, is much higher than the boiling point temperature of the fuel, it is accepted standard (46) to replace T_f by the boiling point temperature of the fuel.

In all cases, the temperature on the surface of the film will be slightly lower than the mean temperature of the film due to evaporation. As the mean film temperature is required to carry out energy balance calculations, a separate calculation is undertaken to determine this value. By considering heat balance on an element of liquid film exchanging heat with its surroundings as shown in Fig. 4.4, the following equation may be derived (41) for the mean film temperature:

$$\frac{dT_f}{dt} = \frac{1}{(s\rho_f - m''t)C_{pf}}\,[q_{CONV} + q_{COND} - q_{EVAP}] \qquad (4.39)$$

where q_{CONV} and q_{COND} refer to the convection conduction heat terms while q_{EVAP} refers to the loss of heat due to evaporation. Radiant

heat is neglected as it is virtually negligible in the absence of combustion. Equations (4.40) - (4.42) give the mathematical expressions defining these heat terms.

$$q_{CONV} = h\,(T_G - T_f) \tag{4.40}$$

$$q_{EVAP} = \dot{m}''[h_{fg} + C_{pf}\,(T_G - T_f)] \tag{4.41}$$

$$q_{COND} = \frac{k_f}{s}\,(T_w - T_f) \tag{4.42}$$

where h is the heat transfer coefficient between the air and the film surface, s is the film thickness, and k_f the thermal conductivity of the fuel. It is worth noting here that just as skin friction is reduced due to mass tranfer, there is a corresponding reduction in the effective heat transfer coefficient, defined in terms of the mass transfer number as given in equation (4.43).

$$h = h_o\,\left[\frac{\ln\,(1+B)}{B}\right] \tag{4.43}$$

In Figure 4.5 the effect of bulk gas temperature on vapour pressure and the corresponding fuel vapour mass fraction are illustrated, and in Figure 4.6 a typical result from equation (4.39) is outlined, giving the effect of mass transfer (varying B) on the mean temperature of the film. In both graphs, all other variables are kept constant as the parameter is varied. As would be expected, the mean temperature of the film rises less steeply and steadies at a lower value as mass transfer increases. Figure 4.7 shows typical velocity and vapour mass fraction profiles, based on equations (4.18) and (4.32) respectively.

4.4 MIXTURE FORMATION DURING COMBUSTION

Introducing combustion within the boundary layer structure outlined above leads to a significant variation in flow field characteristics, which render an analytical solution impossible to achieve. An increase in fuel evaporation will occur, due to combustion, and this in turn will intensify the combustion. The heat and mass transfer

relationships are thus 'coupled' through a set of relationships that, for purposes of this model, are assumed undefined. The boundary layer concept introduced in paragraph 4.1 above is maintained here, with the further inclusion into the boundary layer, of a combustion region (Fig. 4.8).

The general field of reactive boundary layers has generated significant interest in the literature due to its applicability to a number of practical engineering problems such as erosive burning of solid propellants, and hybrid rocket combustion. As would be expected, advances in the development of analytical methods have been made for laminar reactive boundary layers that are more reliable than for those experiencing turbulent flow. Williams (106) has addressed the general problem of combustion of a fuel plate when the oxidising stream is laminar, and provides some solutions for the mass burning rate, and profiles of velocity and scalar quantities. The presentation of his solution, however is not as readily usable as, for example, the mathematical model developed by Andreussi and Petarca (113). They also carried out experiments with ethanol burning in a laminar oxidising stream, showing very favourable results when compared with their model predictions. Their model, which was based on the simplifying assumptions of the Shvab-Zel'dovich formulation outlined earlier under paragraph 4.1, sheds some light on the governing dimensionless parameters that need to be taken into account when modelling such flows. Also using the Shvab-Zel'dovich formulation, Lees (53) arrived at some important general conclusions about the properties of reactive turbulent boundary layer flow which have been extensively developed by the work of Marxman and co-workers (50, 59, 108, 114). Their work has been used as the basis for developing the equations suitable for application in the proposed model. The essential parameters that need to be determined are velocity and scalar quantity profiles within the boundary layer, and the mass transfer rate, from which the combustion rate is obtained.

4.4.1 Velocity Profile

Marxman and Gilbert (59) define a modified velocity profile in the boundary layer over a burning flat plate, based on the 1/7th power law, by:

$$Z = \frac{\xi^{n}\,(1 + \frac{B}{2}\xi^{n})}{(1 + B/2)} \qquad (4.44)$$

Z, ξ , and B are defined earlier in equations (4.1) and (4.37), and n equals 1/7. The equation is valid over the whole range of B likely to be encountered under engine operating conditions (less than 100). Wooldridge and Muzzy (108) have found good agreement between this profile and experimentally obtained data. In the absence of mass transfer from the surface (B = 0), equation (4.44) reduces to the 1/7th power law which is a fairly accurate representation of velocity profile in turbulent boundary layers (56). Fig. 4.9 shows the effect of increased mass transfer on the velocity profile as expressed by equation (4.44).

4.4.2 Flame Position in the Boundary Layer

The schematic diagram of combustion in the boundary layer illustrated in Fig. 4.8 shows a thick combustion zone rather than a surface which assumes an infinitely fast reaction. The position being calculated refers to the mid-point of the combustion zone above the surface. The liquid fuel evaporates from the surface, diffuses outward and reacts with the air in the combustion zone. All the fuel/air reactions take place in the gas-phase. The controlling factors in determining the location of the combustion zone is the rate of air entrainment from the main stream into the boundary layer and its subsequent diffusion to the flame (59). The diffusion of air within the boundary layer to the flame may be defined from Reynolds analogy by:

$$\dot{m}''_a \Big|_b = \rho_b\,(\varepsilon + D)\,\frac{\partial m_a}{\partial y}\Big|_b \qquad (4.45)$$

Where subscript b refers to conditions in the combustion zone, and m_a is the mass fraction of air. According to the Prandtl mixing length hypothesis, the turbulent diffusivity, ε, may be defined by:

$$\varepsilon = 0.16\, y^2 \frac{du}{dy} \tag{4.46}$$

Combining equations (4.44), (4.45) and (4.46) yields the equation for the flame position,

$$\frac{\xi_b^{2n}\,(1 + B\xi_b^{n})^2}{(1 + B/2)\,[1 + \frac{B}{2} - \xi_b^{n}\,(1 + \frac{B}{2}\xi_b^{n})]} = \frac{(\frac{A}{F})_b\,(\frac{\dot{m}''}{\rho_G\, U_G})\,\frac{T_b}{T_G}}{0.16\, n^2\, m_{a,G}} \tag{4.47}$$

Equation (4.47) is a quartic in ξ_b^{n} which can be easily solved iteratively. Some typical solutions are given in Figure 4.10 to 4.12 showing the effect of mass transfer, swirl velocity, and flame zone temperature on the flame height. Reducing swirl velocity lowers the flame height while high mass transfer rates and high combustion zone temperatures result in the raising of the flame. $(A/F)_b$, the air/fuel ratio at the flame is not necessarily equal to stoichiometric, in fact experimental evidence (108) has revealed that this is usually in the rich zone. A simplification may, however be made without much loss of accuracy, by assuming stoichiometric mixture in the combustion zone.

4.4.3 Boundary Layer Thickness During Combustion

Schlichting (56) gives an empirical equation for boundary layer thickness in turbulent flow, without mass transfer from the plate as:

$$\frac{\delta}{x} = 0.037\, Re_x^{-0.2} \tag{4.48}$$

However, since evaporation causes a reduction in skin friction on the film surface, Marxman (50) has observed that this leads to a variation

in boundary layer thickness. The following expression was suggested by Marxman to account for the effect of mass transfer on the thickness of the boundary layer:

$$\frac{\delta}{x} = \left[\frac{0.0281}{I}(1 + B).\frac{\ln(1+B)}{B}\right]^{0.8} . Re_x^{-0.2} \qquad (4.49)$$

where the variable I is defined as:

$$I = \int_0^1 Z\,(1 - Z)\,d\xi \qquad (4.50)$$

It was suggested earlier that the reduction in skin friction due to mass transfer may be approximated by equation (4.20). The variation was illustrated in Figure 3.8, showing a rapid drop in friction as mass transfer increases. The equations in (4.20) cover a wide range of B, up to 100. So they may also be used to represent flow in boundary layers with combustion. This is especially the case in wall-wetting diesel engines where Martin and Ahmad (31) found, from rough estimates, that B remains considerably less than 100. In Figure 4.13 the effect of mass transfer on boundary layer thickness as expressed by equation (4.49) is illustrated.

4.4.4 Scalar Quantity Profiles

The experimental work of Wooldridge and Muzzy (108) has shown that species mass concentration and energy profiles in the reactive boundary layer exhibit similarity with the velocity profile when non-dimensionalised in a suitable way. The non-dimensional similarity parameters are divided into the two regions separated by the conceptual flame position. For conditions below the flame (i.e. between the fuel surface and the flame) equations (4.51) and (4.52) define concentration and energy similarity parameters whose profiles are identical to those of the non-dimensionalised velocity, Z.

$$\phi^* = \left(\frac{\phi_s - \phi}{\phi_s - \phi_b}\right) Z \qquad (4.51)$$

$$h^* = \left(\frac{h - h_s}{h_b - h_s}\right) Z \qquad (4.52)$$

Where subscripts b and s refer to the flame and film surface respectively. The enthalpy, h, is defined simply as $C_p.T$ so that a temperature profile is identical to the h-profile. For conditions above the flame, the two parameters are defined by equations (4.53) and (4.54):

$$\phi^* = 1 - (1 - Z)\left(\frac{\phi_G - \phi}{\phi_G - \phi_b}\right) \qquad (4.53)$$

$$h^* = 1 - (1 - Z).\left(\frac{h - h_G}{h_b - h_G}\right) \qquad (4.54)$$

where subscript G refers to the bulk gas stream. By combining equations (4.51) - (4.54) with equation (4.44), profiles of fuel, oxidant, combustion products, and enthalpy are defined within the boundary layer. Figure 4.14 shows the species concentration profiles in the burning turbulent boundary layer from the experiments of Wooldridge and Muzzy. In Figure 4.15 the experimental results for species concentration are transformed according to equations (4.51) to (4.54) and plotted together with the non-dimensional velocity profile to demonstrate similarity agreement within the mass transfer number range 2.2 to 54. It is thus only necessary to derive the velocity profile equation to completely chacterise the scalar quantity profiles in the boundary layer over a burning fuel film.

4.5 MASS TRANSFER AND MIXING PROCESSES DURING COMBUSTION

The equation defining the evaporation of fuel in the burning boundary layer is identical to that applied in the non-reactive case dealt with earlier in section 4.2.2. Extra terms are included, however, in the expression for B to account for the increase in enthalpy in the bulk

stream due to combustion. Urlaub (20) identifies a phenomenon in wall-wetting engines similar to the second assumption discussed in section 4.1, that initial mixture formation takes place in a vapour layers adjacent to the wall, which persists until the initiation of combustion, when thermal mixing tends to drive the lighter burning zones to the centre of the bowl. So the diffusion of air during the initial stages of mixture formation and also during the early stages of combustion will be of a boundary layer nature similar to that described in the foregoing sections. The onset of thermal mixing on a large scale, coupled with the radial flow of air out of the piston bowl during the expansion stroke, introduce a complex flow field which can only be roughly approximated by the simplified approach adopted in this work. Although equation (1.26) describes the path taken by the burning particles in the centrifugal field as they move towards the centre of rotation, it has a weakness inherent in the assumptions made in its derivation viz:

i. Solid body swirl
ii. Velocity of burning swirl are equal at time t = 0.
iii. Flow resistance opposing radial motion is neglected.

As a result, the path followed by diffusing packets is independent of swirl intensity (i.e. engine speed). It may be necessary at some stage during the development of the flow field from the combustion bowl into the space above the piston to introduce principles of turbulent mixing such as those described in Chapter 2, to account for various complex and not easily characterised phenomena that come into effect. The model in its present form, however, assumes that the entrainment function of Escudier and Nicoll (78), dealt with earlier in this chapter, may be applicable throughout the modelled period. In this way, the discontinuity that results from using several functions, each dealing with a particular period of engine operation, is avoided. By making use of the equivalent Z_E described in equation (4.3), it is possible to cause the entrainment function to respond favourably to engine speed and to give reasonable trends as well as magnitudes. This simplified approach to the process of turbulent mixing may be

justified on the basis that the resulting pressure and temperature diagrams show fairly good agreement with those obtained experimentally. The heat release rate is also fairly reasonable, bearing in mind that this is much more sensitive to mixing processes in the engine. In calculating the heat released in a given crank angle interval, stoichiometric combustion is assumed throughout the cylinder. In regions with a lean mixture, all the fuel is assumed to be burnt,while in rich regions all the air is assumed to take part in combustion. By making use of the entrainment function to determine the mass of air being transported into the "burning region" from the surroundings, and evaporation equations to determine the corresponding fuel vapour mass, the mixture is distributed throughout the zone (in this case, boundary layer) using the profiles specified above. The equivalence ratio profile may be determined from equations giving fuel vapour mass fraction concentration. It may be shown that it has the form shown below:

$$\sigma = \frac{1/FARS}{(\frac{1}{\emptyset} - 1)} \qquad (4.55)$$

where $\emptyset$ is the fuel vapour mass fraction defined earlier in equations (4.32), (4.51) and (4.53). The equivalence ratio at any height above the film surface, is thus defined by equation(4.55), and the heat released in the same interval may thus be calculated. FARS in equation (4.55) is the stoichiometric fuel/air ratio. Figure 4.16 shows the profile for the equivalence ratio. The total heat released in the crank angle interval under consideration, is obtained by numerically integrating the heat release at any position across the thickness of the boundary layer.

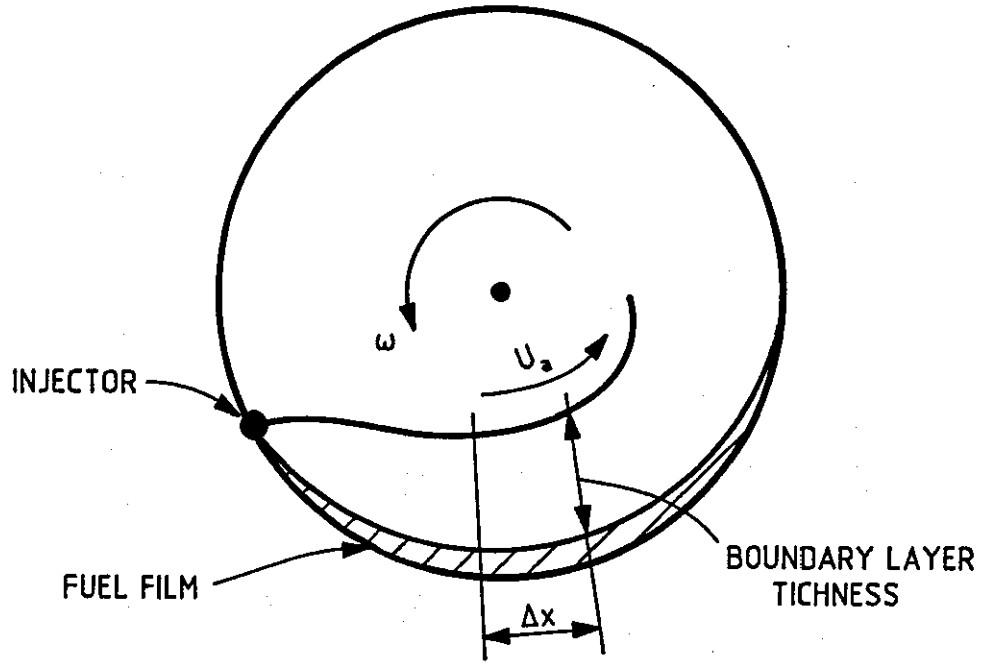

FIGURE 4.1: BOUNDARY LAYER DEVELOPMENT IN THE PISTON BOWL

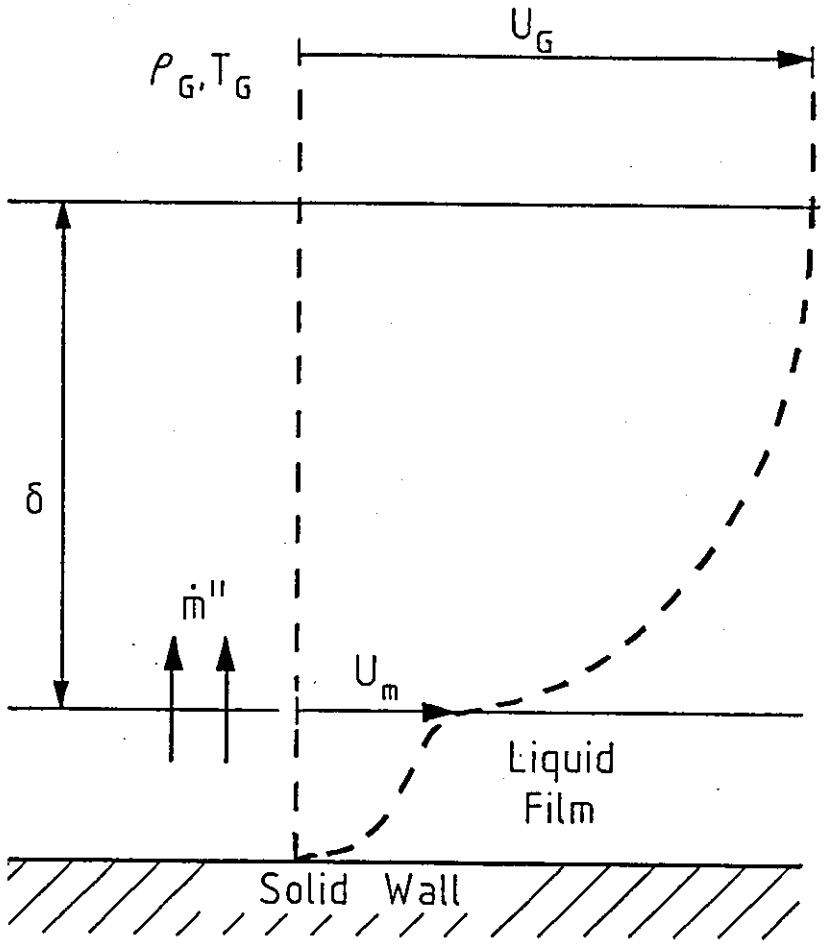

FIGURE 4.2: STRUCTURE OF THE BOUNDARY LAYER

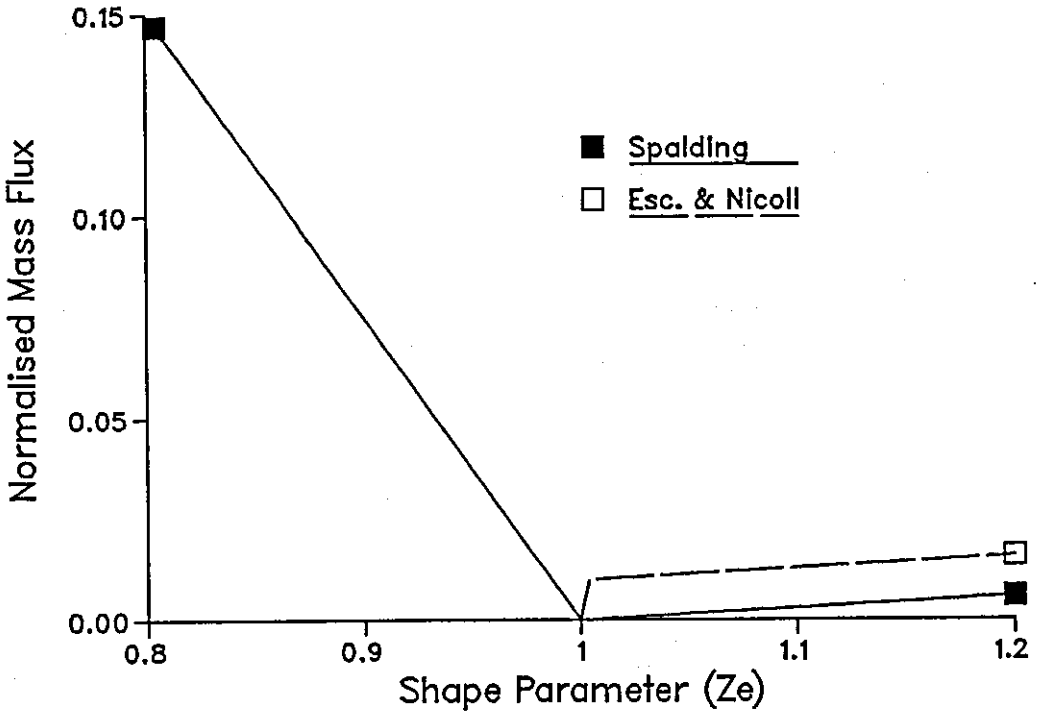

FIGURE 4.3: COMPARISON BETWEEN ENTRAINMENT FUNCTIONS GIVEN BY EQUATIONS (4.33) AND (4.34)

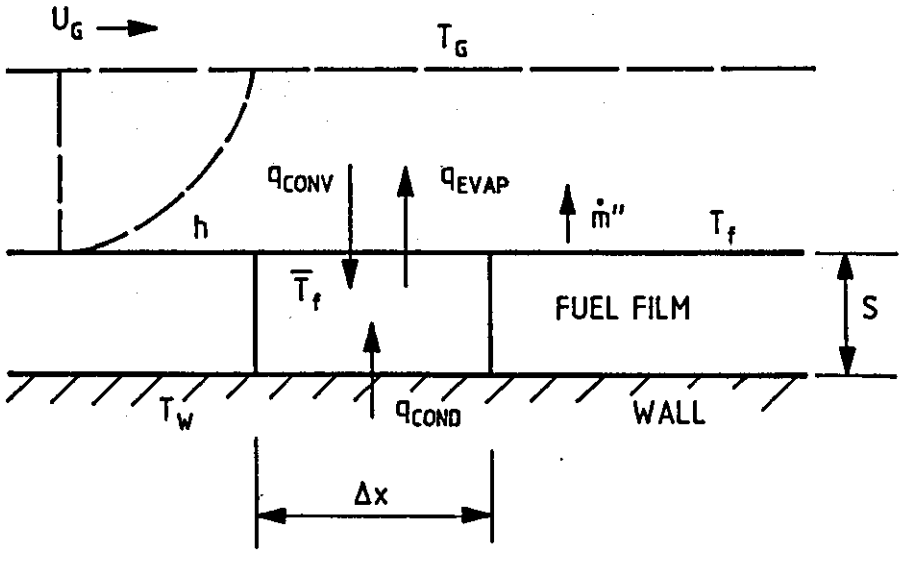

FIGURE 4.4: HEAT BALANCE ON THE LIQUID FILM ELEMENT

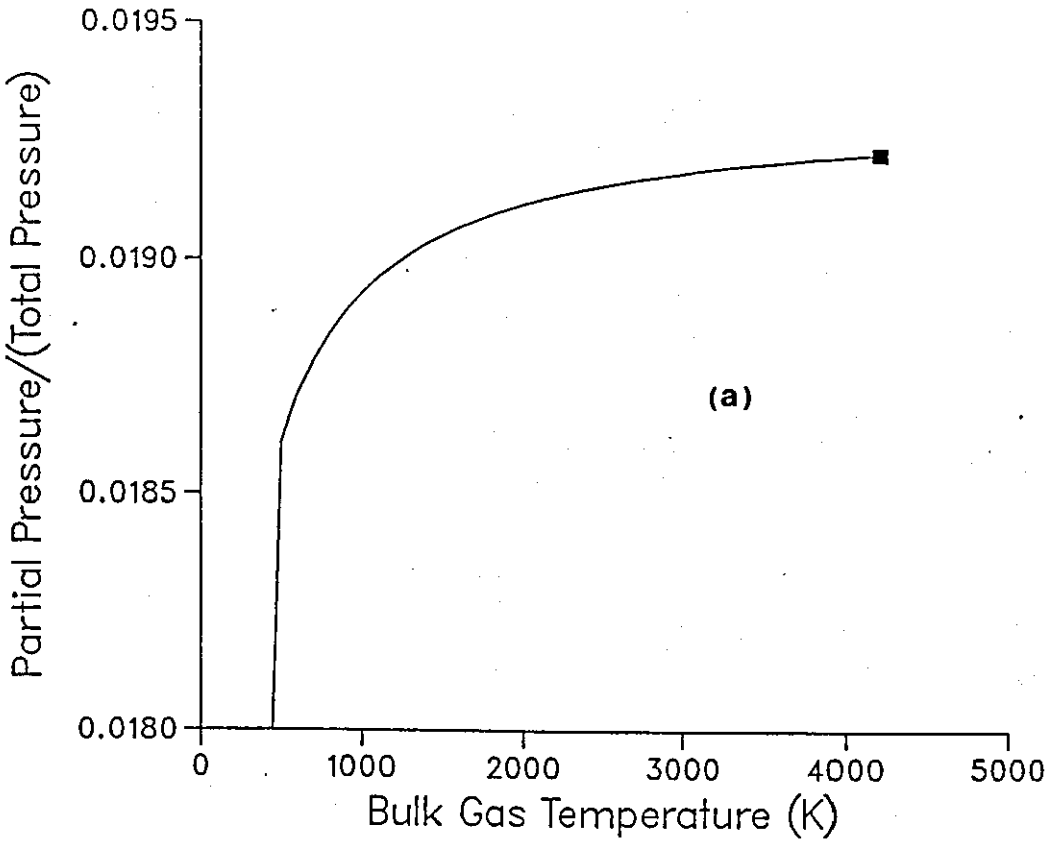

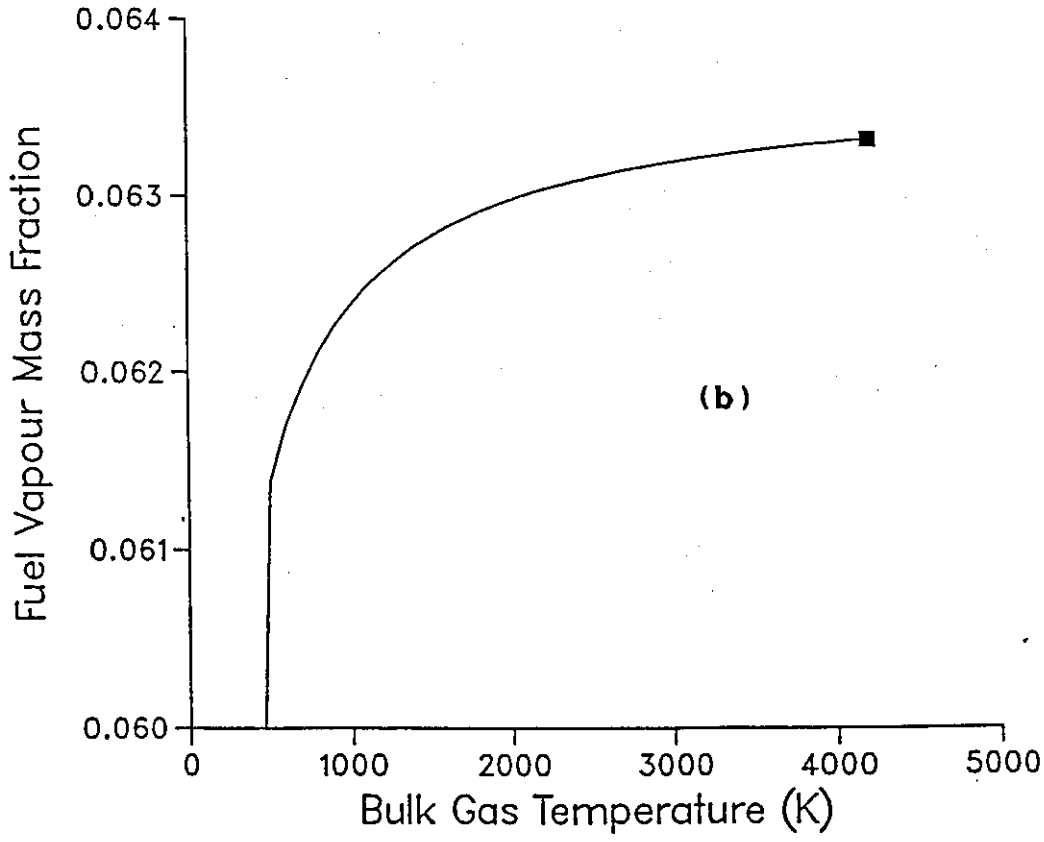

FIGURE 4.5: VAPOUR FRACTION AT THE SURFACE OF THE FUEL FILM

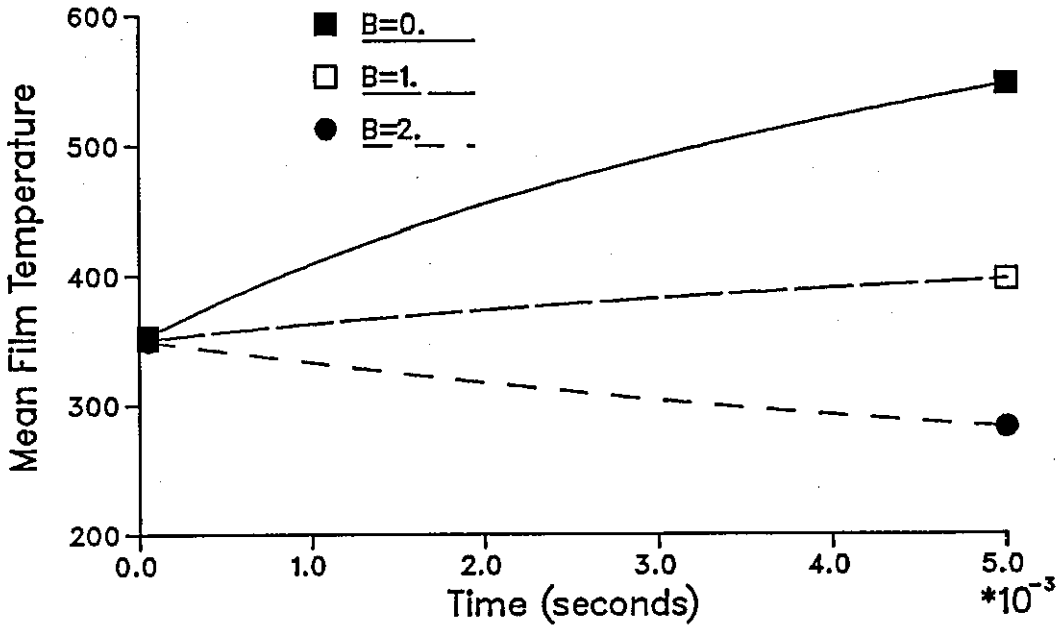

FIGURE 4.6: EFFECT OF EVAPORATION ON MEAN FILM TEMPERATURE

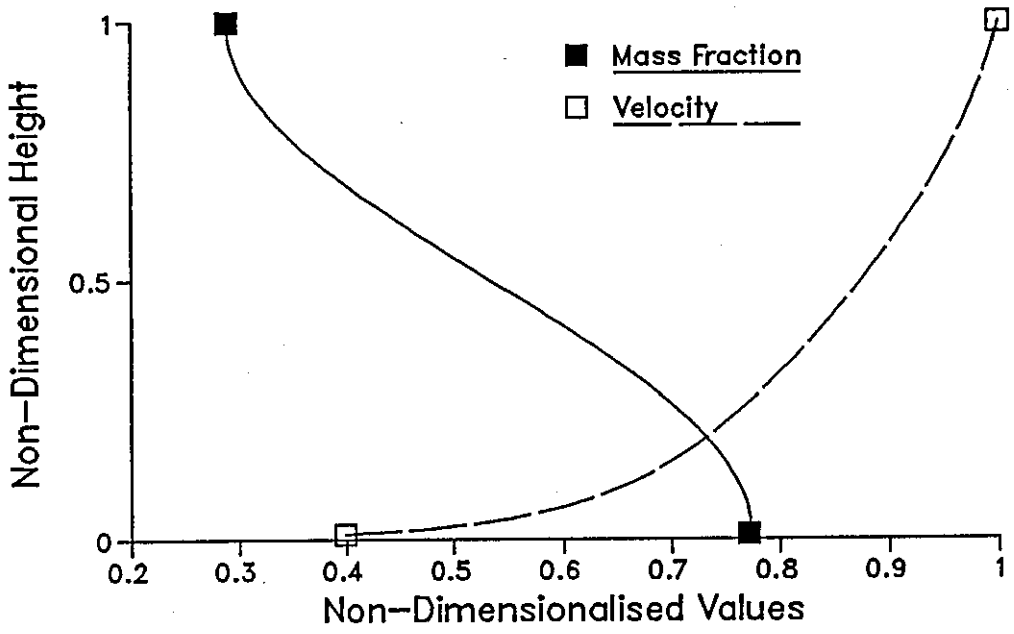

FIGURE 4.7: VELOCITY AND FUEL CONCENTRATION PROFILES IN THE GASEOUS BOUNDARY LAYER

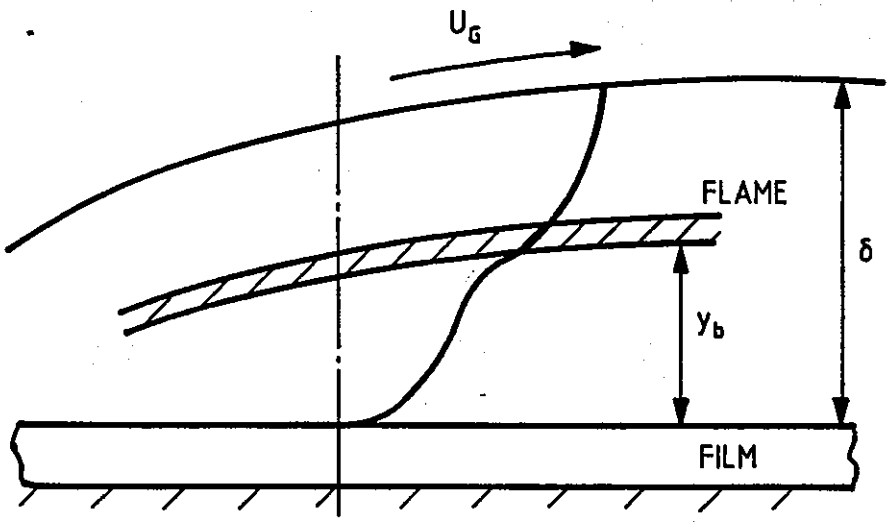

FIGURE 4.8: BOUNDARY LAYER STRUCTURE WITH COMBUSTION

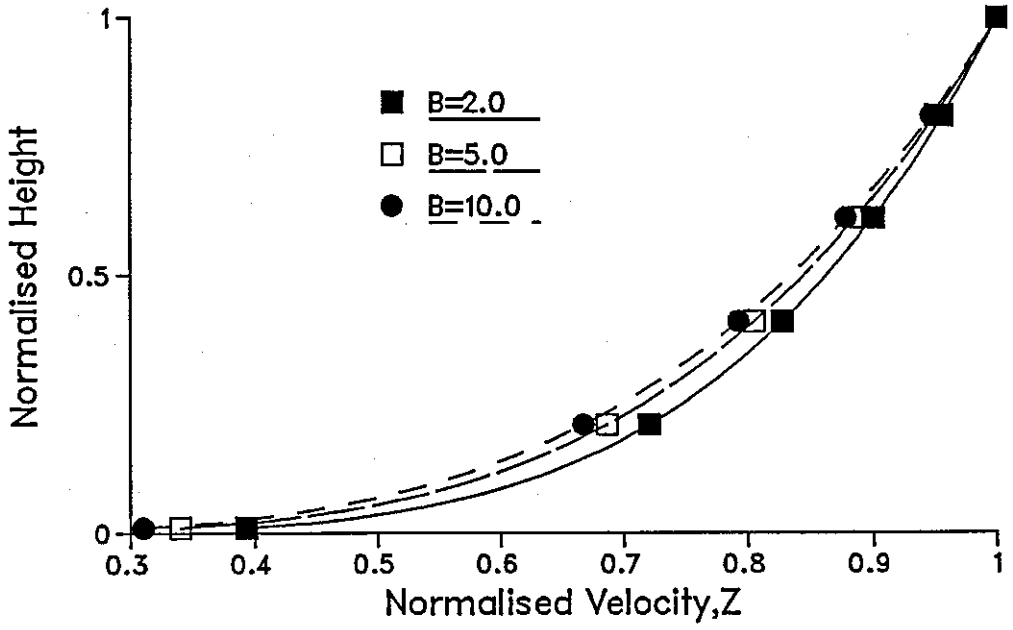

FIGURE 4.9: INFLUENCE OF MASS TRANSFER ON BOUNDARY LAYER VELOCITY PROFILE

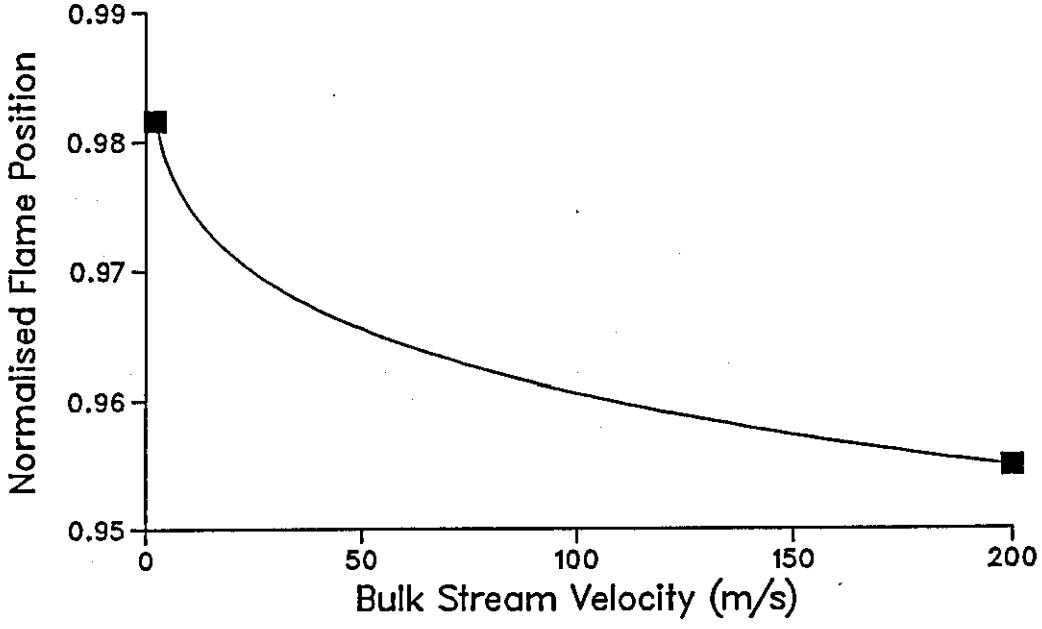

FIGURE 4.10: INFLUENCE OF BULK STREAM VELOCITY ON THE POSITION OF THE FLAME IN THE BOUNDARY LAYER

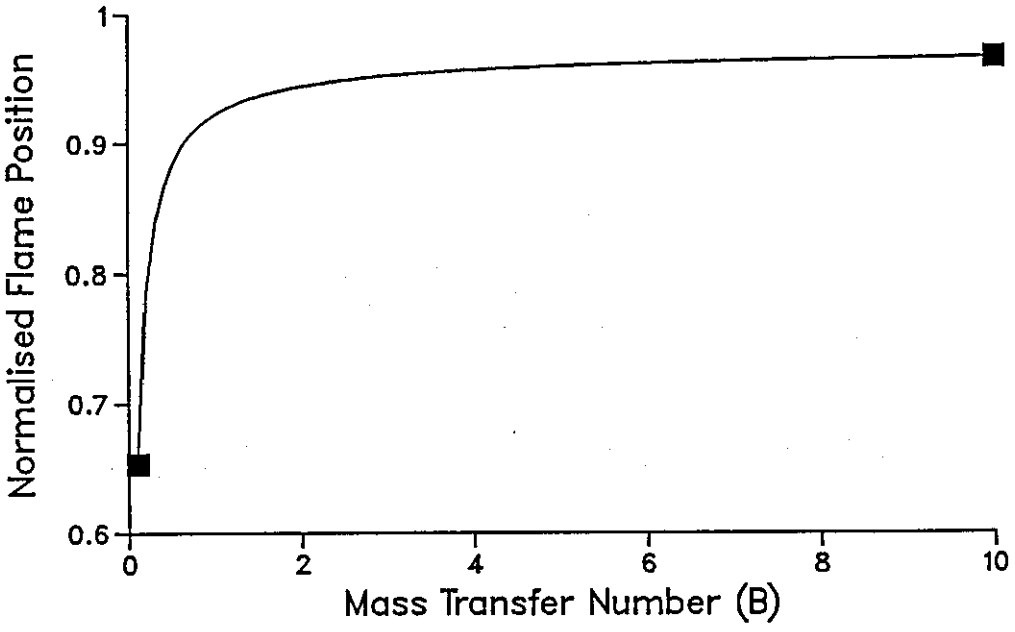

FIGURE 4.11: INFLUENCE OF MASS TRANSFER ON THE POSITION OF THE FLAME IN THE BOUNDARY LAYER

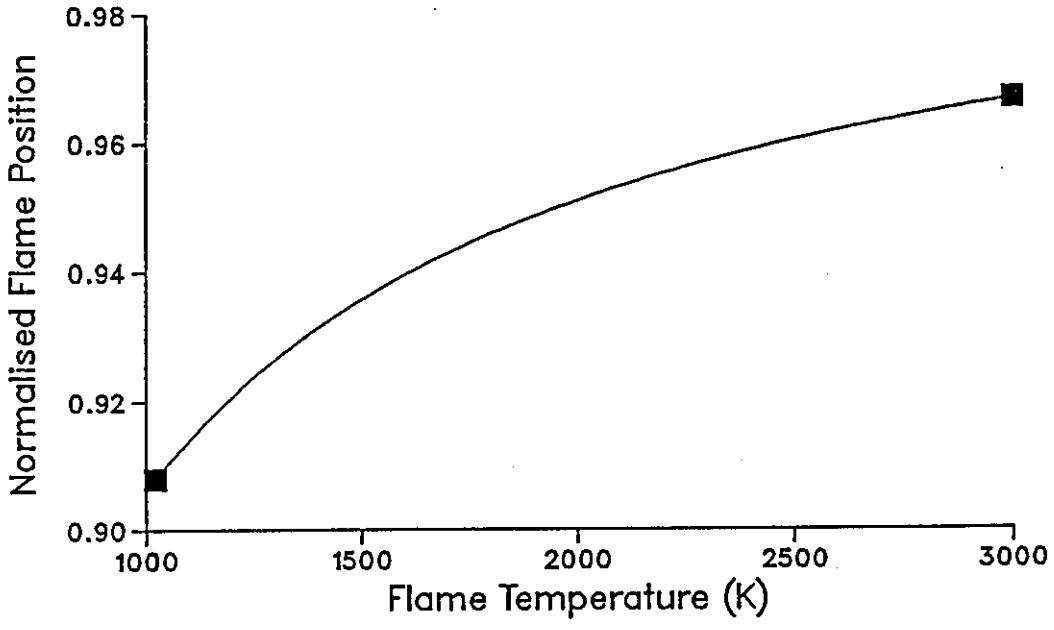

FIGURE 4.12: EFFECT OF FLAME TEMPERATURE ON THE POSITION OF THE FLAME IN THE BOUNDARY LAYER

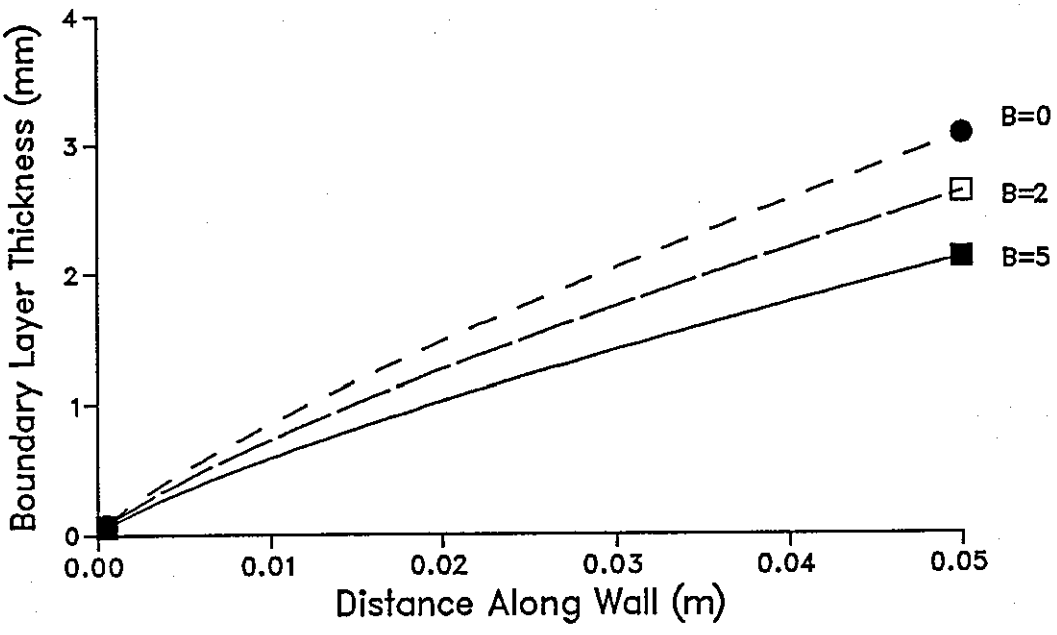

FIGURE 4.13: INFLUENCE OF MASS TRANSFER ON BOUNDARY LAYER THICKNESS

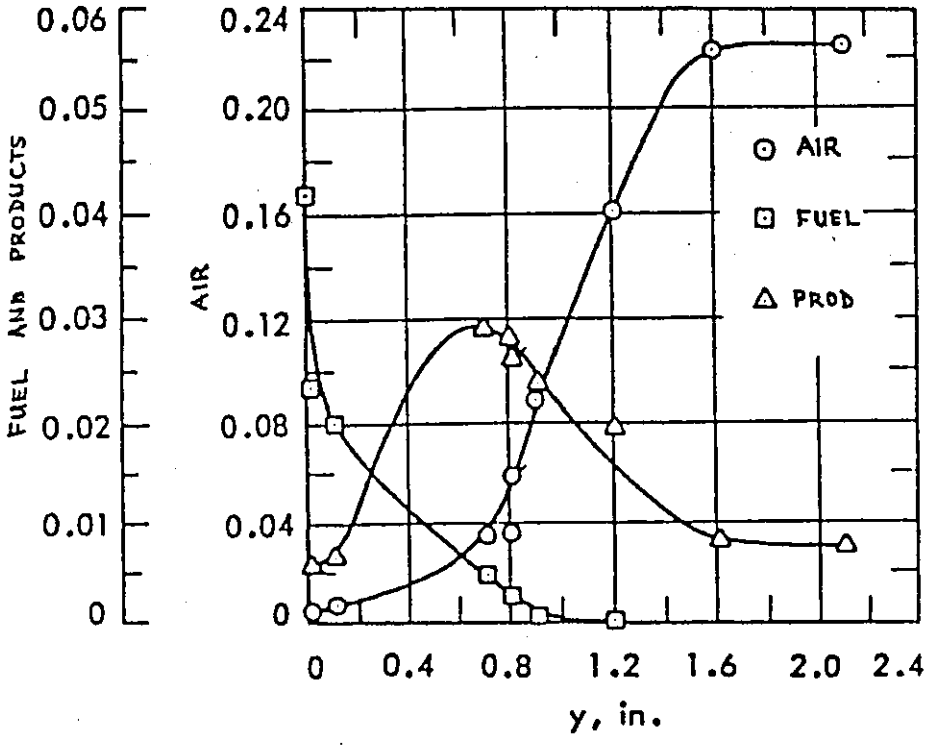

FIGURE 4.14: MEASURED SPECIES CONCENTRATION PROFILES IN THE BURNING TURBULENT BOUNDARY LAYER (108)

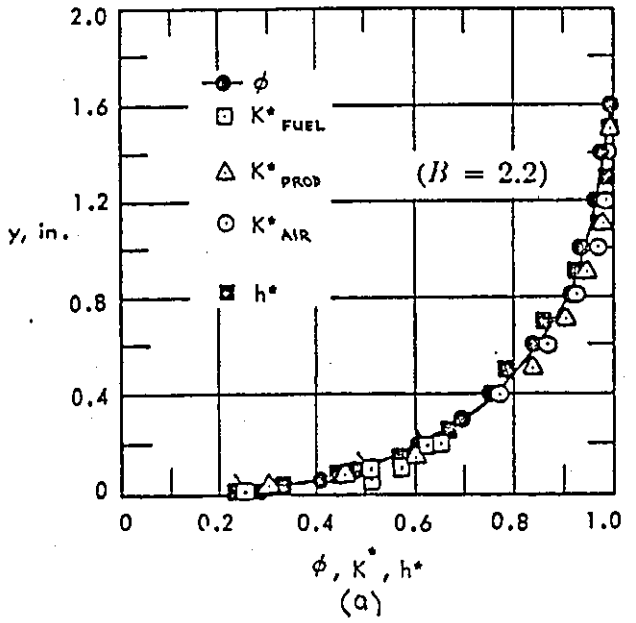

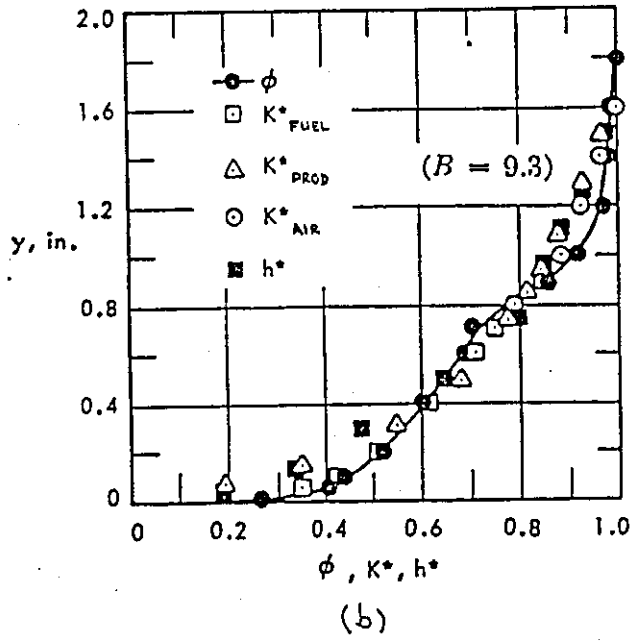

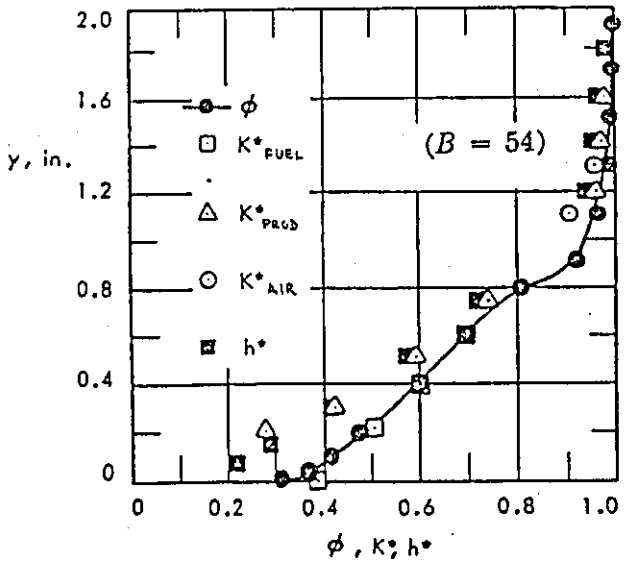

FIGURE 4.15: COMPARISON OF NORMALISED VELOCITY, ENTHALPY AND SPECIES CONCENTRATION PROFILES (108)

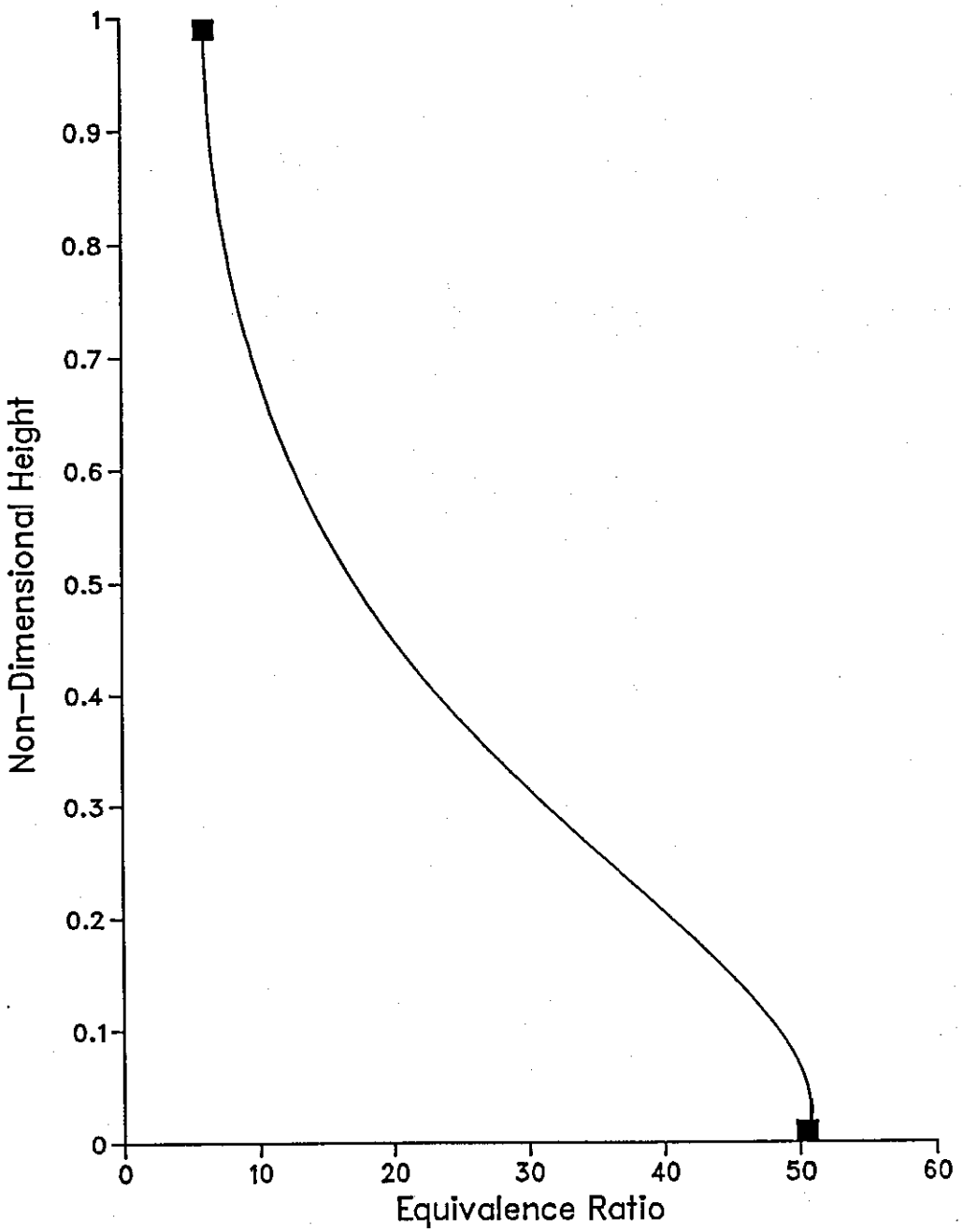

Figure 4.16: Equivalence Ratio Profile in the Boundary Layer

CHAPTER 5

EXPERIMENTAL TECHNIQUES

Several assumptions have been made in developing the proposed model in order to simplify the method of analysis, and also to approximate the results to observed phenomena in identical flow situations. Justification for some of the assumptions can be made on the basis of published experimental data, and this has been done wherever possible. However, as the method of representing mixture formation processes adopted in this work is not generally encountered in the literature, it has been inevitable to make certain assumptions for which experimental validation has become necessary. This is especially the case in the choice of equations governing flow development of the liquid film on the walls of the combustion chamber, and the general applicability of boundary layer theory to the description of velocity and scalar quantity profiles in wall-wetting diesel engines. Several sets of experiments were thus designed to provide data necessary for validating some of these assumptions. The experiments were designed to yield data on the penetration of the film along the piston wall, the thickness of the fuel film and its temporal and spatial variation, wetted surface area, and, in an indirect way, the mean velocity of the film. Limited results were also obtained on validating the assumption that evaporated fuel forms a vapour layer close to the wall, diffusing slowly into the air stream.

5.1 DESCRIPTION OF EXPERIMENTAL RIG

All the experiments were performed in a 'Perspex' simulation rig into which a transient liquid fuel jet was injected, forming a thin film on the vertical sides of the rig. A steady-state airstream, maintained at a pre-determined level, was used to simulate a given engine swirl condition. Salient details of the simulation rig may be found in reference (24). To create the desired velocity profile in the air

stream a deflection vane (Figure 5.1) located in the inlet section of the rig was employed. The design of the vane was experimentally optimised by Morris (24) so that the diffusion of momentum tending to alter the velocity profile was negligible across the test section (covering a sector of 150^{o}). A 10 mm diameter orifice placed in the supply line (Figure 5.2), was used to meter the air flow rate. The pressure drop across the orifice was recorded with a differential water manometer.

To simulate the injection process, a solenoid operated spark ignition engine fuel injector operating at a line pressure of 2.1 bar was used. The injector was operated by means of an electronic injection unit which supplied a single pulse at 12 volts to the solenoid when working in the 'manual' mode. The duration of the pulse was varied by means of a 'decade' potentiometer (Figure 5.3) to correspond, by dynamic similitude, with the injection duration in the engine. The injection unit could also provide continuous operation by connecting to a pulse generator. In this mode, it was possible to obtain 'quasi-steady' pictures of the film by using the same signal from the pulse generator to trigger a stroboscope. Examples of this method of operation are discussed in detail at a later stage when outlining the Photographic Technique (section 5.3.1). The fuel supply system used in the experiments was built around the 'Bosch' type 'A' injection pump. The pump feeds fuel in a loop circuit illustrated in Figure 5.4 to the injector, by maintaining the fuel line pressure at 2.1 bar. Excess fuel returns to the fuel tank via a relief valve as indicated in Figure 5.4. Figure 5.5 provides calibration results of the potentiometer readings against injector characteristics. In Figure 5.5(a), the readings of the potentiometer are plotted against the electrical pulse width as measured with an oscilloscope, while in Figure 5.5(b), the same 'decade' readings are plotted against the corresponding mechanical injection duration from the signal obtained by a pressure transducer placed in the fuel line. In Fig. 5.5(c) 'decade' readings have been plotted against the quantity of fuel injected, based on a mean of ten injections at each setting. The results in Fig. 5.5(c) have been useful in estimating the jet velocity

at the outlet of the modified nozzle.

In order to achieve tangential wall impingement of the jet, the injector nozzle was modified by placing a brass cap with a side hole over the injector (Fig. 5.6). The brass cap was then screwed onto the periphery of the test region so that the fuel outlet was flush with the wall, and film development commenced within the effective test zone.

5.2 BASIS FOR SIMILARITY BETWEEN THE RIG AND THE ENGINE

In their work on the dispersion of a diesel fuel spray, Morris and Dent (23) identified three major criteria for achieving dynamic similitude between the fuel jet in the engine and that in the rig. These are outlined, briefly, below.

i. The mass flux ratio between the air stream and the jet must be identical in the engine and the rig. Equation (5.1) shows the mathematical expression of the criterion.

$$\frac{\rho_f \, d_o^2 \, U_o}{\rho_G \, d_G^2 \, U_G} = \text{constant} \qquad (5.1)$$

ii. The ratio of momentum flux between the air stream and the jet must be identical:

$$\frac{\rho_f \, d_o^2 \, U_o^2}{\rho_G \, d_G^2 \, U_G^2} = \text{constant} \qquad (5.2)$$

iii. The ratio of the Reynolds number of the gas stream, to that of the jet must be identical:

$$\frac{\left(\frac{U_o\, d_o}{\nu_f}\right)}{\left(\frac{U_G\, d_G}{\nu_G}\right)} = \text{constant} \qquad (5.3)$$

which may be expressed in the following, slightly more convenient form:

$$\frac{U_o\, d_o\, \nu_G}{U_G\, d_G\, \nu_f} = \text{constant} \qquad (5.4)$$

Also included with these criteria were conditions for geometric similarity between the piston bowl and the test section of the rig, and the time criterion. Geometric similarity, stated simply, requires that corresponding lengths between the engine and the model are in constant ratio to each other. Giving this ratio as λ, then the following is the mathematical expression:

$$\frac{d_{GR}}{d_{GE}} = \lambda = \text{constant} \qquad (5.5)$$

The time durations can be scaled, according to Morris and Dent, by the following expression:

$$\frac{t_R}{t_E} = \lambda \cdot \left(\frac{U_{oE}}{U_{oR}}\right) \qquad (5.6)$$

where subscripts E and R refer to conditions in the engine and the rig respectively.

When considering similarity in thin liquid films flowing on solid surfaces, additional criteria need to be satisfied. These may be derived from momentum considerations such as has been demonstrated in

Appendix D, so that a non-dimensionalised momentum conservation equation is derived (96).

$$\text{Non-Dimensionalised Momentum Flux} = \frac{1}{R_e} + \frac{1}{F_r} + \frac{1}{W_e} + \frac{1}{C_f} \qquad (5.7)$$

where R_e, F_r, and W_e are the Reynolds, Froude, and Weber numbers, respectively, and C_f the friction coefficient. The significance of Froude and Weber numbers in this type of flow may also be deduced from the work of Fulford (94) which was highlighted in Section 3.2 above. Since the order of magnitude of each term on the right hand side of equation (5.7) denotes the importance of the associated dimensionless number in the similiarity analysis, it is essential to make an approximation, based on data obtained in engine operation, of typical values. The following values, based on the experiments of Müller (41) and Klanner (42) were assumed:

$$\frac{1}{R_e} = 1 \times 10^{-2}, \quad \frac{1}{F_r} = 8 \times 10^{-4}, \quad \frac{1}{W_e} = 8 \times 10^{-2}$$

These values suggest that Froude number may be neglected from any similarity analyses without much loss in accuracy. Although the relative magnitude of W_e and R_e indicates that Weber number is significant in the similarity calculations, it has been pointed out in Chapter 3, after Fulford (94), that Weber numbers in excess of unity, as is the case here, imply that surface effects are infact negligible. So the Reynolds number criterion in equation (5.4) is sufficient to characterise the nature of viscous forces acting on the film since at high flow rates, the friction coefficient C_f is also a function of the Reynolds number.

5.2.1 Deriviation of the Similarity Equation

From the criteria given in equations (5.1) to (5.4), conditions in the rig corresponding to any given set of engine conditions, may be

derived. Combining equations (5.1) and (5.2) results in the simple expression that the ratio of the gas stream to that of the jet at the nozzle exit should be identical:

$$\frac{U_o}{U_G} = \text{constant} \tag{5.8}$$

By substituting equation (5.8) into either equation (5.1) or (5.2) the following expression is obtained:

$$\frac{d_o}{d_G} \cdot \left(\frac{\rho_f}{\rho_G}\right)^{1/2} = \text{constant} \tag{5.9}$$

From which the diameter of the injector nozzle in the rig may be given by:

$$d_{oR} = \left[\frac{\rho_f}{\rho_G}\right]_E^{1/2} \cdot \left[\frac{\rho_G}{\rho_f}\right]_R^{1/2} \cdot \lambda \cdot d_{oE} \tag{5.10}$$

Injection velocity in the rig may be determined by re-arranging equation (5.8) as follows:

$$U_{oR} = \left[\frac{U_o}{U_G}\right]_E \cdot U_{GR} \tag{5.11}$$

From equation (5.6), corresponding time durations in the rig, t_R, may be calculated. To complete the dynamic similitude, it is essential to satisfy the Reynolds number criterion defined in equation (5.4), which may be re-arranged to give:

$$\frac{d_{oE}}{d_{oR}} \cdot \lambda = \left[\frac{\nu_G}{\nu_f}\right]_R \cdot \left[\frac{\nu_f}{\nu_G}\right]_E \tag{5.12}$$

Combining equations (5.10) and (5.12) yields an equation for the injector nozzle diameter in the rig:

$$d_{oR} = \lambda \cdot d_{oE} \cdot \left[\frac{\mu_f}{\mu_G}\right]_E \cdot \left[\frac{\mu_G}{\mu_f}\right]_R \qquad (5.13)$$

5.2.2 Solution Methodology

Equations (5.6), (5.11), and (5.13) constitute the governing set of equations for achieving similarity. By specifying the nozzle diameter in the rig, d_{oR}, and since engine conditions are known at each condition to be modelled, then equation (5.13) has only two unknowns - the geometric linear scale, λ , and the properties of the working fluids (fuel and bulk stream) as represented by their respective viscosities. By specifying working fluids consistent with convenient operation and laboratory safety (kerosene and air operating at ambient conditions were chosen in this case) the equation for the linear scale is given by :

$$\lambda = C_\alpha = \frac{d_{oR}}{\left[\frac{\mu_f}{\mu_G}\right]_E \cdot \left[\frac{\mu_G}{\mu_f}\right]_R \cdot d_{oE}} \qquad (5.14)$$

Substituting equation (5.14) into eqn. (5.6) yields:

$$t_R = \frac{C_\beta}{U_{oR}} \qquad (5.15)$$

where the constant $C_\beta = C_\alpha \cdot t_E \cdot U_{oE}$.

Once d_{oR} is fixed, then U_o will depend on the choice of the injection system, and so will be constant for a given injector and pump, so that t_R will also be a constant. It is thus possible to define swirl in

the rig, U_{GR}, as a function of only the swirl in the engine, U_{GE}, given by equation (5.11) - assuming U_{OE} to be constant (ie. injection nozzle velocity in the engine). Injection duration in the rig, defined by equation (5.6) will also be dependent only on the corresponding injection duration in the engine. Table 5.1 shows typical results, obtained for one operating condition in the engine.

5.3 DESCRIPTION OF EXPERIMENTAL METHODS

The experimental results may be divided into two major categories; those based on experiments performed by the author, and those based on similar experimental work, extracted from the literature. The experiments undertaken by the author were aimed at providing essential details about the development of the film, especially the penetration, velocity, wetted surface area, and the thickness and its subsequent evaporation into the bulk gas stream. Three optical methods were employed to obtain these results:

- 'Strobe-flash' photographic technique
- Laser-excited fluorescence technique.
- Schlieren technique.

The following discussion outlines in detail the procedure involved in each of the three methods.

5.3.1 Photographic Technique

In this method, a sequence of photographs were taken of the liquid film at different times from the start of injection during separate injections, to give a sequential development of the film along the wall. The arrangement of the instrumentation is illustrated in Fig. 5.7, showing the essential equipment used. The injector nozzle is operated by introducing an electrical pulse of known duration to the solenoid. As the nozzle opens, the fuel-line pressure, which is otherwise maintained at a constant value, experiences a sudden sharp

drop. This is sensed by a pressure transducer placed in the fuel-line, which sends a signal, through an electronic delay circuit, to trigger the stroboscope to deliver a single flash of light. The camera, which is operated in 'open-shutter' mode, records the position of the film as the flash comes on. The delay in time between the opening of the injector nozzle, and the introduction of the strobe-light flash gives the time taken by the film to travel the length shown on a corresponding photograph. This was used to obtain the development of the film at different times from the start of injection, covering the time duration corresponding to the calculated injection duration. Typical results are illustrated in Fig. 5.8, showing the development of the film from 3 to 10 ms after injection, at 1 ms intervals. To obtain reasonably repeatable results for penetration and velocity, such as those given in Figs. 5.9 and 5.10 several results were taken at each delay setting and the results averaged.

5.3.2 Laser-excited Flourescence Technique

Collier and Hewitt (115) have reviewed various techniques of measuring the thickness of thin liquid films, and have grouped them into three major categories:

i. Average Methods:- These are based on measuring average thickness over a length of film. A typical example is the film conductance method (as opposed to the conductivity probe technique) where the electrical conductance of a length of film is related to the mean film thickness.

ii. Localised Methods:- Conductivity probe and capacitance measurements fall under this category, which encompasses techniques in which film thickness is reasonably localised, but not as highly resolved as in point methods.

iii. Point Methods:- Methods which provide continuous measurements at a given point are included in this category. Most optical techniques, such as light absorption method, and the fluourescent technique are typical examples.

The conductivity and capacitance probe techniques have been successfully applied under engine conditions (41, 42) and their respective merits and demerits are fairly well known. The conductivity probe technique, when applied to measuring hydrocarbon film thickness, requires the use of fuel additives to make the film conduct. These have side-effects, such as the increase in concentration due to evaporation which affects conductivity, and the effect of film temperature on its conductivity. Both these effects must be accounted for if accurate measurements are to be made. The capacitive probe technique, on the other hand, does not require additives and may thus be used with any hydrocarbon fuel. Its limitations relate to the measurements of film thickness during combustion when it has been found that flame reagents and carbon significantly affect the accuracy of the measurements (41). Both techniques have the added disadvantage that the process of implanting probes in the cylinder is time consuming and rather involved. Although the two techniques have the overiding advantage that they may be applied in making measurements in the engine, it is favourable to use non-intrusive optical techniques to make measurements in an optically accessible simulation test rig, as this is relatively easier to set up, and capable of providing detailed results about the film.

The laser-excited flourescent techniqe is an optical method based on a similar method used by Hewitt et al (116) to measure film thickness and surface waves in two-phase flow. The principle is to irradiate a spot on the film of fuel, in which a fluorescent dye is dissolved, with monochromatic light. This excites flourescence in the film, emitting light of a different wavelength. It is essential that the dye must absorb at the wavelengths present in the irradiating source, and efficiently convert the radiation into flourescent radiation which should, preferably be in the visible spectrum. An additional

requirement relating specifically to engine applications, is that the dye must have very short induction and decay times in order to respond to the rapid fluctuations corresponding to surface waves on the film. 'Rubrene' (tetraphenylnaphthacene) exhibits all of the above requirements (117), and is also soluble in most hydrocarbon fuels. This influenced its choice in the present work. An Argon-ion laser, emitting in the blue waveband (λ = 460 nm), was used as the monochromatic light source to irradiate a Rubrene-Kerosene solution liquid film. A peak emission was observed with this system in the yellow waveband (λ = 555.2 nm) as illustrated in Fig. 5.11. The intensity of light emitted by the film is proportional to its thickness. Some of the emitted light is collected and filtered to remove the reflected and scattered components of the incident beam, and a photomultiplier tube (PMT) used to record the signal. A schematic of the experimental set-up used is illustrated in Fig. 5.12.

5.3.3 Calibration of the Fluorescent Technique

It is necessary, when calibrating the instruments, to reproduce, as closely as possible the exact geometry of the optical system so that effects such as self absorption are identical between the calibration rig and the actual system. The basic principle used was to trap a thin film of dyed fuel between two 6 mm thick 'Perspex' plates separated by thin metal shims of known thickness. A 1 cm diameter hole in the shims was used to create a thin cavity between the 'Perspex' plates when they were cemented together. Fig. 5.13 shows the calibration cell, cemented on three sides only. A range of cells covering thicknesses from 0.025 - 0.8 mm were used in the calibration. A hypodermic needle and syringe were used to inject fuel into the thin cavity, through a hole drilled through one of the plates. The calibration was carried out by placing the cell in the position showing the rig in Fig. 5.12, and focussing the laser beam at the film. The resulting calibration curve is shown in Fig. 5.14.

5.3.4 Schlieren Optical System

To investigate evaporation effects in the 'Perspex' rig, it was necessary to inject a fuel with a high volatility, in order to maintain the air stream at a temperature consistent with safe operation. Iso-Pentane ($C_5 H_{12}$), with a boiling point temperature of 27.85°C, was chosen for this purpose.

A schematic diagram of the optics mounted to obtain high speed photographs of the fuel/air layer above the film surface, is shown in Figure 5.15. The basic principle of operation is that a collimated beam enters the simulation rig, passing through the test section, onto a mirror positioned at 45° to the beam. This reflects the beam into a focussing lens to bring it to a sharp point focus. A knife edge inserted in the focal plane of the focussing lens is adjusted until the image formed on a transluscent viewing screen darkens as uniformly as possible. The edge of the knife-edge must be set perpendicular to the direction in which density gradients are to be observed (118).

The optical arrangement described above was used to acquire high-speed Schlieren photographs of the fuel as it evaporates from the surface of the film, at a rate of 750 frames per second. Three conditions were investigated representing three engine speeds: 1000, 1500, and 2000 rpm. To satisfy conditions of dynamic similitude between the engine and the experimental rig, the mass transfer number, B, was used as the similarity parameter (114).

Mass Transfer Number Calculations:

A typical value of B at TDC, in a motoring wall-wetting diesel engine can be approximated from the right hand side of equation (4.37) which can be re-written as follows:

$$B = \frac{C_{pG}(T_G - T_f)}{h_{fg} + C_{pf}(T_f - T_{ref})} \qquad (5.16)$$

The following values, after the work of Martin and Ahmad (31), are used in the calculations:

$$T_{BP} = 533K$$
$$T_{amb} = 300K$$
$$T_G = 800K$$
$$C_{pG} = 1.1 \text{ kJ/kg.K at } T_G$$

Specific heat capacity of the fuel, C_{pf}, and the heat of vaporisation, h_{fg}, at ambient pressure, are calculated from the following two equations from reference (119):

$$C_{pf} = \frac{1.6848 + 0.00339T}{(\rho_{15.6^oC})^{1/2}} \quad kJ/kg.K \qquad (5.17)$$

$$h_{fg} = \frac{251.3 - 0.377T}{(\rho_{15.6^oC})^{1/2}} \quad kJ/kg \qquad (5.18)$$

where $\rho_{15.6^oC}$ is the density of the fuel (petroleum) in g/cm^3 at 15.6^oC. For diesel this is 0.84 g/cm^3. Once B_E (the value of B in the engine) has been calculated, equation (4.38) is iterated under conditions pertaining in the simulation rig to obtain the required bulk air temperature. The iteration scheme proceeds on two fronts: A value of T_G is chosen, then an iteration for B is undertaken. T_G is progressively increased until B_R (the calculated value of B in the rig) equals B_E. The Antoine Constants for Iso-Pentane, necessary to carry out the iteration are as follows, after reference (112):

$$a = 6.85221$$
$$b = 1064.63$$
$$c = -41.0 \text{ (Temperature in Kelvin)}$$

A temperature of 35^oC was arrived at for the intake air temperature.

5.3.5 The Experimental Work of Müller (Ref. 41)

To evaluate the accuracy of equations developed in Chapter 3 under conditions that pertain in the engine, the results obtained by Müller (41) were used to compare with those predicted.

Müller measured film thickness in a single cylinder AVL experimental engine with the following dimensions:

- Stroke 125 mm
- Bore 120 mm
- Connecting rod 195 mm
- Compression ratio 16.5
- Injector nozzle dia. 0.75 mm with an opening pressure of 175 bar

Three pistons with a spherical bowl, were each implanted with conductivity probes to measure film thickness (Fig. 5.16). The distribution of probes in each of the pistons was designed to cover as much surface area as was practical, and consistent with the limitations of carrying probes on the piston. The three designs chosen are illustrated on a planar representation in Fig. 5.17. Each probe had a diameter of 0.75 mm, and by arranging the circuitry so that the piston body constituted one electrode, each probe represented a measurement of film thickness over a length equivalent to the thickness of the ceramic insulation (Fig. 5.18). In Müller's experiments this was of the order of 0.25 mm. Precise analytical details, and calibration of the technique may be found in reference (41). To meet the requirements for a conducting fuel, Müller dispensed with the need for adding electrolytes to the fuel by using Diethylene Glycol ($C_6H_{14}O_3$) whose physical properties are tabulated, together with those of Diesel, in Table 5.2. This constituted the baseline fuel against which other fuels were compared. Other baseline conditions were as follows:

Engine speed	1500 rpm
Injection timing	22°BTDC
i.m.e.p.	3.75 bar (with combustion)
Injection duration	15°CA

Müller, in effect, studied the fuel film with respect to three major parameters: its thickness, development of the wetted surface, and the rate of evaporation. Parametric studies were carried out experimentally, with the following as the independent variables:

a) Fuel type
b) Engine load
c) Excess air coefficient
d) Engine speed
e) Injection timing
f) Swirl intensity
g) Temperature of the piston wall.

Detailed results are presented in graphical form in reference (41), and, for brevity, only the most pertinent features of Müller's work have been reproduced and compared with predicted results from the model. A limited study of the effects of combustion on film development was also undertaken and the results have been used to validate the model.

5.4 EXPERIMENTAL RESULTS

The values of all the quantities investigated in the experiments described in Section 5.3 are given in graphical form at the end of this chapter. The following discussion outlines the conditions under which these results were obtained and attempts to draw conclusions on the expected behaviour of the model, based on experimental findings. The baseline engine conditions chosen for the modelling work were the same as those of Müller (41). Also the dimensions for the rig were calculated on the basis of the engine used by Müller, given in the

previous section.

5.4.1 'Strobe-Flash' Photographic Results

Typical photographic records of the development of the film on the wall are shown in Fig. 5.8. The figure shows the penetration and wetted area of a Kerosene film from 3 to 10 ms after the start of injection. The air velocity in that instance was maintained at 4.6 m/s corresponding to an air swirl of 42 m/s in the engine, at 1500 rpm. The effect of air swirl velocity on the characteristics of the fuel film was a major aspect of this investigation, and hence measurement of penetration and surface area development were taken over a wide range of swirl velocities corresponding to various engine operating conditions. Figure 5.19 shows velocity profiles obtained within the test section of the rig at the positions indicated in Figure 5.1 by the letters A, B, and C. The profiles at any longitudinal (ie. along the wall) position are shown to exhibit similarity by normalising them suitably as illustrated in Fig. 5.20. The measured profiles show a slight change as the probe is traversed through the test section showing that there was some amount of momentum diffusion. Table 5.3 presents simulation rig swirl characteristics with corresponding values in the engine.

A close examination of the results obtained in the simulation rig at different swirl velocities shows that the influence of swirl velocity on the penetration of the film along the wall is not very high. This is probably due to the fact that the component of the relative velocity between the air stream and the surface of the film is small when compared to the injected component, especially for very thin liquid films. The departure between predicted and experimental results in Figure 5.21 may be attributed to the assumption that the flow of the film along the wall can be approximated by the wall-jet equation. If surface roughness is not adequately accounted for by the Reynolds number criterion, then this also contributes to the departure. A further reason for the departure, which is discussed

further in the next section, is the presence of waves on the surface of the fuel film which reduces the effective penetration.

From the shape of the film on the photographs it was possible to obtain approximate values for the wetted surface area and the nature of spread of the film. This has been done for some of the pictures in the sequence illustrated in Figure 5.8 and the results are compared with predicted values in Figure 5.22. Since the angle of spread of the fuel film was fixed at 26^{o}, the higher predicted film penetration also implies a higher predicted wetted area of the film. If the model over estimates the surface area, this would lead to a higher evaporation rate which, in turn, results in a higher rate of heat release, unless the corresponding air entrainment rate is low.

5.4.2 Fluorescence Technique

This technique was used to measure film thickness and penetration of the film along the piston wall. The laser beam was focussed at several points positioned 5 mm apart along the central axis of the film starting 5 mm from the nozzle. A set of signals such as illustrated in Fig. 5.23 are obtained for the whole wetted length of the film. The signal trace carries a significant amount of information about the film, of which only the film thickness and the penetration were extracted. The film thickness is given by the level of the signal while the penetration is represented by the time taken by the film to travel from the nozzle to the point under consideration. The film was probed at ten positions (0.5 to 5 cm downstream of the nozzle) for each of the engine speeds covered (1000 - 3000 rpm).

Data Reduction and Analysis

The film thickness in the model is calculated on the basis of penetration, x, so that if s is the film thickness, then:

$$s = f(x)$$

The results obtained in the experimental work, however represent the variation of film thickness, at a fixed penetration, with time, ie.

$$s = f(t) \ , \ x = \text{constant}$$

To compare the two sets of results, therefore, it was necessary to convert the experimental results into a compatible format. By assuming that the intensity of the signal representing mean film thickness at any position along the wall, during injection, is not dependent on time, then the mean value of the signal can be represented by the time mean, which is expressed mathematically by:

$$\bar{s} = \frac{1}{T} \int_0^T s\,(t)\,dt \qquad (5.19)$$

The signal is analysed across the duration labelled "window" in Figure 5.23 which represents the period during injection as the film crosses the point under consideration. The standard deviation was also calculated, giving the scatter in the analysed signal. This was found to be quite high (of the order of 40%) in all of the signals, showing that there was considerable variation in measured thickness at each point. This could be attributed to the 'frothiness' of the film resulting from surfactants present in commercial Kerosene which was used in these experiments. To improve the quality of the signals, the experiments were repeated using Heptane, resulting in an improvement of the standard deviation (down to 20%) although the magnitude of film thickness obtained were of the same order as those obtained with Kerosene Fig. 5.24 shows an enlargement of the signal in the 'window' of Fig. 5.23 plotted together with the cummulative time mean of the signal and the cummulative r.m.s. value, representing the intensity of the signal, calculated from the following equation:

$$r.m.s = [\frac{1}{T}\int_{o}^{T} s^2\,(t)\,dt]^{1/2} \qquad (5.20)$$

The r.m.s value will be slightly higher than the time mean as it includes the effect of surface wave frequency.

Fig 5.25 shows the time mean values of film thickness at all positions along the surface of the wall for the two extreme engine speeds considered. In dashed lines, in each case, is the predicted result of the respective engine speed. Both experimental curves show that the film attains maximum thickness at a position downstream of the nozzle. This could be explained in terms of a 'bow' wave formed due to impingement of the jet on the wall. Assuming the wave to have properties identical to those of a hydraulic jump, then the kinetic energy of the faster fluid upstream will be converted into potential energy in the wave, thus increasing its amplitude. The wave amplitude decays after the end of injection as the potential energy converts back into kinetic energy. The pulsations in the line pressure in effect acted like multiple injections, giving multiple 'bow' waves as illustrated in Fig. 5.26. Although these multiple ripples are unique to the petrol injection system used, and may thus not be observed in a typical diesel engine injection system, the formation of a single 'bow' wave, and a 'piling up' of the liquid film characteristic of a hydraulic jump phenomenon, has been observed by Klanner (42) with an impinging diesel jet.

5.4.3 Results of Schlieren Method

A typical sequence of Schlieren photographs is illustrated in Figure 5.27 showing the initiation of vapour diffusion and its subsequent development. The diffusion of fuel vapour in the interval corresponding to the injection duration is illustrated in Figure 5.28, where six frames are re-plotted on a scaled diagram of the test rig section, showing progressive development of the vapour plume. The dotted line represents the computed boundary layer thickness, based on equation (4.49). When vapour diffusion is observed beyond the

duration of injection, as illustrated in Figure 5.29, the series of photographs consistently indicate separation of flow at about 80^{o} from the position of the injector. This could be explained as being due to either of two possible causes:

i. the onset of secondary flow as the air stream flows round the curve section of the rig. This would result in vapour being transferred towards the axis of rotation (away from the wall).

ii. As the air passes through section A-B in Figure 5.30, there is a change in pressure pattern, due to flow in the outlet section, tending to straighten the flow as illustrated by flow lines in Figure 5.30.

To ascertain the cause of this, an experiment was performed using smoke to visualise the flow in the region close to the wall. It was concluded from the experiment, that the second reason is responsible for the movement in the vapour shown by the Schlieren photographs.

In view of the above analysis, comparison between experimental and predicted results can only be made in the region A-B-C shown in Figure 5.30. Such comparison has been shown to yield good agreement as illustrated in Figure 5.28. This renders support to the idea that evaporating fuel forms a layer of vapour close to the wall and only diffuses slowly towards the centre of rotation, thus allowing for boundary layer theory to be applied in analysing mixture formation.

5.4.4 Experimental Results of Müller

As stated earlier in Section 5.3.3, Müller's experiments were conducted, using Diethylene Glycol, to determine the effect of various parameters on the thickness of the film, wetted surface area, and the rate of evaporation. To compare his results with those obtained using the present model, only results dealing with effect of the following parameters on film development, have been considered:

i. engine speed (swirl velocity)
ii. Injection timing
iii. Engine load
iv. Combustion

Although Müller did not explicitly provide information on the penetration of the film with respect to time, Fig. 5.31 may be used to investigate the accuracy of the nature of equation (3.48) used in the model to calculate penetration. Approximately parallel curves would indicate that the equation suitably describes this type of flow and that a change in the constant 'C' may be sufficient to make the necessary correction. Fig. 5.32 shows the result of such a comparison, where it should be noted that the experimental results are only qualitative in nature.The results shown in Fig. 5.31 have also been used to investigate the validity of equation (3.51) in describing the shape of the injected film.

The importance of a proper consideration of viscosity through the Reynolds criteria considered in equation (5.4) is demonstrated by Fig. 5.33 which presents the results of two fuels; Diethyl Glycol and Ethyl Glycol with respective viscosities of 5.0 and 2.1 mPa.s, injected under the same conditions (respective densities are 989.8 and 931.1 kg/m^3). It is clear that there is similarity in the shape of wetted areas as the results in Fig.5.33 demonstrate, showing that results from the model can be used to represent the events in the engine. It should also be pointed out here that the distribution of measurement points on the spherical surface make it more difficult to characterise the longitudinal axis of the film to compare with results for flow on a flat plate. The results of Müller are given in terms of measurements taken at points making up a grid arrangement in the engine bowl. The points are referred to by a latitude/longitude representation, so that measurement point 120/150 refers to latitude 120^{o}, and longitude 150^{o}. Due to the low spatial resolution of the points, it was not possible to obtain a good representation for points lying on the longitudinal axis. This somewhat limits the comparison of these results directly with those from the model. As a rough

estimate, latitude 120 was taken as the longitudinal axis of the film (see Figure 5.31), and inter-sections with longitudes 120, 150, 180, and 210 to represent points on the axis. Fig. 5.34 shows the variation of film thickness at these four points with crank angle (or time in the case of the author's experiments). Clearly, there is no wave effect detected here as the film is shown to taper towards its leading edge until much later in the development (approxm. 25°CA ATDC) when the thickness at the leading edge becomes slightly thicker (at longitude 210°) than that upstream (longitude 180°). The observations of the author and also those of Klanner (42) demonstrate that there is a 'bow wave' formed which makes the film thickest at a position somewhat upstream of the leading edge until the end of injection, after which the wave amplitude starts to diminish. A similar conclusion may be drawn from Müller's results by transferring the data in Figure 5.35 into a distance - film thickness format. The resulting curve is illustrated in Figure 5.36 showing that the film thickness attains a maximum at a position upstream of the leading edge. In this figure, as in Figure 5.32, the length scale is only a proportional representation due to the unavailability of a scale on Müller's results.

5.5 MODIFICATIONS TO THE WALL JET APPROACH

The results given in Figures 5.9 and 5.10 show significant departure between experimental and calculated quantities. It is thus essential to re-correlate them in order to obtain accurate representation in the engine model. By collecting all the constant quantities in equation (3.48) into a single constant, and making use of only one exponent, the equation for film penetration can be re-cast in the following form:

$$x = C\,(U_o\, d_o{}'t)^a + x_o \qquad (5.21)$$

If at time t = 0 the penetration is zero, then $x_o = 0$ and constants 'C' and 'a' may be obtained by re-plotting the results in Figure 5.9

on a bi-logarithmic scale. The resulting linear relationship is shown in Figure 5.37(a). The axes of the figure have been labelled with their corresponding components in equation (5.21). The slope of the straight line yields the value of 'a' while 'c' is obtained from the y intercept. The following constants have been derived in this way:

$$a = 0.2$$
$$c = 0.1198$$

It is worth pointing out here that although 'a' is dimensionless, c is dimensional and the above value is only applicable when SI units are used in equation (5.21).

By differentiating equation (5.21) with respect to time, the following equation is obtained for the velocity of the film:

$$U = \frac{C_2}{t^{a-1}} \qquad (5.22)$$

where $C_2 = C.a.\ (U_o.d_o')^a$

The data in Figure 5.9 have been re-plotted together with equation (5.21). The result is illustrated in Figure 5.37(b) showing marked improvement in the predicted results. By substituting equation (5.21) into equation (3.52), new predictions for the wetted area have been obtained. These are illustrated in Figure 5.38. In both cases improved predictions have been made.

5.5.1 Surface Area Diminution Due to Evaporation

Apart from obtaining accurate surface area predictions, the model must also be able to calculate fairly accurately the diminution of the wetted area due to evaporation. To ensure that the calculated trend follows observed behaviour in empirical situations, photographs of the film surface were taken at pre-set delay times, following the method described in Section 5.3.1. One set of photographs were taken under

conditions of minimum evaporation, while another set were taken with a significantly increased evaporation rate. The rate of evaporations was controlled by raising the temperature of the gas stream from 17°C to 35°C while maintaining its velocity at a constant value of 6.5 m/s, corresponding to an engine speed of 2000 rpm (see Table 5.3). Figure 5.39 shows a typical pair of photographs taken at 7.08 ms after start of injection.

To allow for diminution of the surface area, a cosine function is assumed to characterise the cross-section of the film thickness. This has the following form:

$$\frac{S}{S_m} = \frac{1}{2}\,[1 + \text{Cos}\,(\pi\xi)] \qquad (5.23)$$

where S_m = film thickness of the central axis of the jet

ξ = normalised dimension measured from the axis of the jet, given by $z/(0.5b)$

b = film breadth.

Figure 5.40 illustrates, schematically, the nomenclature adopted. Comparisons between experimental results and those calculated from applying equation (3.52) together with equations (3.53), (5.22), and (5.23) are illustrated in Figures 5.41 to 5.44. The results show that as the delay time of which the photograph is taken increases, the error between the calculated and measured quantities also increases. This may be attributed to the following reason: In the proposed model, the part of the film furthest from the nozzle is assumed to have spent the longest time on the wall, and is thus expected to experience a larger loss of mass due to evaporation. This principle is illustrated in Figure 5.45, where the quantity evaporated is seen to increase rapidly with penetration. Experimental observations such as may be deduced from Figures 5.25 and 5.36, and also as discussed by Urlaub (34), however, suggest that after initial contact with the piston wall, in which the film experiences a large deceleration, subsequent layers 'glide' over the wetted patch, travelling further than the proposed model assumes. The results in Figures 5.41 to 5.44, thus, lend more support to the above

explanation, and it is noticed that at longer time durations, the film patch tends instead to become narrower (due to thin edges evaporating off) rather than having a much shorter penetration. The proposed model, in its present form has not accounted for the phenomenon described above. It is, however, necessary at some stage, to include these effects if the model is to address the problem of significantly higher unburnt hydrocarbons in wall-wetting engines. The relatively cooler fuel film layers 'gliding' over earlier injected layers would result in a slower heating of film which, in turn, would lead to a slower evaporation rate. The experimental results of Müller (41), illustrated in Figure 5.35, demonstrate this delayed evaporation phenomenon to some extent. A 5 micron thick liquid film is seen to persist on the wall of the piston crown well over 35°CA after the end of injection. This may have been compounded by the fact that in the region close to the bottom of the bowl there is a marked reduction in the swirl intensity, as illustrated by the results of CONCHAS model computations illustrated earlier in Figures 1.27 and 1.31. This may lead to a reduction in convective heat and mass transfer in that region. However, the effect of slower film heating due to the earlier explanation cannot be discounted due to the length of time involved.

5.6 CONCLUSION

The experimental results presented in this chapter have highlighted some of the weakness in the conceptual framework of the model. Corrections have been made to some of the equations where this could be done without a completely new approach in the modelling concept. The following assumptions have been verified:

(i) It is plausible to apply wall-jet concepts to the description of film motion on the piston wall. The constants in the wall-jet equation have to be empirically fitted in order to ensure more accurate representation.

(ii) The evaporating fuel forms a layer of vapour in the region

close to the film surface diffusing very slowly into the main stream.

(iii) Simple mass conservation can be used to obtain an estimate of film thickness.

(iv) The method used to compute wetted surface area yields accurate magnitudes as well as trends once the corrections suggested to the wall-jet equations have been implemented.

The major short comings have been identified in the modelling concept, both of which may result in higher evaporation rate than actually occurs:

(i) The unavailability of a method to take into account surface waves may lead to an over-prediction of penetration and wetted surface area.

(ii) The absence of a method to describe the 'gliding' phenomenon, whereby layers of film injected late glide over those injected earlier resulting in a slower heating of the film and hence a lower rate of evaporation.

As pointed out earlier, both of these observations may significantly affect predictions for unburnt hydrocarbon emissions. But as these are not part of the predictions from the model in its present form, they do not affect the results from the model to any great extent.

Table 5.1: Similarity Conditions at 1500 RPM

PARAMETER			ENGINE	MODEL
Air Stream Velocity	(m/s)	UG	42.0	4.62
Linear Scale		λ	1.0	1.0
Injector Nozzle Dia.	(mm)	do	0.75	0.4
Air Density	(kg/m3)	a	11.0	1.2
Density of Fuel	"	f	820.0	780.0
Injection Duration	(ms)	t	1.6	15.85
Injection Velocity	(m/s)	Uo	144.6	28.0
Working Pressure	(Bar)	P	24.0	1.0
Cylinder Temp.	(K)	T	750.0	300.0

Table 5.2: Fuel Properties at 20^{o}C

PROPERTY	ETHYL-GLYCOL C4H1002	ETHYL-DIGLYCOL C6H1403	DIESEL
Molecular Weight	90.12	135.17	250(appr)
Density (kg/m^3)	931.1	989.8	820.0
Boiling Temp.^{o}C (at 1 Bar)	135.1	201.9	170-350
Vapour Pressure (mBar)	5.066	0.133	-
Heat Capacity (kJ/kg.K)	2.324	2.311	1.968
Thermal Conductivity (kW/m.K)	1.73×10^{-4}	1.68×10^{-4}	1.42×10^{-4}
Viscosity (Pa.s)	2.1×10^{-3}	5.0×10^{-3}	5.0×10^{-3}
Calofic Value (MJ/kg)	25.477	25.58	42.915
Stoichiometric A/F Ratio	8.5	8.3	15.1

Latent Heat (MJ/kg)	2.68	2.75	2.763
Electrical Cond. (S/m)- Approx	1.0×10^{-4}	2.0×10^{-5}	1.0×10^{-12}

Table 5.3: Simulation Rig Swirl Characteristics

ENGINE SPEED (RPM)	SWIRL VELOCITY IN ENGINE (m/s)	SWIRL VELOCITY IN RIG (m/s)	VELOCITY PROFILE IN THE RIG
1000	-	3.25	Fig. 5.23
1500	23.90	4.90	Fig. 5.24
2000	35.00	6.50	Fig. 5.25
2500	44.10	8.125	Fig. 5.26
3000	-	12.0	-

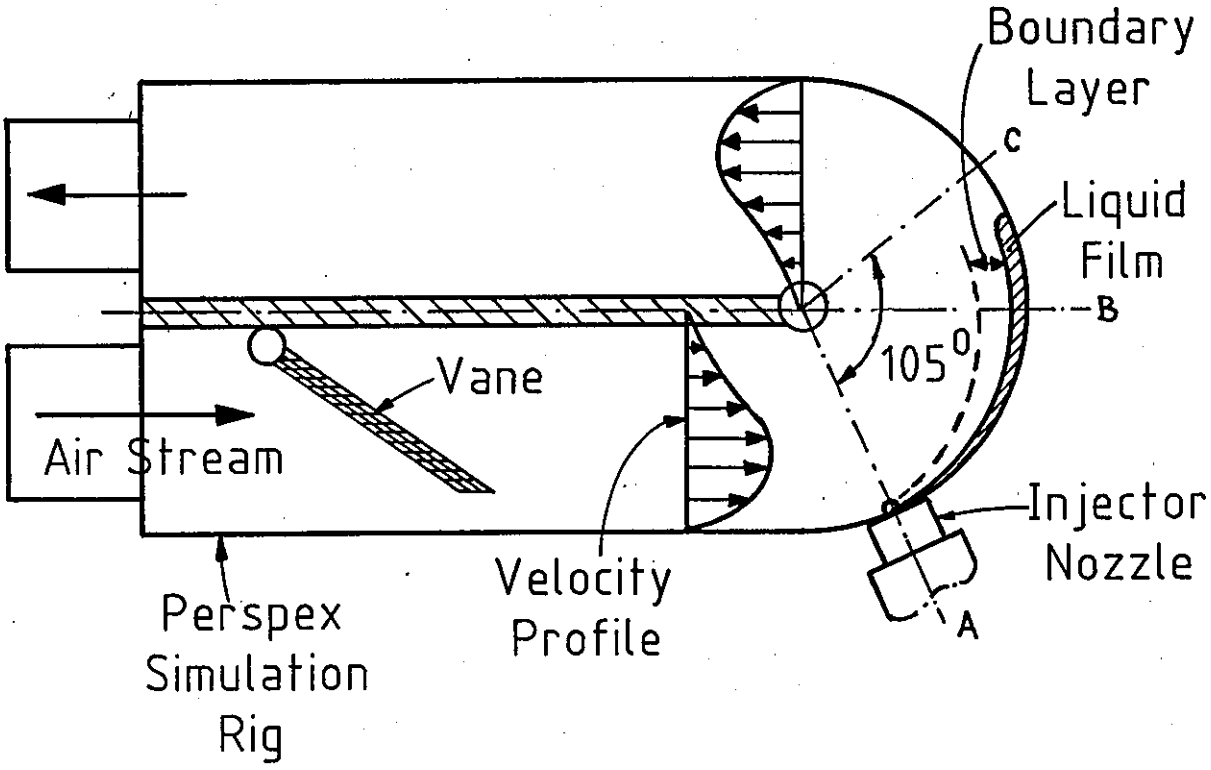

FIGURE 5.1: SCHEMATIC DIAGRAM OF SIMULATION RIG

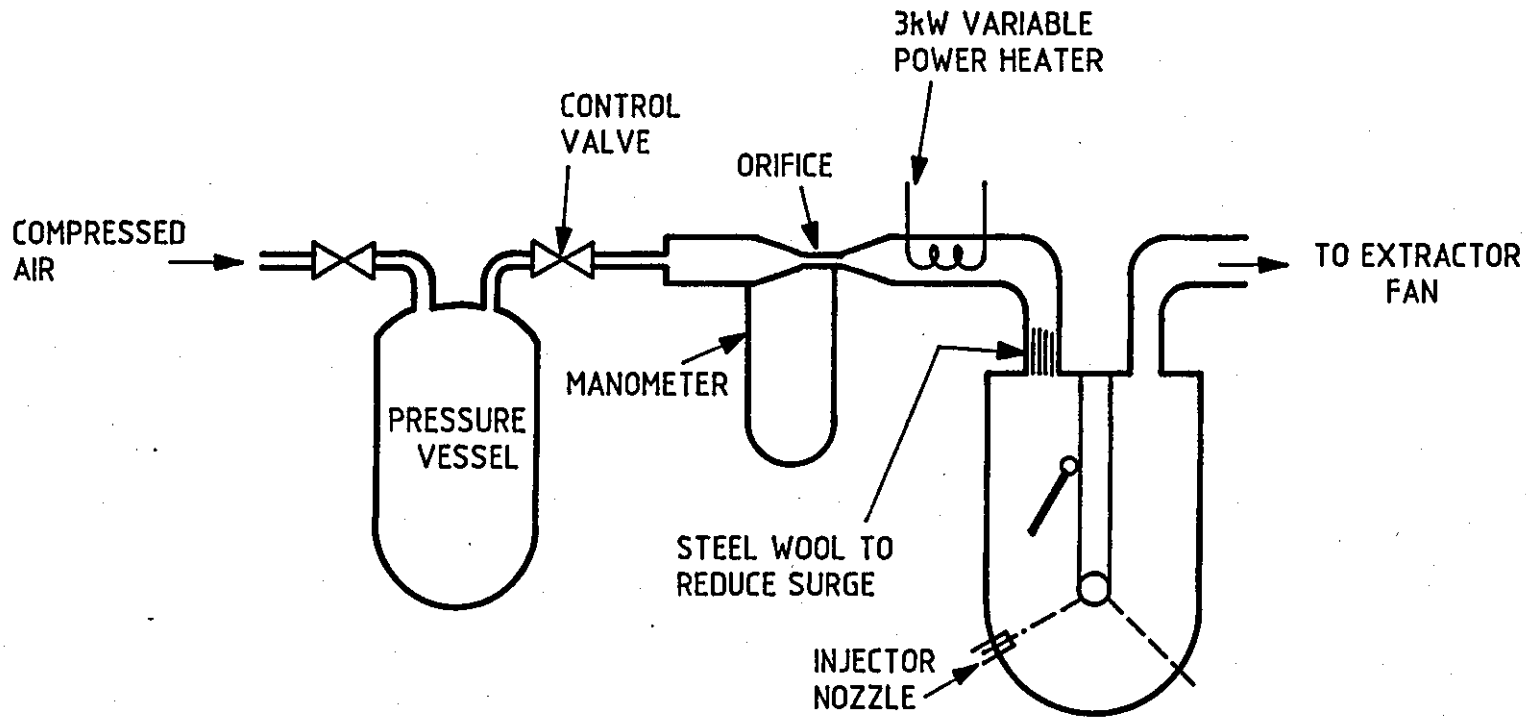

FIGURE 5.2: AIR STREAM SUPPLY SYSTEM

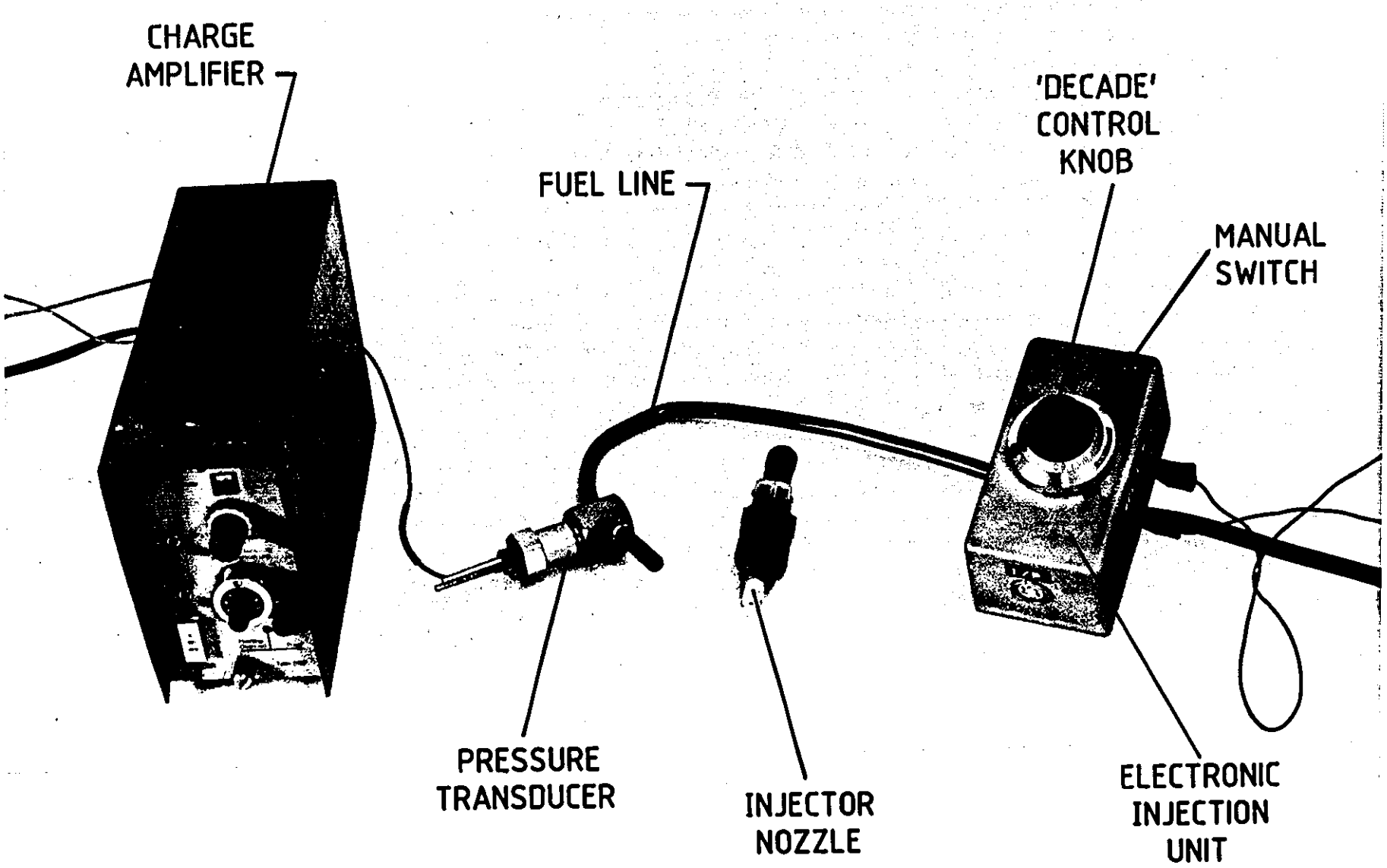

Figure 5. 3. Electronic Fuel Injection Equipment

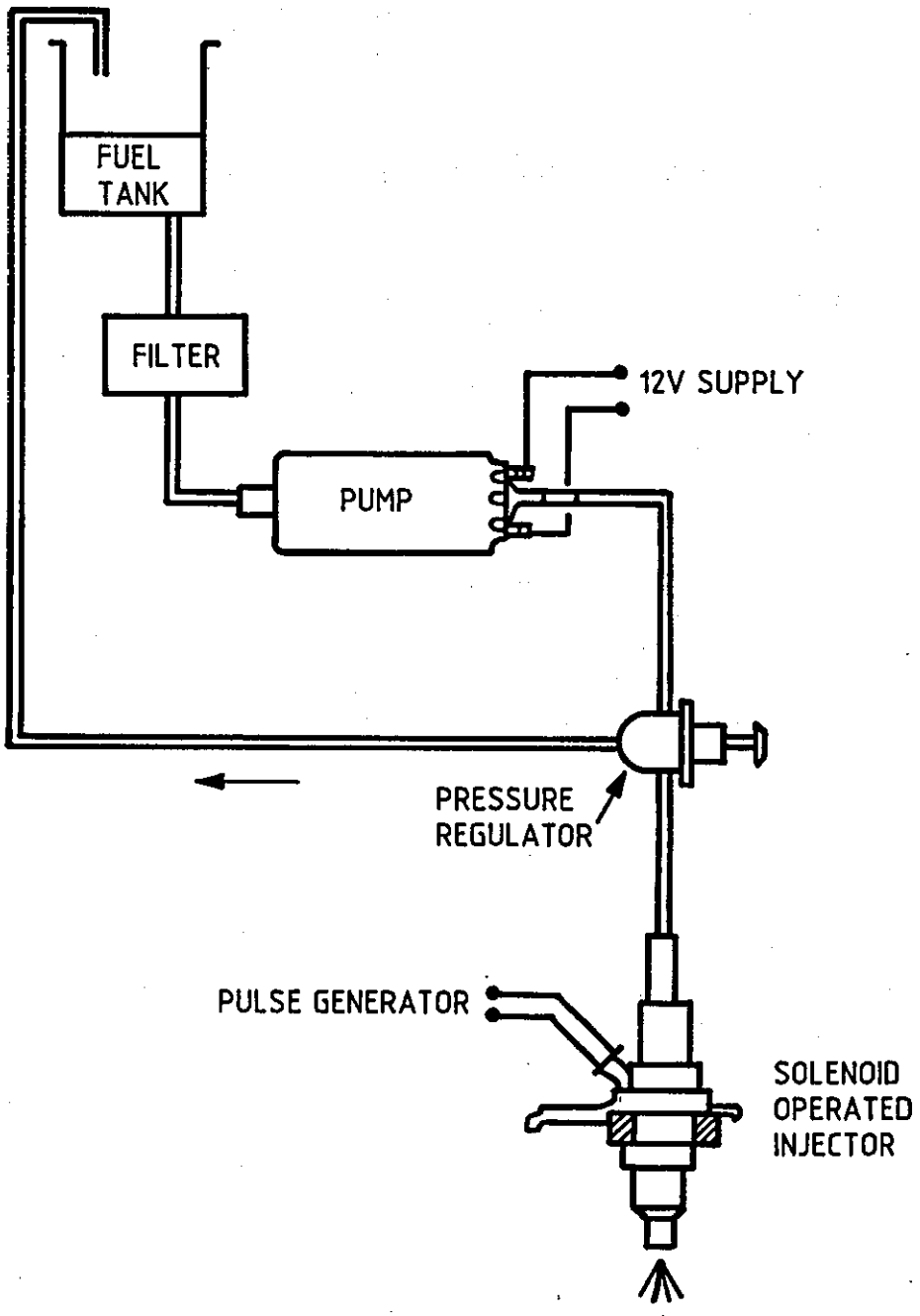

FIGURE 5.4: FUEL SUPPLY SYSTEM

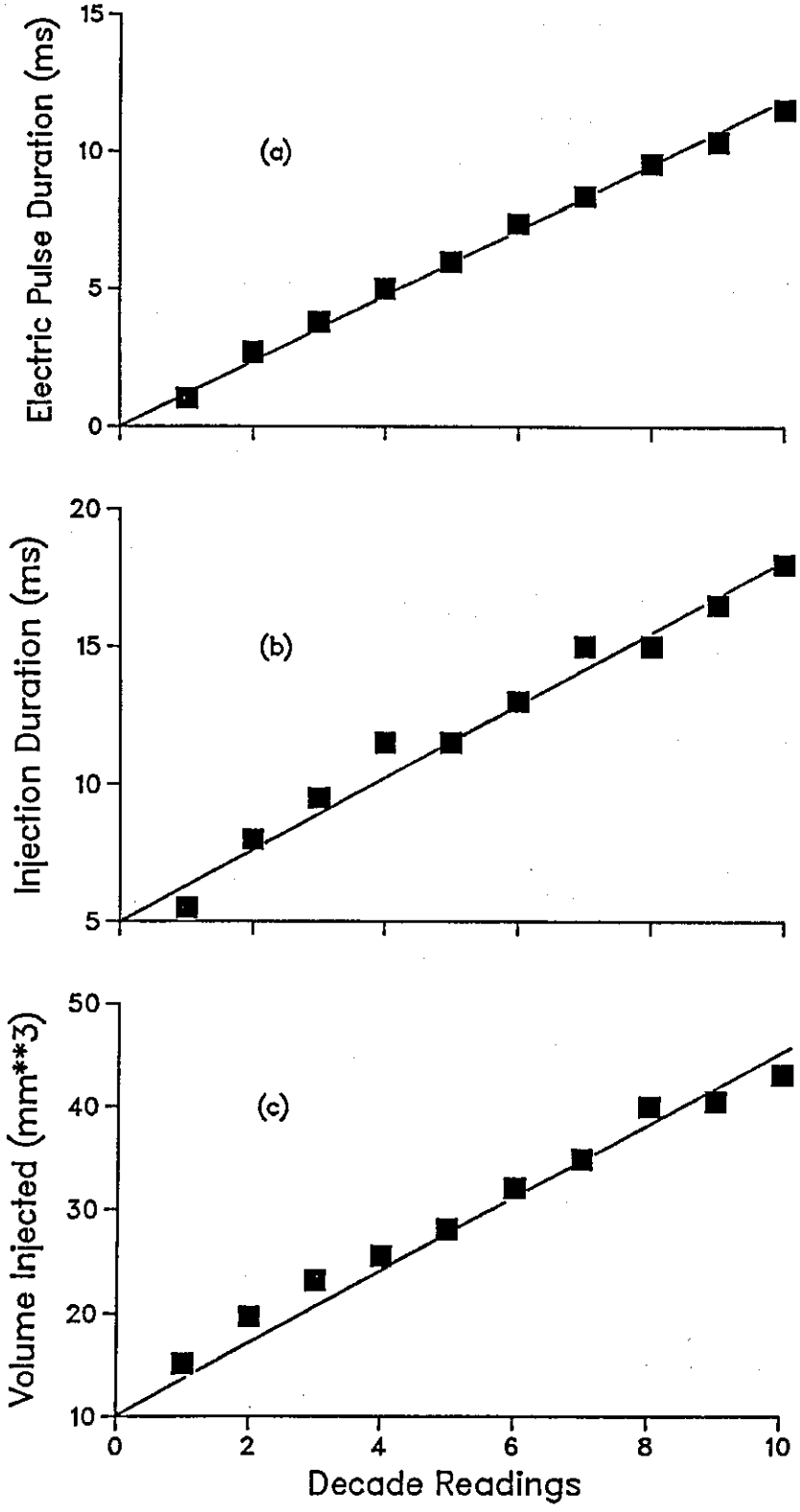

FIGURE 5.5: CALIBRATION OF THE INJECTOR NOZZLE

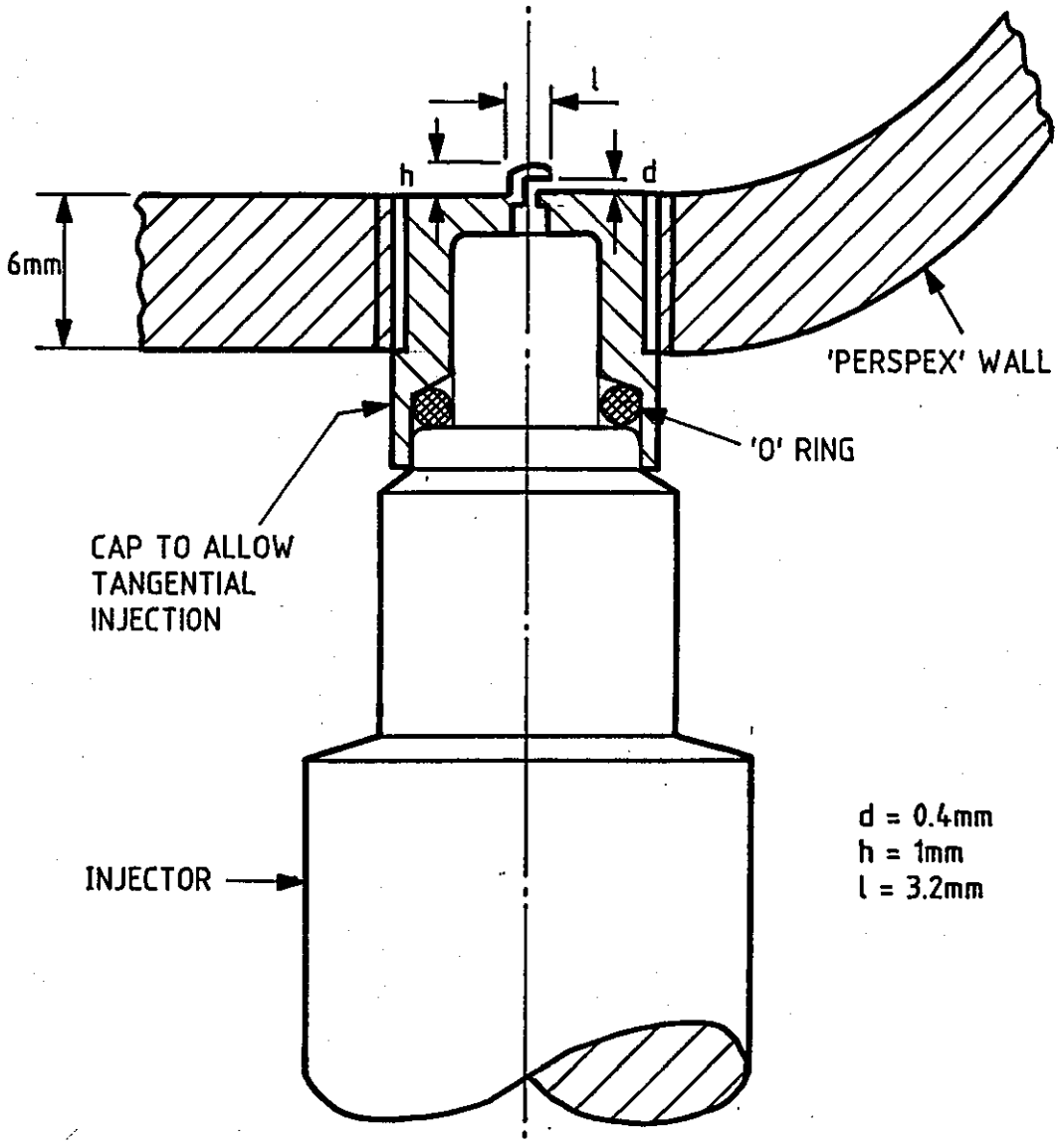

FIGURE 5.6: FITTING INJECTOR TO THE RIG

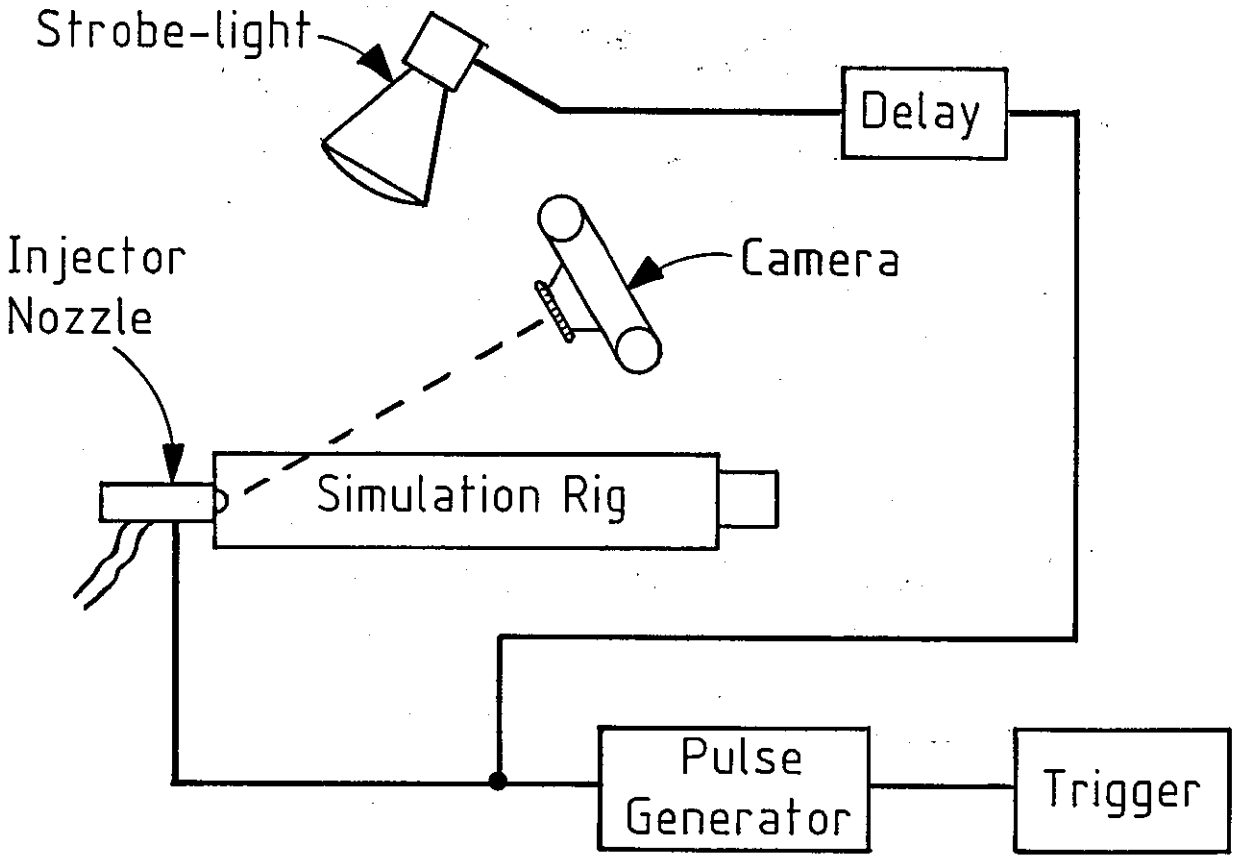

FIGURE 5.7: SCHEMATIC DIAGRAM OF PHOTOGRAPHIC TECHNIQUE

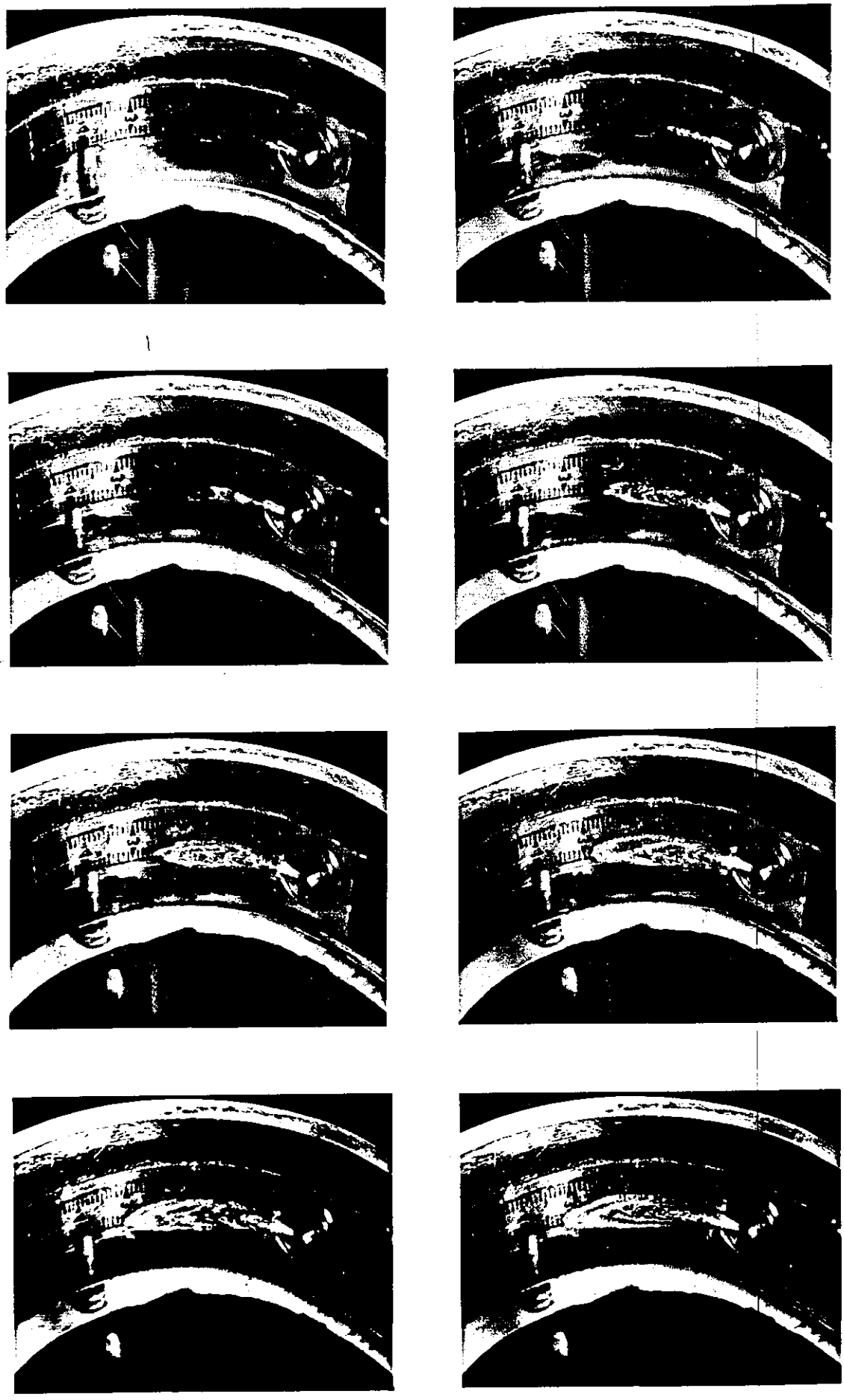

FIGURE 5. 8: TYPICAL SEQUENCE OF PHOTOGRAPHS ILLUSTRATING DEVELOPMENT OF THE FILM (3 - 10 ms FROM START OF INJECTION)

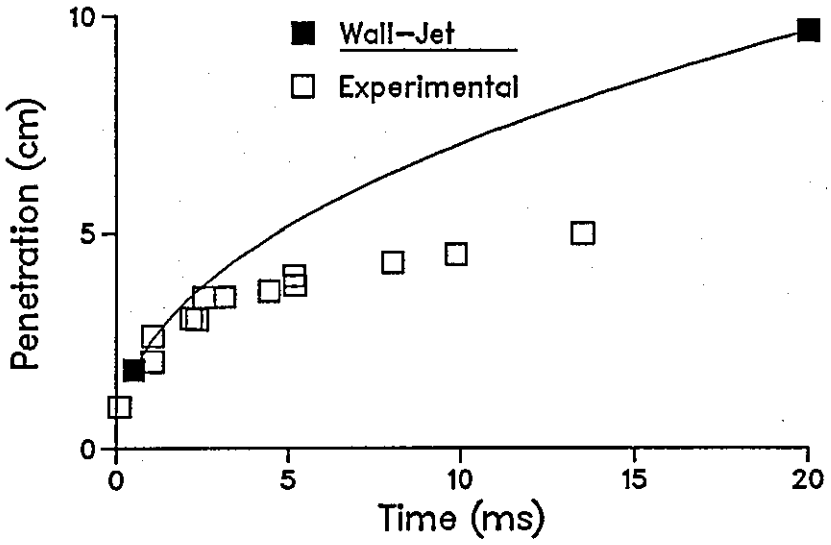

FIGURE 5.9: WALL JET CORRELATION FOR FILM PENETRATION

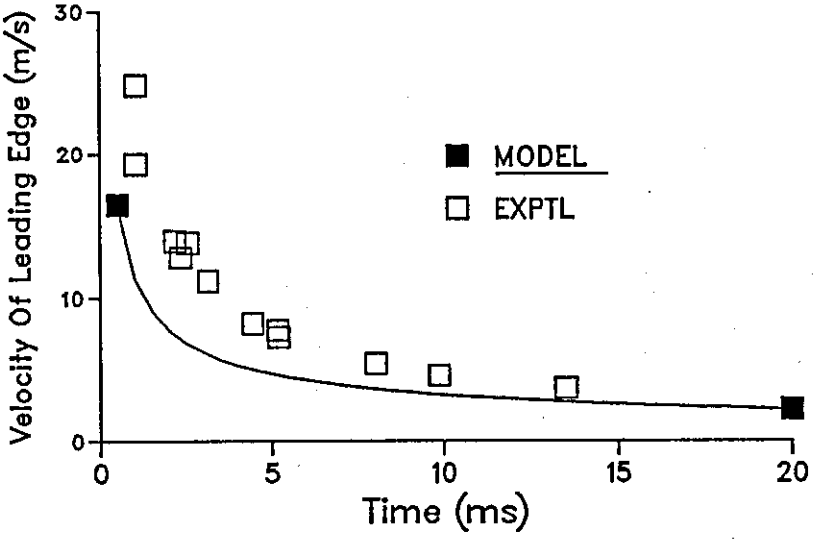

FIGURE 5.10: PREDICTED VS MEASURED (ESTIMATE) FILM VELOCITY

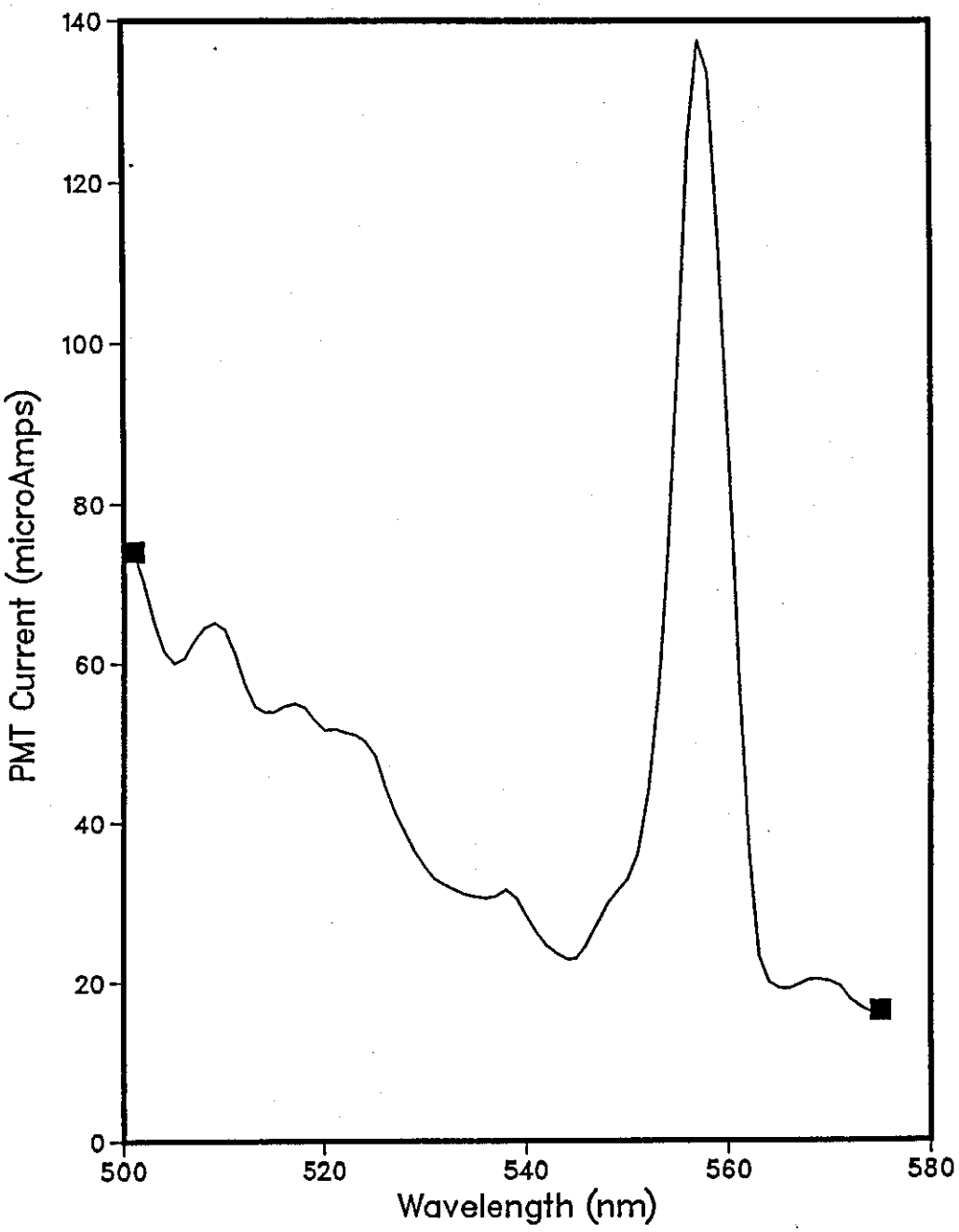

FIGURE 5.11: FLUORESCENCE SPECTRUM FOR RUBRENE IN SOLUTION

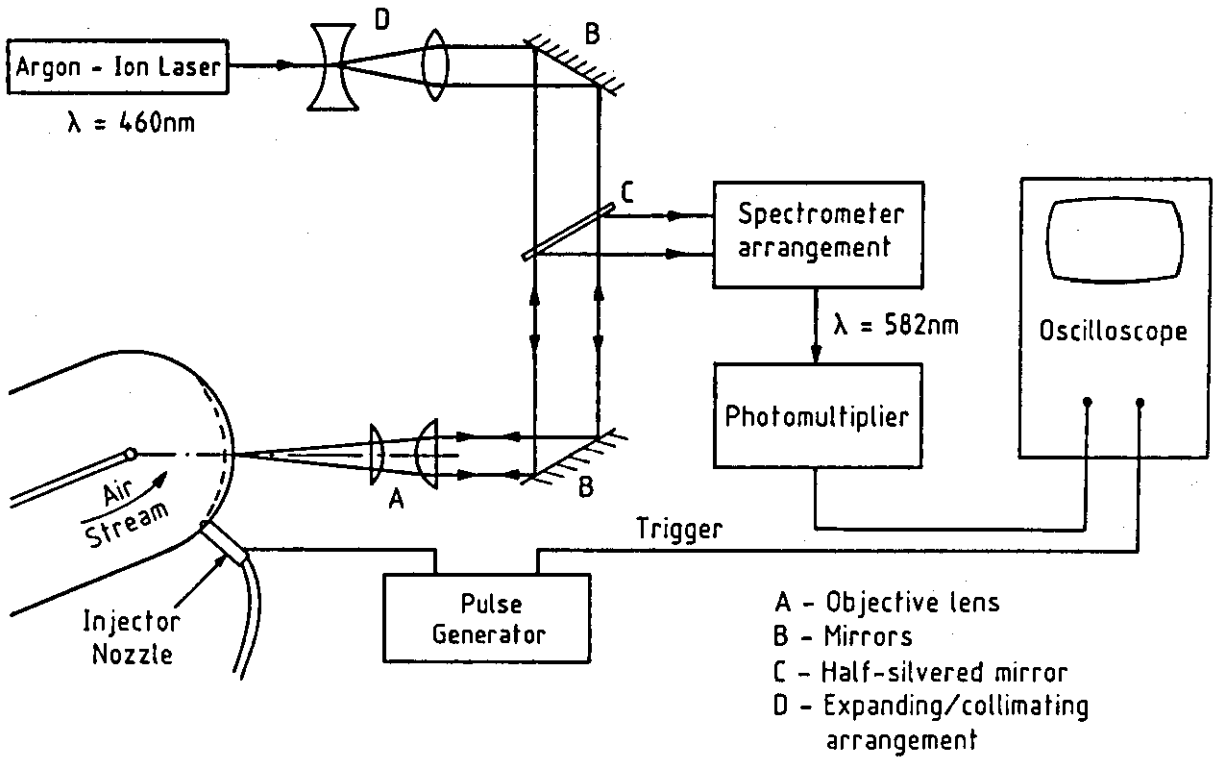

FIGURE 5.12: SCHEMATIC DIAGRAM FOR THE LASER EXCITED FLUORESCENCE TECHNIQUE FOR MEASURING FILM THICKNESS

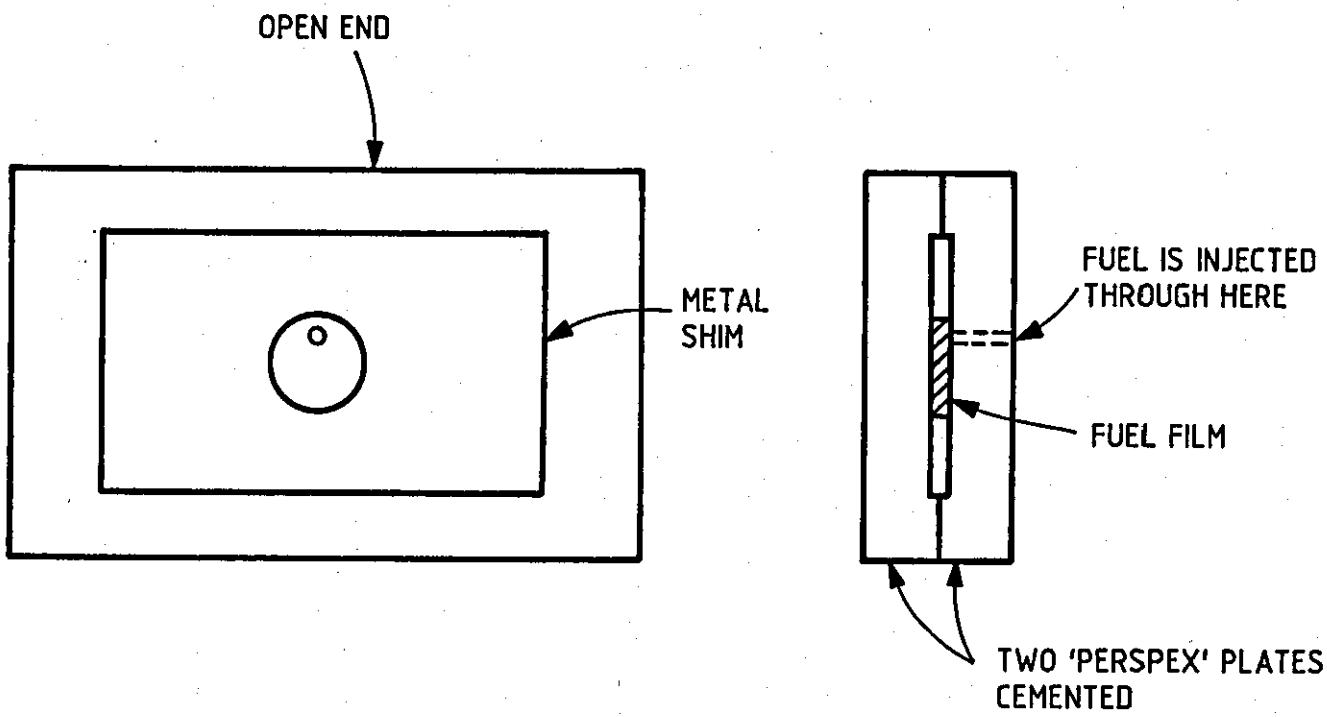

FIGURE 5.13: CONSTRUCTION OF CALIBRATION CELL

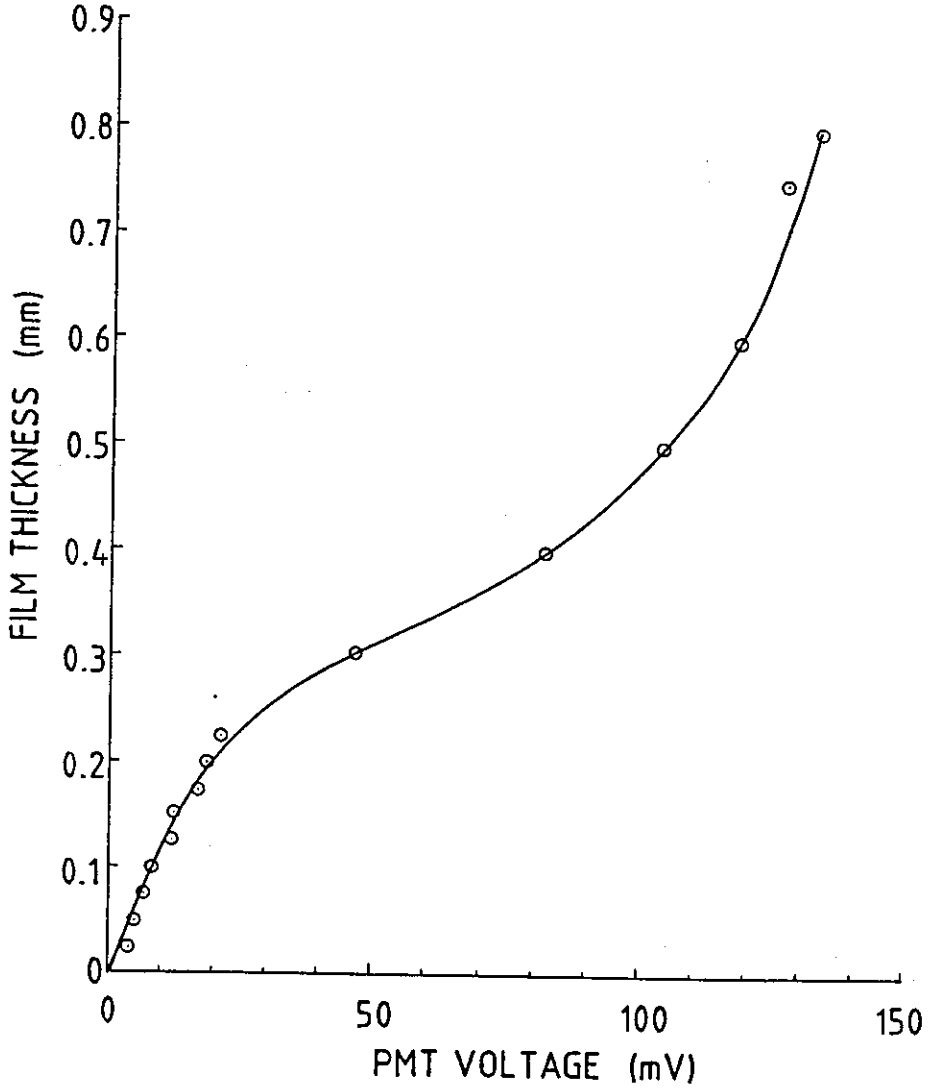

FIGURE 5.14: CALIBRATION CURVE FOR FLUORESCENCE TECHNIQUE

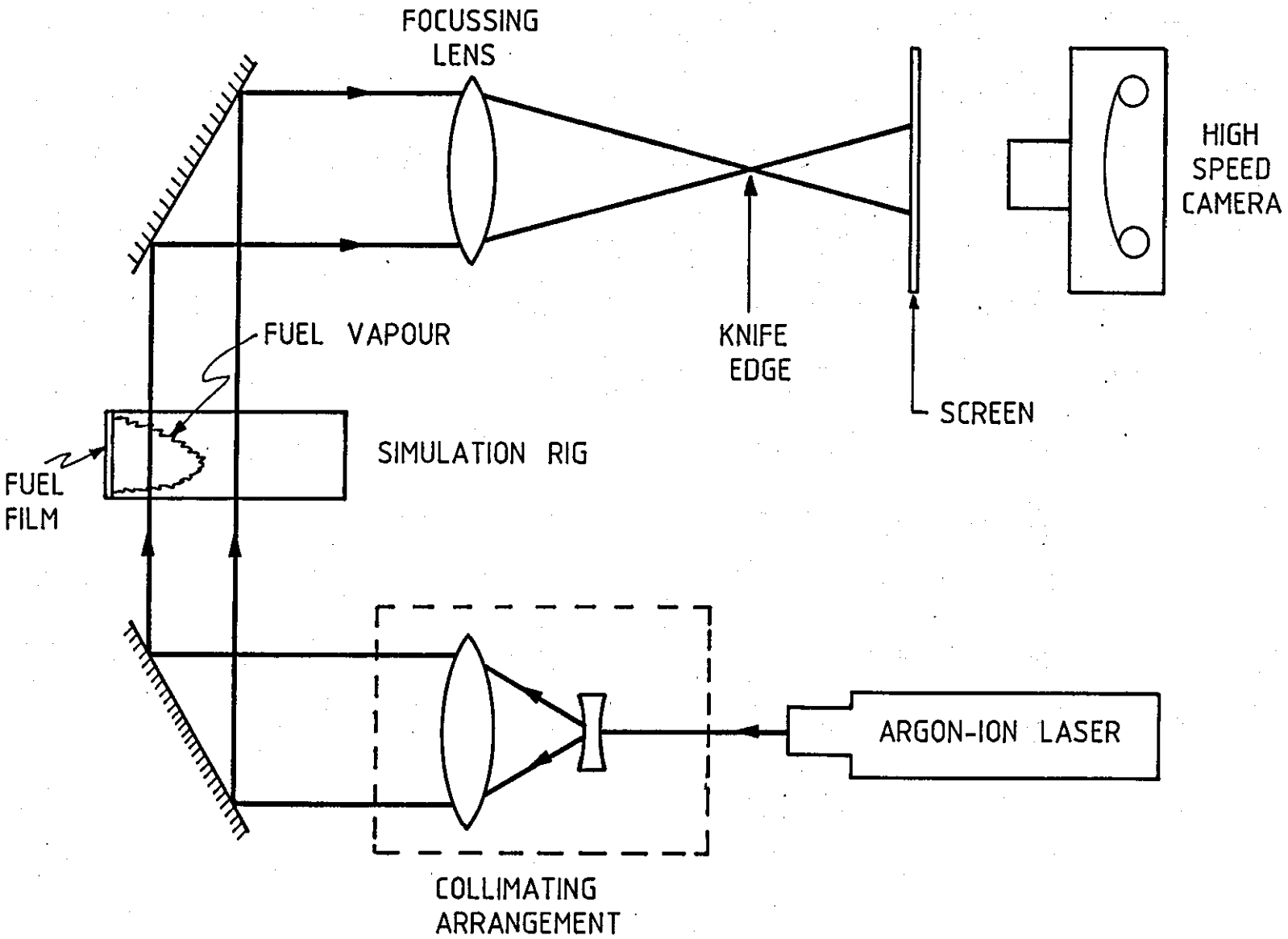

FIGURE 5.15: SCHEMATIC DIAGRAM FOR THE SCHLIEREN OPTICAL SYSTEM

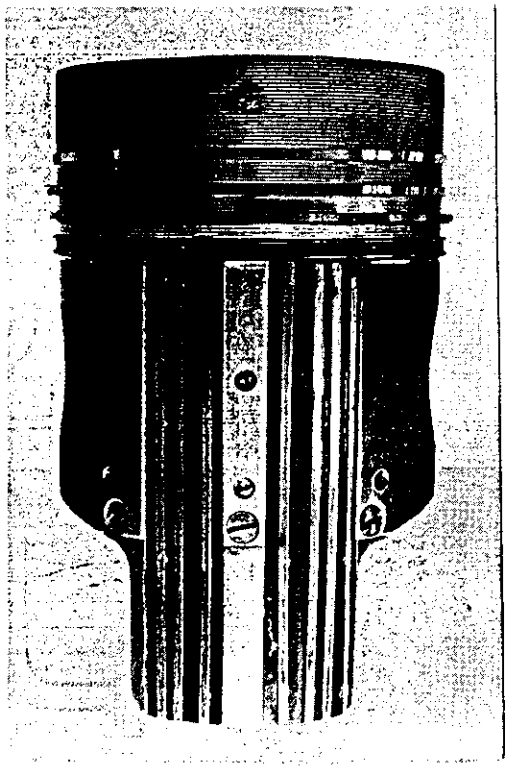

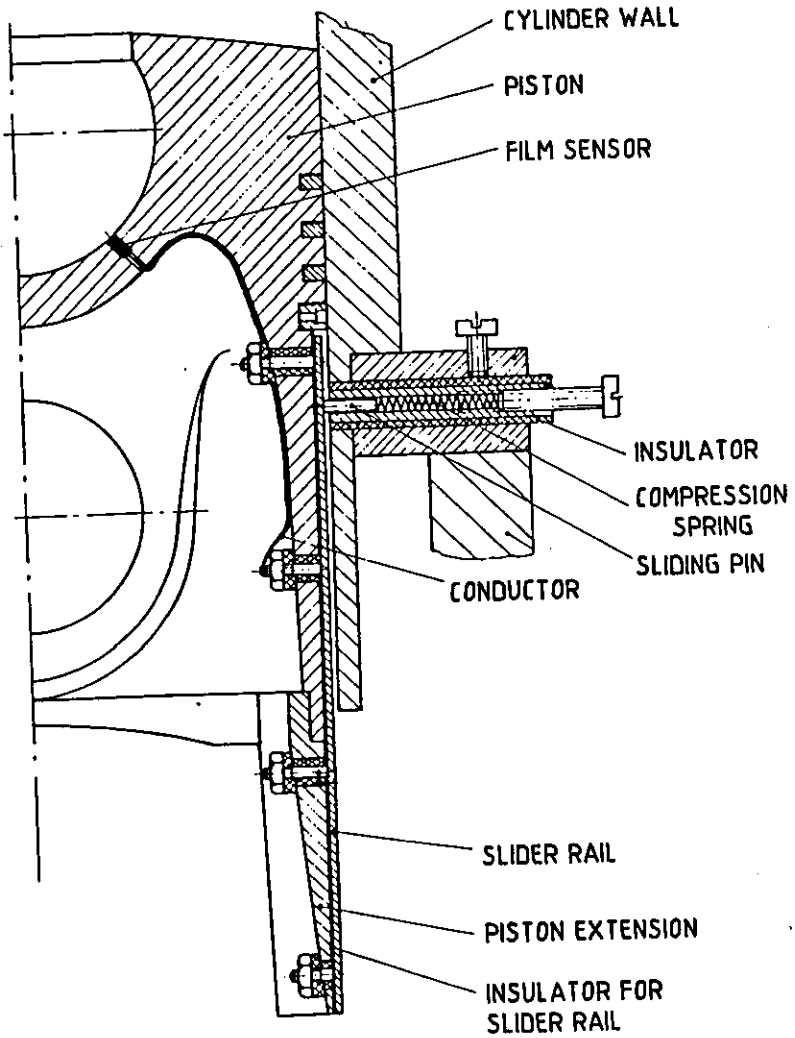

FIGURE 5.16: METHOD USED TO TRANSMIT PROBE SIGNAL FROM THE ENGINE, IN MÜLLER'S EXPERIMENTS (41)

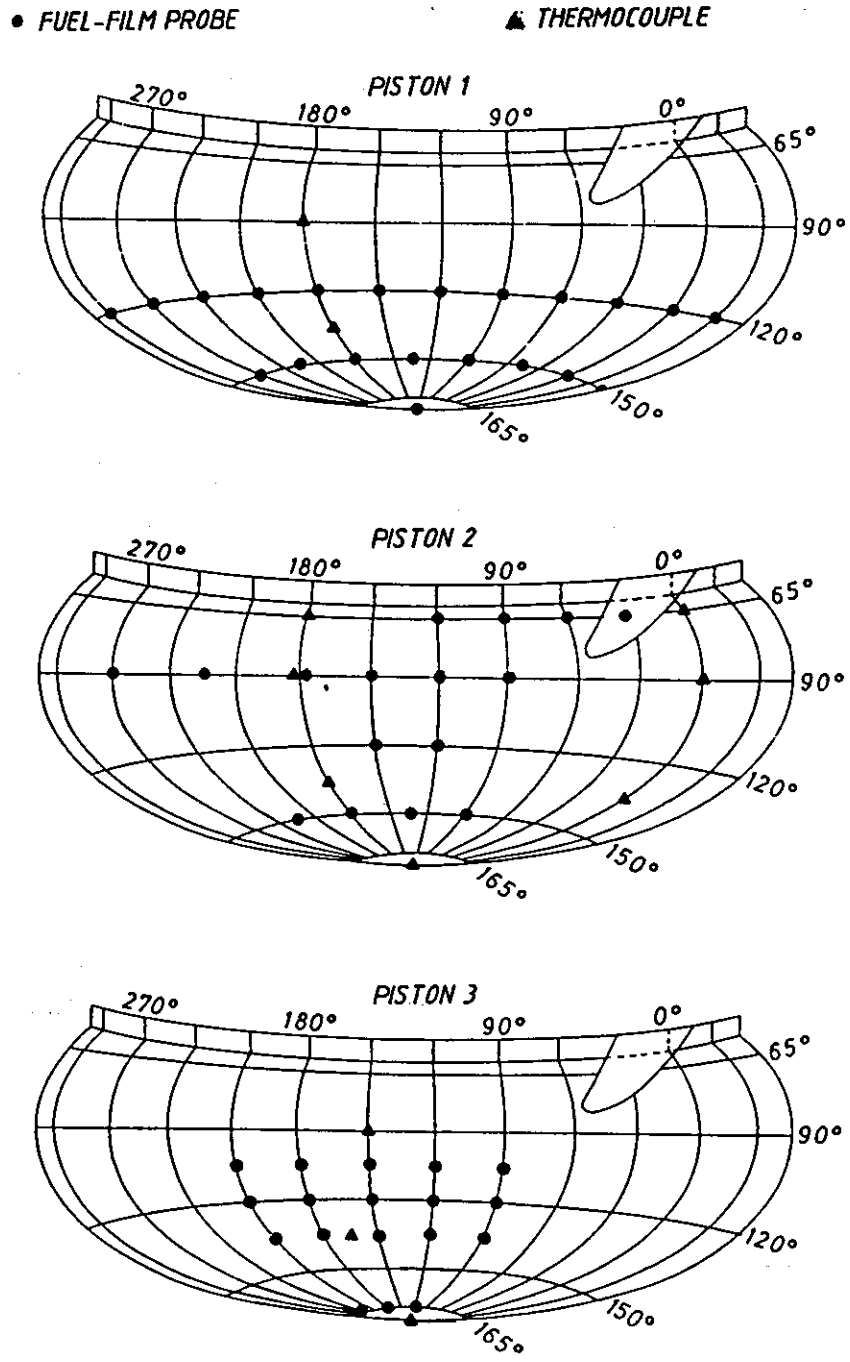

FIGURE 5.17: SCHEMATIC REPRESENTATION OF THE DISTRIBUTION OF PROBES IN THE THREE PISTONS USED BY MÜLLER (41)

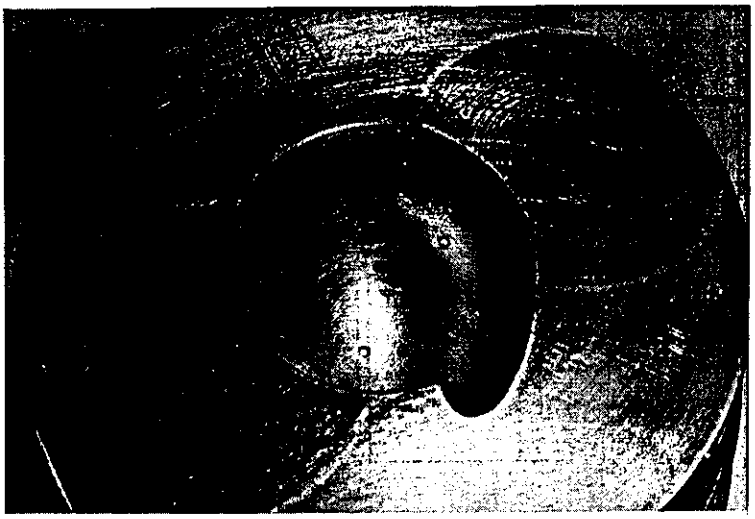

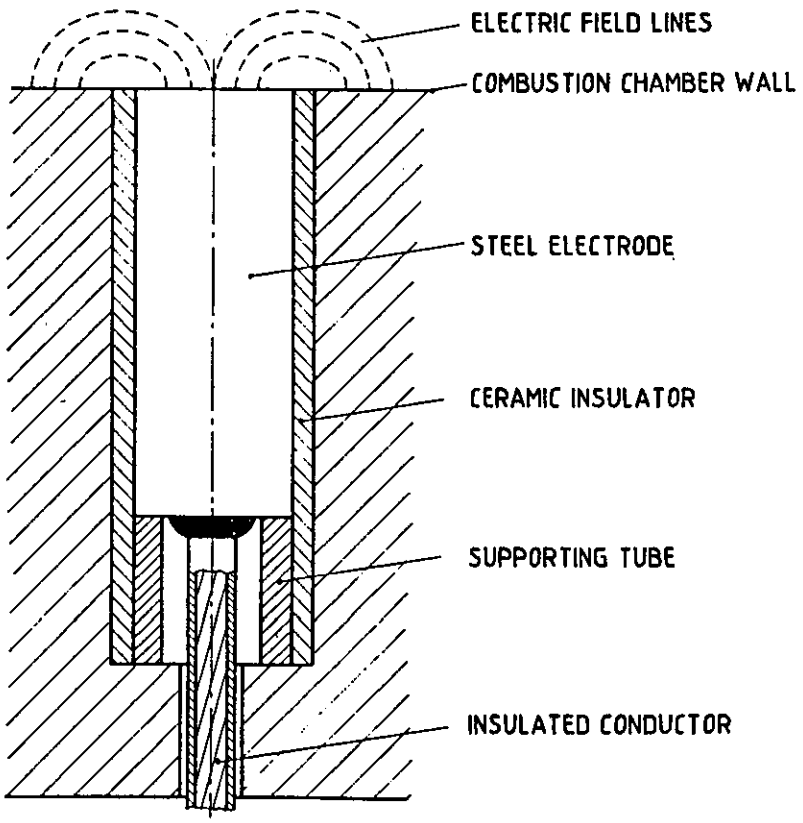

FIGURE 5.18: IMPLANTATION OF FILM MEASURING PROBES ON THE PISTON WALL (41)

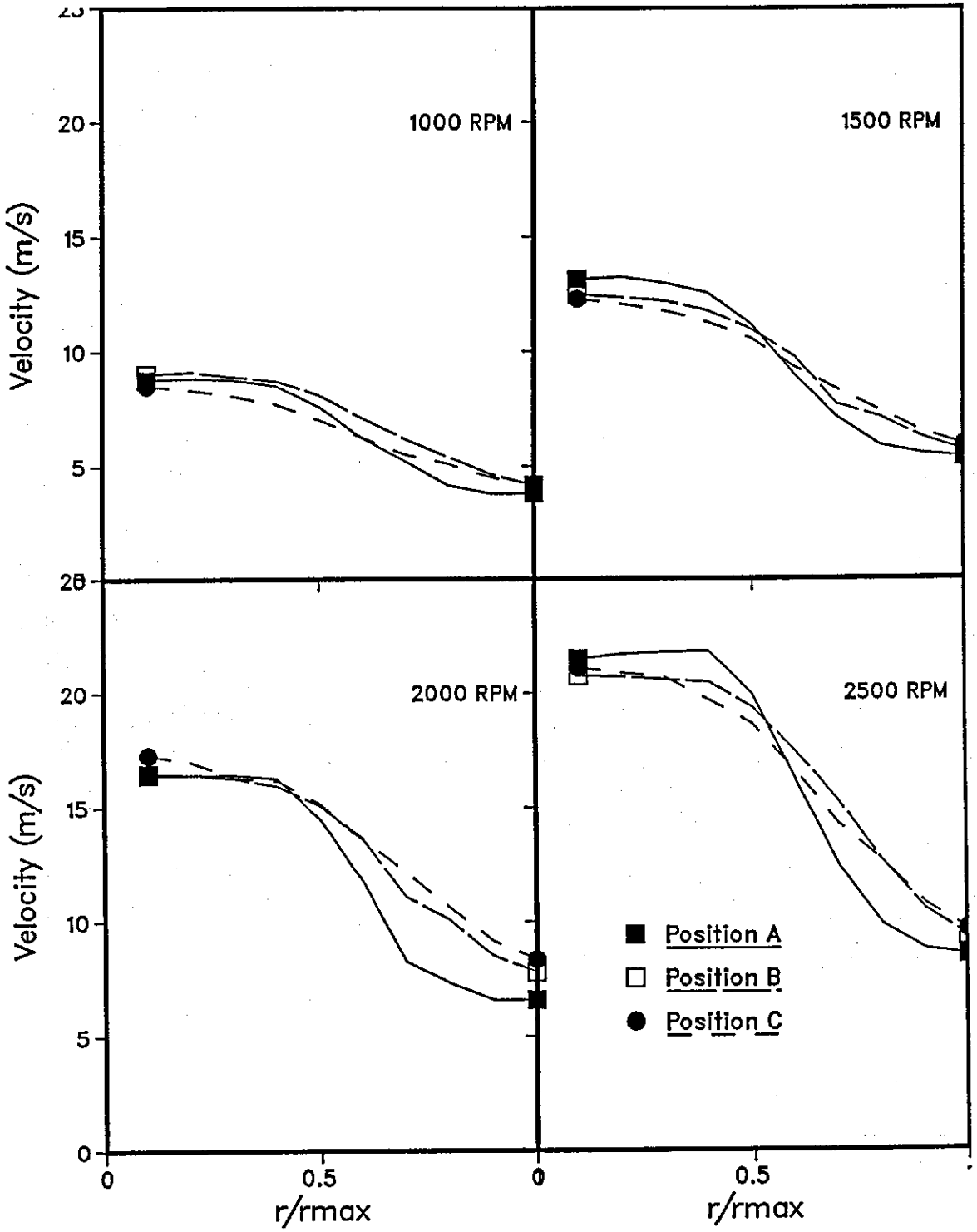

FIGURE 5.19: AIR-STREAM VELOCITY PROFILES IN THE SIMULATION RIG

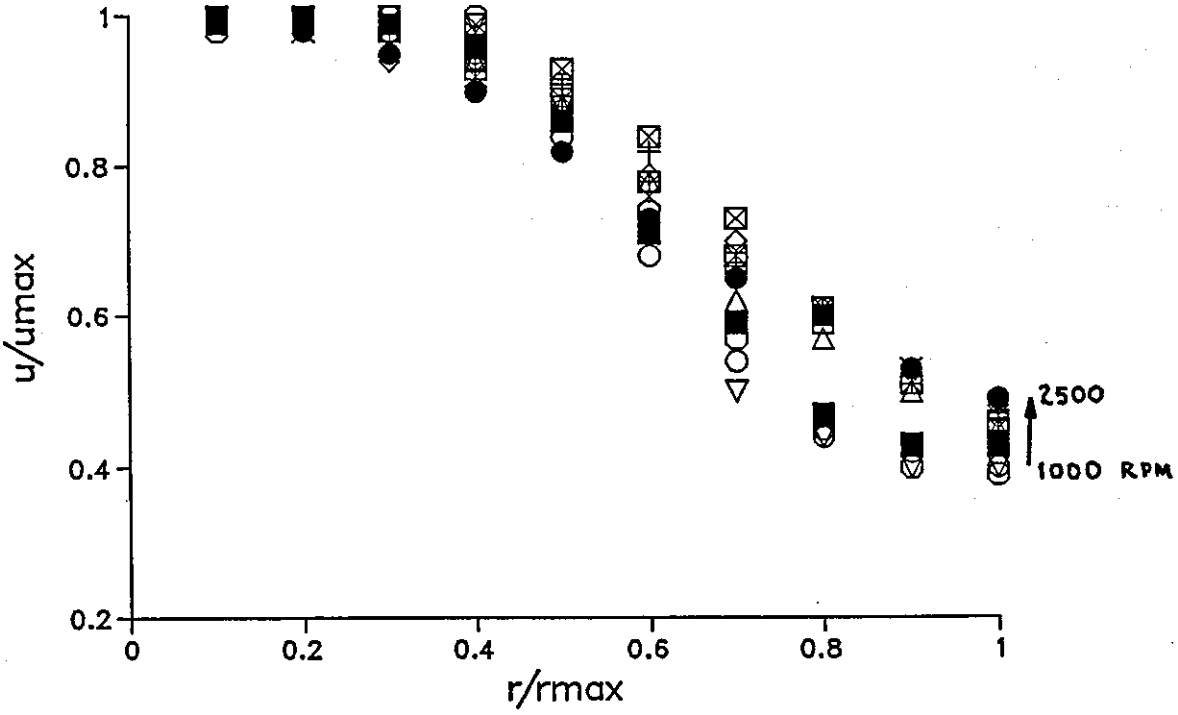

FIGURE 5.20: SIMILARITY IN GASEOUS STREAM VELOCITY PROFILE 1000-2500 rpm

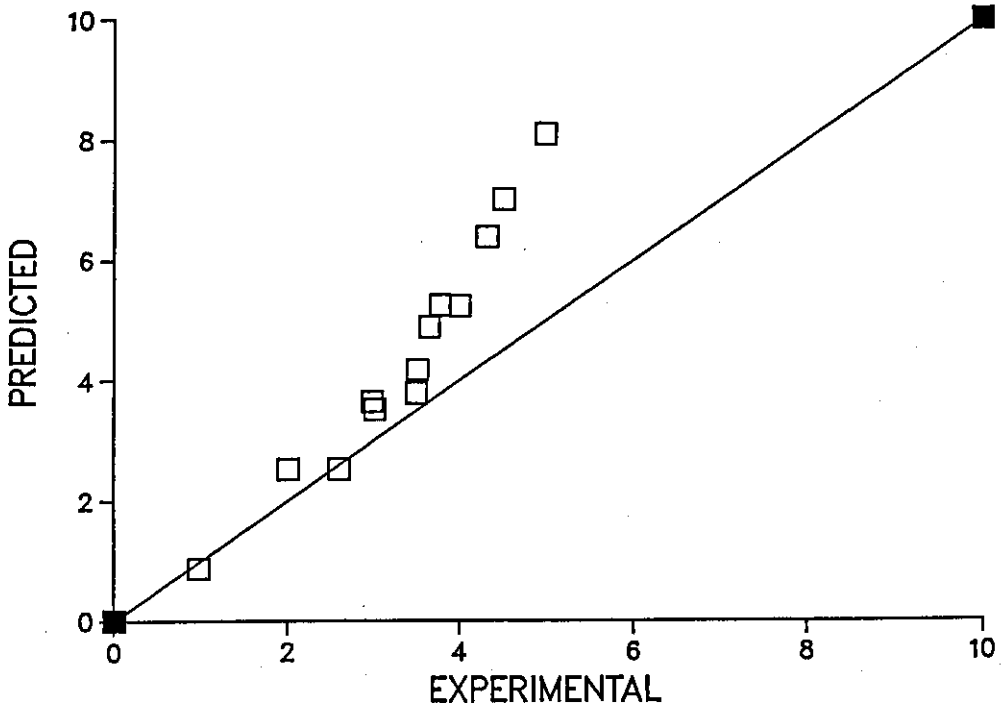

FIGURE 5.21: DEPARTURE BETWEEN PREDICTED AND EMPIRICAL FILM PENETRATION ALONG THE PISTON WALL

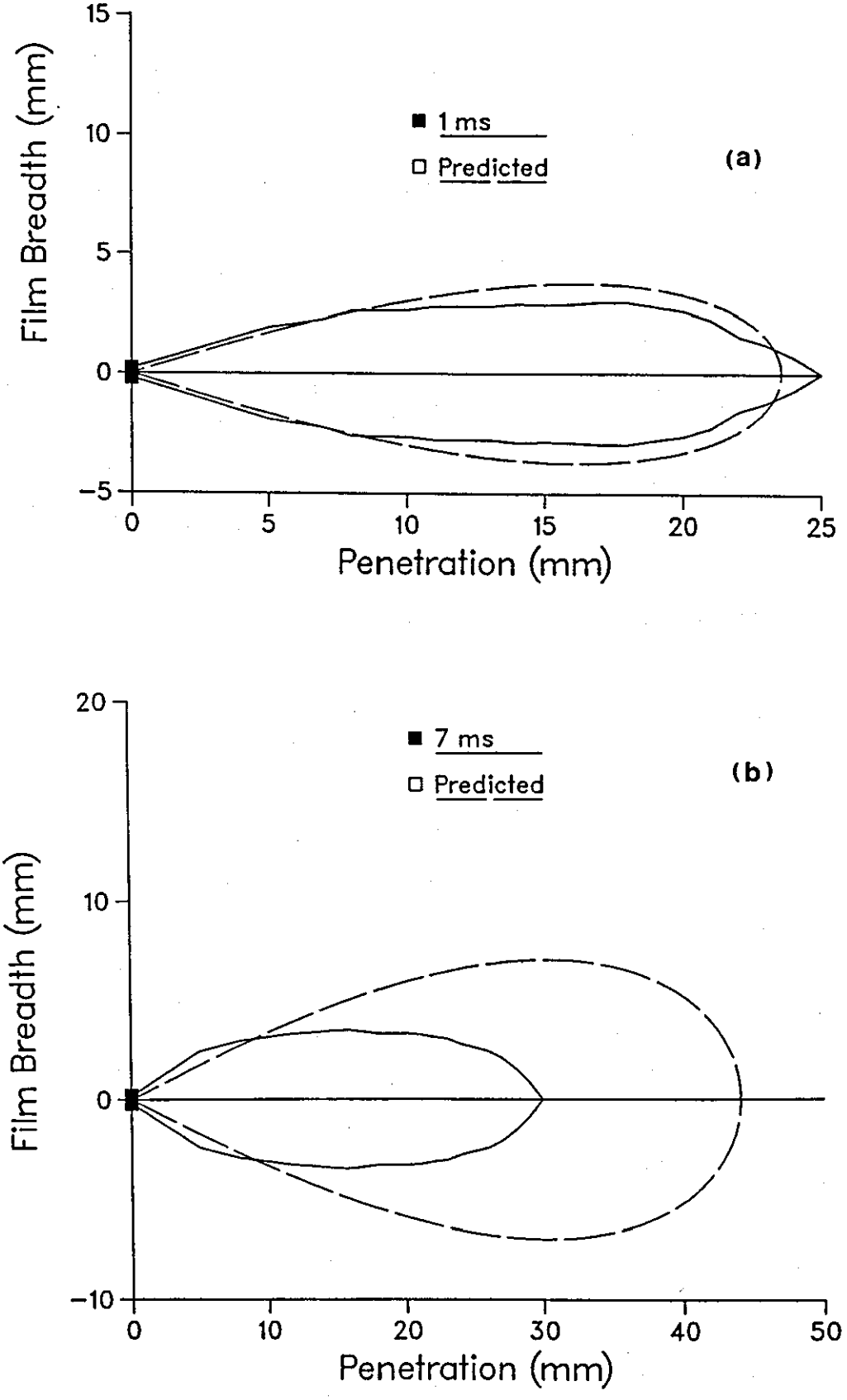

FIGURE 5.22: COMPUTED VS EXPERIMENTAL DEVELOPMENT OF FILM SURFACE AREA

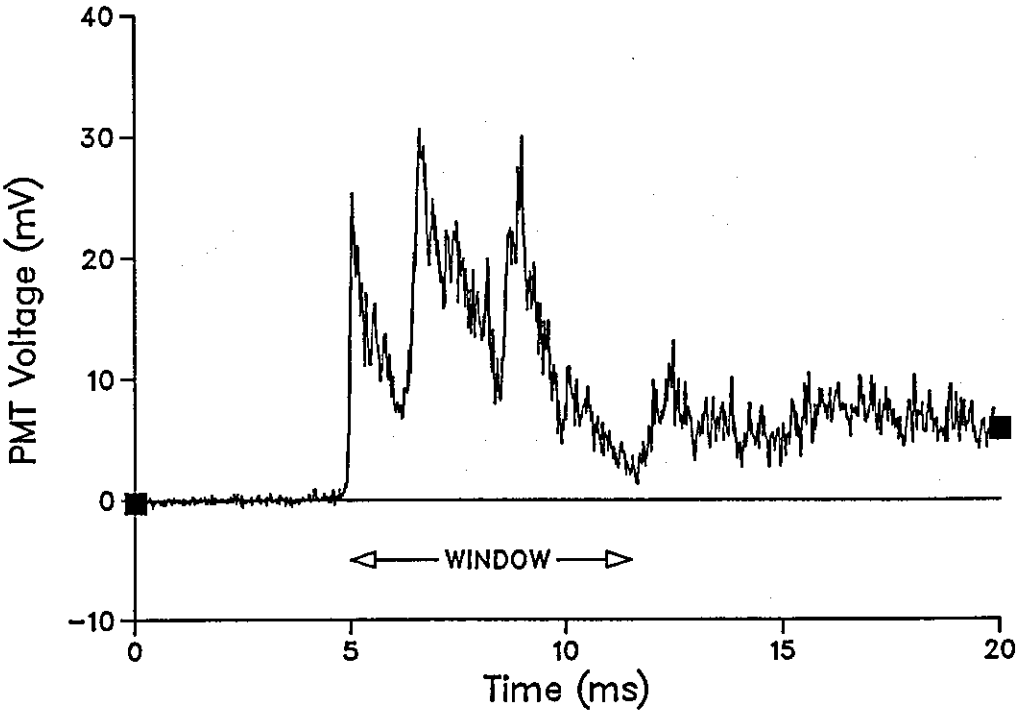

FIGURE 5.23: TYPICAL SIGNAL TRACE FROM FLUORESCENT TECHNIQUE

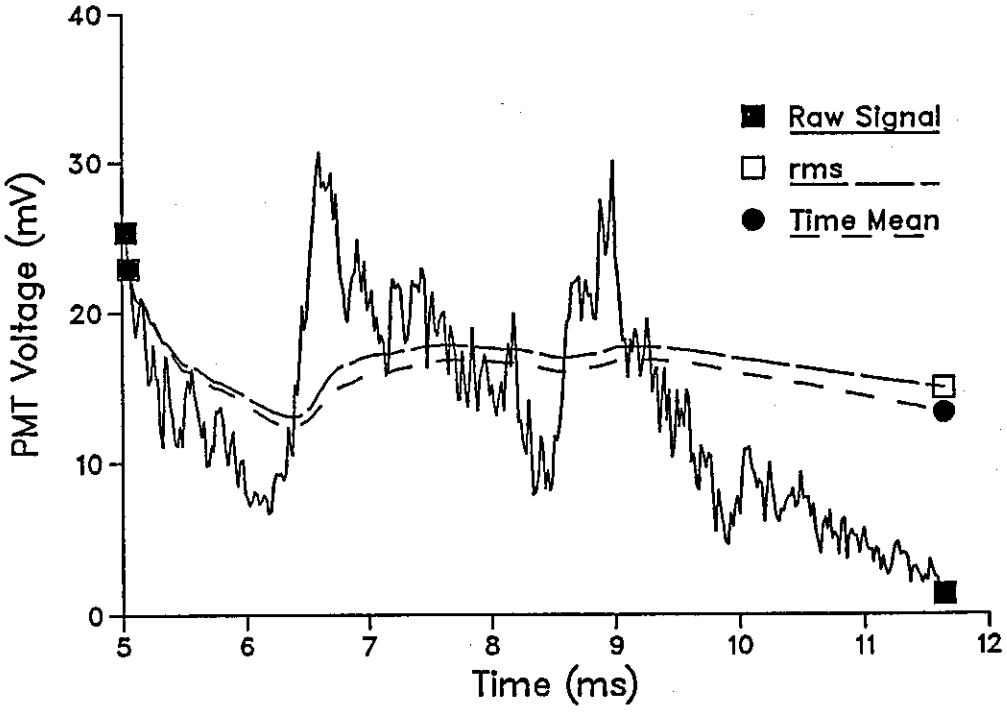

FIGURE 5.24: PROCESSING THE 'WINDOWED' SIGNAL

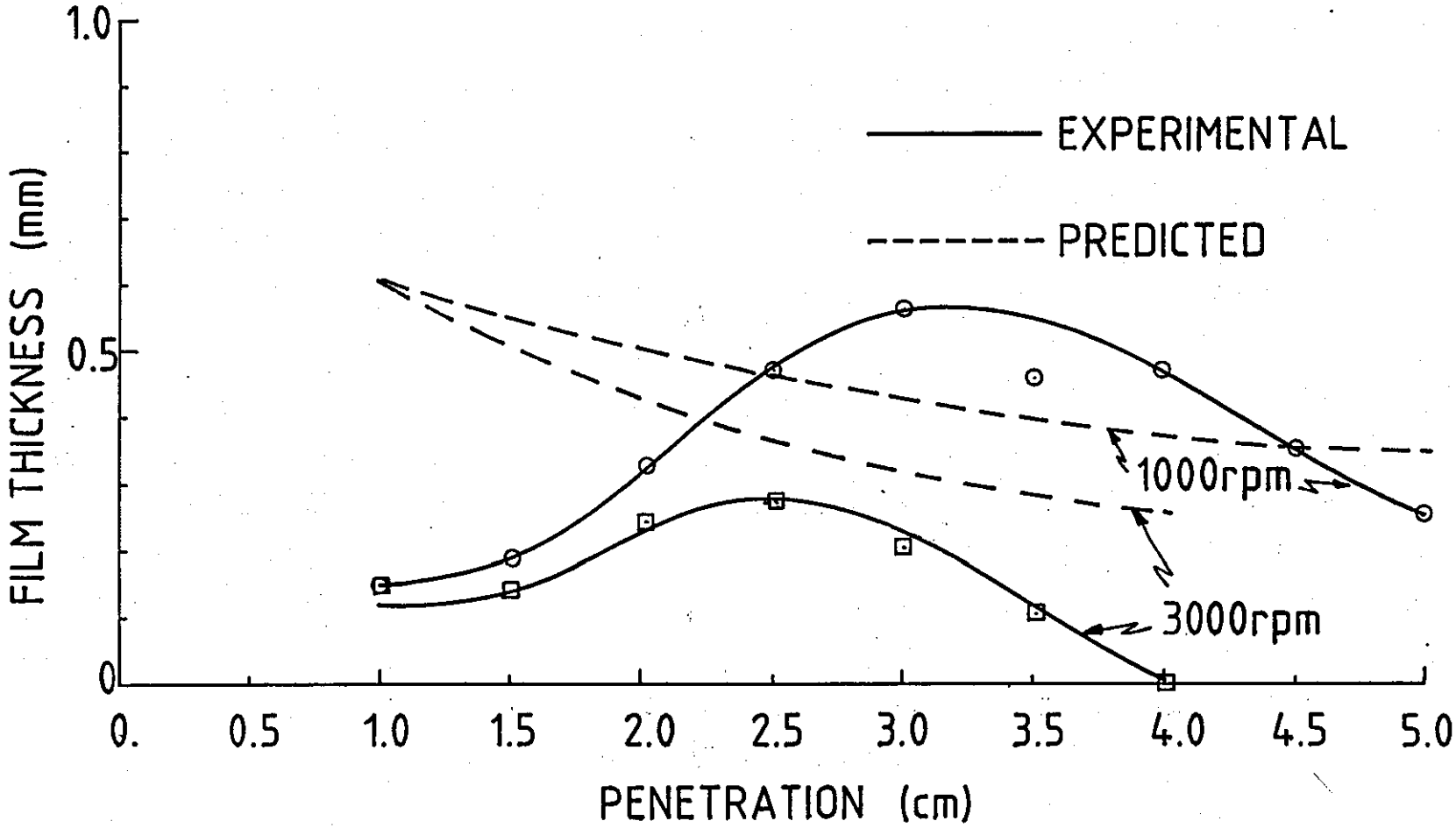

FIGURE 5.25: MEAN FILM THICKNESS ALONG THE AXIS OF THE WETTED AREA

FIGURE 5.26: RIPPLE FORMATION ON THE FILM SURFACE

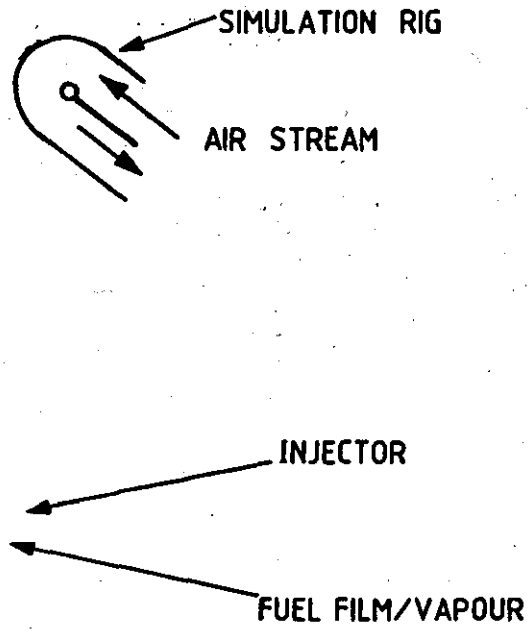
SIMULATION RIG
AIR STREAM
INJECTOR
FUEL FILM/VAPOUR

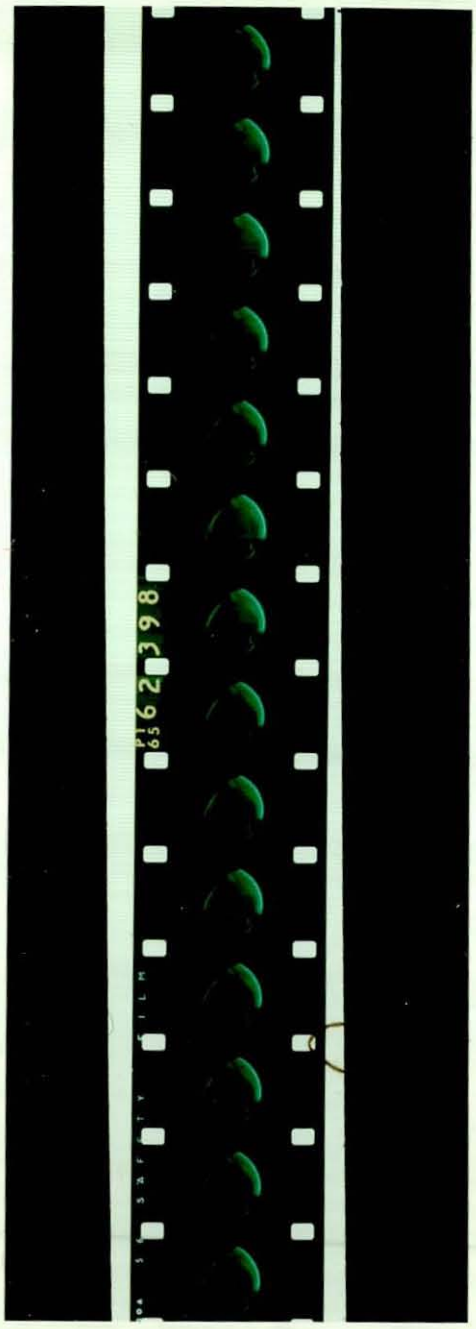

Figure 5. 27. Typical sequence of High Speed Schlieren photographs.
Fuel Vapour appears as a Light Streak on the left of the frame

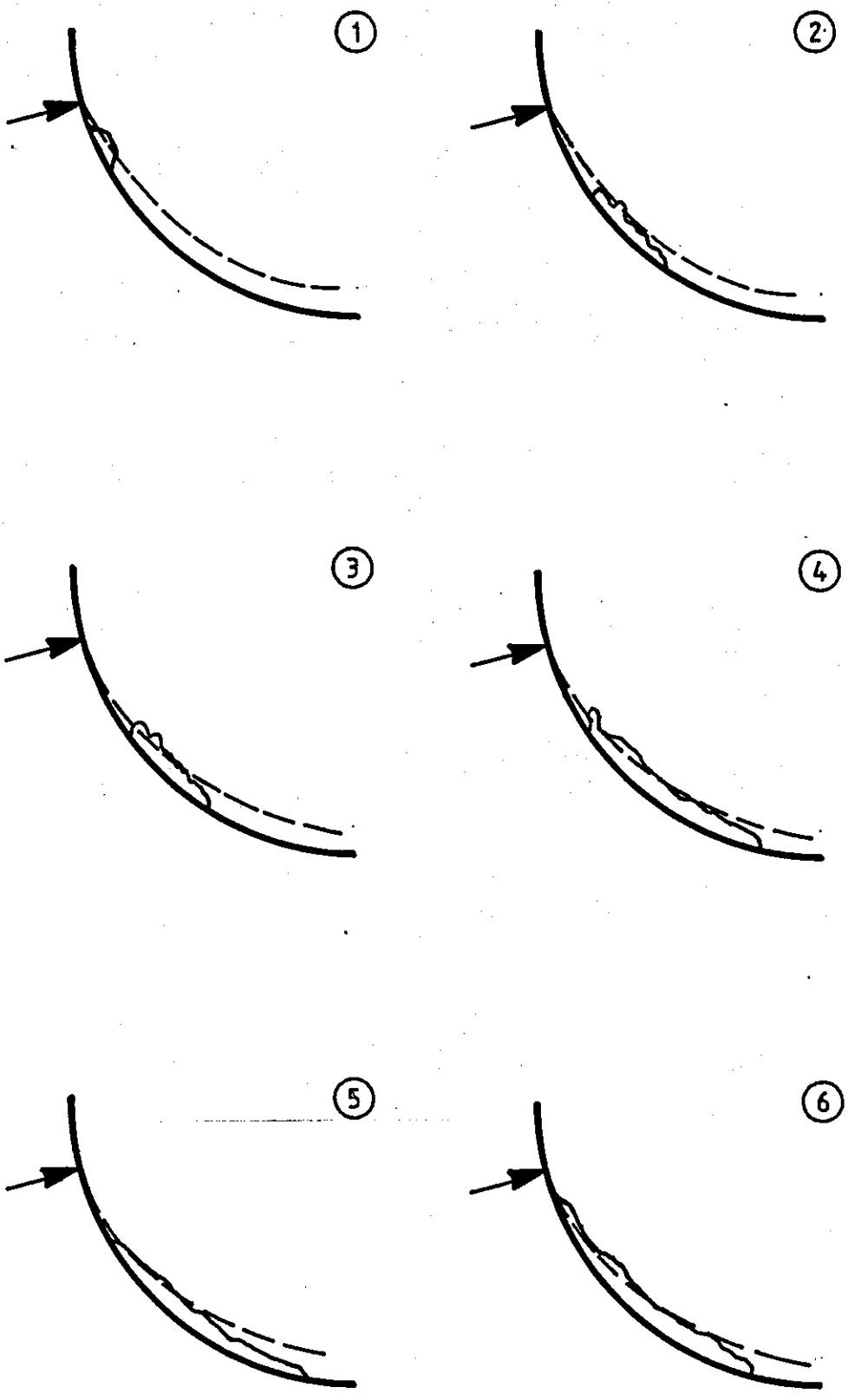

FIGURE 5.28: COMPUTED AND EXPERIMENTAL VAPOUR DIFFUSION DURING INJECTION

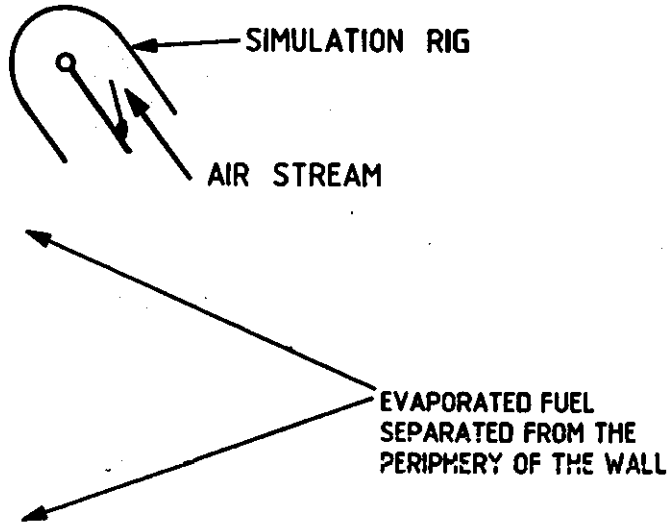
SIMULATION RIG
AIR STREAM
EVAPORATED FUEL
SEPARATED FROM THE
PERIPHERY OF THE WALL

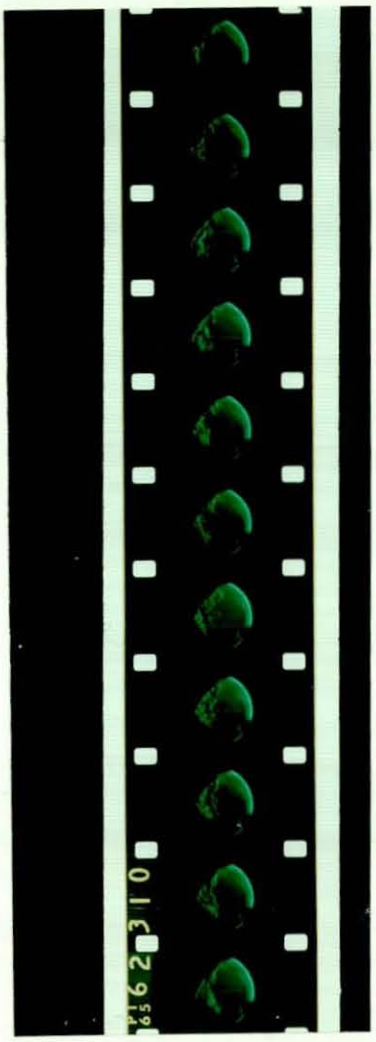

Figure 5. 29. Schlieren High Speed Photographs showing Flow Separation in the Simulation Rig

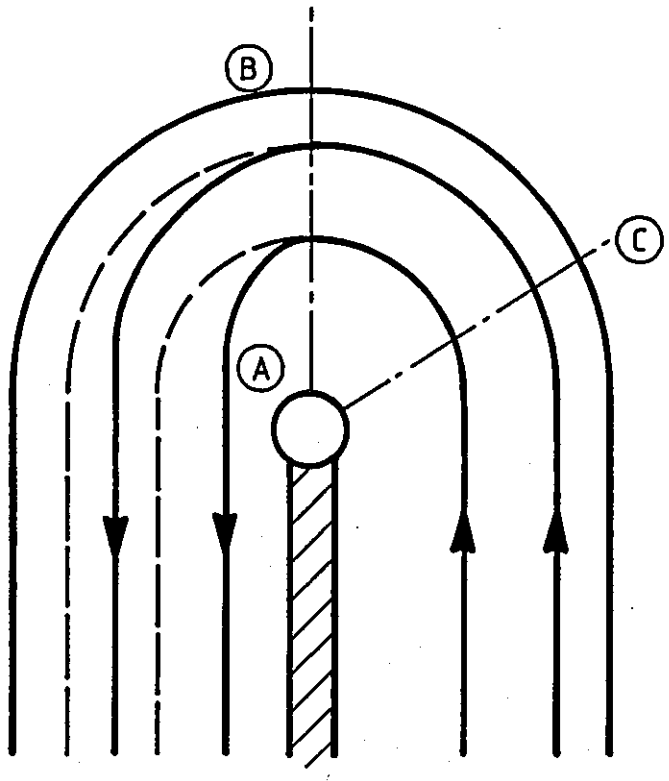

FIGURE 5.30: STREAMLINES IN THE SIMULATION RIG

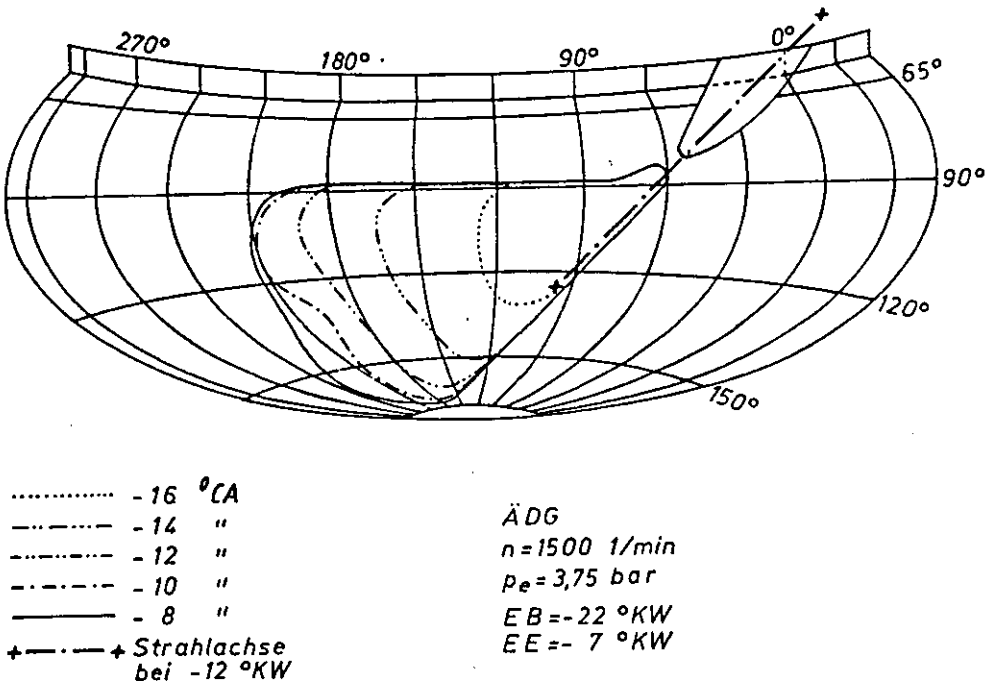

FIGURE 5.31: DEVELOPMENT OF THE INJECTED FUEL FILM (41)

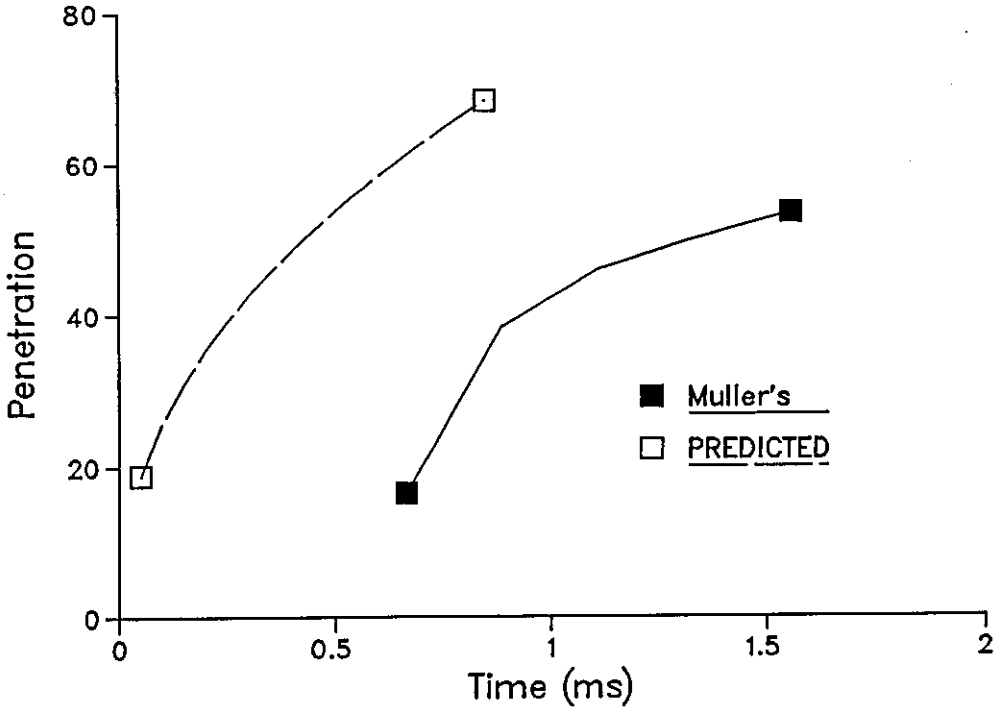

FIGURE 5.32: QUALITATIVE COMPARISON FOR PENETRATION IN THE ENGINE

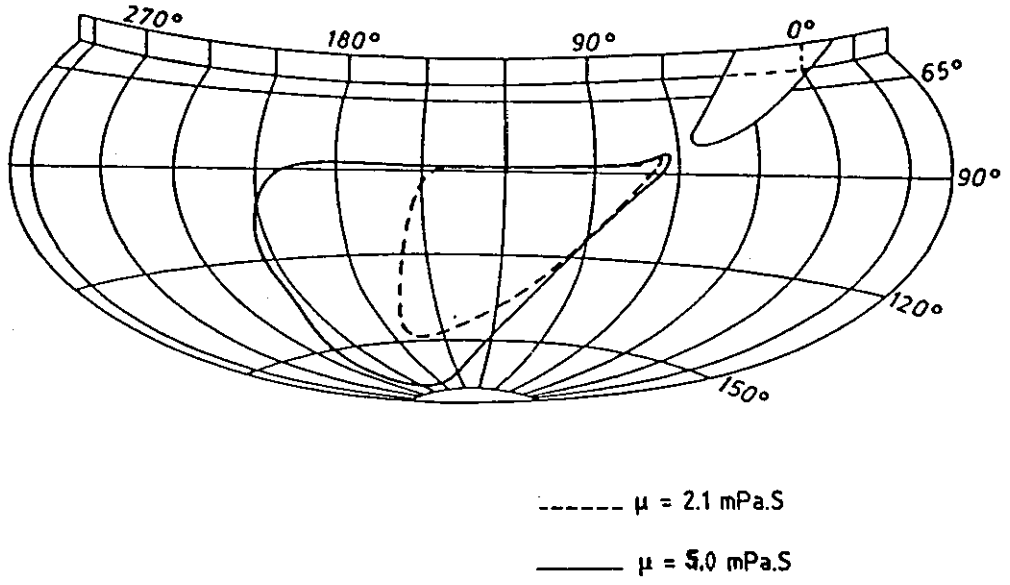

FIGURE 5.33: EFFECT OF FUEL VISCOSITY ON DEVELOPMENT OF THE FILM (41)

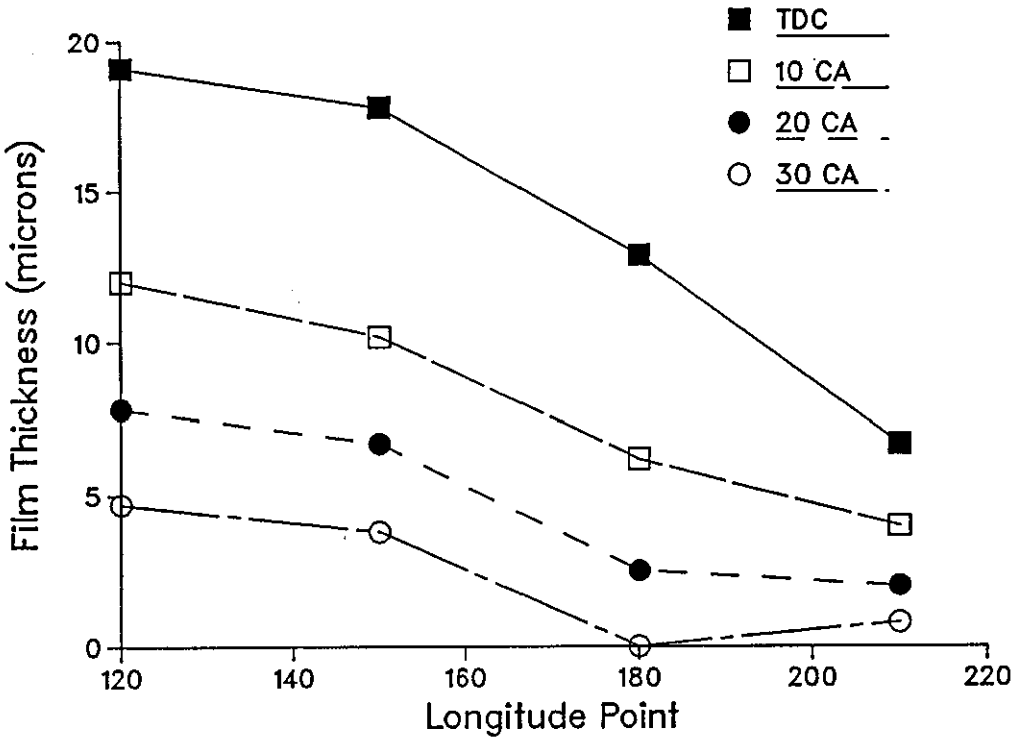

FIGURE 5.34: FILM THICKNESS PROFILES FROM MULLER'S DATA

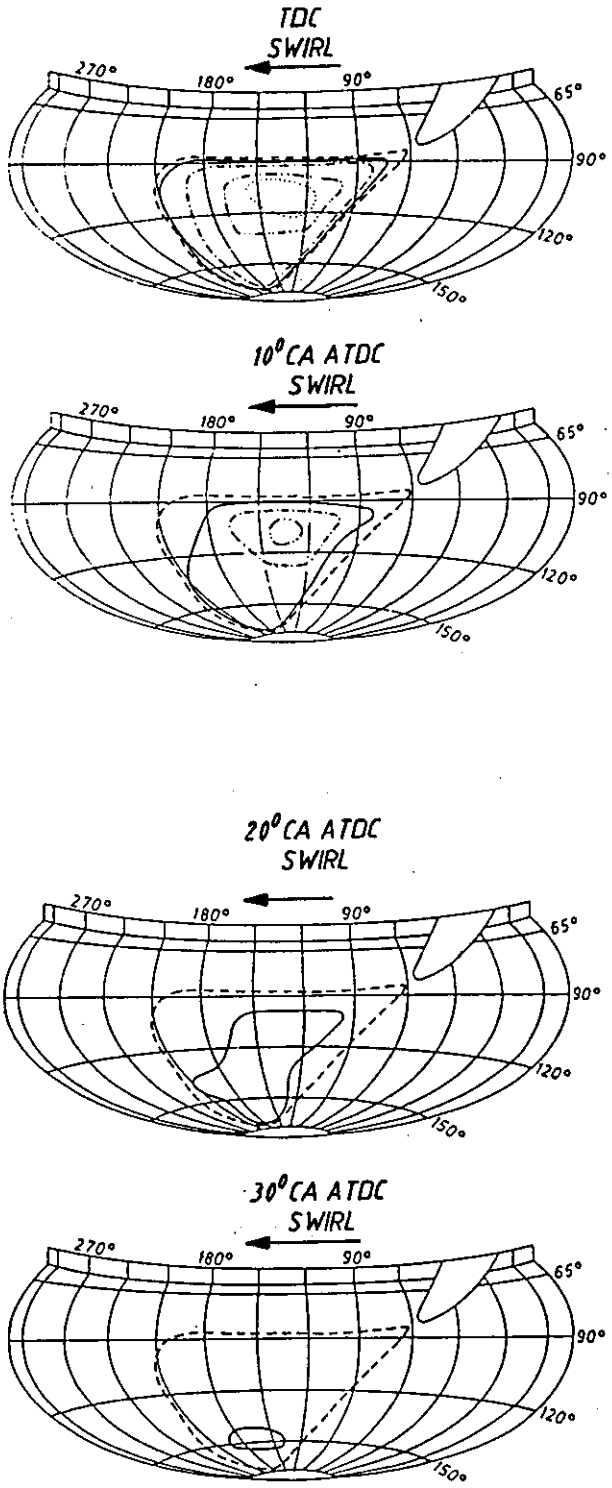

FIGURE 5.35: EVAPORATION OF THE FUEL FILM IN THE ENGINE (41)

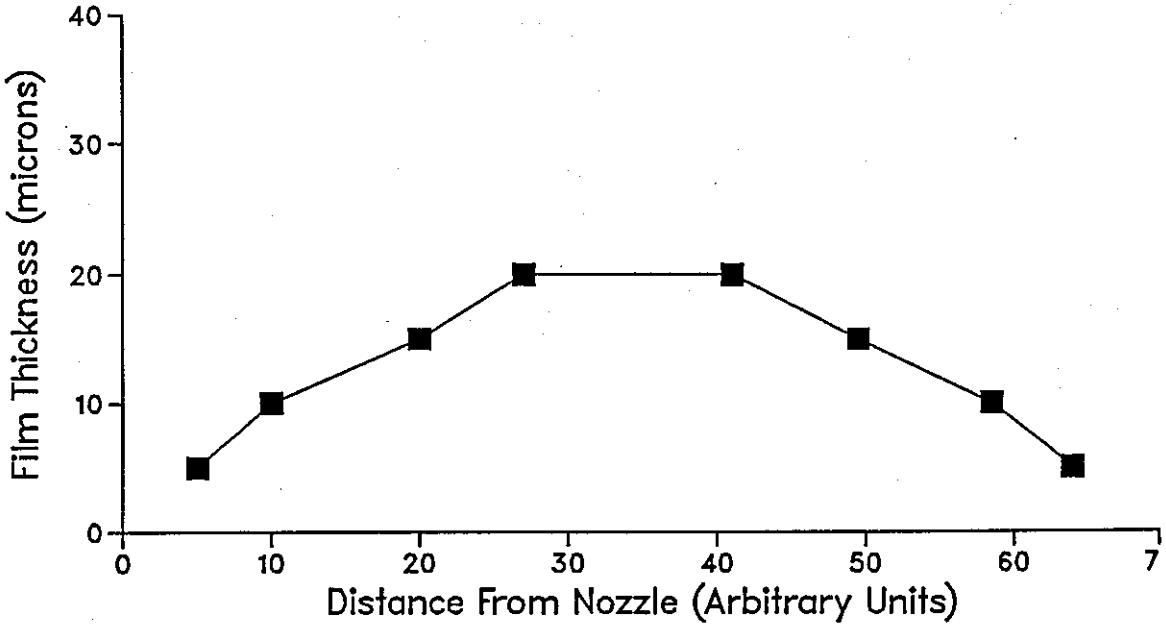

FIGURE 5.36: FILM THICKNESS ALONG JET AXIS (MULLER'S DATA)

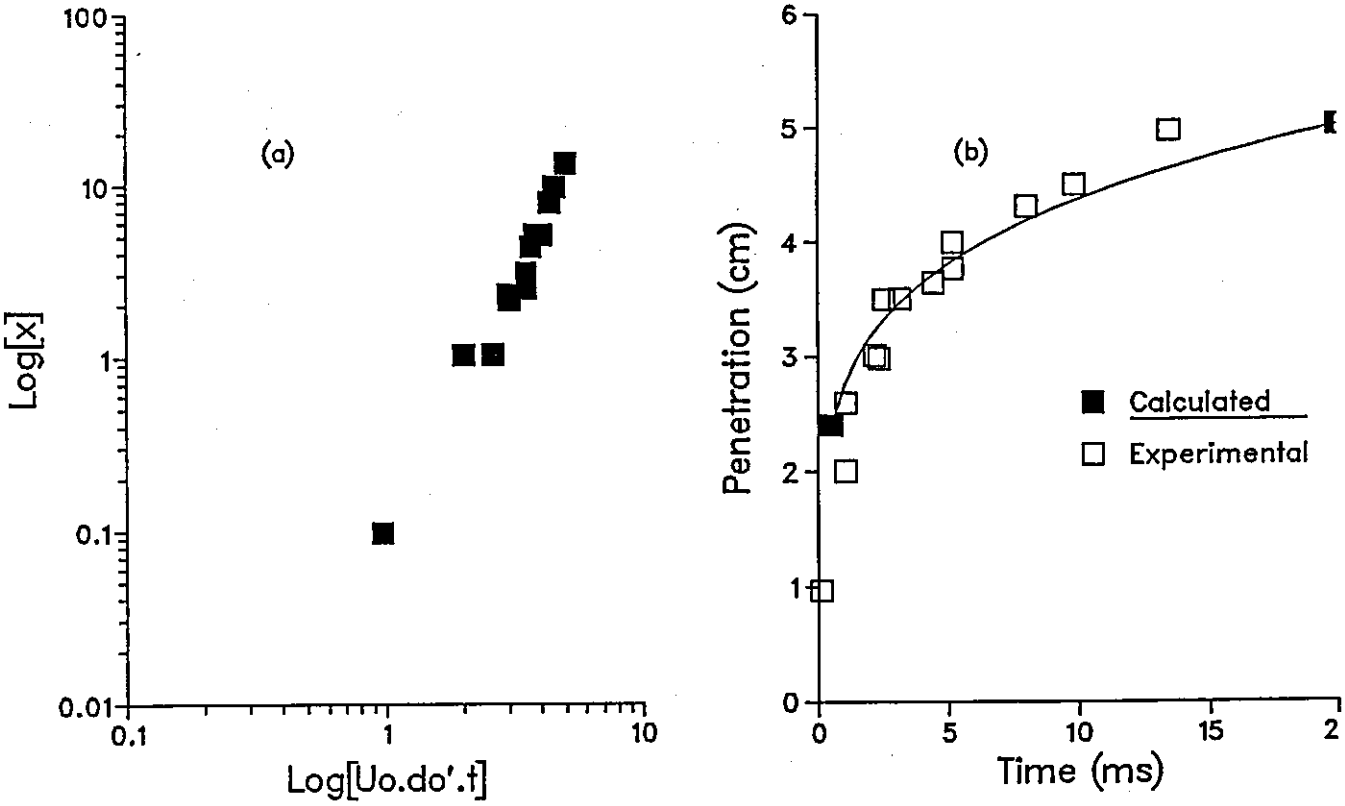

FIGURE 5.37: LOGARITHMIC CORRELATION FOR PENETRATION

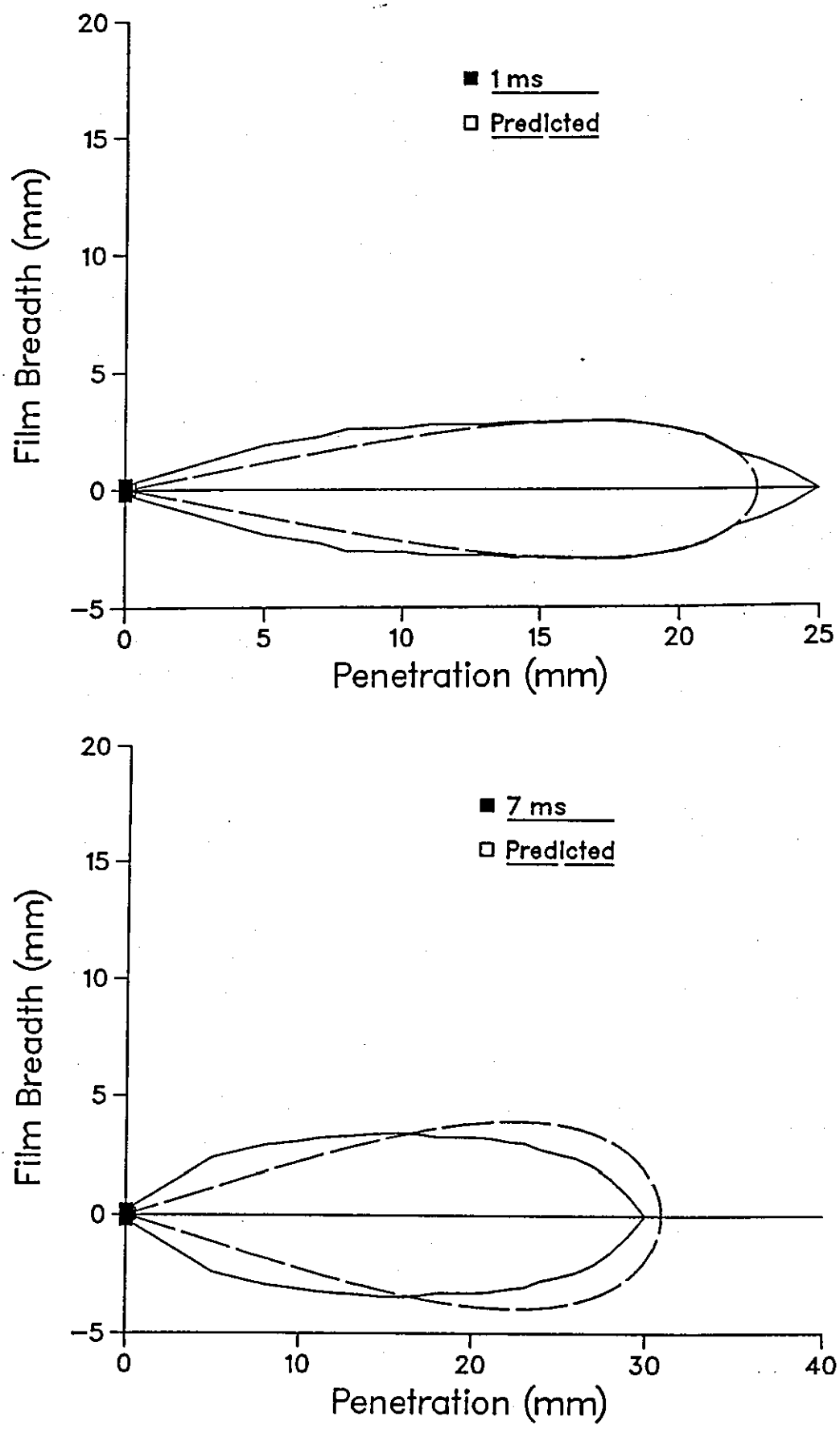

FIGURE 5.38: NEW PREDICTIONS FOR WETTED SURFACE AREA WITH MEASURED DATA

(a) Without Evaporation

(b) With Evaporation

FIGURE 5.39: TYPICAL PAIR OF PHOTOGRAPHS ILLUSTRATING EFFECT OF EVAPORATION (7.08 ms from injection)

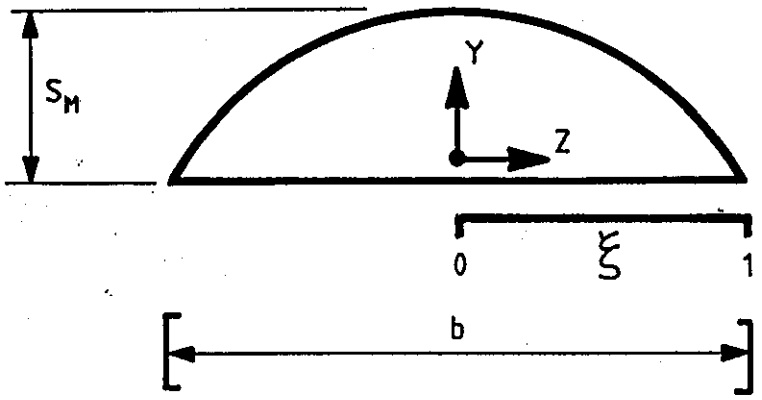

FIGURE 5.40: NOMENCLATURE FOR FILM THICKNESS CROSS SECTION

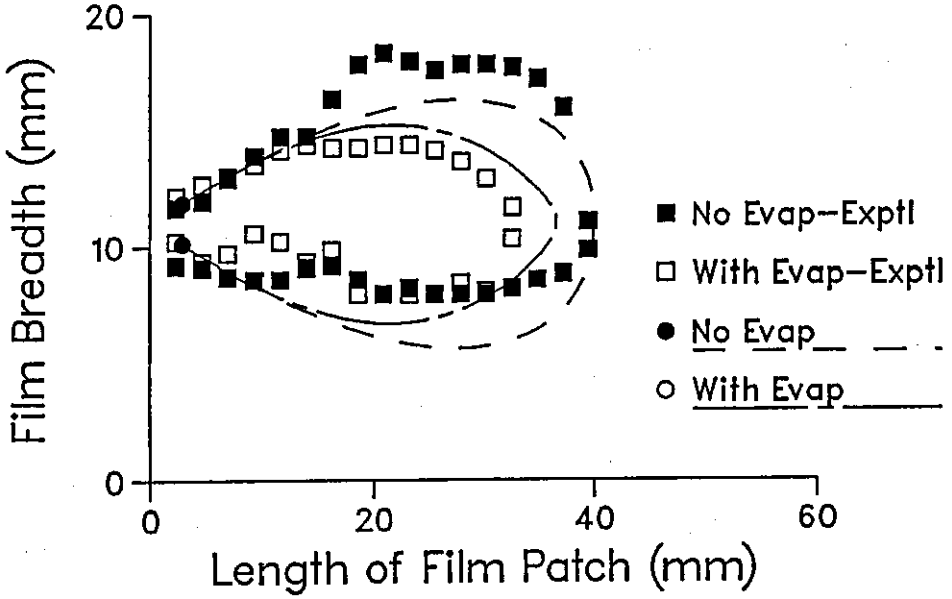

FIGURE 5.41: EVAPORATION OF THE FILM AFTER 7.08 ms

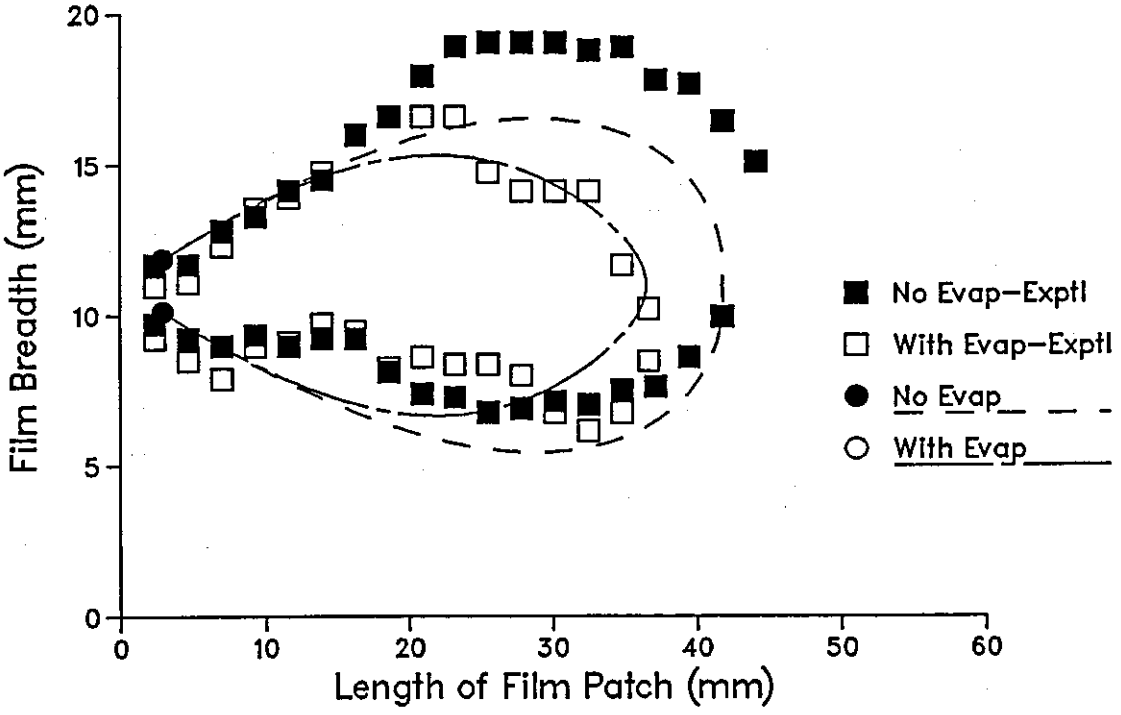

FIGURE 5.42: FILM EVAPORATION AFTER 8.96 ms

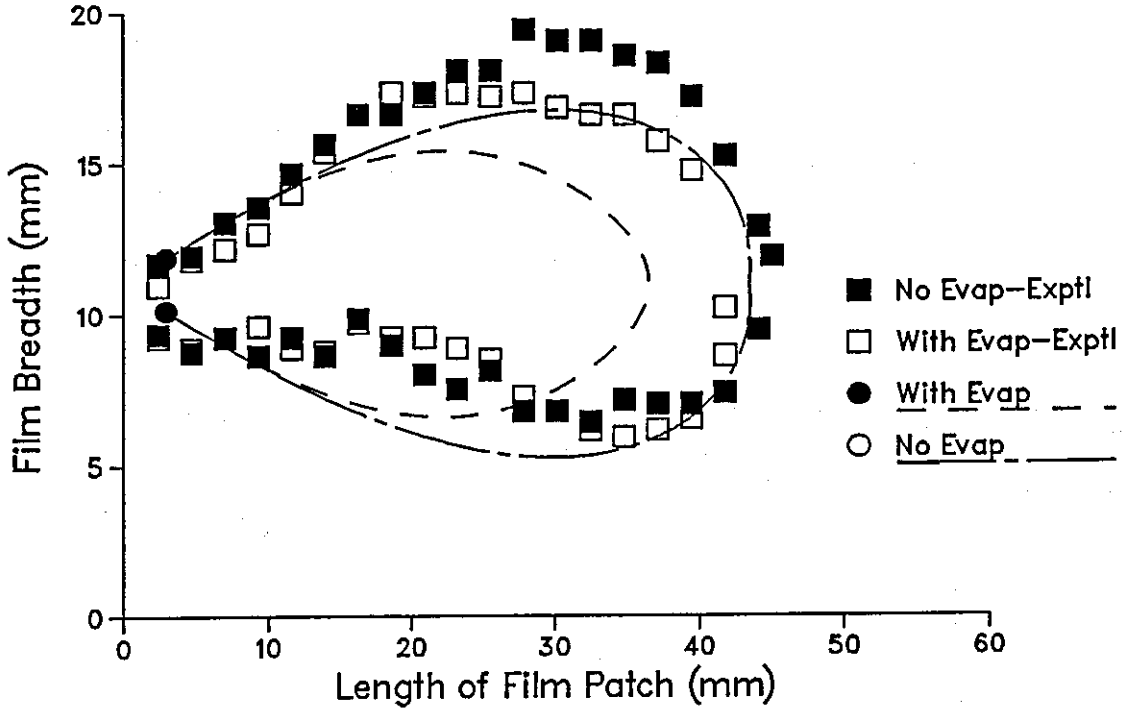

FIGURE 5.43: FILM EVAPORATION AFTER 10.98 ms

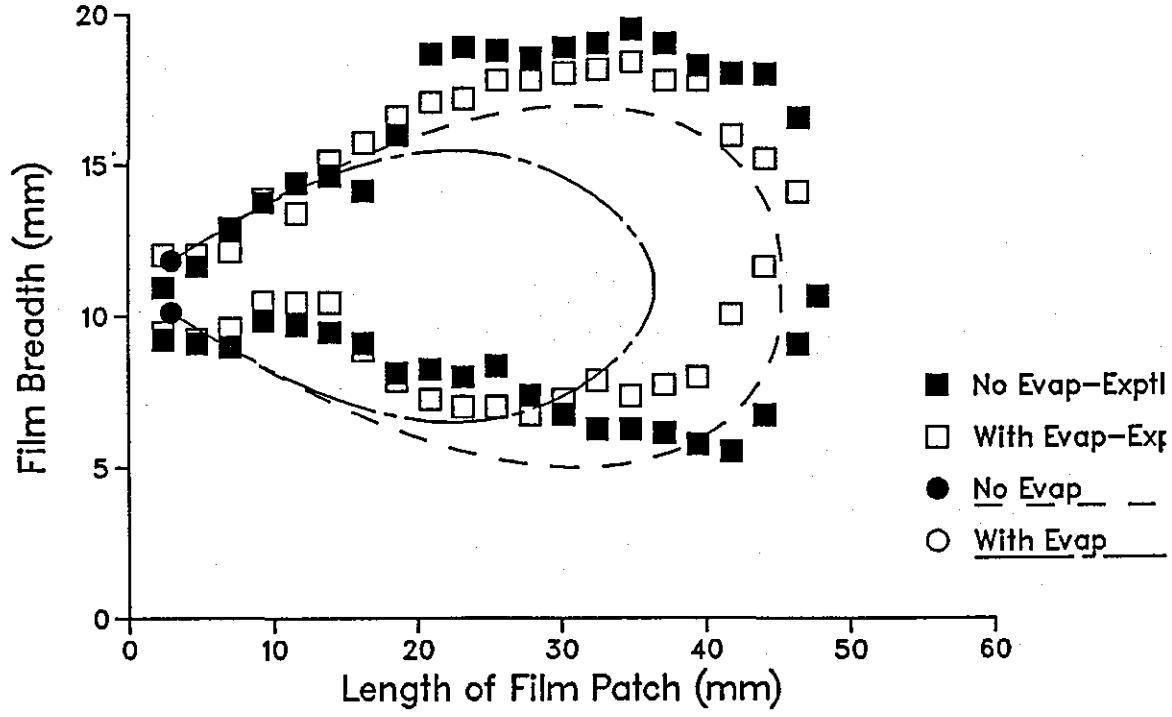

FIGURE 5.44: FILM EVAPORATION AFTER 13.4 ms

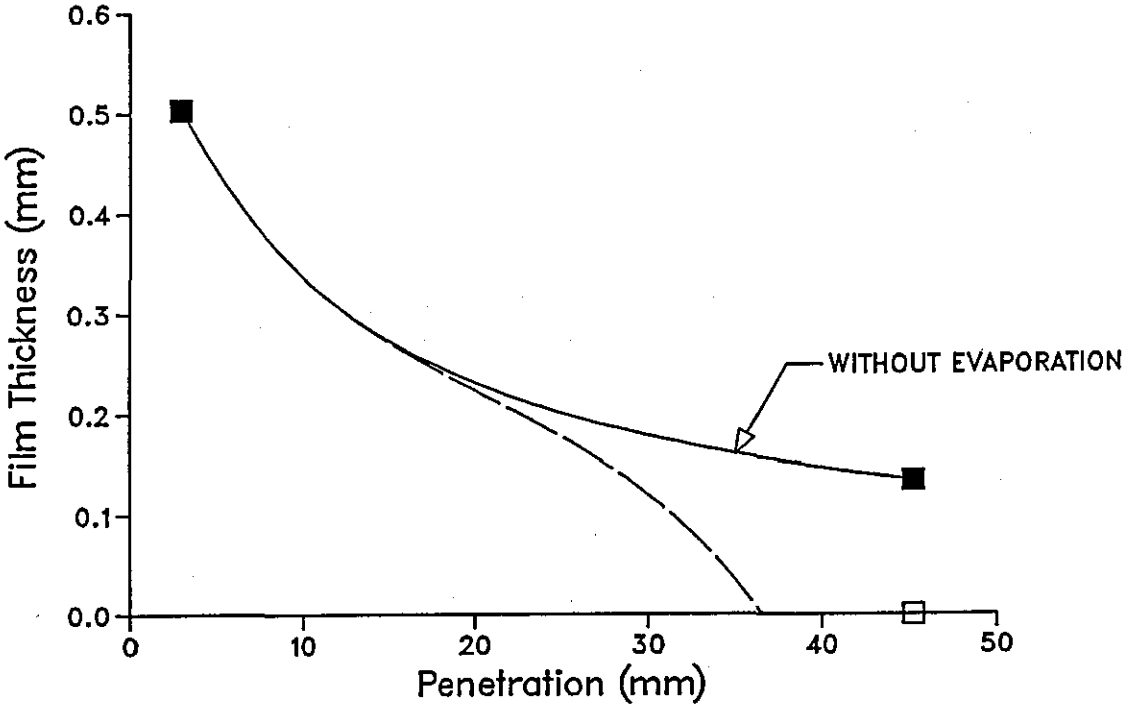

FIGURE 5.45: EFFECT OF EVAPORATION ON FILM THICKNESS

CHAPTER 6

STRUCTURAL OUTLINE OF THE COMPUTER PROGRAM

6.1 INTRODUCTION

The computer code for the simulation program was developed on the Honeywell 'Multics' mainframe computer, in standard FORTRAN 77. The source code is organised in a modular structure made up of several independent subroutines, each dealing with a specific aspect of the simulation. The flexibility of this source organisation allows the program to be developed in stages so that each module can be tested independently, and updated versions can be easily incorporated. This advantage was well demonstrated in an earlier version of the model (8) in which the iterative technique used to evaluate the equilibrium composition of the combustion products slowed down the running of the program. An option to bypass the NO_x routine was thus incorporated so that the program could be implemented to investigate other variables and parameters at a higher computational speed.

The general structure of the basic program is identical to that developed by Mehta (2) for the quiescent chamber DI Engine. The major differences between the existing swirl model and the proposed model will become apparent in this chapter as the structure of the program is discussed.

This chapter is divided into three major sections to allow for a systematic discussion of the structure of the program. The first section presents a general overview of the program. The second deals with the detailed structure of the program, giving brief discussions of the major subroutines and illustrating some of the essential inter-relationships with flow-charts. The final section presents three sample terminal dialogues, and discusses some of the screen-displayed results.

6.2 THE COMPUTER PROGRAM

Figure 6.1 shows a generalised flow-chart of the computer program. To initiate the operation of the program, input data must be supplied to specify engine dimensions and required load conditions. In order to provide the data in an acceptable format to the computer, there is a provision for creating input data-files interactively. This forms part of the 'Introductory Front-End' discussed earlier in Chapter 2.

Once an input data file has been loaded, the program proceeds to calculate a number of variables that constitute the results of the simulation model. Fuel injection simulation may be achieved in either of the following two ways:

a) Providing an injection pressure diagram obtained experimentally on an engine with identical dimensions, and under identical load conditions.

b) Making use of the volume of fuel injected per stroke to construct a trapezoidal injection pressure diagram with a mean injection pressure calculated from equation (6.1), as suggested by Dent(19):

$$\Delta P_{inj} = \frac{2\rho_f}{\pi C_d} \left[\frac{6NQ}{nd_o^2\theta_{ip}}\right]^2 \qquad (6.1)$$

where C_d = Injector nozzle discharge coefficient
θ_{ip} = Injection duration in degrees crank angle
Q = Volume of fuel injected (mm^3/STROKE)

From the injection pressure diagram, the program calculates the velocity of the jet at the nozzle and corresponding characteristics of the fuel film as the fuel jet impinges and flows along the piston wall. The crucial dimensions being the film thickness, the wetted surface area, and the film velocity. The latter, in conjunction with the bulk stream velocity are required to determine the level of

evaporation from the film surface.

The boundary layer theory discussed in Chapter 4 forms the basis of analysis for mixture formation process in the model. Stoichiometric combustion is assumed to be the only form present. To facilitate the analysis, the boundary layer thickness is divided into ten zones of equal width, each forming a combustion sector that is analysed separately. Figure 6.2 shows a schematic representation of the sectors in the burning zone. Over each discretised time step (Δt), heat and mass balance calculations are carried out in each individual sector. Within each sector, combustion is assumed to proceed independently of that occuring in adjacent sectors. The air entrained in the interval Δt is distributed throughout the sectors according to the (1-C) - profile, where the C-profile, illustrated in Figure 6.2 and defined by equation (4.32), refers to the fuel mass fraction profile. Mass conservation at each time step is satisfied when the following equations hold:

$$m''_{air} = \sum_i (1 - C_i)\, \rho_i\, U_i \qquad (6.2)$$

$$m''_f = \sum_i C_i\, \rho_i\, U_i \qquad (6.3)$$

The density, ρ_i is assumed to be linearly proportional to the fuel mass fraction, so that:

$$\rho_i = \rho_a + (\rho_f - \rho_a)\, C_i \qquad (6.4)$$

Following the theory outlined in Chapter 4, when combustion is present the sectors are further subdivided into two groups; those lying below the position of the flame, and those lying above it. For simplicity, the sector containing a mixture closest to stoichiometric is assumed to constitute the flame position, although calculations for heat

release are carried out in all the sectors simultaneously. This allows for the temperature profile to be related to the concentration profile. The energy released in all the sectors due to combustion is integrated to yield total energy released in the burning zone, before the energy balance equations outlined in Chapter 2 are applied to the two regions (i.e. burning region and surrounding air). Thus two values of temperature are computed at each crank angle; T_j, the mean temperature of the burning region, and T_a, the temperature of the surrounding charge. The mean cylinder temperature is then calculated from the following mass mean equation:

$$T_{ch} = \frac{m_a.T_a + m_j.T_j}{m_a + m_j} \qquad (6.5)$$

where m_a and m_j are the respective masses in the surrounding charge and the burning zone. For purposes of calculating exhaust emissions, the temperature T_j is used as it refers to the region where all the kinetic reactions take place. The volume of the burning zone is one of the four variables calculated from the energy balance equations. Cylinder pressure is the fourth variable. The heat transfer coefficient between the charge mass and the cylinder walls is determined from Woschini's correlation (87).

The modelling of soot, which is based on the equations of Tesner et al (71) and Magnussen's (72) eddy-dissipation concept (details of which were outlined earlier in Chapter 2) is defined in such a way that it can be applied to each sector in the burning zone. The variables necessary for such operation are:

1. Local temperature (based on the assumed profile)
2. Local mass concentration of the following:
   - unburnt fuel vapour
   - combustion products
   - air
3. Partial pressures of oxygen and water vapour (for the oxidiation equations).

An alternative approach is to invoke the soot routine with global mean values in the burning zone. This results in a more generalised analysis which is not sensitive to assumed velocity and scalar quantity profiles in the gaseous stream. As a result, it is only used after the profiles have been tested for accuracy within the range of conditions being considered. The advantage here is that computation time is significantly reduced since to determine partial pressures of O_2 and H_2O in the various sectors, the equilibrium composition routine must be invoked ten times at each time step. As has been discussed in Chapter 2, this involves solving 4 non-linear simultaneous equations by the iterative Newton-Raphson technique. The process is, therefore, time consuming.

The formation of NO in diffusion as well as pre-mixed flames is several orders of magnitude slower than the main heat release reactions (123) and so is kinetically limited. The slow mechanism postulated by Zel'dovich is widely accepted as a fairly accurate description of NO formation. This mechanism and the method of solution employed in the model, have been discussed in detail in Chapter 2.

Implementation of the NO routine in individual sectors is much more critical than the implementation of the soot subroutine. This is because NO formation is strongly dependent on temperature and mixture fraction, both of which are highly localised. The following is a list of variables that are required to implement the NO-routine in each sector:

i. Pressure (assumed uniform throughout the cylinder)
ii. Local temperature
iii. Local equivalence ratio.

The scheme used to determine equilibrium composition is based on the program developed by Olikara and Borman (122). The original program does not calculate equilibrium composition in rich sectors, and

returns instead, a statement to the effect that solid carbon would form, making a solution impossible to achieve. To get round this problem, equivalence ratio of 1 is assumed in all the rich zones (consistent with the assumption of a simple chemically reacting system), and calculation is based only on the fixed mass of products resulting from stoichiometric combustion.

The net soot and NO_x formed at each crank angle are integrated throughout the closed period. At the opening of the exhaust valve, the integrated quantities are corrected to normal temperature and pressure (NTP) and the resulting values are displayed on the screen to show the level of exhaust emissions in the engine while operating under the conditions at which the simulation has been carried out.

The Exhaust/Induction model which has been discussed in detail in Chapter 2, is based on isentropic flow equations derived by Sherman and Blumberg (86) and the energy balance equations derived by Horlock and Woods (87). It is activated once the exhaust valve opens and calculates mass flow rates out of the cylinder during the exhaust stroke, and also into the cylinder during induction. In order to ensure that pressure and temperature at the start of exhaust and end of induction are matched with corresponding values calculated in the combustion model, the Exhaust/Induction model is iterated using charge mass as the criterion. The benefit of incorporating induction and exhaust calculations within the model is that the indicated mean effective pressure, power output and the specific fuel consumption may be calculated, and also valve timing effects may be investigated.

The results at the end of each simulation are presented in two ways. Instantaneous values corresponding to each crank position are written to file during the running of the program. These are then used to provide graphical presentation of the variables with crank angle. The following is a list of parameters that are given in this way:

1. Cylinder pressure
2. Temperature of the burning zone

3. Mean charge temperature
4. Cumulative quantity of fuel injected
5. fuel mass fractions:
   - Evaporated
   - Burned
6. Heat release rate
7. Heat flux between cylinder contents and the walls
8. Equilibrium concentration of NO_x
9. Kinetically controlled NO_x formation
10. Instantaneous net soot formed
11. Air entrainment rate.

The second method is to display results on the screen at the end of the simulation run. Cummulative values of exhaust emissions, and performance related variables are presented in this way. Also presented is a summary of the input load conditions under which the model has been operated.

6.3 DETAILS OF ESSENTIAL SUBROUTINES

To illustrate how the theory developed in Chapters 3 and 4 has been linked together to form a coherent simulation model, it is necessary to describe some of the subroutines in more detail. From Figure 6.1 it is apparent that the first four subroutines are concerned with the initialisation of variables and the preparation of the program for simulation. These have been classified together below under Section 6.3.1.

6.3.1 Initialising Subroutines

The following is the list of subroutines concerned with the input and initialisation of data before simulation:

i) SPEC
ii) READ

iii) PREINJ

iv) INICAL

SPEC:

This is part of the 'Introductory Front-End' in the main program, which has been discussed in Chapter 2. Its main purpose is to establish an interactive dialogue with the user, guiding the creation of a SPECification input data file. The flow chart in Fig. 6.1 shows that it is only called when new specifications are to be supplied and operates according to the schematic flow-chart in Fig. 6.3. The required input parameters to the subroutine will be demonstrated in a sample terminal dialogue in Section 6.4. The first question on the flow-chart in Fig. 6.3 implies that if the dimensions of the engine to be modelled are identical to those supplied earlier (on a file that must still exist), then by entering the file name the computer copies the relevant data from that file into the new name. So only the new load conditions need be supplied. In this way, setting-up time is minimised for studying identical or the same engine under various operating conditions. The data relating to each condition investigated is automatically saved under a filename supplied by the user so that subsequent runs of the same engine under conditions already supplied during an earlier run does not call subroutine SPEC.

READ:

Subroutine READ is called every time the program is run. Its sole purpose is to read data from files already created by the user using subroutine SPEC. The subroutine also reads in values of the experimental injection pressure diagram when this is to be used.

No input data is required into this subroutine, and all the data read from file here are carried through to the rest of the program by means of common blocks.

INICAL:

Before subroutine INICAL is executed, subroutine PREINJ carries out monitoring computations for the period prior to injection. This is essentially done in order to calculate pressure and temperature at the start of the injection. Subroutine MOTOR is used by PREINJ to compute the motoring variables from the closure of the inlet valve to the start of injection. Once the crank angle equals the supplied experimental value for dynamic injection timing, subroutine INICAL is called from the main program. Its usage is to initialise all the variables that require initialising and also to assign value of zero to all counters and indicators.

6.3.2 Fuel Spray and Film Development

Modelling computations are initiated at the start of injection once the initialisation of variables is completed. With the start of injection, it becomes necessary to characterise the formation and development of the fuel film. The two subroutines that perform this task in the model are:

i. FILM
ii. FILM2

FILM:

The first time subroutine 'FILM' is invoked, the user is offered an option in fuelling from the following:

1. Experimentally obtained injection pressure diagram
2. Sinusoidal fuelling rate (discussed in Chapter 2)
3. Trapezoidal injection pressure diagram.

The first option is, obviously, only available if a digitised injection pressure diagram exists in a data-file accesible to the computer, at the condition to be modelled.when the crank angle being considered has no corresponding value of injection pressure in the digitised diagram, a linear interpolation is performed by the subroutine. Extrapolation either side of the supplied curve is not undertaken, and the computer prints out an error message. This acts as a safe-guard against using the wrong injection pressure diagram.

When the third option is selected, the user is asked to specify a scheduling ratio. This refers to the ratio rs given in Figure 6.4. Values of rs greater than 0.5 are rejected (an error message is printed) since only symmatrical trapezoids are currently considered. Whatever value of rs is selected, the routine is written in such a way that the injection pressure adjusts to yield the correct quantity of injected fuel over the specified duration. The subroutine calculates the following major variables:

1. Injection pressure (unless experimental is being used)
2. Injection velocity at the nozzle
3. Quantity of fuel injected over the interval Δt.

It should be noted here that in the wall-wetting type engine, the actual shape of the injection pressure diagram does not have a strong influence on the course of combustion which is predominantly wall-type diffusion burning. Only the injection pressure (a mean value would thus be adequate), the quantity of fuel injected, the injection duration, and the dynamic timing have direct and observable effects.

FILM2:

This subroutine evaluates all the essential dimensions of the fuel film necessary for estimating fuel evaporation rate. The required input data to the subroutine are:

i. Elapsed time since start of injection

ii. Fuel spray velocity at the injector nozzle, calculated in FILM.

The subroutine returns the following parameters relating to the crank position under consideration:

i. Penetration of the film along the piston wall
ii. Mean film velocity
iii. Mean Film thickness
iv. Surface area wetted by the film on the piston wall

It may also be possible to obtain a shape for the injected fuel film patch, although this is not usually necessary, and so is presently not evaluated.

The significance of values evaluated in this subroutine lies in their influence on the rate of evaporation. The wetted surface area, for example, is necessary for determining the mas of fuel evaporated in time interval Δt as illustrated below:

$$m_f = A_f . \dot{m}'' . \Delta t \qquad (6.6)$$

where $\dot{m}''$ is the mass flux from a fuel film with surface area A_f.

6.3.3 Mixture Preparation Subroutines

Once the nature of the fuel film has been characterised in a quasi-steady mode, a number of essential variables that collectively constitute mixture formation are then calculated. The following list briefly describes the procedure used to specify mixture formation:

- Evaluation of fuel film temperature
- Determination of the saturation vapour pressure on the film surface
- Determination of heat and mass transfer levels between the bulk air stream, film surface and the boundary layer

- Finally determination of the velocity and scalar quantity profiles in the gaseous boundary layer above the film.

Several subroutines are involved in the calculations for formation of the combustible mixture, among which the following are the most significant:

i. EVAP1
ii. BOUND
iii. EVAP2
iv. ZEL

As the rates of heat and mass transfer are strongly influenced by the presence of combustion, an auxilliary subroutine - AUXMN - performs the task of directing the combination of routines for either the 'pre-ignition' period, or that during combustion. Figure 6.5 illustrates the working of subroutine AUXMN. The determination of mixture formation at each crank position starts with subroutine ZEL. This computes parameters Z_E, 1, S, and E (see Chapter 4) necessary for determining velocity and scalar quantity profiles, and the entrainment of air in the boundary layer. The process involved is iterative, taking in values of mass transfer number, B, bulk stream velocity, U_G, and charge temperature to yield the required parameters. The profiles for mass fraction and velocity in the boundary layer are calculated in subroutine BOUND and EVAP1 during the 'pre-ignition' period, and in EVAP2 during combustion.

6.3.4 Combustion and Energy Balance

Subroutine EVAP2, beside calculating air entrainment rate, film evaporation, and velocity and scalar quantity profiles, also calculates the following variables relating to combustion for each sector in Figure 6.2:

i. Heat release rate

ii. Fuel mass fraction burned
iii. Temperature profiles in the boundary layer.

To satisfy the non-flow energy equation and the semi-perfect gas law between the burning region and the surrounding charge, according to the conceptual framework discussed in Chapter 2, subroutine ENEBAL is used to organise the equations in matrix form, and Subroutine GAUSS is then called to solve the equations using Gaussian elimination, to provide increments in the following variables:

i. Cylinder pressure
ii. Temperature of burning zone
iii. Temperature of the surrounding charge
iv. Volume of the burning zone.

6.3.5 Exhaust Emissions

The following subroutines dealing with engine exhaust emissions (NO_x and smoke) are invoked after the combustion related parameters are calculated:

i. SOOT - solves the equations of Tesner et al (71)
ii. SMOX - soot oxidatin according to the theory discussed in Chapter 2.
iii. NITRO - solves kinetic equation for NO formation
iv. ECP - calculates equilibrium composition in the exhaust.

The major input parameters into subroutine SOOT are:

1. Temperature of the burning region (or local temperature in a sector when the routine is invoked from the sectors).

2. Concentrations of fuel and air.

The screen-displayed output from the routine is grams of soot per

cubic metre of cylinder charge while instantaneous values of formation and oxidation rates calculated at each crank angle are written into a data file. At the opening of the exhaust value, net soot formed is corrected to Normal Temperature and Presure (NTP) and then converted to Bosch units by subroutine BOSCH which interpolates from the values in Table 6.1. The BOSCH value is also screen-displayed.

NO_x Routine:

The routine for determining NO_x emissions is in two parts: calculation of equilibrium composition of combustion products at the pressure and temperature pertaining in the burning zone, and the solution of the kinetic rate differential equation. Subroutine ECP evaluates equilibrium compositions necessary in the solution of the kinetic rate equation which is solved using a 4th-Order Rumge-Kutta scheme.

6.3.6 Exhaust/Induction Routine

The final stage of the model calls subroutine EXHA which carries out calculations relating to the gas exchange process (open period). The input variables from the main program are:

i. Valve timings
ii. Cylinder dimensions
iii. Pressure and temperature at the opening of the exhaust valve.

The subroutine then returns instantaneous values of outgoing mass increment (dm_{ex}) and incoming mass increment (dm_{in}) with a provision to account for backflow in either valve. The inlet and exhaust manifold pressures and temperatures are assumed constant and the following are the major variables returned by the subroutine:

i. Cylinder charge mass (criterion for iteration procedure)

ii. Pressure
iii. Temperature

The model is thus prepared for the next cycle, thus offering a means for undertaking multi-cyclic modelling.

6.4 SAMPLE INTERACTIVE TERMINAL DIALOGUES

The sample terminal dialogues presented in this section show the three available ways in which the simulation program may be implemented:

i. Loading new engine dimensions
ii. Maintaining engine dimensions, but varying load conditions
iii. Repeating certain load conditions already on file.

The objective filename used here is 'wwe', standing for 'wall-wetting-engine'.

6.4.1 Loading New Engine Dimensions

In the remainder of this section words typed by the user are shown in lower case while computer responses are printed in upper case except where dimensional units are indicated. The following is a typical dialogue to run the program and specify new engine dimensions and load specifications:

```
wwe

THIS PROGRAM SIMULATES WALL-WETTING DIESEL ENGINE COMBUSTION.
ENGINE DIMENSIONS AND OTHER OPERATING CONDITIONS ARE READ FROM
EXTERNAL FILE BY ENTERING THAT FILENAME.  IF YOU WISH TO ENTER NEW
SPECIFICATIONS TYPE 1, AND FOLLOW THE INSTRUCTIONS TO CREATE A DATA
FILE, ELSE PRESS 'RETURN' OR TYPE ANY OTHER NUMBER.
```

1

ENTER NEW DATA FILE-NAME

file.dat

INPUT FILE-NAME WITH INJECTION PRESSURE DATA

inj.dat

IF ENGINE DIMENSIONS ARE SIMILAR TO THOSE IN AN EXISTING DATA FILE TYPE 2

1

ENTER THE FOLLOWING ENGINE SPECIFICATIONS:

STROKE (m)

0.08598

CYLINDER BORE (m)

0.10305

COMPRESSION RATIO

19.05

CONN ROD LENGTH (m)

0.1495

TO INPUT DIMENSIONS RELATING TO THE COMBUSTION BOWL, IT MAY BE NECESSARY TO HAVE WITH YOU THE SKETCH SHOWING THE NOMENCLATURE OF THE

PISTON BOWL GEOMETRY. IF YOU WISH TO SUSPEND THE RUNNING OF THE PROGRAM AT THIS STAGE TYPE 971; ELSE TYPE ANY OTHER NUMBER

The above statement is used to allow the user to suspend the program in a situation where the user may be unfamiliar with the nomenclature used to specify bowl geometry. This is illustrated in Figure 2.5 - with the correct nomenclature. The 'awkward' number 971 is deliberately chosen to avoid inadvent suspension of program execution.

1

INPUT ANGLES ALPHA AND BETA (IN DEGREES)

0, 180

INPUT RADII R1 AND R2 (mm)

0., 0.

INPUT HB AND DB (mm)

24.5, 45.0
INPUT SWIRL RATIO AT INLET VALVE CLOSURE

2.0

ENTER THE FOLLOWING FOR THE INJECTOR:

NUMBER OF HOLES

1.

NOZZLE DIA. (mm)

0.34

ENTER THE FOLLOWING VALVE TIMINGS:

INLET VALVE CLOSURE (DEG. CA, -VE IF BEFORE TDC)

-137.

EXHAUST VALVE OPENING (DEG. CA)

126.

ENTER THE FOLLOWING LOAD SPECIFICATIONS:

ENGINE SPEED (RPM)

1500.

INJECTION DYNAMIC TIMING (DEG. ATDC)

-9.0

INJECTOR NOZZLE DISCHARGE COEFFICIENT

0.45

INJECTION DURATION (DEG. CA)

20.

CHARGE VOLUMETRIC EFFICIENCY

0.887

IGNITION DELAY CAN BE ENTERED IN EITHER ONE OF THE FOLLOWING FORMS:

1. IN DEG. CA
2. IN MILLISECONDS
3. DEFAULT- THE MODEL CALCULATES ONE USING HADENBERG AND HASE'S

EQUATION

TO CHOSE YOUR OPTION TYPE THE NUMBER BESIDE IT.

1

INPUT IGNITION DELAY (DEG. CA)

9.0

ENGINE LOADING CONDITION.

ENGINE LOAD CAN BE SPIED AS ONE OF THE FOLLOWING:

1. AIR/FUEL RATIO

2. VOLUME OF FUEL INJECTED

TYPE IN THE NUMBER BESIDE THE OPTION YOU PREFER

1

INPUT THE A/F RATIO

45.

A short delay follows after the last response as a new input data file is created. Then a summary of the input conditions is displayed on the screen:

==========

A SUMMARY OF INPUT CONDITIONS:

Engine Speed = 1500.000 RPM
Stroke = 0.086 metres

```
Bore                    =     0.103 metres
Comp. Ratio             =    19.100 metres
Start of Injection      =    -9.000 ATDC
Injection Duration      =     20.00  Deg. CA
Injected Fuel Vol.      =    19.1000 mm**3/stroke

================================================================

INPUT PERCENTAGE EGR - 0, 10, 20 (INTEGER)

0
```

This completes the data input stage and simulation automatically follows. At the end of injection, the computer prints on the screen the injection duration and the end of injection. This is given in order to assist the user to select the correct value for injector nozzle discharge coefficient so that the experimental and computed values of injection duration are equal. Also given at this stage is the turbulence strain rate ($1/\tau$) which plays a central role in the modelling of smoke. The format of the results, for the above data, appear on the screen as follows:

```
END OF INJECTION (ATDC)              =     11.75
INJECTION DURATION (DEG. CA)         =     20.25
TURBULENCE MIXING RATE (1/s)         = 98945.25
```

Another delay follows as the rest of the simulation proceeds, before the model displays values of exhaust emissions in the following format:

```
NET EXHAUST SMOKE (AT NTA)           =      0.37634 gr/m**3
EQUIVALENT BOSCH UNITS               =      4.552
EXHAUST NOx EMISSION (AT NTP)        =   1511.88 ppm
```

A data file called DATA.NEW is also created which contains detailed crank variations of all the data outlined in Section 6·2 . This is

presented in the format:

Crank Angle, [All other variables]

6.4.2 Varying Engine Loading

When simulating the same engine under various load conditions desired, it is not necessary to go through all the steps outlined in 6.4.1 above. The first three responses by the user are the same as those above, save for a change in the data file name, until the following prompting from the computer:

IF ENGINE DIMENSIONS ARE SIMILAR TO THOSE IN AN EXISTING DATA FILE TYPE 2

2

INPUT THAT FILE NAME

file.dat

The computer will then copy engine dimensions from 'file.dat' into the new file-name and only ask for the engine load as in 6.4.1, starting from:

ENTER THE FOLLOWING LOAD SPECIFICATINS:
ENGINE SPEED (RPM)

The remainder of the dialogue is identical to that given in Section 6.4.1 above, and the display of input data summary and modelling results is the same.

6.4.3 Repeating Data on File

This is the simplest method of implementing the simulation model. The response to the first introductory prompting is to press 'RETURN' and the computer proceeds to give the following prompt:

INPUT DATA FILE

Then only EGR needs to be specified.

Table 6.1: Conversion From Mass Concentration to BOSCH units

SOLID CONTENT (gm/cubic metre)	BOSCH UNITS	SOLID CONTENT (gm/cubic metre)	BOSCH UNITS
0.028	1.0	0.279	4.0
0.033	1.1	0.295	4.1
0.037	1.2	0.311	4.2
0.041	1.3	0.329	4.3
0.046	1.4	0.347	4.4
0.051	1.5	0.366	4.5
0.056	1.6	0.386	4.6
0.062	1.7	0.407	4.7
0.068	1.8	0.429	4.8
0.074	1.9	0.450	4.9
0.079	2.0	0.474	5.0
0.086	2.1	0.499	5.1
0.092	2.2	0.525	5.2
0.099	2.3	0.551	5.3
0.107	2.4	0.579	5.4
0.115	2.5	0.607	5.5
0.123	2.6	0.636	5.6
0.131	2.7	0.666	5.7
0.139	2.8	0.698	5.8
0.147	2.9	0.730	5.9
0.156	3.0	0.763	6.0
0.166	3.1	0.796	6.1
0.175	3.2	0.832	6.2
0.186	3.3	0.869	6.3
0.197	3.4	0.906	6.4
0.209	3.5	0.943	6.5
0.222	3.6	0.980	6.6
0.236	3.7	1.019	6.7
0.249	3.8	1.058	6.8
0.264	3.9	1.097	6.9
0.279	4.0	1.136	7.0

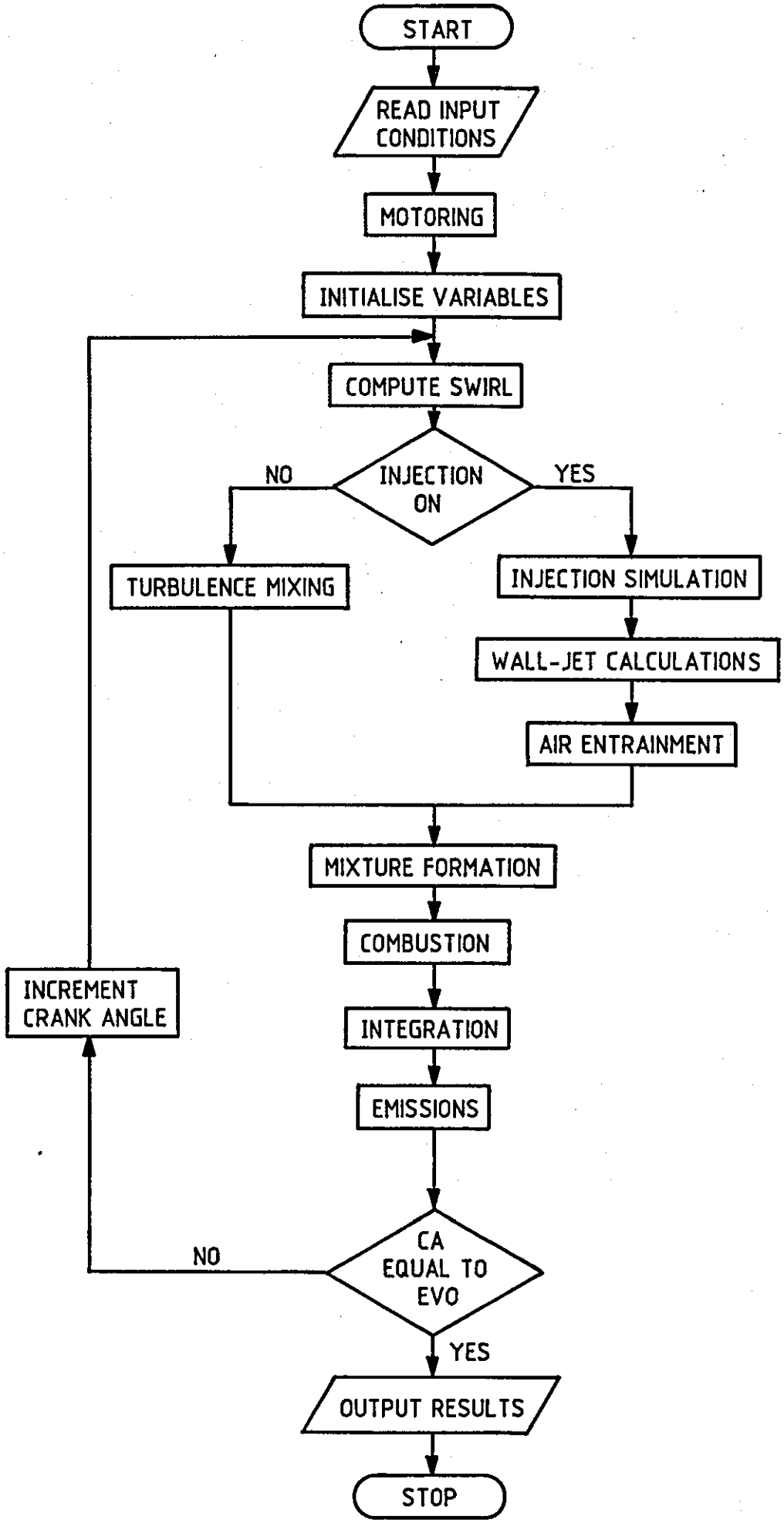

FIGURE 6.1: WALL-WETTING ENGINE MODEL FLOW-CHART

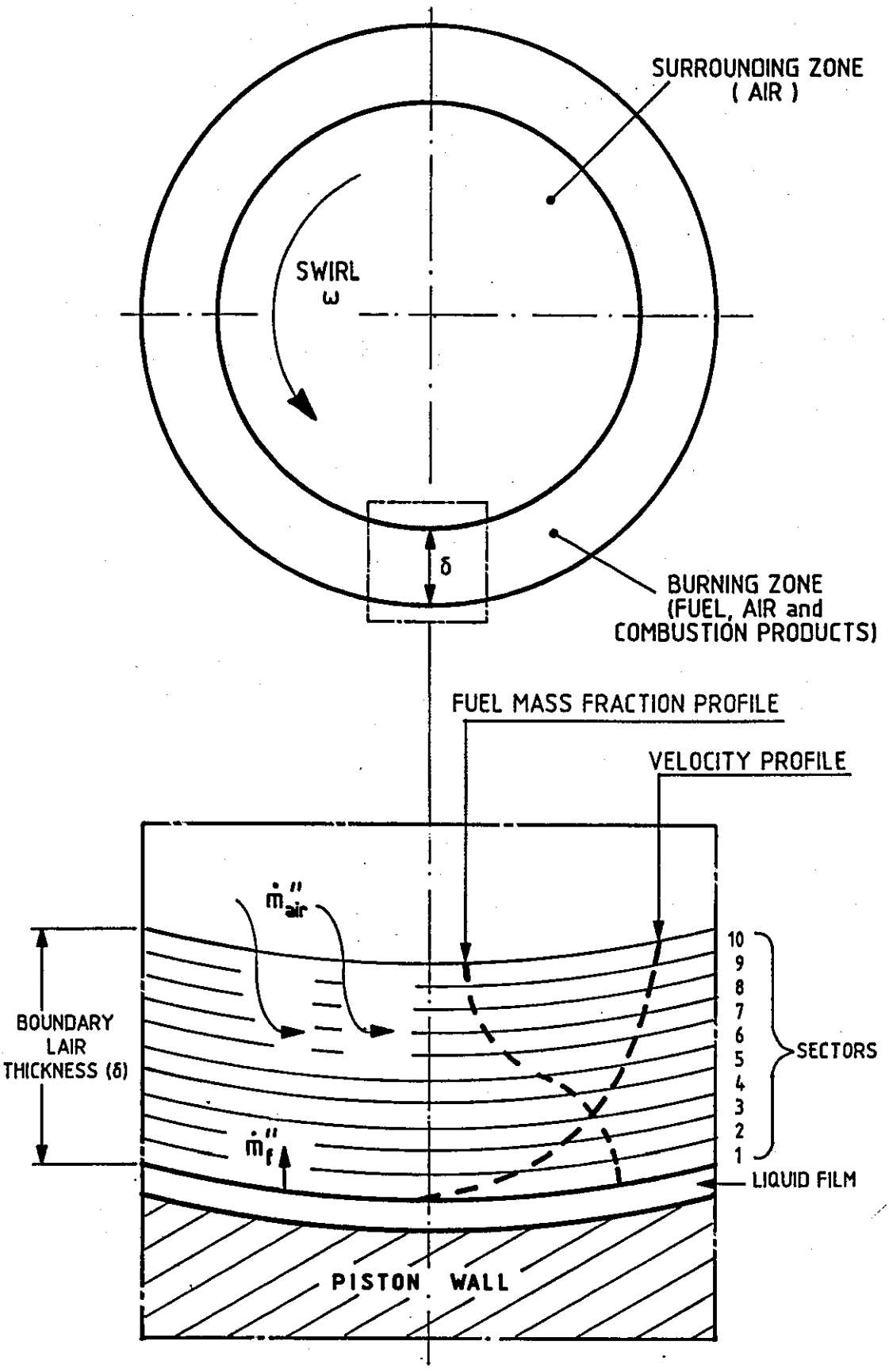

FIGURE 6. 2. : STRUCTURE OF THE COMPUTATIONAL SECTORS IN THE BOUNDARY LAYER.

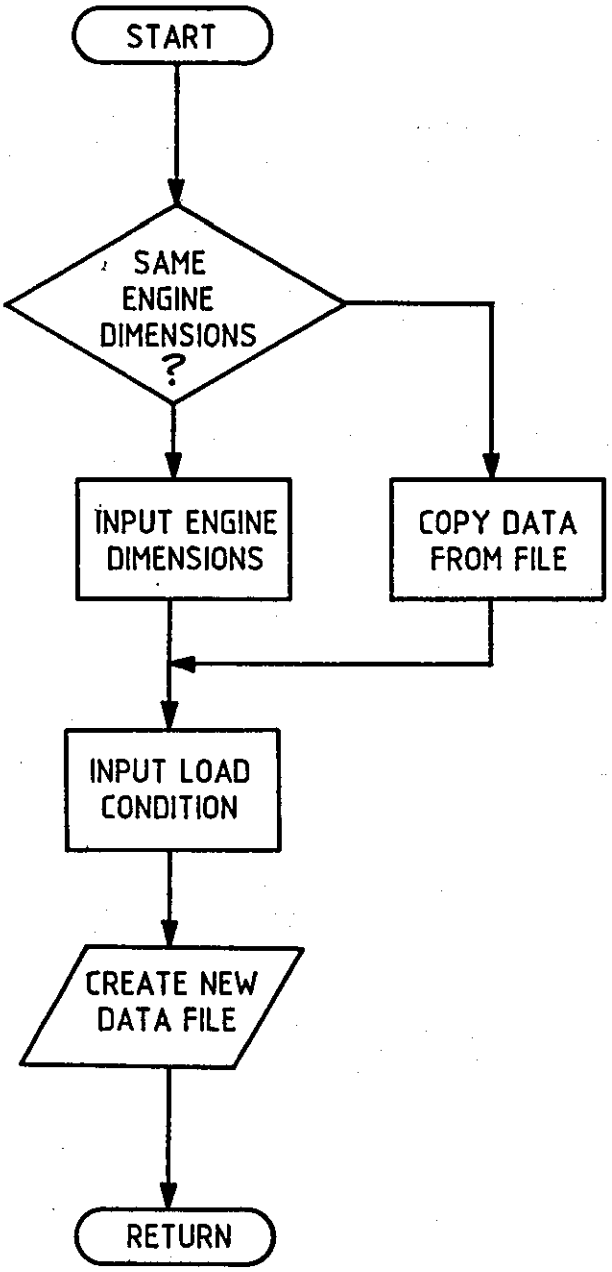

FIGURE 6.3: OPERATION OF SUBROUTINE SPEC

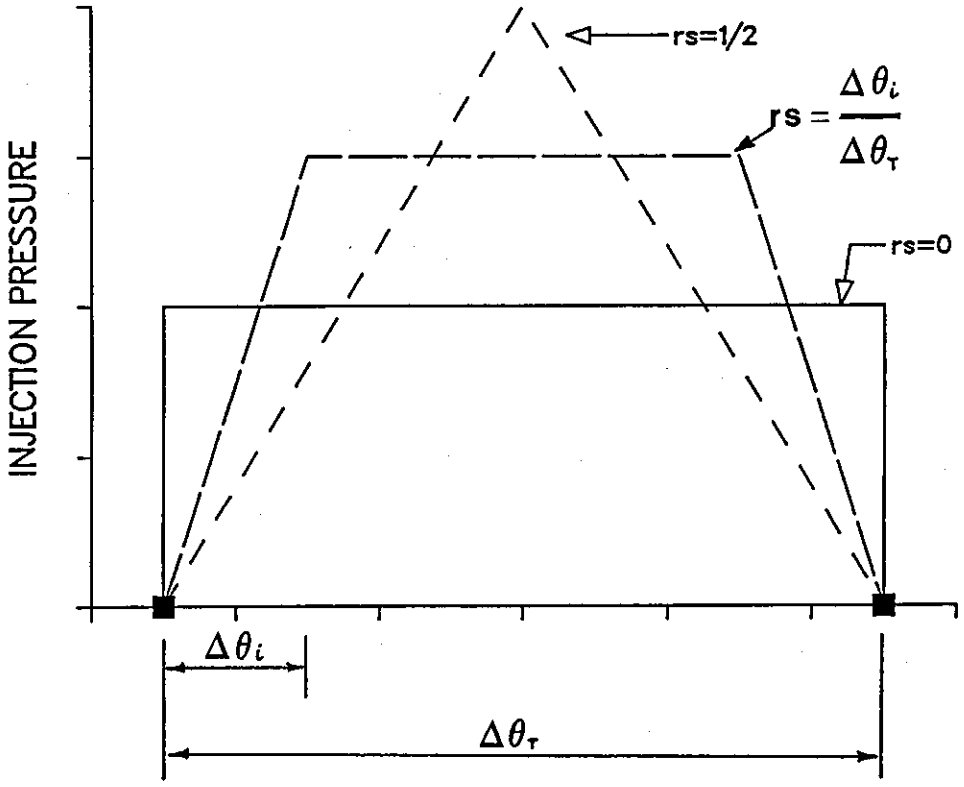

FIGURE 6.4: CHARACTERISATION AT TRAPEZOIDAL INJECTION PRESSURE DIAGRAM

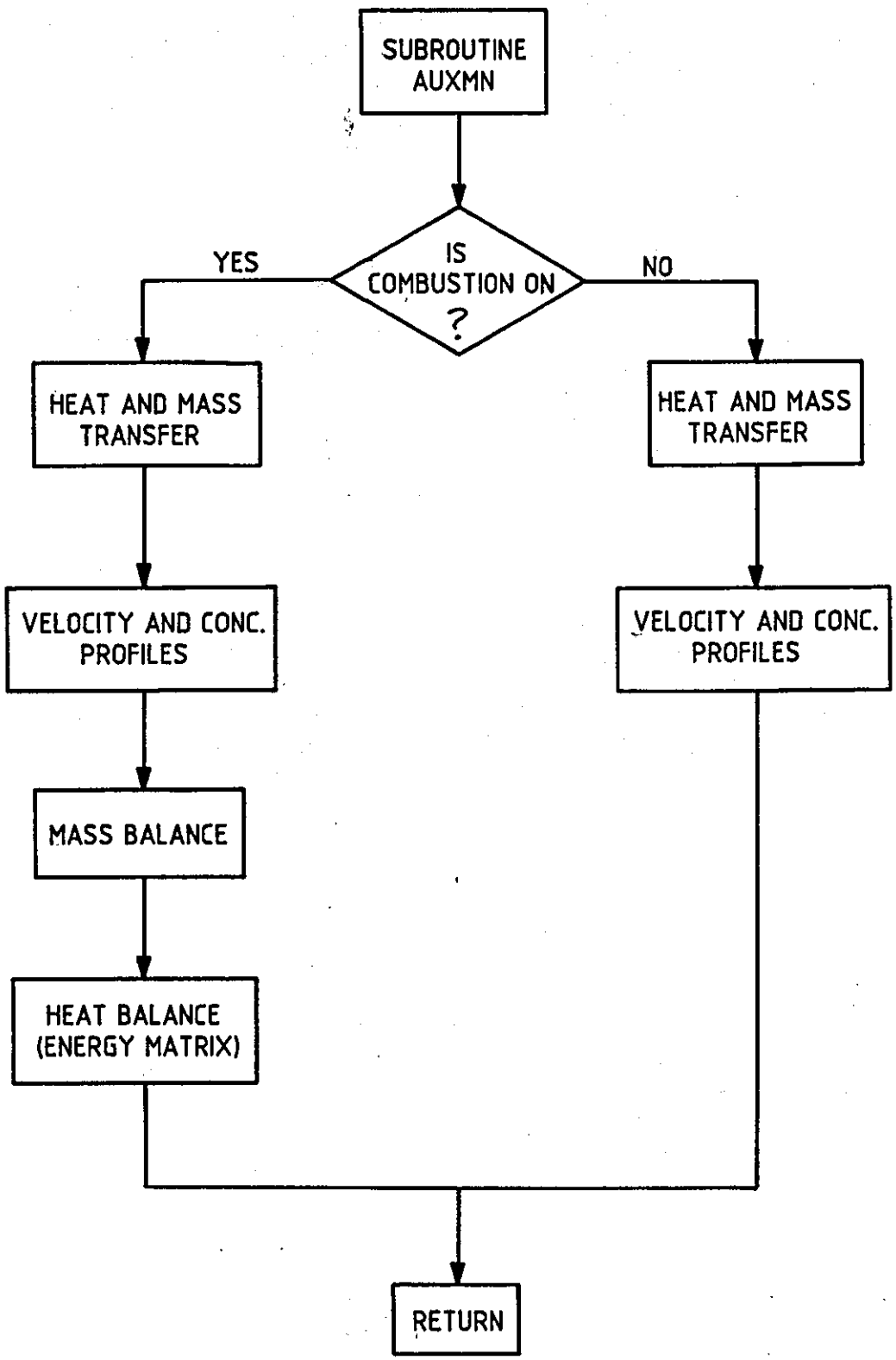

FIGURE 6.5: OPERATION OF SUBROUTINE AUXMN

CHAPTER 7

MODEL SIMULATION RESULTS

7.1 INTRODUCTION

A brief synopsis of engine performance variables that may be calculated using the model were outlined in Section 6.3 above. Detailed results, such as those outlined in Section 6.2 are recorded on a data file so as to make graphical representation and diagnostic analysis convenient. All the results on the output file may be plotted against crank angle, from the start of injection to the opening of the exhaust valve. In this chapter, comparison is made between calculated variables using the model under several engine test conditions, and experimental results measured under similar operating conditions. The following is a list of parameters against which the engine variables are investigated:

i. effect of injection dynamic timing
ii. effect of engine speed
iii. effect of overall air/fuel ratio (load)

Variables which are not easily measured experimentally, such as air entrainment, have been given for completeness, and also to provide diagnostic tools for analysing engine performance. As the suitability of assumed mass fraction, temperature, and velocity profiles are not readily perceived from the resulting pressure trace in the model, other means of evaluating these have to be sought. In this case the accuracy in the trends of predicted exhaust emissions have been used since NO_x and smoke emission levels are sensitive to local values of equivalence ratio and temperature. However, owing to the unavailability in the published literature, of empirical data relating to time dependent local concentrations of combustion products in wall-wetting type engines, only the final value, measured when the exhaust valve opens, has been compared.

7.2 DETAILS OF EXPERIMENTAL ENGINE

Validation of the model against empirical results is based on data collected at General Motors in connection with research on a similar engine (31, 58), with the following specifications:

Number of cylinders	=	1
Stroke	=	85.98 mm
Bore	=	103.05 mm
Conn. Rod	=	149.50 mm
Compression Ratio	=	19.05
Bowl Volume	=	31.80 millilitres.

The geometrical shape and dimensions of the piston bowl are illustrated in Figure 7.1, and the CAV pintle injector nozzle specifications are summarised below:

Number of holes	= 1
Opening pressure	= 130 bar

The nozzle cross-sectional area corresponding, respectively, to a needle lift range 0-0.9 mm, varied from 0 to 0.61 mm^2. Table 7.1 gives the set of conditions under which the engine was operated to obtain the results listed below:

i. Cylinder pressure
ii. Smoke
iii. NO_x
iv. Specific fuel consumption
v. Mean effective pressure.

A semi-empirical heat release diagram, based on the measured cylinder pressure was also calculated, and this has been used to compare with the heat release diagram calculated using the model. The baseline

load conditions for the engine, which was used as reference, are as follows:

Engine speed = 1500 rpm
Air/fuel ratio = 45.0
Injection timing = -9.0°CA
Fuel injected = 19.1 mm^3/STROKE.

While maintaining the charge air mass constant, engine load was varied by adjusting the quantity of fuel injected to obtain the desired overall Air/Fuel ratio.

7.3 RESULTS AT BASELINE CONDITION

To illustrate the nature of graphical results that are possible from the model, a comprehensive set of graphs is given only at baseline condition. For conditions other than baselines only the essential variables are investigated and presented in parametric form in paragraph 7.4.

7.3.1 Cylinder Pressure

Pressure in the cylinder is one of the most fundamental and easy to measure variables in engine experiments, providing a fairly accurate preliminary picture of engine performance and response to parametric variations. Figure 7.2 shows results of the present model against empirical data at baseline condition. Good agreement between the two results is observed at this condition. To test for the correctness of trend under varying load, timing and engine speed, parametric results are provided in a subsequent section of this chapter.

7.3.2 Charge Mean Temperature

Martin and Ahmad (31) have given a computed estimate of the bulk gas

temperature based on an ideal gas calculation. Although it is not possible to accurately evaluate the model on the basis of their calculated results, it is however expected that general order of magnitude and trends with crank angle should show fair agreement. The two bulk gas temperatures are illustrated in Figure 7.3(a) where it is seen that the model calculates a lower temperature than that obtained by Martin and Ahmad. This can be improved by increasing intake air temperature in the model from 333K to 400K. The improved trend is shown in Figure 6.3(b). A similar improvement can also be obtained if, instead of raising intake air temperature, the polytropic exponent used during the pre-injection period was raised from 1.325 to 1.37. However, this does not offer a suitable solution as it also leads to a higher cylinder pressure.

For completeness, parametric responses of charge temperature to engine speed, timing, and air/fuel ratio are discussed in section 7.4. As Martin and Ahmad did not give corresponding values for these, only outputs from the present model are provided.

7.3.3 Other Computed Results

The charge mean temperature in the model is calculated from a weighted average between the temperature of the burning zone and its surroundings, as shown in equation (6.2). The values used in plotting Figure 7.3 were calculated in this way. In Figure 7.4 the corresponding temperature of the burning zone for the baseline condition is illustrated. The early portion of the burning zone temperature shows a very high rate of increase which can be explained in terms of the assumed conceptual burning zone volume. The initial value of this volume is calculated from the thickness of the gaseous stream boundary layer, which is very low, thus resulting in a rapid increase in temperature as the initial pre-mixed charge in the boundary layer is burned. This transient in temperature, however, does not significantly affect NO_x or smoke emission levels predicted at a rate limited by their respective kinetic rates. In both cases,

this is lower than the rate of rise in Figure 7.4. As earlier discussed in paragraph 6.2, this temperature is significant in determining the formation of NO_x and particular carbon (smoke) during combustion.

The major controlling variable for the temperature is the air entrainment rate from the surrounding air into the jet. Figure 7.5 shows variation of air entrainment with crank angle, and in Figure 7.6 the corresponding heat release rate is illustrated. The dominance of mixing controlled combustion in diesel engines is not obvious from the two diagrams, especially as the entrainment rate curve is not identical to the heat release rate diagram. This is because in wall-wetting engines, a further limitation on the heat release rate is effective, viz. the rate of fuel evaporation from the piston wall. This was discussed in Chapter 1 where the rate of combustion was given by the following equation:

$$\dot{m}''_{COMB} \propto MIN\left[\dot{m}''_f, \frac{\dot{m}''_{o2}}{r}\right] \qquad (1.27)$$

Equation (1.27) implies that combustion proceeds at a rate controlled by the lower rate between air entrainment and fuel evaporation. The results of Urlaub (34), demonstrated in Figure 1.21, illustrate the strong influence of fuel evaporation rate on heat release rate. The results in Figure 7.6(b) show a similar trend is obtained in the model. The rate of heat release is seen to follow the rate of fuel evaporation (depicted by the rate of diminution of mean film thickness due to evaporation).

In Figure 7.7, the variation of mass transfer number, B, is shown to have a form identical to that of the burning zone temperature due to the dominance of temperature effects on enthalpy which is the basis for the definition of B.

The instantaneous mass fractions of fuel injected, evaporated and burned are depicted in figure 7.8. The slow rate of evaporation

(lasting 60 degrees crank angle or more), which is a characteristic of wall-wetting diesel engines as has been observed experimentally by Müller (41), and also by Meurer and Urlaub (40), further illustrates the point made above with respect to the shape of the heat release rate. It is quite likely that this significantly contributes to the severe unburnt hydrocarbon emissions associated with wall-wetting engines.

The results for the predicted exhaust emissions at baseline condition - smoke and NO_x are shown in Figures 7.9 and 7.10. The smoke results are obtained from the simultaneous solution of equations (2.17), (2.19), and (2.40) to give the net soot formed at every crank angle. The method used in the soot model of Kyriakides et al (8), based on calculating the difference at exhaust valve opening between the cumulative soot formed and that oxidised has been replaced by an algorithm in which the two processes proceed simultaneously. It is clear from the figure that oxidation occurs mainly during the high temperature period and rapidly subsides as the temperature drops below 1600K.

As has been pointed out in Chapters 2 and 6, the rate at which NO is formed in the engine is governed by the Zel'dovich kinetic mechanism. The differential equation in (2.39) represents the rate equation which is integrated to yield the results in Figure 7.10. The kinetic rate, which is highly dependent on temperature, is shown to be much slower than equilibrium concentration rate.

7.4 INFLUENCE OF OPERATING PARAMETERS

In discussing cylinder pressure, the results are presented on two sets of diagrams for each of the three parameters investigated (i.e. timing, speed and overall air/fuel ratio). The first diagram illustrates the level of agreement in trends between experimental and predicted pressure as the parameters are varied. The second set shows individual predicted pressure traces to illustrate agreement in orders

of magnitude and trends with respect to crank angle.

7.4.1 Effect of Injection Timing

Experimental results of Martin and Ahmad (31) show that advancing injection timing increases the peak pressure in the cylinder, leading to sharper and louder combustion noise. This effect is demonstrated by the model in the results shown in Figure 7.11(a and b), and in Figure 7.11(c), good agreement between individual traces is shown.. In Figure 7.12, the influence of timing on charge temperature is also illustrated, although as explained earlier, it has not been possible to corroborate these with empirical results. However the trend demonstrated is acceptable since higher cylinder temperature corresponds to higher pressure and so a trend identical to that shown in Figure 7.11 would result. Figure 7.13, showing variation in heat release rate, is based on the calculation by Martin and Ahmad (31) from measured cylinder pressure. Corresponding results from the model are overplotted, showing fairly good parametric response.

Figure 7.14(a) illustrates the effect of injection timing on exhaust smoke at the baseline engine speed and overall Air/Fuel ratio. Also plotted on the same figure is the empirical trend. Computed values show that corresponding to low temperature in the cylinder at retarded timing, low smoke levels are result. However the experimental results show a mixed trend with an increase in smoke emission as timing is retarded, followed by a reduction in smoke for very retarded timing. Plee (58) attributes this variability partly to the effect of timing on the location where the fuel spray strikes the piston wall. The CONCHAS flow model computations for the turbulence flow field, illustrated in Figures 1.27 and 1.31, imply that if the fuel spray strikes the wall in the bottom half of the bowl, relatively high exhaust smoke would result due to reduced turbulence mixing. This may also be inferred from the measurements of Brandl et al (124), as correlated by Dent (19), for turbulence mixing time at the base of the combustion bowl. Based on the argument that

fuel concentration is highest in the base of the bowl, Dent shows that high smoke emissions result due to low rates of turbulence mixing. As these effects could not be investigated realistically owing to the fact that experimental data were not so detailed, and also the model does not effectively take into account piston bowl geometry, it can only be assumed that these factors contribute significantly to the variability in the results.

The level of NO_x in the exhaust is highly dependent on temperature, and linearly on oxygen availability. Advanced timing, therefore, results in higher NO_x levels corresponding to the high temperatures illustrated in Figure 7.12. The results of the model predictions in Figure 7.14(b) illustrate these trends fairly well. Some variability would be expected due to the linear variation of NO_x with oxygen concentration. This reflects the level of acceptability of the assumed scalar quantity profiles and the air entrainment rate function.

Specific fuel consumption is frequently used in internal combustion engines as a criterion to measure performance rather than brake thermal efficiency. It is defined as the rate of fuel consumption per unit of brake (or indicated) power. The mean effective pressure gives an indication of power output per unit of swept volume. The experimental data are reported on the indicated basis (i.e. i.s.f.c and i.m.e.p) and so may be directly compared with the output from the model. As the results of Martin and Ahmad do not show pressures corresponding to the exhaust and induction strokes, the mean effective pressure and the specific fuel consumption calculated in the model cannot be adequately analysed with respect to any departure from experimental results. Consequently, 'dummy' mean effective pressures, based only on the portion of pressure given by Martin and Ahmad, have been plotted instead. These are given in Figures 7.14(c), 7.17(c), and 7.21(c), showing good agreement within this limited range.

7.4.2 Effects of Engine Speed

The motored component of the pressure traces obtained by Martin and Ahmad increases with increasing engine speed. This is mostly due to a reduction in heat transfer and to a lesser extent, blow-by during compression both of which lead to increased temperature and pressure. To obtain the results presented here at the high engine speed (i.e. higher than 2000 rpm), it has been necessary to increase intake temperature as engine speed increases, otherwise low motored pressures are obtained. Figure 7.15 shows the effect of engine speed on cylinder pressure. Increasing engine speed results in a monotonically rising peak pressure. This may be attributed, in part, to improved air/fuel mixing that results from the high level of air movement. The effect of this on emissions is a reduction of exhaust smoke (14), and, resulting from the higher charge temperatures (illustrated in Figure 7.16) an increase in NO_x levels. The results shown in Figure 7.17(a and b), thus render support to the idea of improved fuel-air mixing at high engine speed. Similar trends can also be observed with the conventional diesel engine (125). In Figure 7.17(c), the 'dummy' mean effective pressures are illustrated, showing fair agreement in magnitudes as well as trends.

Figure 7.17(b) shows an almost linear increase in NO_x with increasing engine speed. Although this is in agreement with the explanation given in the previous paragraph, Plee (58) appears to suggest that this depends on the baseline A/F ratio, and quotes results which show decrease in NO_x with increasing engine speed for a lower Air/Fuel ratio. This implies that there is a level of overall Air/Fuel ratio, at a given engine speed, for which optimum turbulence mixing conditions in the engine obtain. The work of Morris (24) referred to in Chapter 1 looked at this effect in conventional DI diesel engines, and concluded that the ratio of jet to cross swirl momenta constituted the controlling parameter. It is thus possible that the same parameter is also effective in wall-wetting engines. This has been one of the underlying assumptions in the design of the simulation rig used to obtain the results in Chapter 5. Section 7.4.3 discusses in more detail the effect of Air/Fuel ratio on other engine performance

the injection duration). This is one of the areas of further investigation, especially if hydrocarbon emissions predictions are to be included in the modelling procedure.

The experimental results in Figure 7.20 show that as the load is increased (i.e. reduction in Air/Fuel ratio), there is a general reduction in magnitude for the portion of heat release rate representing the premixed region. Plee (58) attributes this to increased wall deposition of the fuel at high load due to increased jet momentum associated with a high rate of injection. This effect has also been demonstrated by the model results. The general trends for the smoke emissions results in Figure 7.21(a) show fairly good agreement. Increasing Air/fuel ratio also causes a decrease in NO_x emissions, (Figure 7.21(b)) which would be contrary to Plee's results as depicted in Figure 1.15. In fact Plee's discussion on Figure 1.15 suggests that he interprets the results to imply increased NO_x emission results from high air/fuel ratio. However, the index used to normalise the results (i.e. grams of NO_x per kilogram of fuel) is rather misleading. It can easily be shown that the data in Figure 1.15 can be converted to the more familiar units of parts per million (ppm) by the following equation:

$$ppm = N \left(\frac{W_{exh}}{W_{NO}}\right) \frac{10^3}{(1+AFR)} \qquad (7.1)$$

where W_{exh}, W_{NO} = Molecular weights of exhaust products and NO respectively.

N = g NO/kg of fuel

AFR = Overall Air/fuel ratio.

Applying equation (7.1) to Plee's results in Figure 1.15 shows the trend illustrated in Figure 7.21(b) which is opposite to the original trend. Bearing in mind the strong influence of temperature on NO formation, the experimental pressure trends in Figure 7.18(a) would appear to suggest that the temperature trends in Figure 7.19 are reasonable, in which case a reduction in NO with increasing air/fuel

ratio would be more likely. This, however, cannot be conclusive as the discussion in Chapter 2 has pointed out, production of NO is also linearly dependent on the availability of oxygen which controls the rate of the dominant reaction in the Zel'dovich mechanism.

7.5 CONCLUSION

The discussion of results presented in this chapter has emphasised the correctness of trends rather than magnitude due to the multiplicity of factors that influence the magnitudes. In a simplified phenomenological approach such as adopted here, such factors cannot be investigated in sufficient detail and accuracy without losing some of the initial objectives outlined in Chapter 3. It is thus understood that parametric studies may be carried out to yield reliable analysis once accurate trends have been established.

The importance of air motion is illustrated by parametric results involving engine speed, where it has been shown that increased fuel-air mixing enhances engine combustion and also leads to reduced exhaust smoke. The experimental results of Plee (58) show that the wall-wetting engine produces more smoke and NO_x than IDI engines, but lower NO_x than the traditional DI engine.

One of the major advantages of the wall-wetting engine is reduced engine noise. The model has been successful in predicting this by showing the reduced magnitude of the pre-mixed region of the heat release rate in comparison to that in other DI engines.

The results illustrate the general applicability of the model to the investigation and analysis of engine performance. Areas of further investigation have been highlighted by results.

Table 7.1: Injection and Combustion Characteristics

DATA SET NO.	ENGINE SPEED (RPM)	A/F RATIO	INJECTION TIMING (ATDC)	INJECTION DURATION (^{O} CA)	IGNITION DELAY (^{O} CA)
1	1500	45	-20	20.0	14.0
2	"	"	-14	"	11.0
3	"	"	-9	"	9.0
4	"	"	-7	"	10.0
5	"	"	-2	"	8.0
6	"	60	-11	18.0	11.0
7	"	30	-10	28.0	10.0
8	"	25	-10	29.0	10.0
9	600	45	-7	20.0	7.0
10	1000	"	-9	22.0	9.0
11	2000	"	-14	24.0	14.0
12	2400	"	-18	27.0	18.0

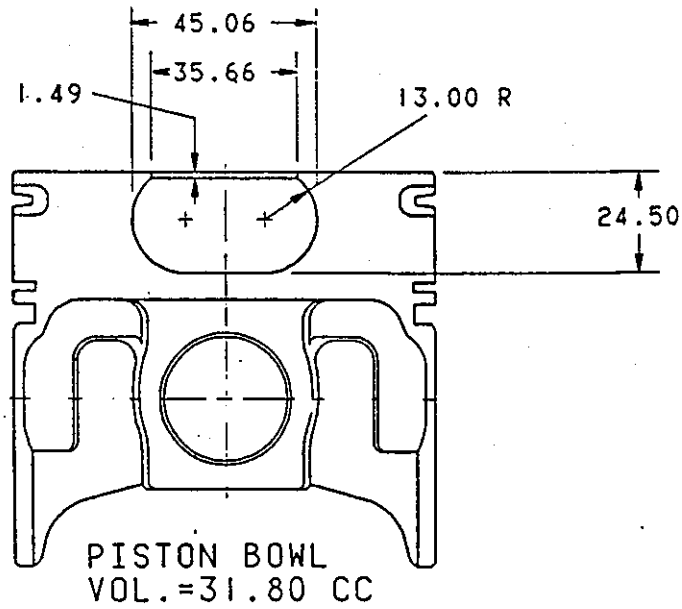

FIGURE 7.1: EXPERIMENTAL PISTON BOWL DIMENSIONS

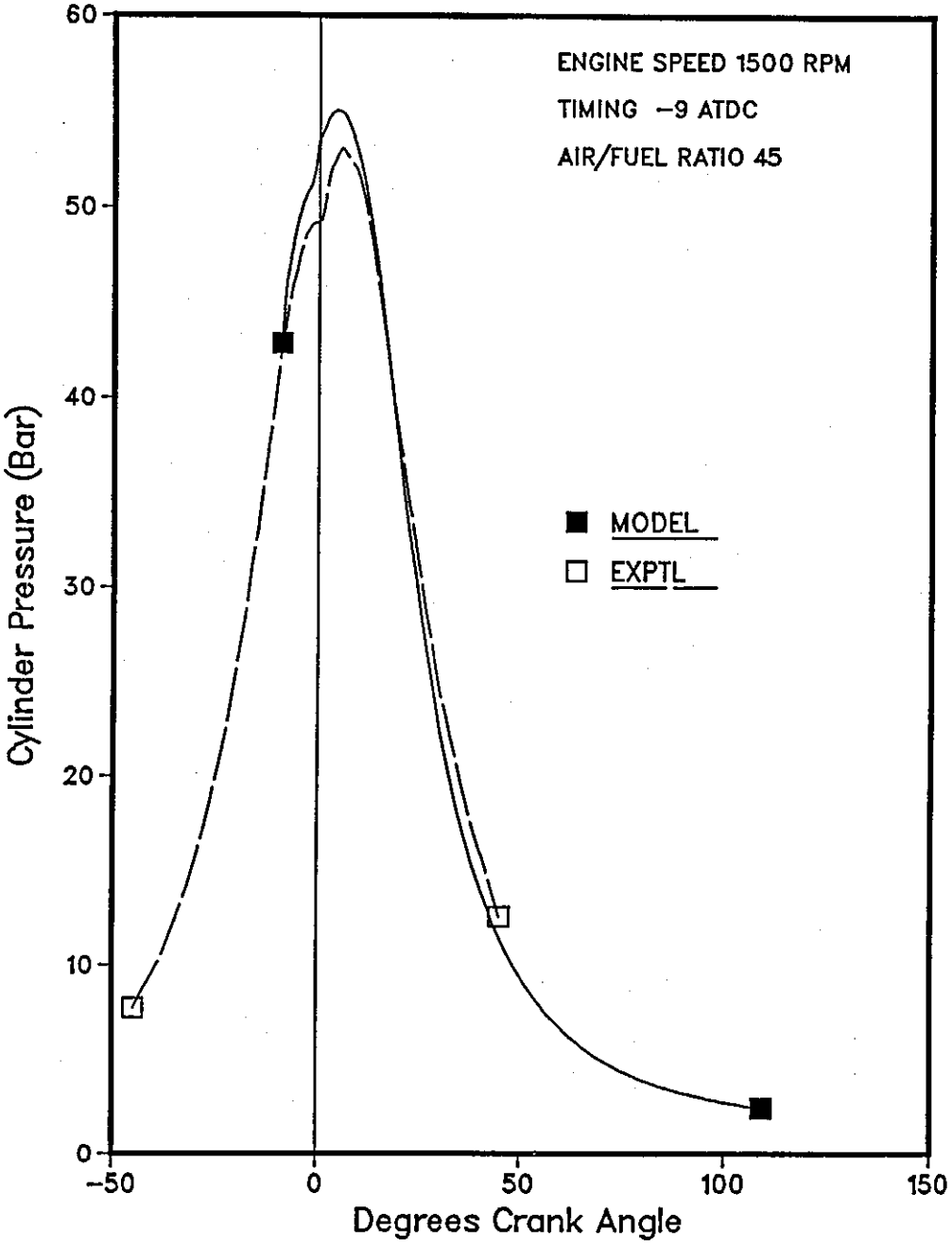

FIGURE 7.2: CYLINDER PRESSURE AT BASELINE

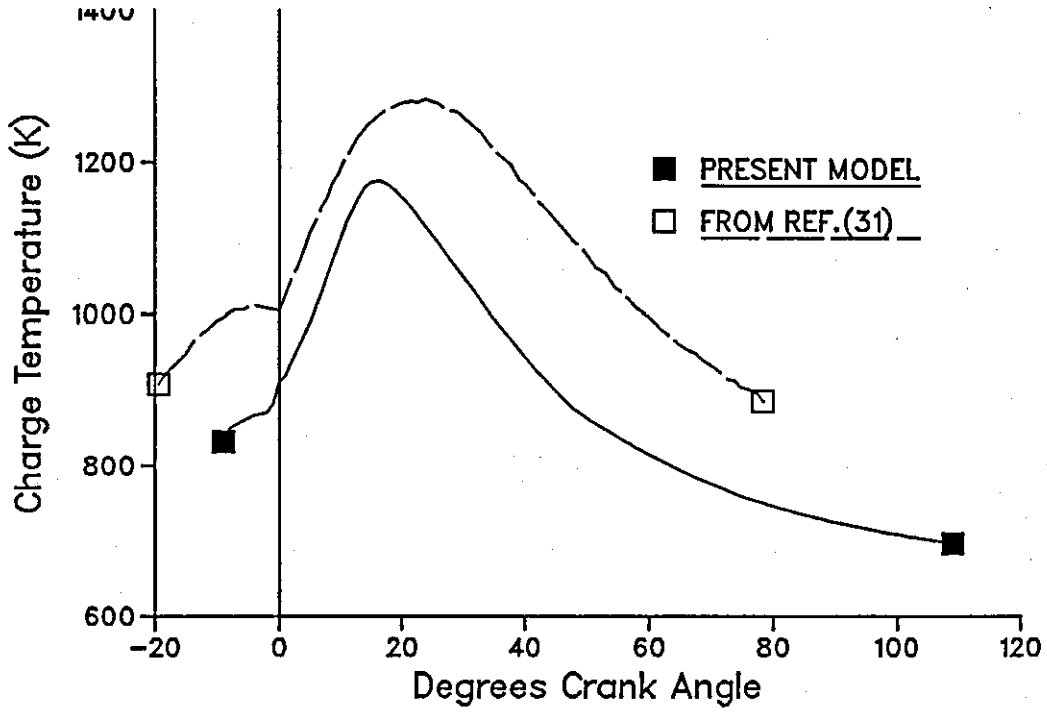

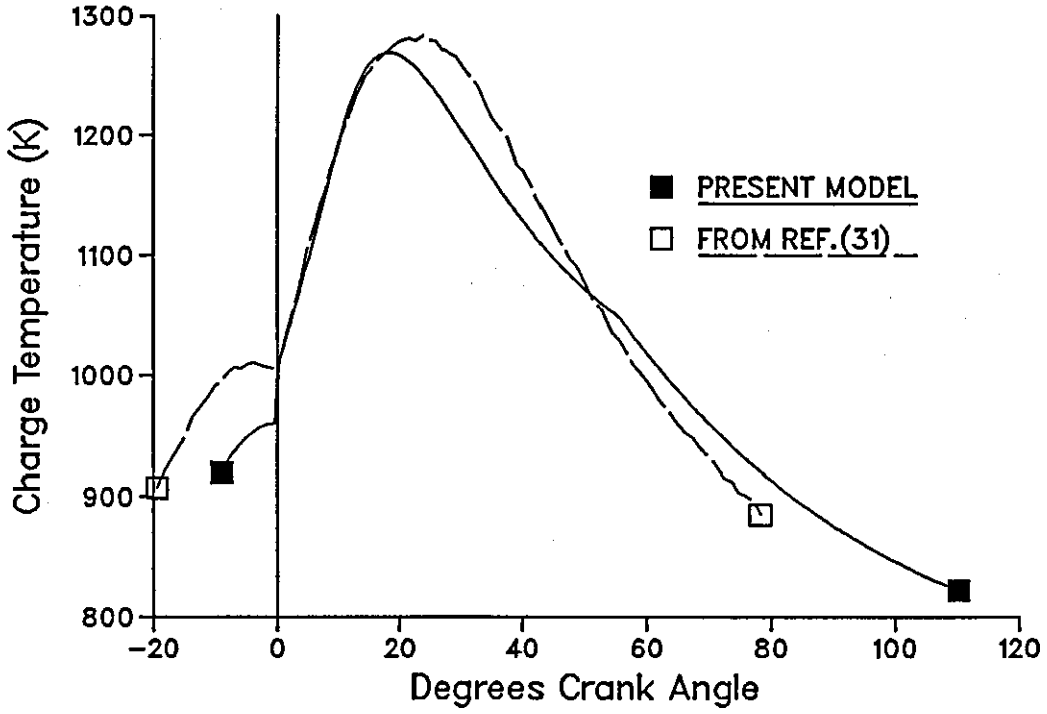

FIGURE 7.3: CHARGE TEMPERATURE AT BASELINE

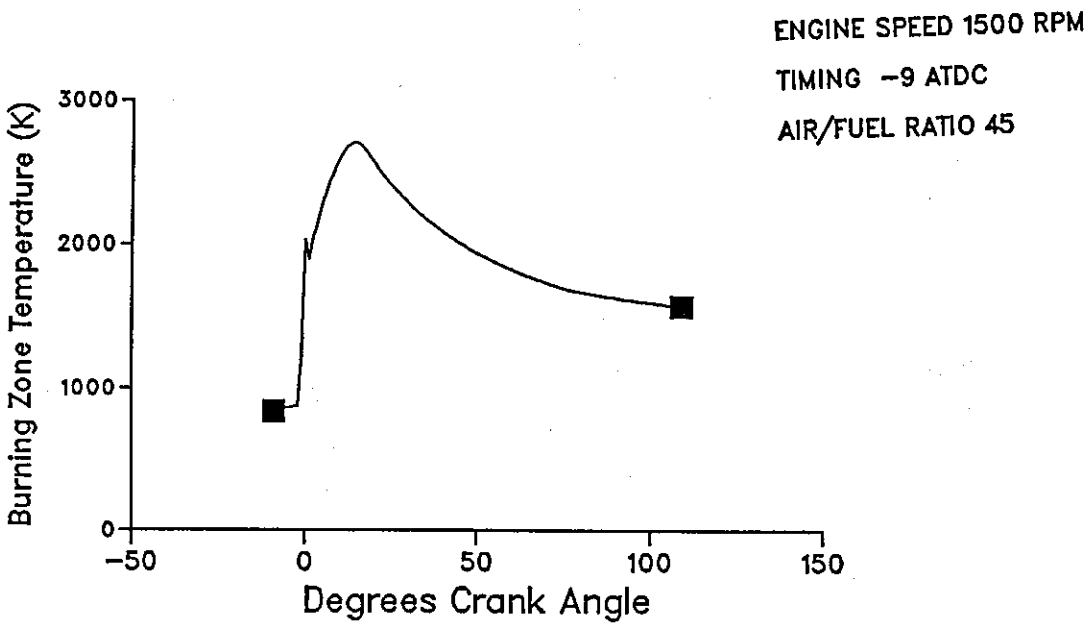

FIGURE 7.4: BURNING ZONE TEMPERATURE (BASELINE)

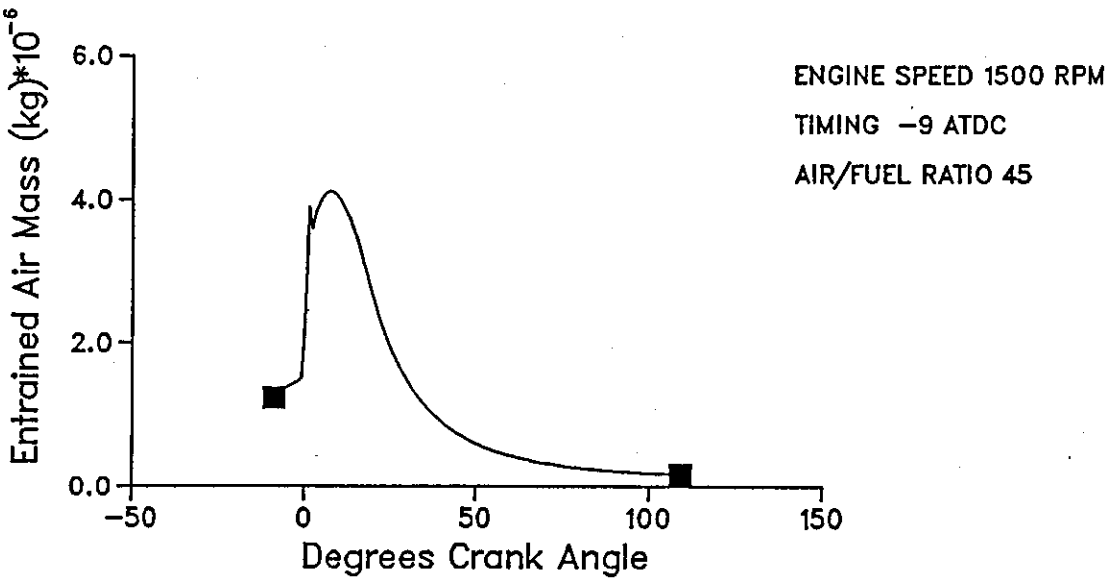

FIGURE 7.5: AIR ENTRAINMENT AT BASELINE

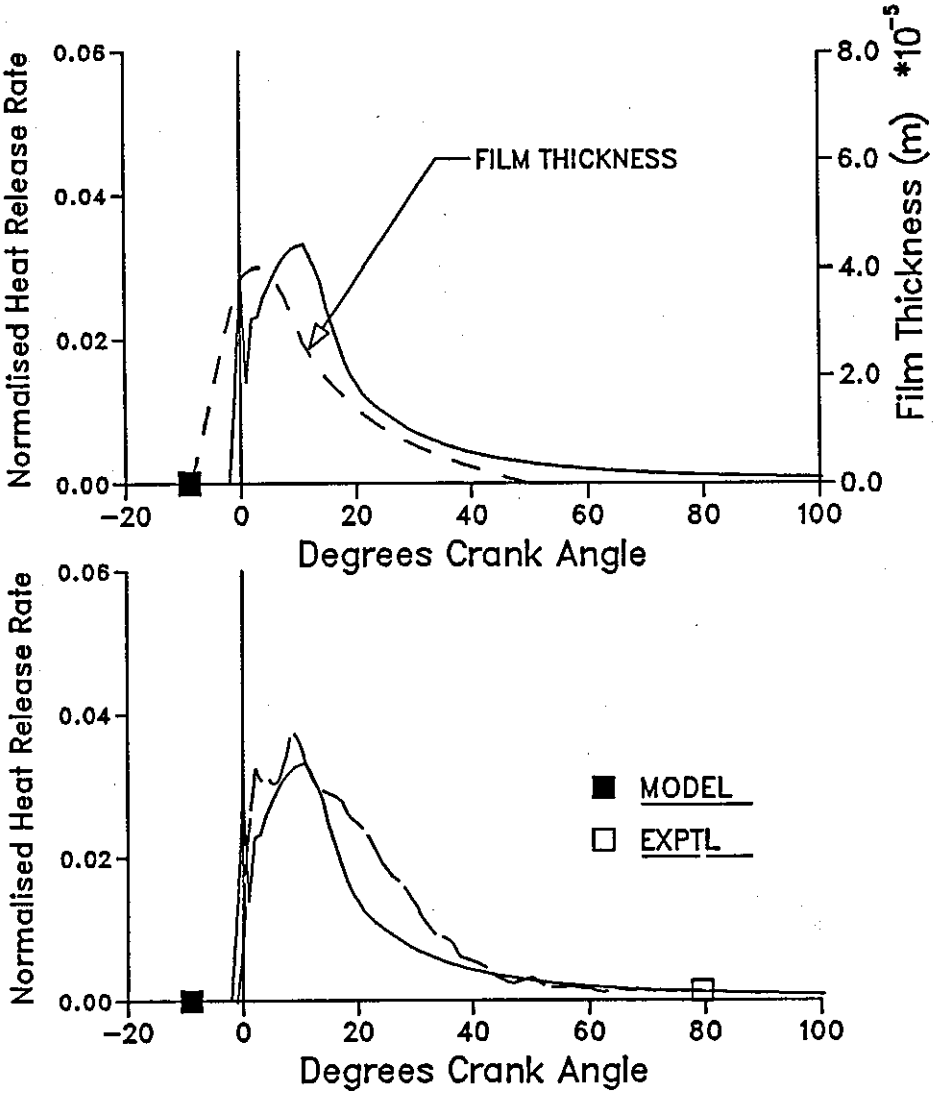

ENGINE SPEED 1500 RPM

TIMING −9 ATDC

AIR/FUEL RATIO 45

FIGURE 7.6: HEAT RELEASE RATE OF BASELINE CONDITION

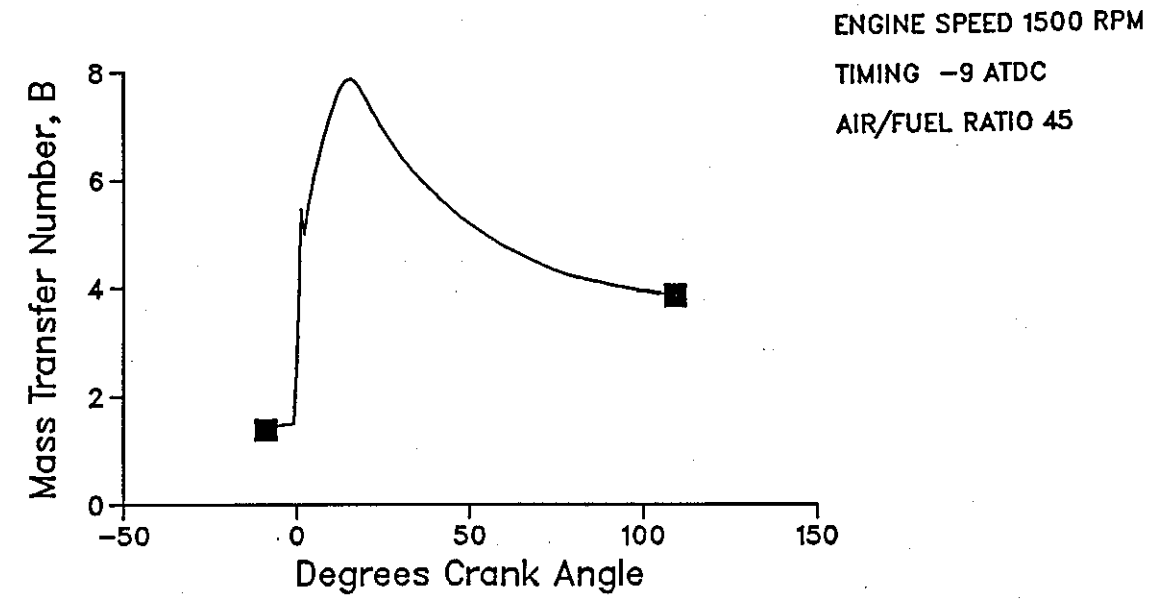

FIGURE 7.7: VARIATION OF MASS TRANSFER NUMBER (BASELINE)

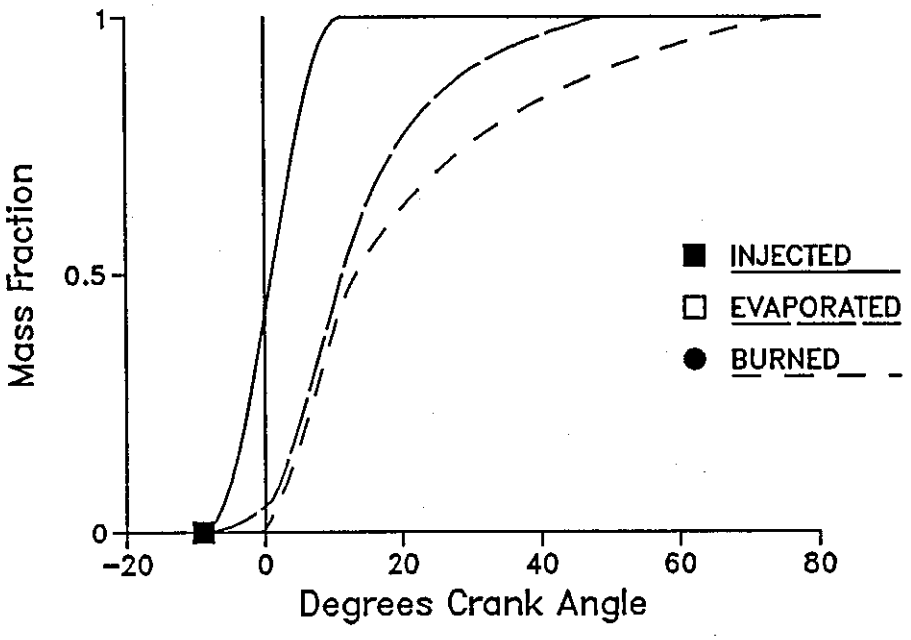

FIGURE 7.8: MASS FUNCTIONS OF FUEL AT BASELINE

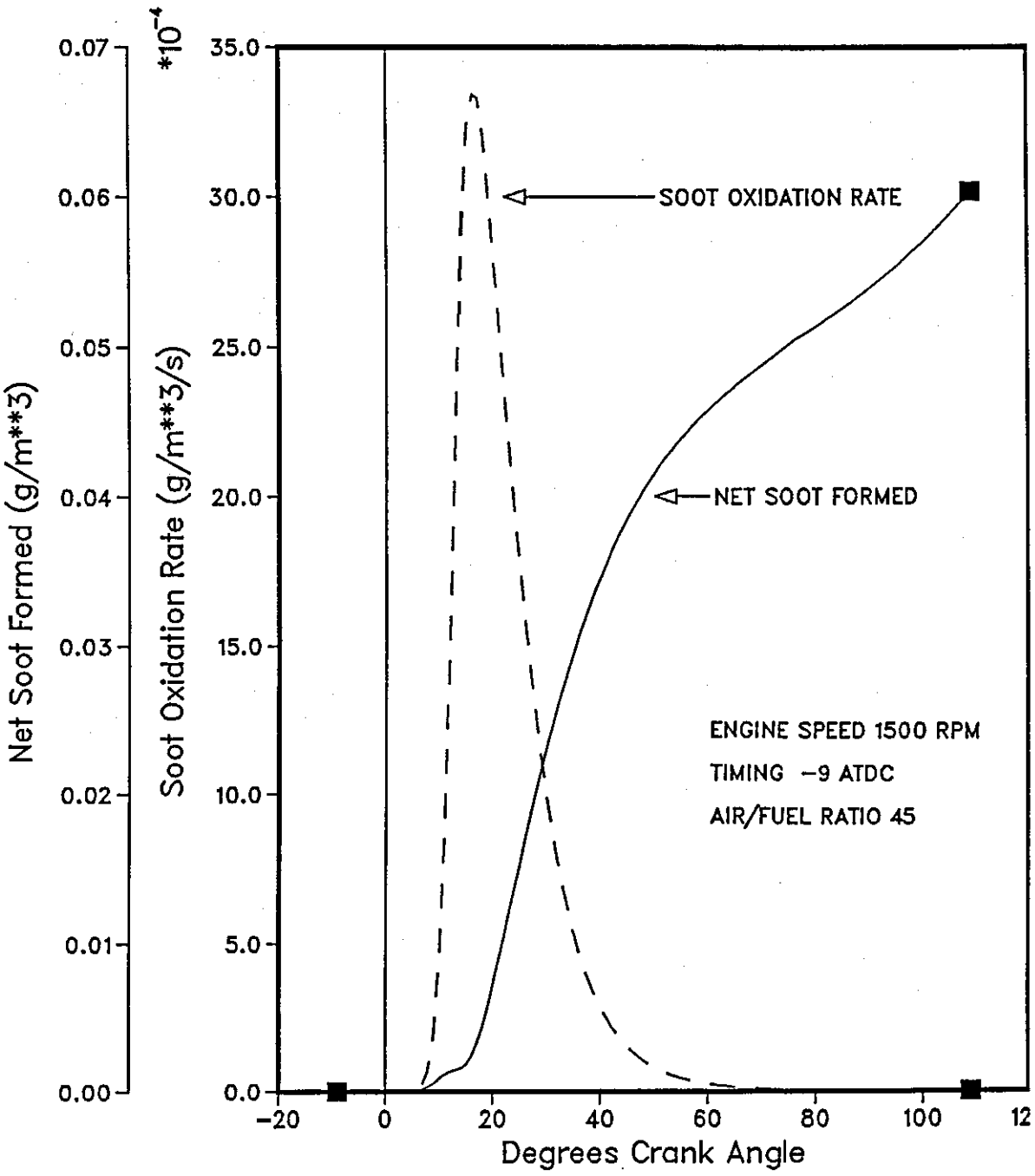

FIFURE 7.9: FORMATION AND OXIDATION OF SOOT AT BASELINE CONDITIONS

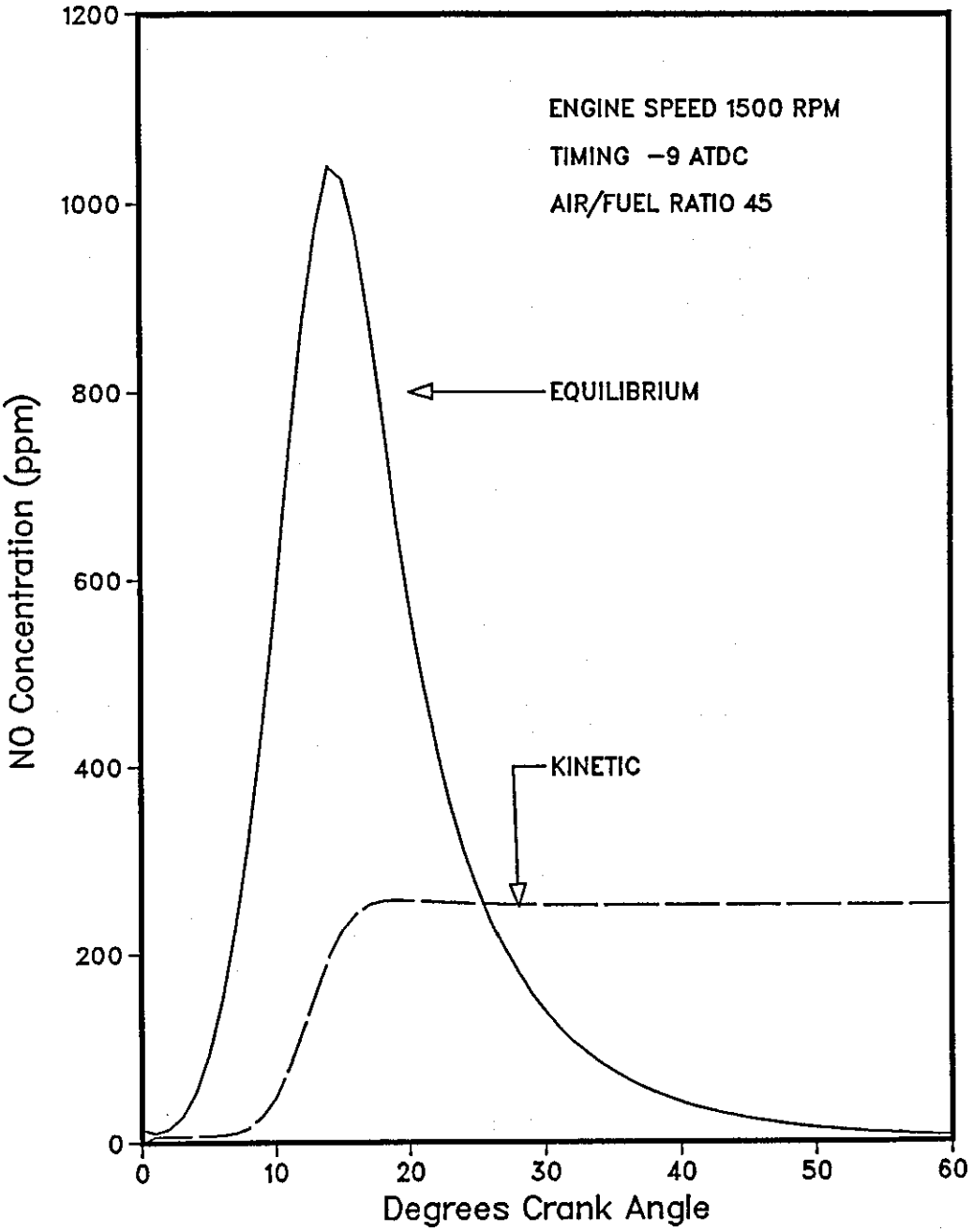

FIGURE 7.10: NO_x FORMATION AT BASELINE

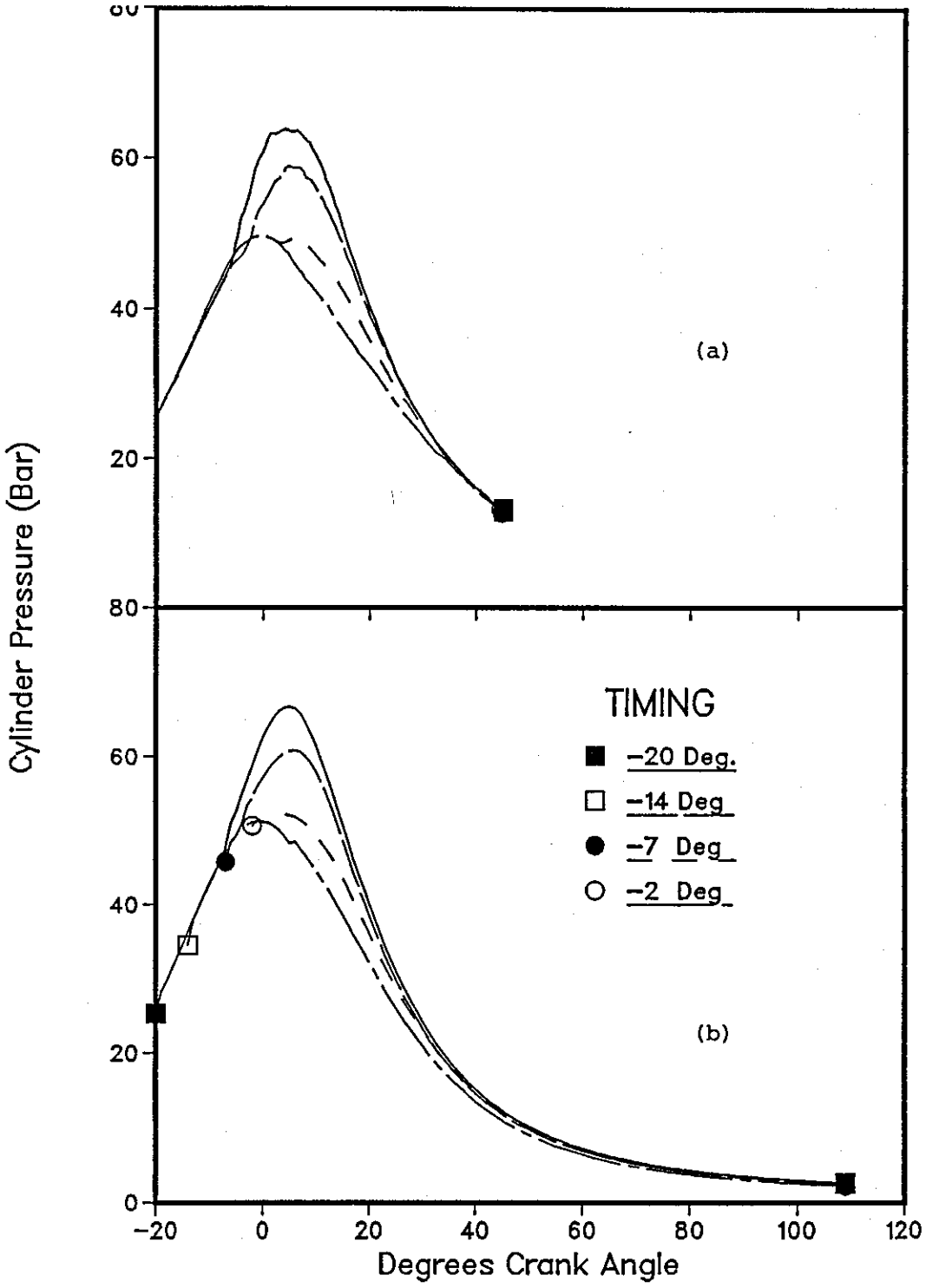

FIGURE 7.11: EFFECT OF INJECTION TIMING ON CYLINDER PRESSURE
a) EXPERIMENTAL
b) MODEL

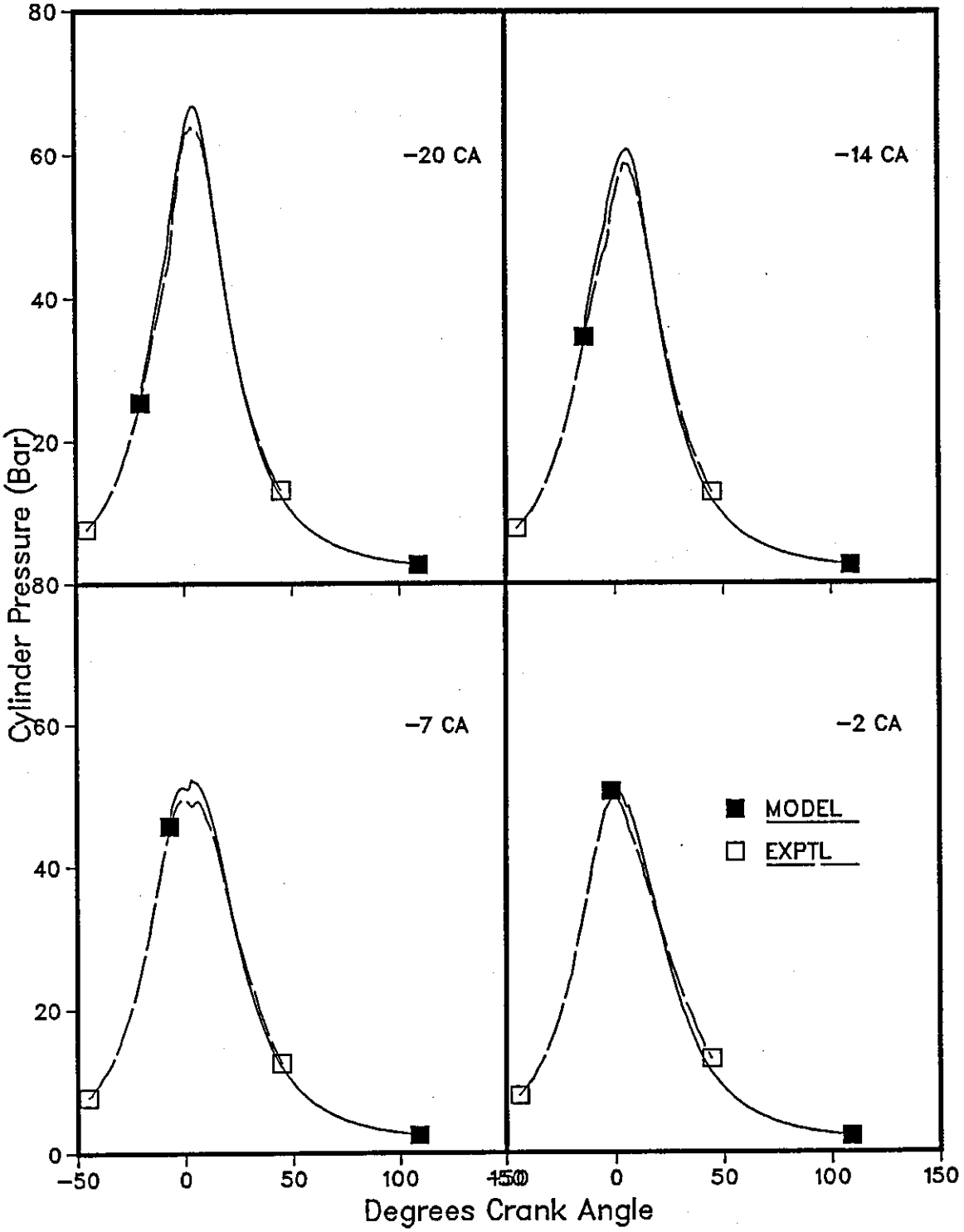

FIGURE 7.11(c): EFFECT OF INJECTION TIMING ON CYLINDER PRESSURE

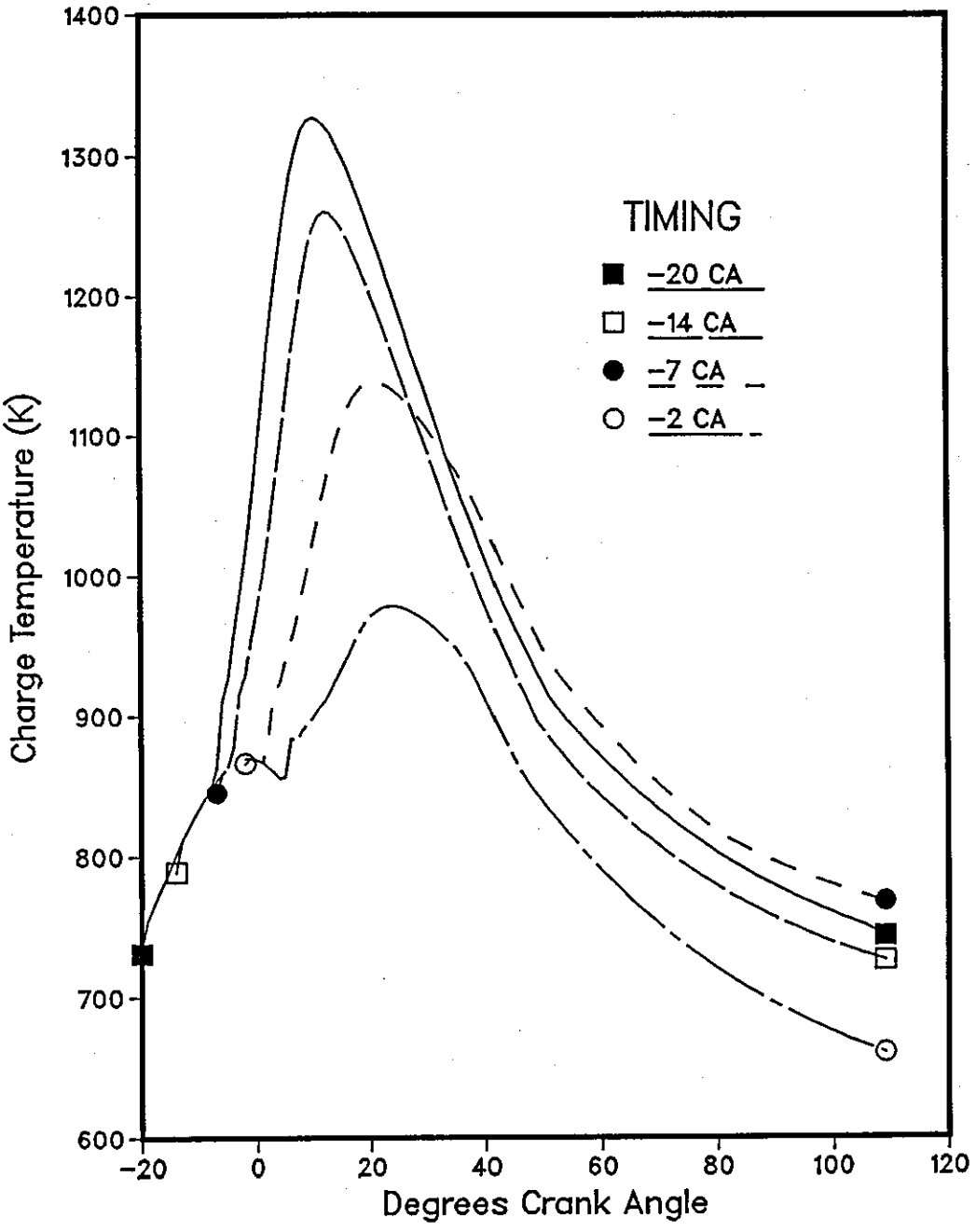

FIGURE 7.12: EFFECT OF INJECTION TIMING ON CHARGE TEMPERATURE

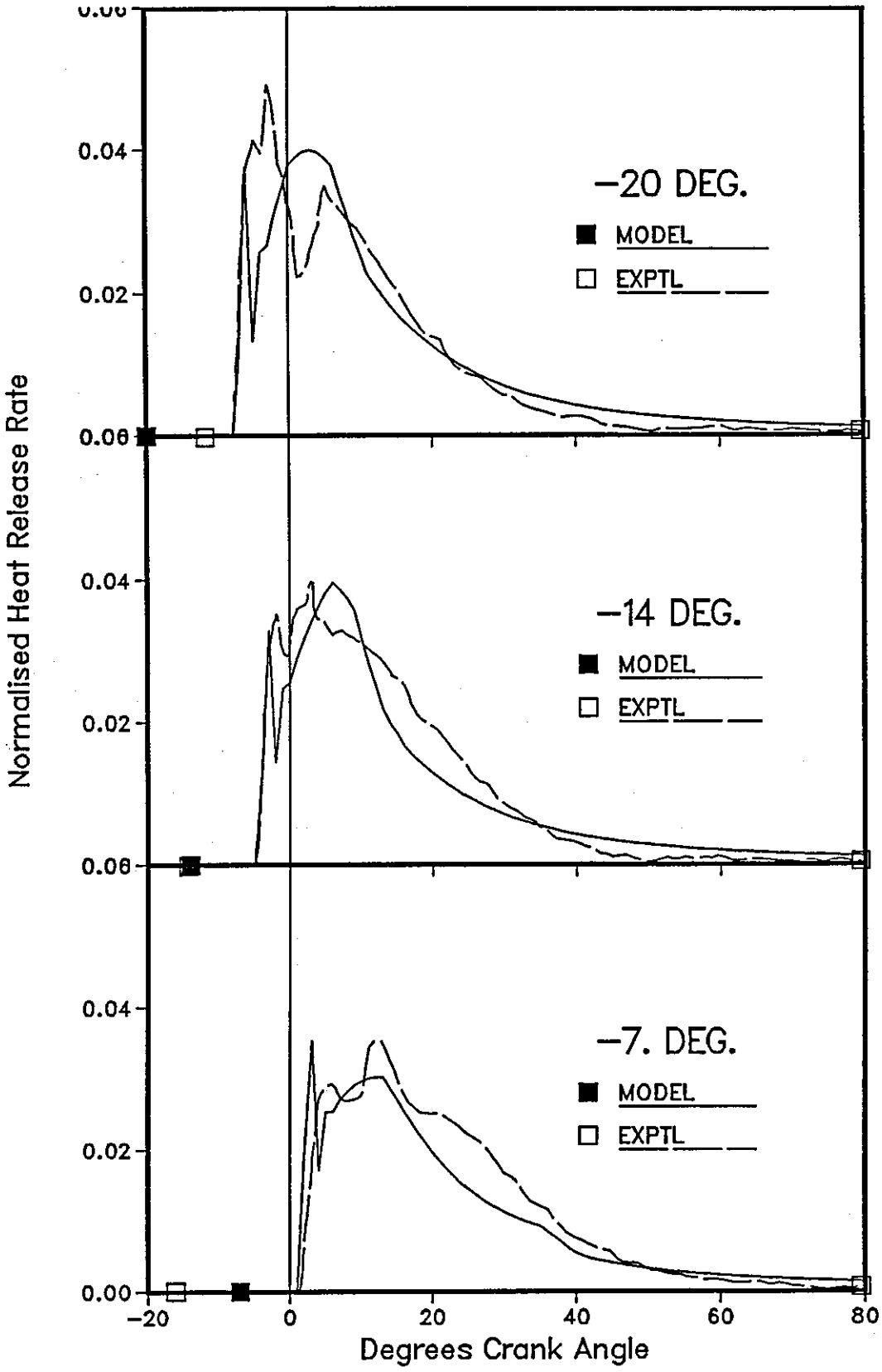

FIGURE 7.13: EFFECT OF INJECTION TIMING ON HEAT RELEASE RATE

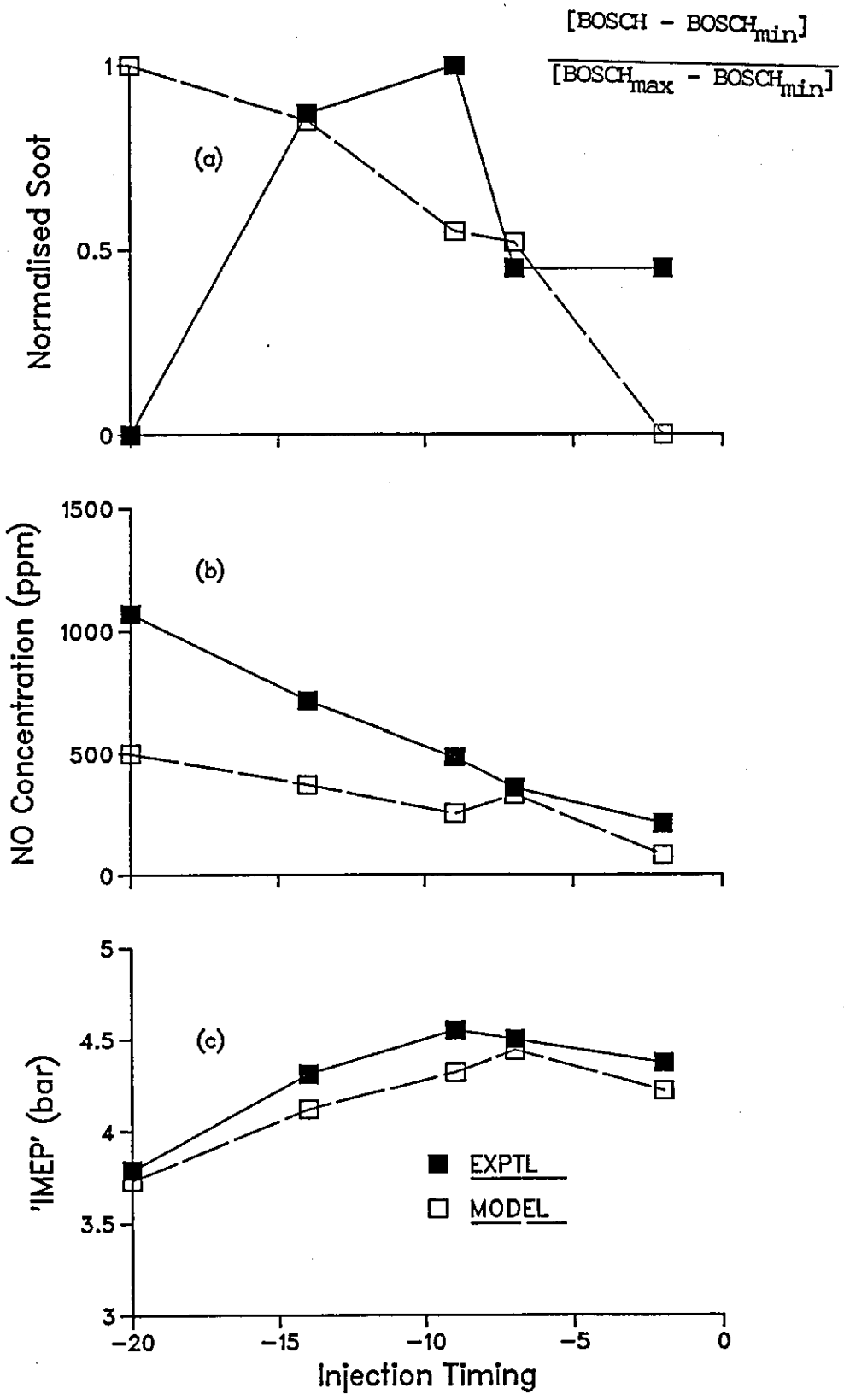

FIGURE 7.14: EFFECT OF INJECTION TIMING ON ENGINE PERFORMANCE

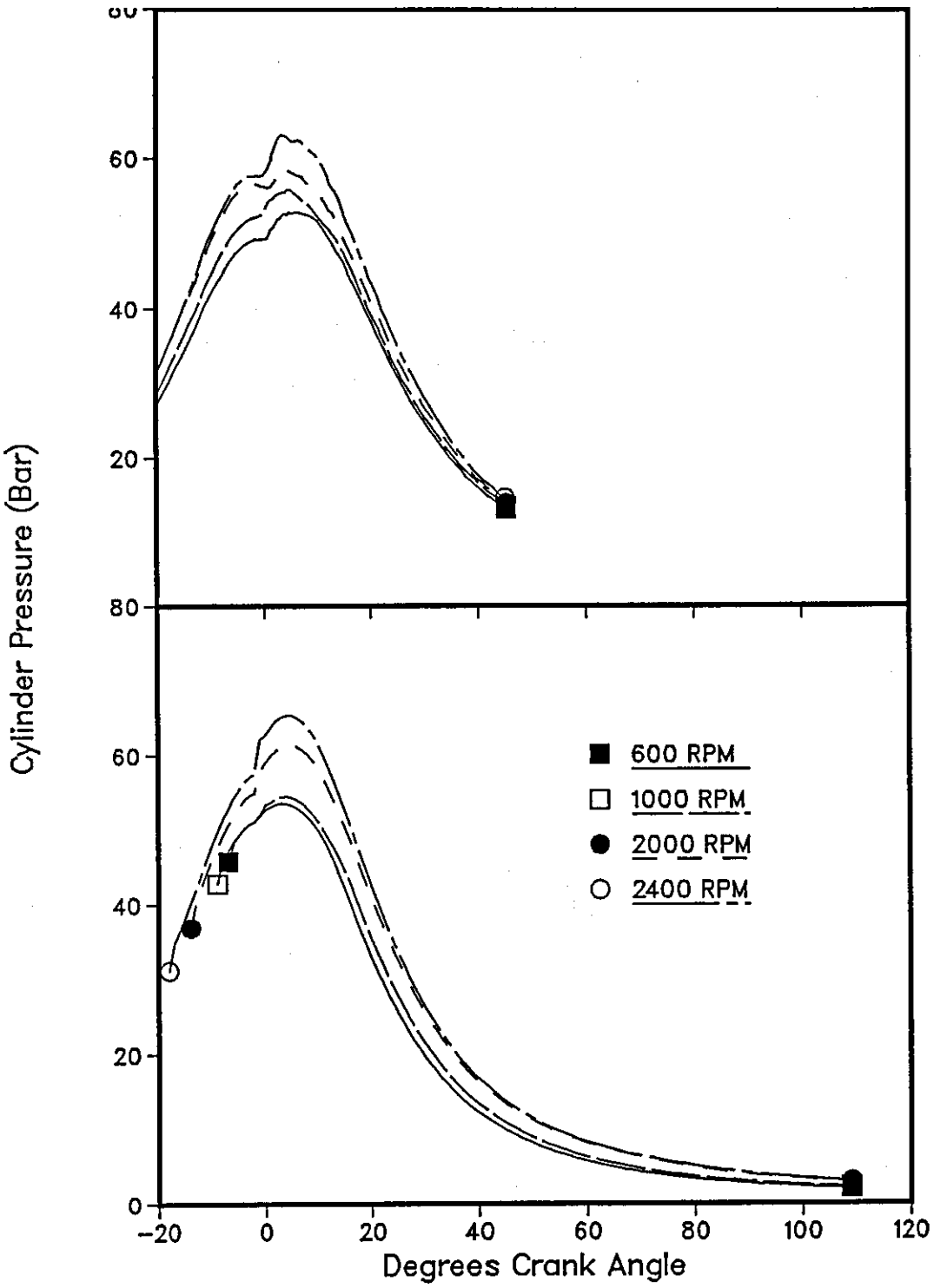

FIGURE 7.15: EFFECT OF ENGINE SPEED ON PRESSURE
a) EXPERIMENTAL
b) MODEL

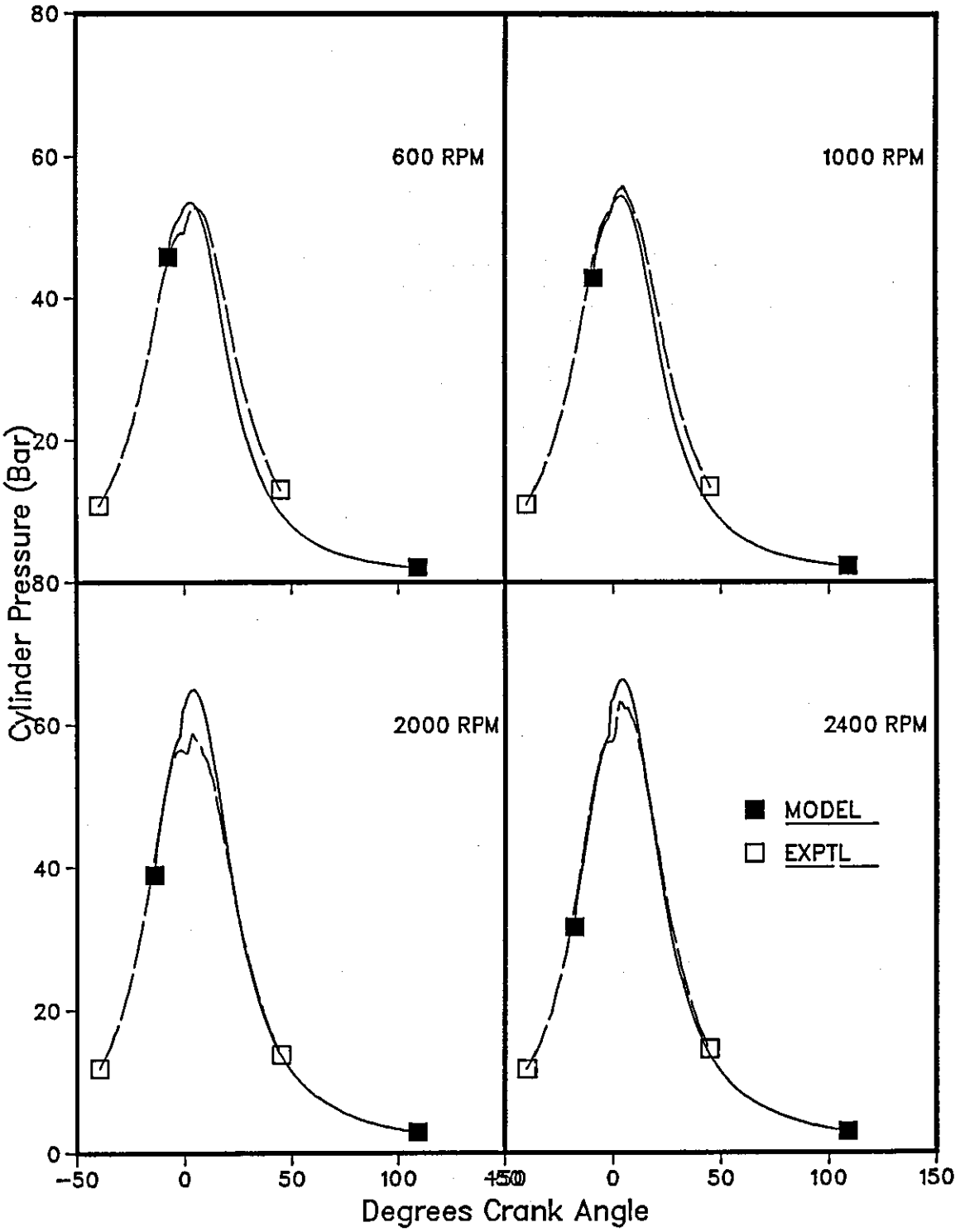

FIGURE 7.15e: EFFECT OF ENGINE SPEED ON CYLINDER PRESSURE

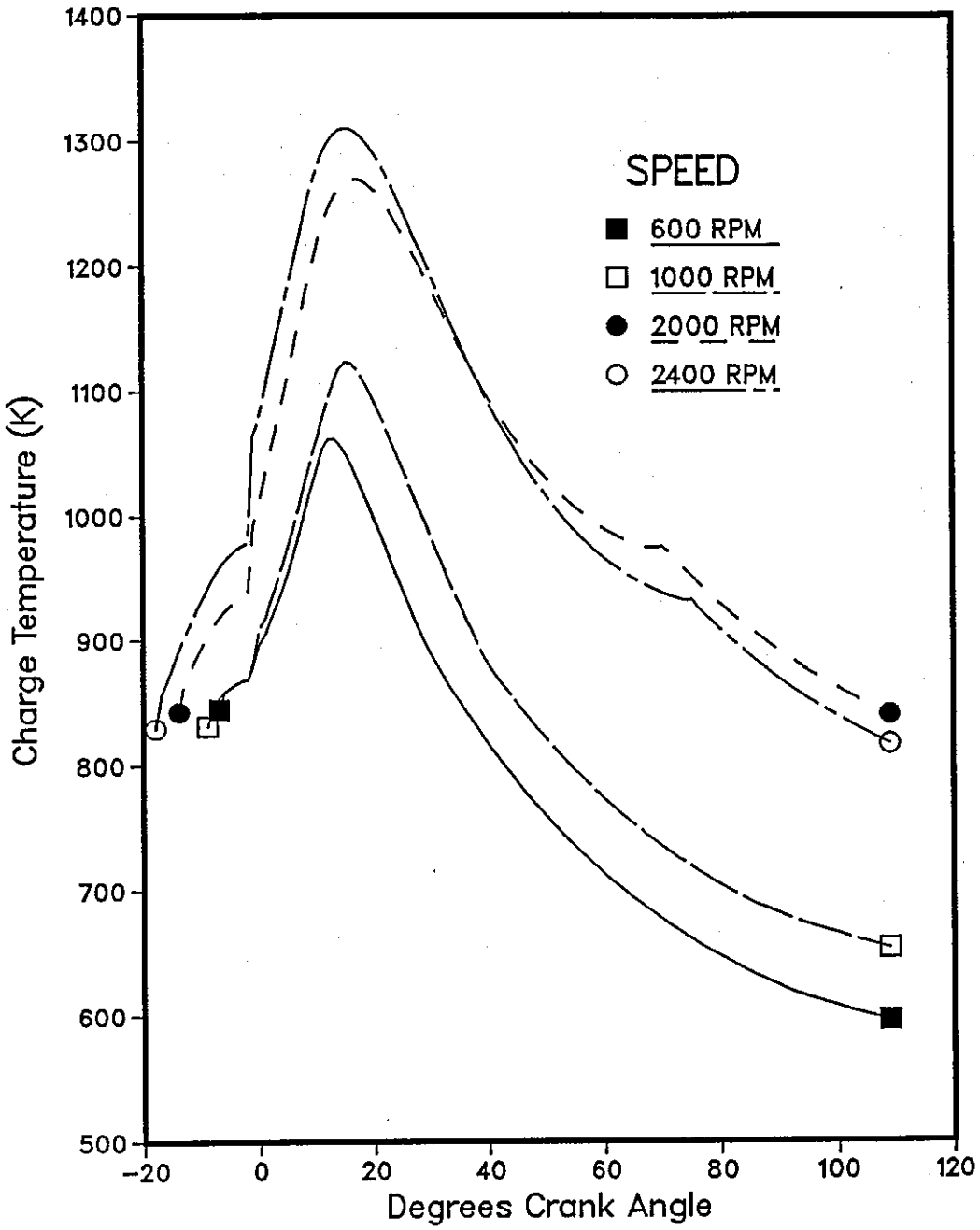

FIGURE 7.16: EFFECT OF ENGINE SPEED ON MEAN CHARGE TEMPERATURE

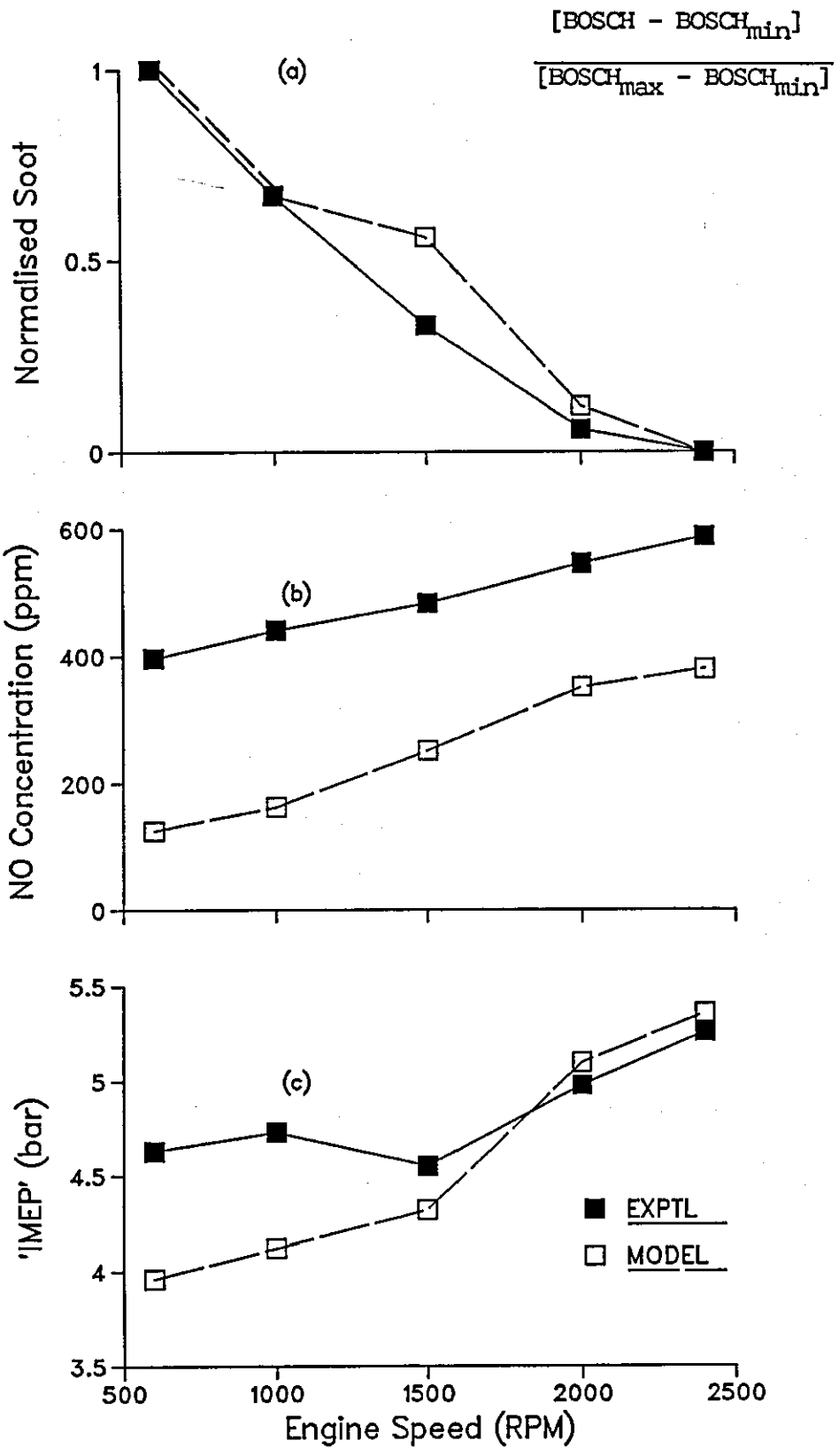

FIGURE 7.17: EFFECT OF SPEED ON ENGINE PERFORMANCE

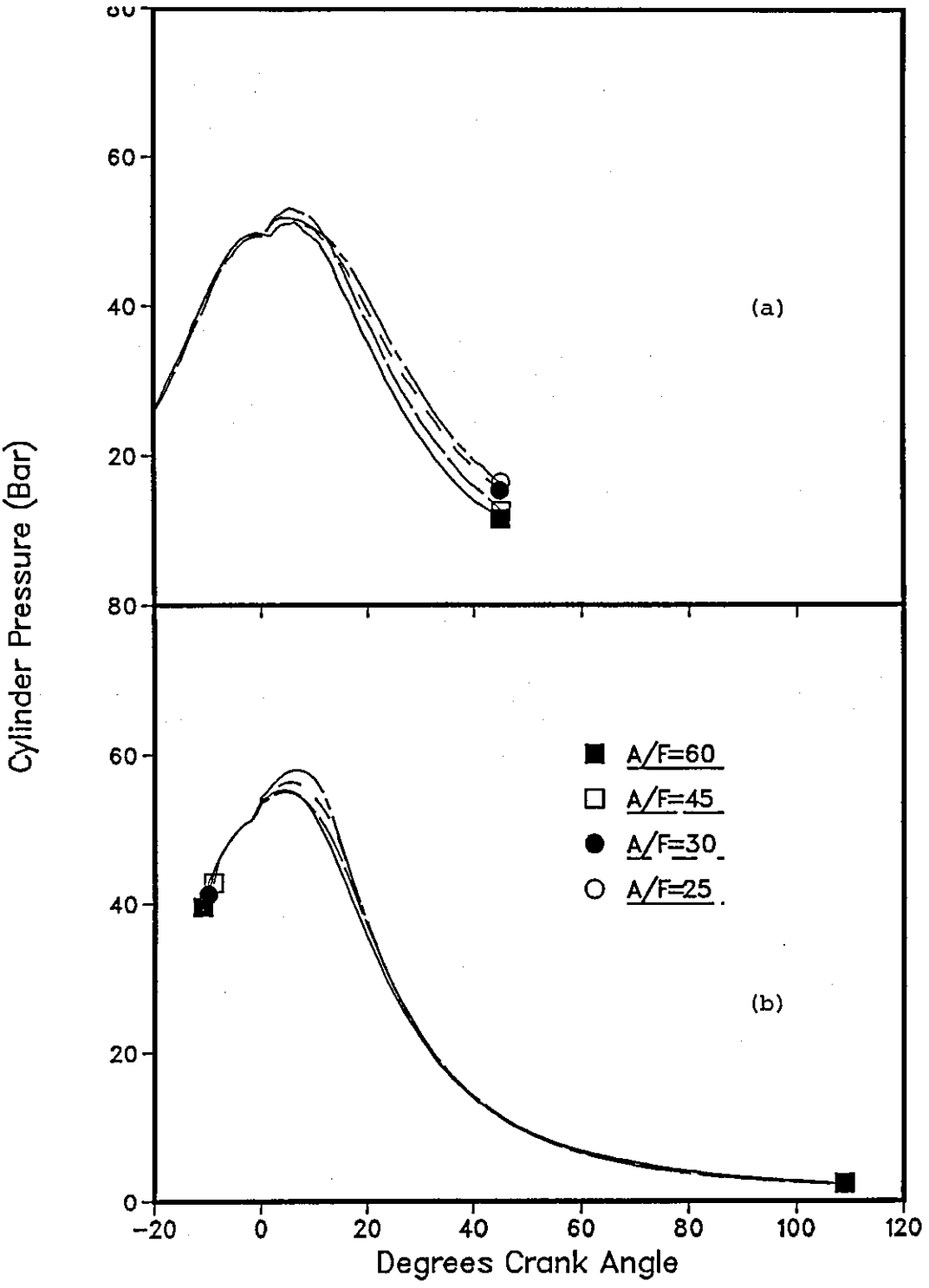

FIGURE 7.18: EFFECT OF AIR/FUEL RATIO ON PRESSURE
a) EXPERIMENTAL
b) MODEL

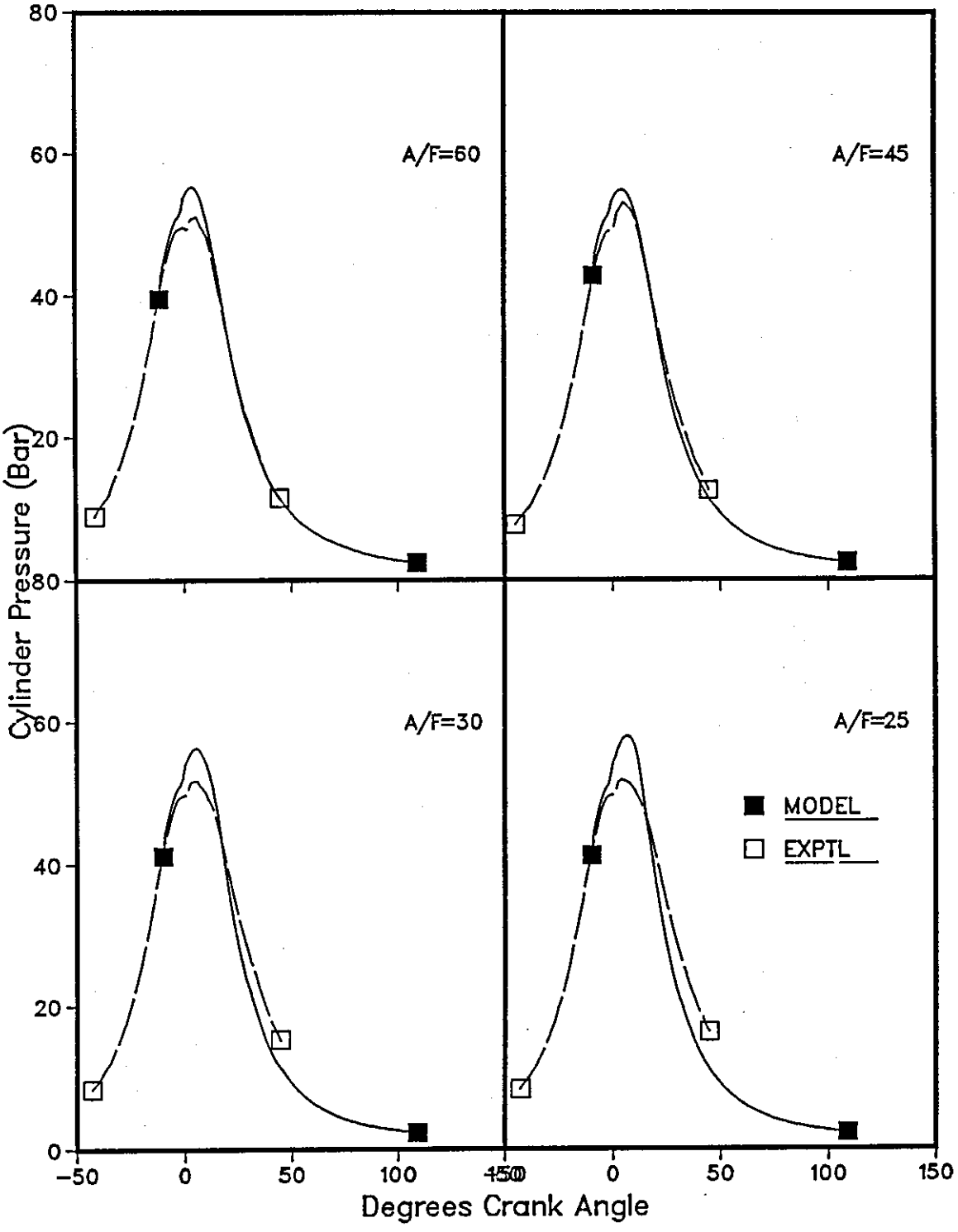

FIGURE 7.18(c): EFFECT OF AIR/FUEL RATIO ON CYLINDER PRESSURE

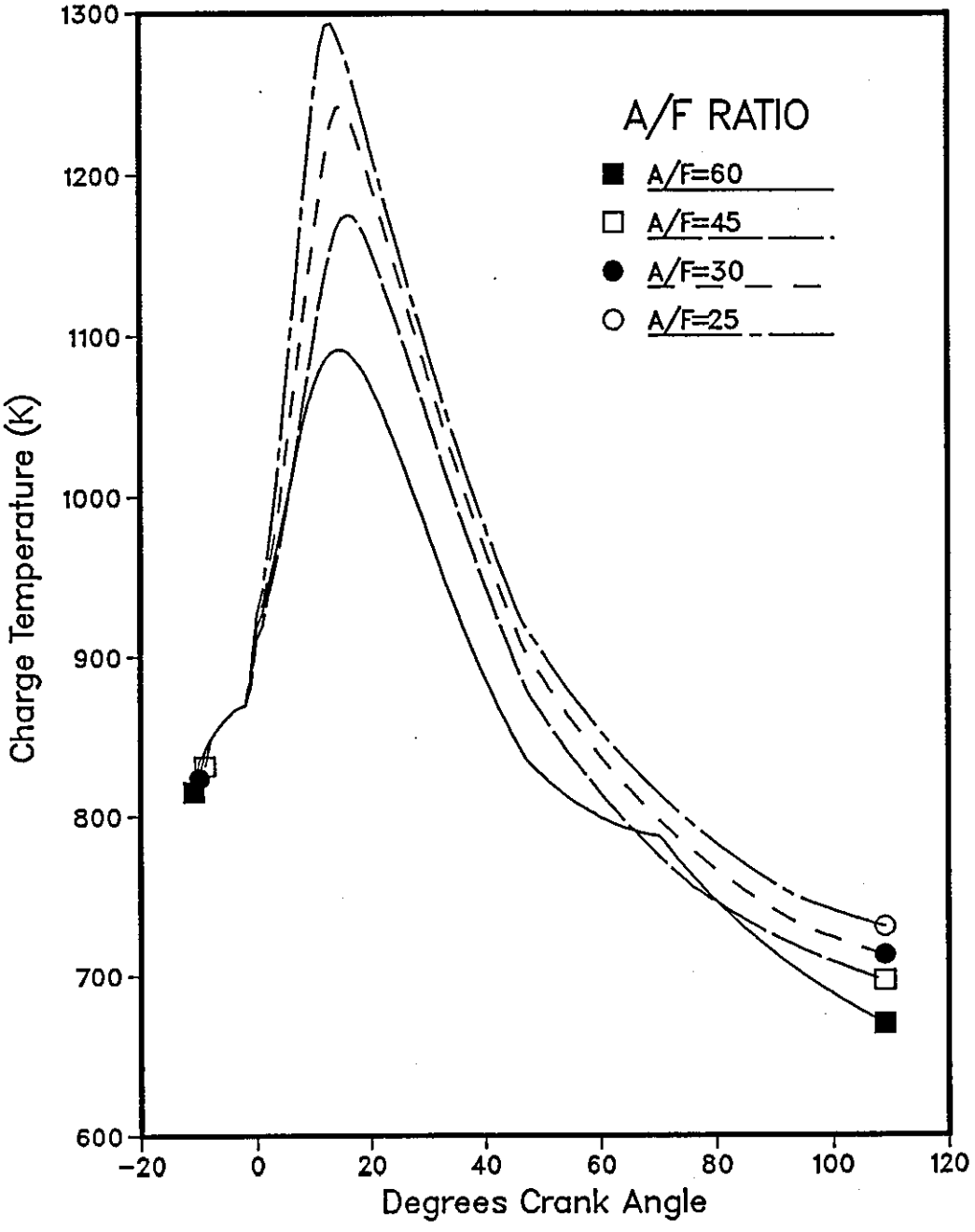

FIGURE 7.19: EFFECT OF OVERALL AIR/FUEL RATIO ON TEMPERATURE

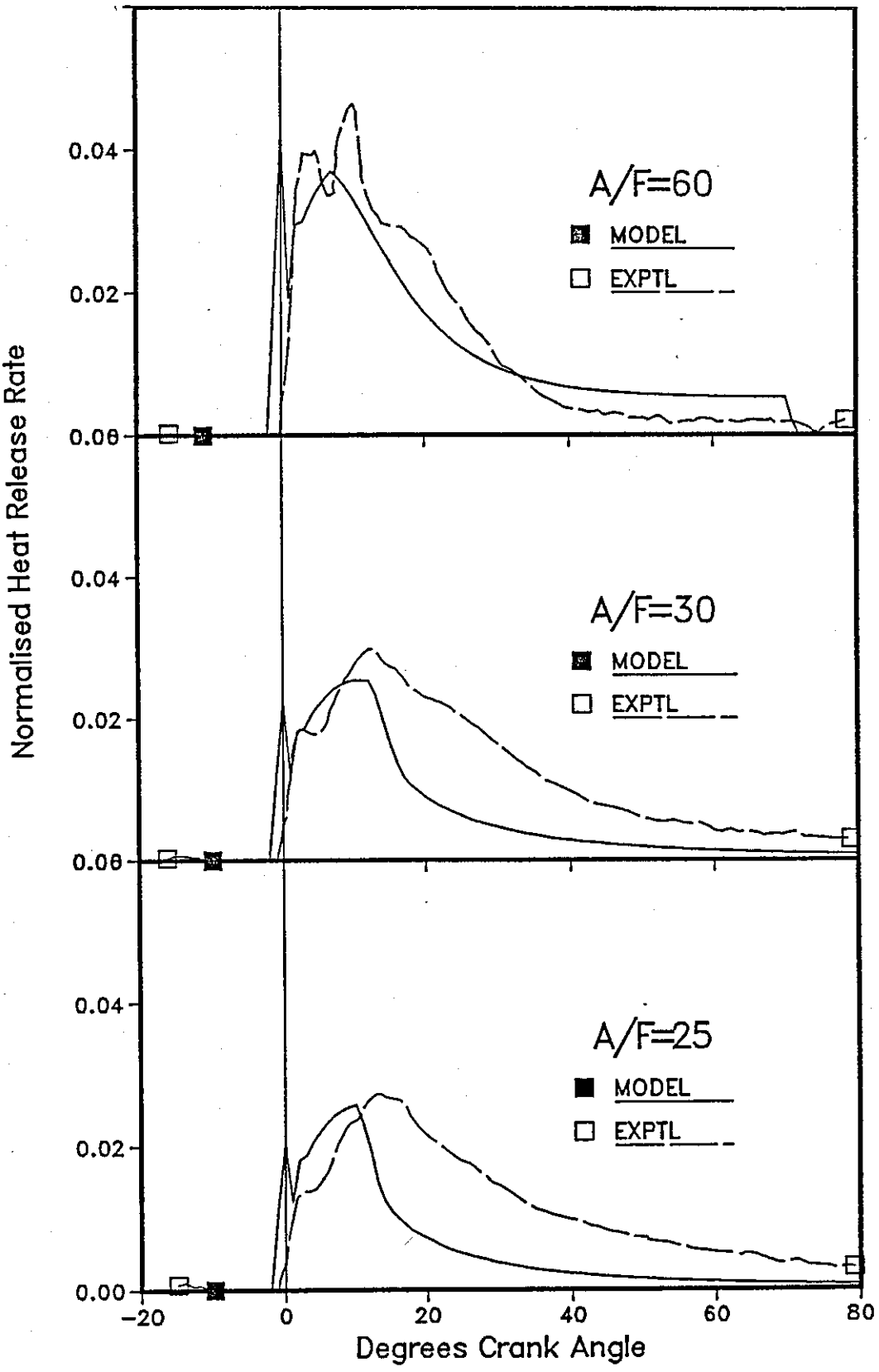

FIGURE 7.20: EFFECT OF OVERALL AIR/FUEL RATIO ON RATE OF HEAT RELEASE

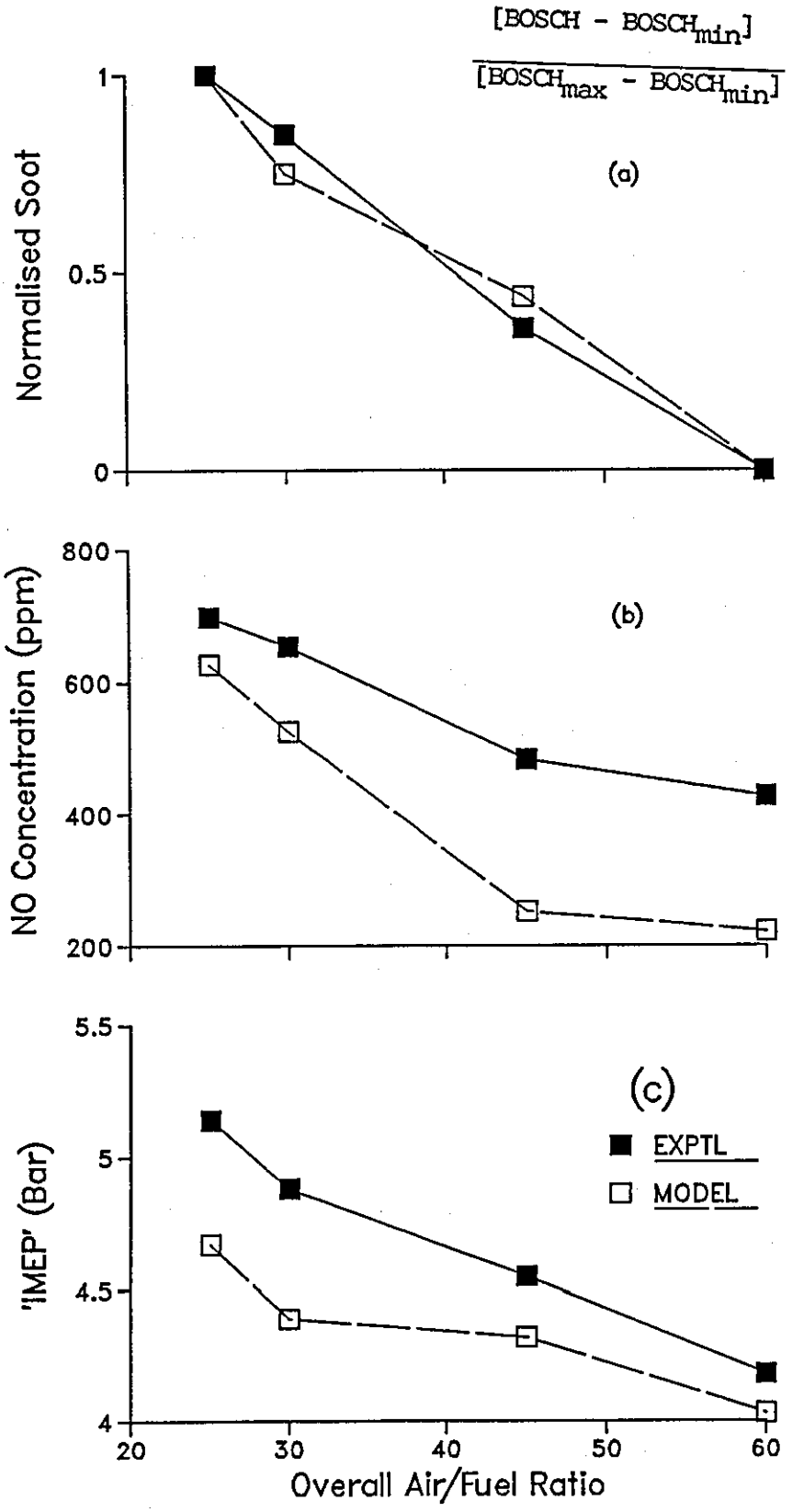

FIGURE 7.21: EFFECT OF OVERALL AIR/FUEL RATIO ON ENGINE PERFORMANCE

CHAPTER 8

CONCLUDING DISCUSSION

8.1 DISCUSSION

One of the major points of uncertainty in wall-wetting engine performance relates to the identification of dominant parameters that influence the rate of burn. Whereas Martin and Ahmad(31) were only able to estimate the rate of combustion to be slower than the fastest rate as determined by the injection rate, but faster than the slowest rate as determined by the total burn duration, this model has demonstrated that rate of fuel film evaporation is the dominant variable. This corroborates the results of Meurer and Urlaub(40) shown in Figure 1.21, and also explains the smooth combustion which results in 'gentle' pressure curves obtained by Martin and Ahmad and also by other workers. The slow rate of evaporation (typically up to 100 Degrees Crank Angle) demonstrated by the model is corroborated by the empirical results of Müller(41) which were obtained in a fired engine using fuel with a slightly lower latent heat of vaporisation (see Table 5.2). As a result, the wall-wetting engine is characterised by a slower burn rate (see Figure 7.8) than the convetional DI engine as demonstrated in Figures 2.27 to 2.30. Due to the reduced surface area of the fuel discussed in the literature survey (p.9), there is little of the initial pre-mixed charge that charactrises conventional DI engine burning immediately after auto-ignition. The heat release diagrams in Figures 7.13 and 7.20 illustrate this point clearly.

Since in the low engine speed range air swirl is proportional to engine speed(20), the increase in the mass fraction of unburnt fuel as engine speed reduces is a result of the progressive reduction in the relative velocity of swirl air on the film surface, which leads to unsatisfactory evaporation rate, and hence poor burn rate. The model has been successful in predicting this behaviour, which was one of the

reasons that led to the development of the 'Controlled Direct Injection' engine discussed under literature survey. It thus offers a possibility for analysing load effects on the performance of the wall-wetting engine, especially under extreme load conditions.

Some assumptions in the mathematical model have been tested for realistic behaviour in a set of experiments designed to investigate characteristic dimensions of the injected fuel film as it develops on the piston wall. The optical methods used have highlighted important details about the fuel film and its subsequent evaporation into the air stream. Section 5.6 summarises some of the findings from the experimental work in as far as they affect the modelling concept.

8.2 CONCLUSION

A method for modelling combustion and engine performance in a direct injection wall-wetting diesel engine has been demonstrated. The proposed model draws on a consistent and coherent set of ideas from Fluid Mechanics, Heat and Mass Transfer, and Combustion that have formed the basis of the conceptual framework. The model has successfully been applied to the evaluation of a single cylinder experimental engine and shown to be fairly reliable over a wide load range (Air/Fuel ratio from 25 to 60), engine speed (from 600 to 2400 RPM), and injection timing (from 20^{o} BTDC to 2^{o} BTDC).

Exhaust emission modelling has been improved through the use of more efficient numerical techniques to solve differential equations and systems of linear and non-linear equations. General trends have been predicted fairly accurately under most of the conditions investigated.

8.3 RECOMMENDATIONS FOR FUTURE WORK

In the course of carrying out the experiments, it has become clear that there is need for more investigation on the governing equations

for the behaviour of the film as it develops on the piston wall. Although the simplified equations based on wall jets have been able to yield good predictions for penetration and velocity along the wall, they do not provide detailed information about the hydrodynamic nature of the fuel film. There is need to study the formation of ripples on the surface of the injected film, and whether these have any bearing on the level of exhaust emissions, especially unburnt hydrocarbons.

Another aspect of the present work that needs further investigation is the significance of piston bowl geometry in influencing engine performance. This has been briefly discussed with respect to the level of smoke emissions at different settings of injection timing. The disparity in the results has been partly attributed to the changes in impingement location as injection timing is varied. It is thus necessary, for accurate predictions of smoke and unburnt hydrocarbon emissions, to address bowl geometry effects in detail. This cannot be achieved effectively with the phenomenological scheme adapted in this work, and may entail incorporation of multi-dimensional features in the model. The benefits of a more rigorous and fundamental approach in this case justify the relatively marginal sacrifice in computation time.

REFERENCES

1. Heywood, J. B.: Engine Combustion Modelling - An Overview. Symposium on Combustion Modelling in Reciprocating Engines, General Motors Research Laboratories, 1978. Plenum Press, New York 1980. Edited by Mattavi, J.N. and Amann, C.A.

2. Mehta, P.S.: Phenomenological Combustion Model for Direct Injection Diesel Engines. Ph.D Thesis, Loughborough University, 1981.

3. Shahed, S.M., Chiu, W.S., and Lyn, W.T: A Mathematical Model of Diesel combustion. IMechE Paper C94/75, 1975.

4. Lyn, W.T: Study of the Burning Rate and Nature of Combustion in Diesel Engines. 9th Symposium on Combustion, 1962.

5. Shahed, S.M., Flynn, P.F., and Lyn, W.T: A Model for the Formation of Emissions in a Direct-Injection Diesel Engine.

6. Dent, J.C. and Mehta, P.S: Phenomenological Combustion Model for a Quiescent Chamber Engine. SAE Technical Paper 811235.

7. Dent, J.C., Mehta, P.S., and Swan, J: A Predictive Model for Automotive DI Diesel Engine Performance and Smoke Emissions. IMechE Paper C126/82, 1982.

8. Kyriakides, S.C., Dent, J.C., and Mehta, P.S: Phenomenological Diesel Combustion Model Including Smoke and NO Emission. SAE Technical Paper, 860330, 1986.

9. Monaghan, M.L: The High Speed Direct Injection Diesel for Passenger Cars. SAE Trans. 810477.

10. Cichoki, R and Cartellieri, W: The Passenger Car Direct-Injection Diesel - A Performance and Emissions Update. SAE Technical Paper 810480.

11. Taylor, C.F: The Internal Combustion Engine in Theory and Practice. Vol. II, MIT Press, 1985.

12. Whitehouse, N.D., and Baluswamy, N: Calculations of Gaseous Products During Combustin in a Diesel Engine Using a Four-Zone Model. SAE Transactions 770410.

13. Lavoie, G.A., Heywood, J.B., Keck, J.C: Experimental and Theoretical Study of Nitric Oxide Formation in Internal Combustion Engines. Combustion Science and Technology, Vol. 1, 1970.

14. Fraas, A.P: Combustion Engines. McGraw-Hill, New York, 1948.

15. Judge, A.W: High Speed Diesel Engines, Chapman and Hall, London, 1967.

16. Lilly, L.C.R. (Ed.): Diesel Engine Reference Book, Butterworths, London, 1984.

17. Burman, P.G. and DeLuca, F: Fuel Injection and Controls for Internal Combustion Engines. The Technical Press Ltd., London, 1962.

18. Chiu, W.S., Shahed, S.M., and Lyn, W.T: A Transient Spray Mixing Model for Diesel Combustion. SAE Trans. 760128.

19. Dent, J.C.: Turbulent Mixing Rate - Its Effect on Smoke and Hydrocarbon Emissions from Diesel Engines. SAE Technical Paper 800092.

20. Urlaub, A.C: The Effect of Air Motion on Mixture Formation In Direct-Injection Diesel Engines. VDI Zeitschrift, Series 6, No. 2, 1965. MIRA Translation No. 55/65.

21. Watts, R. and Scott, W.M: Air Motion and Fuel Distribution Requirements in High Speed Direct Injection Diesel Engines, IMechE Symposium - Diesel Engine Combustion, London, 1970.

22. Davis, G.C. and Kent, J.C: Comparison of Model Calculations and Experimental Measurements of the Bulk Cylinder Flow Processes in a Motored PROCO Engine. SAE Paper No. 790290.

23. Morris, C.J. and Dent, J.C: The Simulation of Air-Fuel Mixing in High Swirl Open-Chamber Diesel Engines. Proc. IMechE, Vol. 190, C47/76, 1976.

24. Morris, C.J: The Modelling of Fuel Dispersion and Concentration in Direct Injection Diesel Engines. Ph.D Thesis, Loughborough University, 1975.

25. Alcock, J.F: Air Swirl in Oil Engines. Proc. IMechE, Vol. 128, 123, 1934.

26. Gosman, A.D., Tsui, Y.Y., Vafidas, C: Flow in a Model Engine with a Shrouded Valve - A Combined Experimental and Computational Study. SAE 850498.

27. Pinchon, P. and Baritaud, T: Modelling of Flow and Combustion in a Spark Ignition Engine with a Shrouded Valve - Comparison and Experiments. Inter. Conf. on Heat and Mass Transfer in Gasoline and Diesel Engines. August, 1987, Dubrovnik, Yugoslavia.

28. Lee, D.W: A Study of Air Flow in an Engine Cylinder NACA Rep. No. 653, 1939.

29. Nagao, F., Ikegami, M., Kujota, Y., Mitsuda, T., and Kawatei, K: A Study of Combustion in Direct Injection Diesel Engines - 1st Report. Bul. J.S.M.E. Vol. 16, No. 93, 1973.

30. Neitz, A. and D'Alfonso, N: The MAN Combustion System with Controlled Direct Injection for Passenger Car Diesel Engines. SAE Technical Paper 810479.

31. Martin, J.K. and Ahmad, T: Heat Release Characteristics of an Open-Chamber Diesel Engine Employing a Wall-Wetting Combustion System. SAE Technical Paper 860420.

32. Meurer, J.S: Evaluation of Reaction Kinetics Eliminates Diesel Knock - The M-Combustion System of MAN. SAE Trans., Vol. 64, 1956.

33. Meurer, J.S: Present Experience with Startified Charge Engines Working with Initial Separation of Mixture Components. IMechE Paper No. C250/76, 1976.

34. Urlaub, A.C: Progress in Mixture Formation and Combustion. XII FISITA Congress, Paper No. 1-09, 1968. MIRA Translation No. 3/69.

35. Neitz, A. and Müller, E: Exhaust Gas Improvement in MAN Automotive Engines by Controlled Injection 14th CIMAC, Helsinki 1981.

36. Chmela, F: High Compression Stratified Charge Engines and their Suitability for Conventional and Alternative Fuels. IMechE, 1980, C400/80.

37. Zinner, K: Influence of the Cylinder Size of Diesel Engines on the Combustion System. 9th International Congress on Combustion Engines (CIMAC). Stockholm, 1971.

38. Urlaub, A.C: Investigations into the Question of Exhaust Gas Odour from Direct Injection Diesel Engines. CIMAC, 1975.

39. Monaghan, M.L: A Wall-Wetting Direct Injection Diesel for Passenger Cars. XX FISITA CONGRESS, VIENNA 1984. SAE 845040.

40. Meurer, J.S. and Urlaub, A.C: Development and Operatinal Results of the MAN FM-Combustion System. SAE Trans. 690255.

41. Müller, E: Gemischbildung im Dieselmotor bei Kraftstoffwandanlagerung. Dr. Ing. Thesis, Technical University, Darmstadt, 1976.

42. Klanner, W: Experimentelle und Theoretische Undersuchung der Krafftstoffilmverdampfung im Dieselmotor. Dr. Ing. Thesis, Technical University, Munich, 1971.

43. Meurer, J.S: Progress in the Formation of the Mixture and In Combustion in Diesel Engines. Proc. IMechE, Vol. 181, Pt. 1.

44. Squire, L.C: The Motion of a Thin Oil Sheet Under the Boundary Layer on a Body. AGARDOGRAPH 70, 1962. (Compiled by R.L. Maltby).

45. Shembharkar and Pai: Prediction of Film Cooling with a Liquid Coolant. Inter. J. Heat and Mass Transfer, Vol. 29, June 1986.

46. Kanury, A.M: Introduction to Combustion Phenomena. Gordon and Breach, New York, 1975.

47. Warner, C.F. and Emmons, D.L: Effects of Selected Gas Stream Parameters and Coolant Properties on Liquid Film Cooling. Trans. ASME, J. Heat Transfer, May 1964.

48. Zucrow, M.J. and Graham, A.R: Some Considerations of Film Cooling for Rocket Motors. Jet Propulsion, American Rocket Soc., N. York 1957.

49. Zucrow, M.J. and Sellers Jr., J.P: Experimental Investigations of Rocket Motor Film Cooling. Journal of the American Rocket Soc. May, 1961.

50. Marxman, G.A: Combustion in the Turbulent Boundary Layer On a Vaporizing Surface. 10th Sym. (International) on Combustion. Combustion Institute, 1965.

51. Spalding, D.B: Unified Theory of Friction, Heat Transfer and Mass Transfer in the Turbulent Boundary Layer and Wall Jet. ARC Current Papers, CP No. 829, 1964.

52. Kays, W.M. and Crawford, M.E: Convective Heat and Mass Transfer. 2nd Edition. McGraw-Hill, New York, 1980.

53. Lees, L: Combustion and Propulsion. Third AGARD Colloquium, Pergamon, 1958.

54. Kays, W.M: Convective Heat and Mass Transfer. McGraw-Hill, 1966.

55. Spalding, D.B: Some Fundamentals of Combustion, Butterworth, London 1955.

56. Schlichting, H: Boundary Layer Theory. McGraw-Hill, 4th Edition, 1960.

57. Magnussen, B.F: Modelling of Reaction Processes in Turbulent Flames with Special Emphasis on Soot Formation and Combustion. Symposium on Particulate Carbon Formation During Combustion, General Motors, Warren, Oct. 1980.

58. Plee, M: General Motors Research Laboratories, Internal Report No.EN 335 (1986).

59. Marxman, G. and Gilbert, M: Turbulent Boundary Layer Combustion in the Hybrid Rocket. 9th Symposium (International) on Combustion, 1962.

60. Dent, J.C. and Mehta, P.S: Quiescent Chamber Diesel Engine Combustion Simulation Program. Internal Report, Dept. of Mech. Eng., Loughborough University, March 1981.

61. Burden, R.L. and Faires, J.D: Numerical Analysis. Prindle, Weber and Schindt. 3rd Edition, Boston 1985.

62. Abramovich: Turbulent Jets. MIT Press, Cambridge, Mass., USA.

63. Simmons, H.C: The Correlation of Drop-Size Distributions In Fuel Nozzle Sprays - Parts I and II. J. Engineering Power, July 1977.

64. Knight, B.E: Communication on the Performance of a Type of Swirl Atomiser. Proc. I.Mech.E., Vol. 169, 1955.

65. Ricou, F.P. and Spalding, D.B: Measurements of Entrainment by Axisymmetrical Turbulent Jets. J. Fluid Mechanics, Vol. II, 1961.

66. Rajaratnam, N: Turbulent jets. Developments in Water Science, No. 5, Elsevier, New York 1976.

67. Giralt, F., Chia, C.J., and Trass, O: Characterisation of the Impingement Region in an Axisymmetric Turbulent Jet. Industrial Engineering Chem., Vol. 16, 1977.

68. Hertel, H: Strömungsvorgange beim Freien Hubstrahler. Luft Fartteckmik, Vol. 8, 1962.

69. Corrsin, S: Simple Theory of an Idealised Turbulent Mixer. AIChE Journal, Vol. 3, No. 3, 1957.

70. Tennekes, H. and Lumley, J.L.: A First Course in Turbulence. MIT Press, Cambridge, 1972.

71. Tesner, P.A., Snegiriova, T.D., Knorre, V.G: Kinetics of Dispersed Carbon Formation. Combustion and Flame, Vol. 17, 1971.

72. Mugnussen, B.F. and Hjertager, B.H: On Mathematical Modelling of Turbulent Combustion with Special Emphasis on Soot Formation and Combustion. 16th (International) Symposium on Combustion.

73. Lee, K.B., Thring, M.W., Beer, J.M: On the Rate of Combustion of Soot in a Laminar Soot Flame. Combustion and Flame, Vol. 6, 1962.

74. Dent, J.C. and Derham, J.A: Air Motion in a Four-Stroke Direct Injection Diesel Engine. Proc. IMechE., Vol. 188, 21/74, 1974.

75. Sinnamon, J.F., Lancaster, D.R., Stiener, J.C: An Experimental and Analytical Study of Engine Fuel Spray Trajectories. SAE Trans. 800135.

76. Adler, D. and Bacon, A: Prediction of a 3-Dimensional circular Turbulent Jet in Cross-flow. AIAA Journal, Vol. 17, 1979.

77. Adler. D. and Lyn, W.T: The Evaporation and Mixing of a Liquid Fuel Spray in a Diesel Air Swirl. Symposium on Diesel engine Combustion, IMechE, 1970.

78. Escudier, M.P., and Nicoll, W.B: Entrainment Function in Boundary Layers and Wall Jets. J. Fluid. Mech., Vol. 25.

79. Shahed, S.M., Chiu, W.S., Yumlu, V.S: A Preliminary Model for the Formation of Nitric Oxide in Direct Injection Diesel Engines and in in Parametric Studies. SAE Trans. 730083.

80. Ferguson, C: Internal Combustion Engines: Applied Thermosciences. John Wiley and Sons, New York 1986.

81. Appleton, J.P: Soot Oxidation Kinetics at Combustion Temperatures. AGARD CP-125. Paper No. 20. 1973.

82. Nagle, J. and Stickland-Constable, R.F: Oxidation of Carbon Between 1000-2000^{o}C. Proceedings of the Fifth Conference on Carbon. Pergamon Press, London, 1962.

83. Neoh, K.G., Howard, J.B., and Sarofirm, A.F: Soot Oxidation in Flames. Particulate Carbon Formation During Combustion, Plenum Press, New York, 1981.

84. Ahmad, T., Plee, S.L., and Myers, J.P. - General Motors Engine Research Department. Internal Report No. E

85. Fenimore, C.P. and Jones, G.W: Oxidation of Soot by Hydroxyl Radicals. J. Phys. Chem., Vol. 71, 1967.

86. Sherman, R.H. and Blumberg, P.N: The Influence of Induction and Exhaust Processes on Emissions and Fuel Consumption in the Spark Ignition Engine. SAE Trans. 770880.

87. Horlock, J.H. and Woods, W.A: Calculation of Non-Steady Flows Using Filling and Emptying Methods and Quasi-Steady Flow Models. The Thermodynamics and Gas Dynamics of Internal Combustion Engines, Vol.II, Oxford University Press (1986). Edited by Horlock, J. H. and Winterbone, D. E.

88. Kastner, L.J., Williams, T.J., and White, J.B.: Poppet Inlet Valve Characteristics and Their Influence on the Induction Process. Proceedings of the IMechE, Vol. 178, 1963.

89. Tabaczynski, R.J.: Effects of Inlet and Exhaust System Design on Engine Performance. SAE 821577.

90. Fukutani, I. and Watanabe, E.: Air Flow Through Poppet Inlet Valves - Analysis of Static and Dynamic Flow Coefficients. SAE 820154.

91. Hewitt, G.F. and Hall-Taylor, N.S: Annular Two-Phase Flow Pergamon Press, Oxford, 1970.

92. Calvert, S. and Williams, B: Upward Annular Flow of Air and Water in Smooth Tubes. AIChE Journal, Vol. 1, 1955.

93. Nicklin, J. and Kock, C.T: A Model of Two-Phase Annular Flow. CONCURRENT GAS-LIQUID FLOW (pp. 242-252), Plenum Press, New York, 1969 (Rhodes, E. and Scott, S.D. Ed.).

94. Fulford, G.D.: The Flow of Liquids in Thin Films. Advances in Chemical Engineering, Vol. 5, 1964.

95. Craik, A.D.D: Wind Generated Waves in thin Liquid Films. J. Fluid Mech., Vol. 26, Part 2, 1966.

96. Kreider, J.F: Principles of Fluid Mechanics. Allyn and Bacon, Boston 1985.

97. Glauert, M.B: The Wall-Jet. J. Fluid Mech., Vol. 1, 1956.

98. Bradshaw, P. and Gee, M.T: Turbulent Wall Jets With and Without an External Stream. ARC R and M No. 3252, June 1960.

99. Chesters, J.H., Holden, C., and R.D: Journal of the I.S.I. Vol. 185, 1957.

100. Kruka, V. and Eskinazi, S: The Wall-Jet in a Moving Stream. J. Fluid Mech,. Vol. 20, 1964.

101. Gartshore, I.S. and Newman, B.G: The Turbulent Wall Jet in an Arbitrary Pressure Gradient. Aeronautical Quarterley, February, 1969.

102. Schwartz, W.H. and Cosart, W.P.: The two-dimensional Turbulent Wall Jet. J. Fluid Mech., Vol. 10 1960.

103. Coles, D: The Law of the Wake in the Turbulent Boundary Layer. J. Fluid Mech. Vol. 1, 191, 195604. Sigalla, A:

104. Sigalla, A.: Experimental Data on Turbulent Wall Jets. Aircraft Engineering, Vol. 30, 1958.

105. Eskinazi, S. and Kruka, V: Mixing of a Turbulent Wall jet into a Free Stream. Trans. ASCE, Vol. 128, 1963.

106. Williams, F.A: Combustion Theory. Benjamin/Cummings, California. 2nd Edition, 1985.

107. Strehlow, R.A.: Combustion Fundamentals, McGraw-Hill, New York, 1984.

108. Wooldridge, C.E. and Muzzy, R.J: Measurements in a Turbulent Boundary Layer with Porous Wall injection and Combustion. 10th Symposium (International) on Combustion, 1965.

109. Kutateladze, S.S. and Leont'ev, A.L: Turbulent Boundary Layers in Compressible Gases. (Translated by D.B. Spalding). Arnold, London 1964.

110. Black, T.J. and Sarnecki, A.J: The Turbulent Boundary Layer with Suction or Injection. ARC R and M No. 3387, October 1958.

111. Partankar, S.V. and Spalding, D.B: Heat and Mass Transfer in Boundary Layers. Morgan-Grampian, London 1967.

112. Hirata, M., Ohe, S., Nagahama, K: Computer Aided Data Book of Vapour-Liquid Equilibria. Kodansha-Elsevier, 1975.

113. Andreussi, P. and Petarca, L: Film Combustion of Ethyl Alcohol in a Parallel Air Stream. 18th Symposium (International) on Combustion, 1981.

114. Marxman, G: Boundary Layer Combustion in Propulsion. 11th Symposium (International) on Combustion, 1964.

115. Collier, G. and Hewitt, G.F: Film Thickness Measurements. ASME Paper 64-WA/HT-41.

116. Hewitt, G.F., Lovegrove, P.C., and Nicholls, B.: Film Thickness Measurement Using a Fluorescence Technique. Pt. 1 Description of the Method. AERE-R4478, Harwell, 1964.

117. Benson, G.M., El-Wakil, M.M., Myers, P.S., and Uyehara, O.A: Fluorescent Technique for Determining the Cross-Sectional Drop-Size Distributions in Liquid Sprays ARS Journal, May 1960.

118. Holder, D. W. and North, R. J.: Schlieren Methods, Notes on Applied Science, No. 31, H.M.S.O., London 1963.

119. Rose, J.W. and Cooper, J.R: Technical Data on Fuel. The British National Committee, World Energy Conf., 7th Edition, London, 1977.

120. Woschini, A.G: A University Applicable Equation for the Instantaneous Heat Transfer Coefficient in the Internal Combustion Engine. SAE Trans. 670931.

121. Delichatsios, M.A. and Probstein, O.R.F: Coagulation in Turbulent Flow - Theory and Experiment. Fluid Mech. Lab., MIT, July 1974.

122. Olikara, C. and Borman, G.L.: A Computer Program for Calculating Properties of Equilibrium Combustion Products with Some Applications to I.C. Engines. SAE 750468.

123. Kuo, K.K.: Principles of Combustion, John Wiley and Sons, New York, 1986.

124. Brandl, F., Reverencic, I., Cartellieri, W., and Dent, J.C.: Turbulent Air Flow in the Combustion Bowl of a D.I. Diesel Enginie and Its Effect on Engine Performance. SAE 790040.

125. Khan, M., Greeves, G., and Wang, C.H: Factors Affecting Smoke and Gaseous Emissions from Direct Injection Engines and a Method of Calculation. SAE 730169.

APPENDIX A

EQUILIBRIUM CALCULATIONS

By assuming that the combustion reaction can be approximated by the following equation:

$$C_n H_m + \text{Air} \longrightarrow H + O + N + H_2 + OH + CO + NO + O_2 + H_2O + CO_2 + N_2$$

the appropriate balanced equation can be written as:

$$y[C_nH_m + (n + \frac{m}{4})(O_2 + 3.76\ N_2)] \longrightarrow X_1H + X_2O + X_3\ N + X_4\ H_2 + X_5\ OH + X_6\ CO + X_7\ NO + X_8\ O_2 + X_9\ H_2O + X_{10}\ CO_2 + X_{11}\ N_2$$

where X_i = mole fraction of product specie i.

y = moles of fuel that will give one mole of combustion products.

The left hand side of the reaction equation can be given as:

$$y(nC + mH + rO_2 + r_1\ N_2)$$

where $r = n + m/4$

$r_1 = 3.76r$

Atom mass balances for Carbon, Hydrogen, Oxygen and Nitrogen can be carried out as follows:

$$\text{C balance} : X_6 + X_{10} = ny \quad \text{(A1)}$$

$$\text{H balance} : X_1 + 2X_4 + X_5 + 2X_9 = my \quad \text{(A2)}$$

$$\text{O balance} : X_2 + X_5 + X_6 + X_7 + 2X_8 + X_9 + 2X_{10} = 2ry \quad \text{(A3)}$$

$$\text{N balance} : X_3 + X_7 + 2X_{10} = 2r_1y \quad \text{(A4)}$$

When properly balanced and solved, the mole fractions will add up to unity, i.e.

$$\sum_{i=1}^{11} X_i = 1 \qquad \text{(A5)}$$

Equations A1 to A5 have to be solved simultaneously, but as there are 12 unknowns - X_i and y - we need to introduce seven more equations. By introducing 7 equilibrium constants chosen to represent seven non-redundant reactions, the equations can be made soluble. The following reactions are considered:

$1/2\ H_2 \longrightarrow H$	$k_1 = X_1\ P^{1/2}/X_4^{1/2}$
$1/2\ O_2 \longrightarrow O$	$k_2 = X_2\ P^{1/2}/X_8^{1/2}$
$1/2\ N_2 \longrightarrow N$	$k_3 = X_3\ P^{1/2}/X_{11}^{1/2}$
$1/2\ H_2 + 1/2\ O_2 \longrightarrow OH$	$k_4 = X_5/(X_8^{1/2}.X_{11}^{1/2})$
$1/2\ O_2 + 1/2\ N_2 \longrightarrow NO$	$k_5 = X_7/(X_8^{1/2}.X_{11}^{1/2})$
$H_2 + 1/2\ O_2 \longrightarrow H_2O$	$k_6 = X_9/(X_4.X_8^{1/2}.P^{1/2})$
$CO + 1/2\ O_2 \longrightarrow CO_2$	$k_7 = X_{10}/(X_6.X_8^{1/2}.P^{1/2})$

k_1 to k_7 represent partial pressure equilibrium constants for the respective reactions, and P is the total pressure (in atmospheres) in the cylinder. By making proper substitutions as shown below, it is possible to re-write equations (A1) to (A5) in terms of only four variables: the mole fractions of H_2 (X_4), CO (X_6), O_2 (X_8), and N_2 (X_{11}):

$X_1 = C_1\ X_4^{1/2}$	where	$C_1 = k_1/P^{1/2}$	(A6)
$X_2 = C_2\ X_8^{1/2}$	where	$C_2 = k_2/P^{1/2}$	(A7)
$X_3 = C_3\ X_{11}^{1/2}$	where	$C_3 = k_3/P^{1/2}$	(A8)
$X_5 = C_4\ X_4^{1/2}\ X_8^{1/2}$	where	$C_4 = k_4$	(A9)
$X_7 = C_5\ X_8^{1/2}\ X_{11}^{1/2}$	where	$C_5 = k_5$	(A10)
$X_9 = C_6\ X_4.X_8^{1/2}$	where	$C_6 = k_6P^{1/2}$	(A11)
$X_{10} = C_7.X_6.X_8^{1/2}$	where	$C_7 = k_7.P^{1/2}$	(A12)

Re-arranging equation (A1) gives y as:

$$y = \frac{X_6 + X_{10}}{n} \qquad \text{(A13)}$$

Substituting equations (A6) to (A13) into eqns. (A2) to (A5) yields four equations of the form:

$$f_i = f_i\,(X_4,\ X_6,\ X_8,\ X_{11}) = 0$$

The four equations are non-linear, and so are solved iteratively using Newton-Raphson for a system of equations. This involves linearising the equations by formulating the following matrix equation:

$$\begin{bmatrix} \frac{\partial f_1}{\partial X_4} & \frac{\partial f_1}{\partial X_6} & \frac{\partial f_1}{\partial X_8} & \frac{\partial f_1}{\partial X_{11}} \\ \frac{\partial f_2}{\partial X_4} & \frac{\partial f_2}{\partial X_6} & \frac{\partial f_2}{\partial X_8} & \frac{\partial f_2}{\partial X_{11}} \\ \frac{\partial f_3}{\partial X_4} & \frac{\partial f_3}{\partial X_6} & \frac{\partial f_3}{\partial X_8} & \frac{\partial f_3}{\partial X_{11}} \\ \frac{\partial f_4}{\partial X_4} & \frac{\partial f_4}{\partial X_6} & \frac{\partial f_4}{\partial X_8} & \frac{\partial f_4}{\partial X_{11}} \end{bmatrix} \cdot \begin{bmatrix} \Delta X_4 \\ \Delta X_6 \\ \Delta X_8 \\ \Delta X_{11} \end{bmatrix} = \begin{bmatrix} -f_1 \\ -f_2 \\ -f_3 \\ -f_4 \end{bmatrix}$$

The linearised equations are solved using Gaussian elimination to give the first approximations of ΔX_4, ΔX_6, ΔX_8, ΔX_{11} from which:

$$X'_j = X_j + \Delta X_j \qquad \text{where } j = 4,\ 6,\ 8,\ 11$$

Using this new approximation as the next input in the solution of the matrix, the procedure is repeated until convergence is obtained in all the f_i (they should all approach zero). The following expressions represent the partial derivatives involved:

$$\frac{\partial f_1}{\partial X_4} = \frac{1}{2} C_1 X_4^{-1/2} + 2 + 2 C_6 X_8^{1/2} + \frac{1}{2} C_4 X_4^{-1/2} X_8^{1/2}$$

$$\frac{\partial f_1}{\partial x_6} = - d_o \, (1 + C_7 \, x_8^{1/2})$$

$$\frac{\partial f_1}{\partial x_{11}} = \frac{1}{2} \, [C_4 \, x_4^{1/2} + 2 \, C_6 \, x_4 - d_0 \, C_7 \, x_6] \, x_8^{-1/2}$$

$$\frac{\partial f_1}{\partial x_{11}} = 0$$

$$\frac{\partial f_2}{\partial x_4} = \frac{1}{2} \, C_4 \, x_8^{1/2} \, . \, x_4^{-1/2} + C_6 \, x_8^{1/2}$$

$$\frac{\partial f_2}{\partial x_6} = 1 - d_1 + (2 - d_1) \, C_7 \, x_8^{1/2}$$

$$\frac{\partial f_2}{\partial x_8} = \frac{1}{2} \, C_4 \, x_4^{1/2} \, x_8^{-1/2} + \frac{1}{2} \, C_6 \, x_4 . x_8^{-1/2} + \frac{1}{2} \, [\, C_2 + (2 - d_1) \, C_2 \, x_6 \,]$$

$$x_8^{-1/2} + 2 + \frac{1}{2} \, C_5 \, x_{11}^{1/2} \, x_8^{-1/2}$$

$$\frac{\partial f_2}{\partial x_{11}} = \frac{1}{2} \, C_5 \, x_8^{1/2} \, x_{11}^{1/2}$$

$$\frac{\partial f_3}{\partial x_4} = 0$$

$$\frac{\partial f_3}{\partial x_6} = - d_2 \, [1 + C_7 \, x_8^{1/2}]$$

$$\frac{\partial f_3}{\partial x_8} = - \frac{1}{2} \, C_7 \, x_6 \, d_2 \, x_8^{-1/2} + \frac{1}{2} \, C_5 \, x_{11}^{1/2} \, x_8^{-1/2}$$

$$\frac{\partial f_3}{\partial x_{11}} = 2 + \frac{1}{2} C_3 \, x_{11}^{-1/2} + \frac{1}{2} C_5 \, x_{11}^{1/2} \, x_8^{-1/2}$$

$$\frac{\partial f_4}{\partial x_4} = 1 + \frac{1}{2} C_1 \, x_4^{-1/2} + \frac{1}{2} C_4 \, x_8^{1/2} \, x_4^{-1/2} + C_6 \, x_8^{1/2}$$

$$\frac{\partial f_4}{\partial x_6} = 1 + C_7 \, x_8^{1/2}$$

$$\frac{\partial f_4}{\partial x_8} - 1 + \frac{1}{2} [C_2 + C_4 \, x_4^{1/2} + C_6 \, x_4 + C_7 \, x_6 + C_5 \, x_{11}^{1/2}] . x_8^{-1/2}$$

$$\frac{\partial f_4}{\partial x_{11}} = 1 + \frac{1}{2} C_3 \, x_{11}^{-1/2} + \frac{1}{2} C_5 \, x_8^{1/2} \, x_{11}^{-1/2}$$

where $f_1 = x_1 + 2x_4 + x_5 + 2x_9 - \frac{m}{n} (x_6 + x_{10}) = 0$

$$f_2 = x_2 + x_5 + x_6 + x_7 + 2x_8 + x_9 + 2x_{10} - \frac{2n}{n} (x_6 + x_{10})$$

$$f_3 = x_3 + x_7 + 2x_{11} - \frac{2r_1}{m} (x_6 + x_{10})$$

$$f_4 = x_1 + x_2 + x_3 + x_4 + x_5 + x_6 + x_7 + x_8 + x_9 + x_{10} + x_{11} - 1$$

APPENDIX B

BOWL GEOMETRY CALCULATIONS

REQUIRED INPUT DATA (see Figure 2.7)

1. d_B
2. α
3. h
4. r_1, r_2
5. β

Define $r_B = d_B/2$.

1. Curve (1):

This part is defined by the basic equation for a straight line:

$$y = m_1 X + C_1 \qquad \text{(B1)}$$

where $m_1 = \tan \emptyset$

$\emptyset = \pi/2 - \alpha$

At $X = r_B$, $y = h$, so that equation (B1) can be expressed as:

$$h = r_B.m_1 + C_1$$

from which

$$C_1 = h - m_1.r_B \qquad \text{(B2)}$$

2. Curve (2):

This represents an arc of radius r_1, centred at $y = r_1$ (the x-axis forms a tangent to the arc). To determine the coordinates of the centre, a line parallel to curve (1) at a distance r_1 from it, is

defined by:

$$y' = m_1 X + C'_1 \qquad \text{(B3)}$$

The diagram below shows a graphical representation:

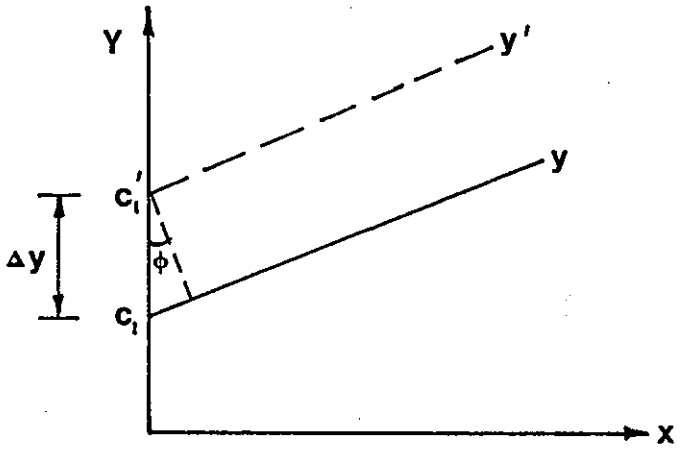

The slope of line y' is equal to that in equation (B1), i.e. m_1, but with a different intercept, C'_1 defined by:

$$C'_1 = C_1 + \Delta Y \qquad \text{(B4)}$$

Δy is defined by the following equation:

$$\Delta y = \frac{r_1}{\cos \phi} \qquad \text{(B5)}$$

Combining equations (B2), (B4) and (B5) yields:

$$C'_1 = h - r_B . \tan \phi + \frac{r_1}{\cos \phi} \qquad \text{(B6)}$$

Equation (B3) intersects the line $y = r_1$ at the centre of the circle for which curve (B2) forms a part, so that:

$$r_1 = m_1 X + C'_1 \qquad \text{(B7)}$$

which then yields the X-coordinate for the centre of the circle by:

$$X_2 = \frac{r_1 \left(1 - \frac{1}{\cos \phi}\right) - C_1}{m_1} \qquad \text{(B8)}$$

The corresponding y-coordinate is:

$$Y_2 = r_1 \qquad \text{(B9)}$$

The equation defining a circle of radius r_1, whose centre is at (X_2, Y_2) is:

$$X^2 + y^2 - 2X_2.X - 2y_2.y + C2 = 0 \qquad \text{(B10)}$$

where $$C_2 = X_2^2 + y_2^2 - r_1^2$$

By substituting equation (B9) into the definition, it is seen that C_2 acquires the following simpler form:

$$C_2 = X_2^2 \qquad \text{(B11)}$$

Curve (2) is defined between curve (1) on one side, and curve (3) on the other. The arc meets both lines at tangents, so by translating the axes so that the origin is at the centre defined by the coordinates (X_2, y_2), the point of contact between curve (2) and curve (1) is (X'_{12}, y'_{12}) where X_{12} and y_{12} are defined by:

$$x'_{12} = -\frac{m_1 C''_1}{1 + m_1^2} \qquad y'_{12} = \frac{C''_1}{1 + m_1} \qquad \text{(B12)}$$

As X'_{12} and y'_{12} are taken w.r.t (X_2,y_2), the constant C''_1 is the corresponding translated equivalent of C_1 defined by:

$$C''_1 = y_2 - (m_1.X_2 + C_1) \qquad \text{(B13)}$$

Written in terms of the original coordinate axes, the point of contact between curves (1) and (2) is given by (X_{12}, Y_{12}) where:

$$X_{12} = X_2 - X'_{12} \qquad \text{(B14)}$$

$$Y_{12} = Y_2 - Y'_{12} \qquad \text{(B15)}$$

The point of contact between curves (2) and (3) is similarly derived, after defining the equation for the straight line representing curve (3). The slope for curve (3), m_3, is:

$$m_3 = - \tan \psi \qquad \text{(B16)}$$

$$\text{where} \quad \psi = 1/2 \ (\pi - \beta) \qquad \text{(B17)}$$

3. Equation (B18) thus defines the straight line, curve (3).

$$Y = m_3 + C_3 \qquad \text{(B18)}$$

The coordinates (X_{23}, Y_{23}) define the point of contract between curves (2) and (3) which is defined as shown in Figure (B1).

$$X_{23} = X_2 - r_1 \sin \psi \qquad \text{(B19)}$$

$$Y_{23} = Y_2 - r_1 \cos \psi \qquad \text{(B20)}$$

The point (X_{23}, Y_{23}) lies on the line represented by equation (18), i.e.

$$Y_{23} = m_3 . X_{23} + C_3 \qquad \text{(B21)}$$

From which the constant C_3 is derived as:

$$C_3 = Y_{23} - m_3 . x_{23} \qquad \text{(B22)}$$

4. <u>Curve (4):</u>

The method used to find the centre of the arc (2) is also used to find that of arc (4). A line parallel to (3) is drawn at a distance r_2 from curve (3). The centre of the circle lies at X = 0, so the intercept corresponds to the y-coordinate. The equation is:

$$y' = m_3X' + C'_3 \tag{B23}$$

where

$$C_3' = C_3 - \frac{r_2}{\sin(\beta/2)} \tag{B24}$$

The equation for the circle of radius r_2 with a centre at (0, C'_3) is thus:

$$X^2 + y^2 - 2C'_3\, y + C_4 = 0 \tag{B25}$$

where

$$C_4 = C'^2_3 - r_2^2 \tag{B26}$$

This is defined in the interval $0 \leqslant X \leqslant X_{34}$.

The roots of equation (B10), in terms of X_o and y respectively are:

$$X = X_2 + \sqrt{2r_1\, y - y^2} \tag{B27}$$

$$y = r_1 + \sqrt{r^2 - X^2 + 2X_2.X - X_2^2} \tag{B28}$$

By assuming an elemental section of height dy to be a truncated cone with a base radius of (X + dx) and an upper radius X, then the corresponding slant height is:

$$S = (dX^2 + dy^2)^{1/2} \tag{B29}$$

And the surface area of the sides of the cone is:

$$dA = \pi.s.\ (D + d) \qquad (B30)$$

where $D = 2(X + dX)$

$d = 2X$

The total surface area is obtained by integrating equation (B30):

$$A = \int \pi\ s\ (D + d) \qquad (B31)$$

The bowl geometry is calculated as the volume of a cylinder of diameter d_B and height h, less the volume of any protrusions into the cylinder i.e.

$$V = \frac{\pi d_B^{\,2}}{4}.h - \int\int \pi\ y\ (2X + dX)\ dx \qquad (B32)$$

Numerical integration is used in the model to determine answers to equations (B31) and (B32).

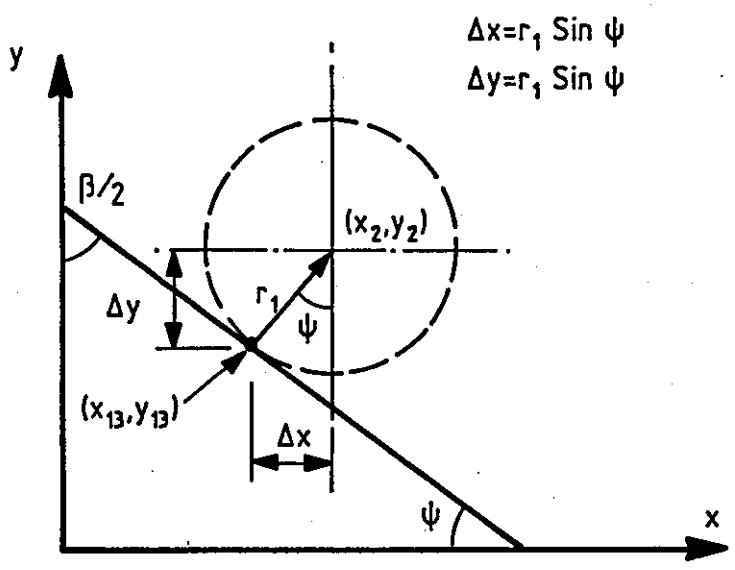

FIGURE B1: DERIVATION OF COMBUSTION BOWL EQUATION

APPENDIX C

DERIVATION OF SWIRL MOTION EQUATION

The equation describing the variation of swirl intensity in the combustion bowl during compression is based on the assumption that angular momentum is conserved. As the piston moves upwards through a distance ds (Fig. 3.4), a proportion of air in the annular space is displaced to the central zone. This leaves a volume dV_a which is refilled by air pushing in from the outer radii. Urlaub (15) expresses the mass of air vacating dV_a by the following equation:

$$dm_a = \rho_a \cdot dV_a \cdot (1 - \frac{V_a}{V}) \qquad (C1)$$

where V_a is the volume of the annular space and V the total cylinder volume, both refering to a given crank position. The annular volume, dV_a, may be expressed by equation (C2).

$$dV_a = \pi r_B y \, dr \qquad (C2)$$

The angular momentum of the air mass in volume dV_a, which is transferred to the central zone may be expressed by equation (C3).

$$d\alpha = I \cdot \omega_o \qquad (C3)$$

where I, the mass moment of inertia of the cylindrical element of mass dm, with a radius $(r_B + dr)$ is defined as follows:

$$I = dm \, (r_B + dr)^2 \qquad (C4)$$

The angular momentum in the section with thickness dr_2 in Fig. 3.4(b) is given by:

$$d\alpha_2 = \omega_o \, (r_B + dr_1 + dr_2)^2 \, dm_2 \qquad (C5)$$

and in the i^{th} section, the angular momentum is

$$d\alpha_i = \omega_o (r_B + \sum_i dr_i)^2 \, dm_i \qquad (C6)$$

In the limit, as dr→0, equation (C6) may be given by equation (C7).

$$d\alpha_i = \omega_o (r_B + \int dr)^2 \, dm_i \qquad (C7)$$

The total angular momentum transferred into the central zone during compression is obtained by integrating equation (C7) from the closure of inlet valve (IVC) to TDC.

$$\alpha = \int \omega_o (r_B + \int dr)^2 \, dm \qquad (C8)$$

Re-arranging equation (C2) and substituting into equation (C8) yields the following equation:

$$\alpha = \int \omega_o (r_B + \int \frac{dV_a}{\pi r_B y})^2 \, dm \qquad (C9)$$

A simplifying assumption may be made by equating dV_a to the change in annular space due to the upward motion of the piston given in equation (C10).

$$dV_a = \frac{\pi}{4} (B^2 - d_B^2) \cdot ds \qquad (C10)$$

The integral within brackets in equation (C9) may then be expressed in terms of the instantaneous stroke, s, and integrated, as shown in equation (C11), from the start of compression (stroke = S_o) to any crank position (stroke = s).

$$\int_{S_o}^{s} \frac{dV_a}{\pi r_B y} = \frac{B^2 - d_B^2}{8 r_B} \int_{S_o}^{s} \frac{ds}{y} \qquad (C11)$$

The variable y is composed of the stroke, s, and the clearance height y_o. Substituting these into equation (C11) and integrating, yields the following expression:

$$\int_{S_o}^{s} \frac{dV_a}{\pi r_B y} = \frac{B^2 - d_B^2}{8 r_B} \cdot \ln \left[\frac{y_o + s}{y_o + s_o}\right] \qquad (C12)$$

It is thus possible to express equation (C9) as shown in (C13).

$$\alpha = \int_{S_o}^{s} \omega_o \left[r_B + \frac{B^2 - d_B^2}{r_B} \cdot \ln \left(\frac{y_o + s}{y_o + s_o}\right)\right]^2 \cdot dm \qquad (C13)$$

This is the form in which the equation appears in the proposed model.

Urlaub (20) has suggested that for all practical purposes, the motion of air in the cylindrical recess may be treated as that of a solid body so that the angular velocity in the bowl at any crank position is given by equation (C14), where α_o is the angular momentum of air in the bowl at the start of compression, I_o and m_o the corresponding moment of inertia and mass of air.

$$\omega = \frac{\alpha_o + \alpha}{I_o} \qquad C14)$$

I_o is defined as follows:

$$I_o = \frac{1}{2} m_o r_B^2 \qquad (C15)$$

APPENDIX D

THEORETICAL TREATMENT OF FILM FLOW

The following analysis shows the derivation of the velocity decay equation for a two-dimensional film flow on the wall, based on momentum considerations. Let us consider a control element such as that illustrated in Fig. D1.

The force exerted on the film by shear stress at the wall is:

$$F_o = - \tau_o \, b \Delta x \tag{D1}$$

where b is the breadth of the film, which is considered constant. The net momentum flux in the x-direction is:

$$M_x = \frac{\partial}{\partial x} (\rho U_x^2 A) \Delta x \tag{D2}$$

The time rate of increase of momentum is:

$$\Delta M_t = \frac{\partial}{\partial t} (\rho U_x A \, . \Delta x) \tag{D3}$$

The time variable is included as the flow of the injected film is a transient phenomenon and, therefore, essentially time dependent.

A force balance on the control element yields the following:

$$(\tau_i - \tau_o) \, b . \Delta x + \frac{\partial}{\partial x} (\rho U_x^2 A) \, \Delta x + \frac{\partial}{\partial t} (\rho U_x A \, . \Delta x) = 0 \tag{D4}$$

The combination $\rho . A . \Delta x$ represents the mass of the element, which may be expressed as Δm, and A is the cross-sectional area of the film, which may be given by (S.b). Expanding equation (D4) and dividing through by the mass yields:

$$\frac{\tau_i - \tau_o}{\rho s} + 2U \frac{\partial U_x}{\partial x} + \frac{U_x^2}{A} \cdot \frac{\partial A}{\partial x} + \frac{U_x}{A} \frac{\partial A}{\partial t} + \frac{\partial U_x}{\partial t} = 0 \tag{D5}$$

Applying continuity to the control volume yields:

$$\rho\, q\Delta x - \frac{\partial}{\partial x}(\rho A U_x)\,.\Delta x = \frac{\partial}{\partial x}(\rho A \Delta x) \qquad \text{(D6)}$$

where q is the volume flow rate from the surface of the film, per unit length ($m^3/m.s$). Expanding equation (D6) and dividing through by $\rho.\Delta x$ gives:

$$U_x \frac{\partial A}{\partial x} + \frac{\partial A}{\partial t} + A \frac{\partial U_x}{\partial x} = q \qquad \text{(D7)}$$

multiplying through by U_x/A in equation (D7):

$$\frac{U_x^2}{A} \cdot \frac{\partial A}{\partial x} + \frac{U_x}{A} \frac{\partial A}{\partial t} + U_x \frac{\partial U_x}{\partial x} = U_x \frac{q}{A} \qquad \text{(D8)}$$

Equations (D5) and (D8) must be solved simultaneously as they refer to the same control volume. Subtracting equation (D8) from (D5):

$$\frac{(\tau_i - \tau_o)}{\rho s} + U_x \frac{\partial U_x}{\partial x} + \frac{\partial U_x}{\partial t} + U_x \frac{q}{A} = 0 \qquad \text{(D9)}$$

The continuity equation may now be re-written as:

$$U_x\, b \frac{\partial U_x}{\partial x} + b \frac{\partial Y}{\partial t} + A \frac{\partial U_x}{\partial x} - q = 0 \qquad \text{(D10)}$$

This can be seen to be so since the assumption of a constant film breadth, b, implies:

$$\frac{\partial A}{\partial x} = \frac{\partial A}{\partial y} \cdot \frac{\partial y}{\partial x} = b \frac{\partial y}{\partial x}$$

$$\frac{\partial A}{\partial t} = \frac{\partial A}{\partial y} \cdot \frac{\partial y}{\partial t} = b \frac{\partial y}{\partial t} \qquad \text{(D11)}$$

Equations (D9) and (D10) are non-linear partial differential equations describing the behaviour of gradually varying unsteady free-surface flows.

The method of characteristics may be used to obtain a solution of the two equations. By making the following substitutions:

$$L_1 = \frac{(\tau_i - \tau_o)}{\rho s} + U_x \frac{\partial U_x}{\partial x} + \frac{\partial U_x}{\partial t} + U_x \frac{q}{A} = 0$$

$$L_2 = b\, U_x \frac{\partial Y}{\partial x} + b \frac{\partial Y}{\partial t} + A \frac{\partial U_x}{\partial x} - q = 0$$

the two equations can be linearly combined using an unknown multiplier, λ:

$$L = L_1 + \lambda L_2 = 0 \qquad \text{(D12)}$$

This gives the following expression for L:

$$L = f(U_x) + b\lambda g(y) + \left(\frac{\tau_i - \tau_o}{\rho s}\right) + q\left(\frac{U_x}{A} - \lambda\right) \qquad \text{(D13)}$$

where the functions f and g are defined by:

$$f(U_x) = (U_x + \lambda A)\frac{\partial U_x}{\partial x} + \frac{\partial U_x}{\partial t} \qquad \text{(D14)}$$

$$g(y) = U_x \frac{\partial Y}{\partial x} + \frac{\partial Y}{\partial t} \qquad \text{(D15)}$$

$f(U_x)$ will yield the total derivative, $\frac{dU_x}{dt}$, if:

$$\frac{dx}{dt} = U_x + \lambda A \qquad \text{(D16)}$$

and g(y) will yield $\frac{dy}{dt}$ if:

$$\frac{dx}{dt} = U_x \qquad \text{(D17)}$$

Equations (D16) and (D17) must be equal for this to be sensible, hence $\lambda = 0$. Substituting this into equation (D12) yields the following equation for the velocity decay:

$$\frac{dU_x}{dt} = \frac{(\tau_i - \tau_o)}{\rho s} - U_x \frac{q}{A} \qquad (D18)$$

Although it may be possible to derive equation D18 from physical arguments, with appropriate assumptions (91, 93), the importance of starting the analysis from equations D4 and D6 is to demonstrate the governing equations which form the basis of the problem to be solved, thus offering possibilities for enhancing the capability of the computer code by devising numerical techniques to solve the basic equations without making the simplifying assumptions given by equations D10 and D11. A more accurate method, however, can only be obtained if a variation of the film breadth, b, is given. Otherwise closure is not possible, with three unknowns; U_x, s, b, and only two equations.

Non-Dimensional Linear Momentum Equation

Assuming steady state flow in the film, the linear momentum equation is expressed by equation (D4). The film is subjected to the following major forces:

i. Viscous forces, F_v
ii. Gravity forces, F_g
iii. Forces on the free surface (surface tension), F_s
iv. Frictional forceson the wall, F_f

So equation (D4) may be expressed in the following form:

$$F_v + F_g + F_s + F_f = \frac{d}{dt}(MU_x) \qquad (D19)$$

Conservation of linear momentum implies that the momentum flux at any

position x, given by $\rho_x U_x^2 A_x$, equals that at the nozzle exit, given by $\rho_o U_o^2 A_o$. Since the right hand side of equation (D19) may be written as $\rho_x U_x^2 A_x$ and the equation will still hold if both sides are divided by $\rho_o U_o^2 A_o$ (which is a constant), the following is the non-dimensionalised form of equation (D19):

$$\frac{F_v}{\rho_o U_o^2 A_o} + \frac{F_g}{\rho_o U_o^2 A_o} + \frac{F_s}{\rho_o U_o^2 A_o} + \frac{F_f}{\rho_o U_o^2 A_o} = \rho' U'^2 A' \qquad \text{(D20)}$$

$$\text{where } \rho' = \frac{\rho_x}{\rho_o} \quad , \quad U' = \frac{U_x}{U_o} \quad , \quad A' = \frac{A_x}{A_o}$$

The terms on the left hand side of equation (D20) represent reciprocals of Reynolds, Froude, Weber numbers, and the friction coefficient, respectively, so that the equation may be written as shown in equation (D21).

$$\frac{1}{R_e} + \frac{1}{F_r} + \frac{1}{W_e} + \frac{1}{C_f} = \rho' U'^2 A' \qquad \text{(D21)}$$

The order of magnitude of each term on the left hand side signifies its importance in influencing the momentum flux inthe flow. This has been utilised in Chapter 5 to develop equations for the dynamic similitude of film flow.

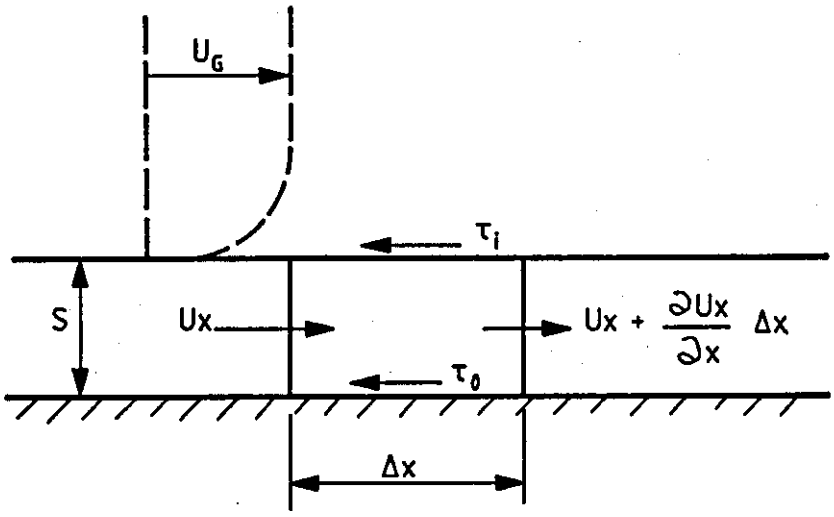

FIGURE D1: FORCE BALANCE ON THE ELEMENTAL SECTION OF FILM THICKNESS

APPENDIX E

DERIVATION OF THE POSITION VECTOR OF FILM SURFACE LEADING EDGE

The characteristics of the film patch can be estimated without much loss of accuracy by considering a paraboloic velocity profile across the patch, having the form in equation (E1):

$$U_z = U_m \left(1 - \frac{z^2}{b^2}\right) \tag{E1}$$

where quantities are as defined in Figure 3.9(a). The position vector, r, defining any point on the advancing edge of the film can be expressed algebraically as

$$\frac{dr}{dt} = U_z \tag{E2}$$

By substituting equations (3.45) and (E1) into equation (E2) the following expression results:

$$\frac{dr}{dt} = \frac{C\,U_o}{\left(\frac{x}{d_o'}\right)^a}\left(1 - \frac{z^2}{b^2}\right) \tag{E3}$$

The variable b, defining half the breadth of the film, can be expressed as

$$b = x \tan \theta \tag{E4}$$

Hence equation (E3) can be integrated to yield the following expression for the position vector:

$$r = \left[\frac{C(a+1)\, U_o d_o'^{a}}{(\cos \phi)^{a}} \left(1 - \frac{\tan^2 \phi}{\tan^2 \theta}\right) t\right]^{\frac{1}{a+1}} + \frac{x_o}{\cos \phi} \qquad \text{(E5)}$$

Equation (E4) may be rewritten, by substituting equation (3.48) into it, as:

$$r = x \left[\frac{1 - \left(\frac{\tan \phi}{\tan \theta}\right)^2}{\cos^{a} \phi}\right]^{\frac{1}{1+a}}$$

where x is the film penetration along the piston wall.